In situ and ex situ characterization of the ion-irradiation effects in third generation SiC fibers

Juan Francisco Huguet-Garcia

Université Pierre et Marie Curie

Physique et Chimie des Matériaux (ED 397)

Commissariat à l'énergie atomique et aux énergies alternatives

Service de Recherches Métallurgiques Appliquées

Laboratoire d'Etude du Comportement Mécanique des Matériaux

In situ and *ex situ* characterization of the ion-irradiation effects in third generation SiC fibers

A thesis submitted by

Juan HUGUET-GARCIA

for the degree of

Docteur de l'Université Pierre et Marie Curie

under the direction of

Dr. Jean-Marc COSTANTINI

and supervision of

Dr. Aurélien JANKOWIAK

Presented and defended on Friday, October 2nd, 2015.

In front of a jury composed by:

Prof. D. GOURIER	as	President
Prof. W.J. WEBER	as	Reviewer
Dr. N. MONCOFFRE	as	Reviewer
Dr. M.F. BEAUFORT	as	Reviewer
Dr. A. LERICHE	as	Examiner
Dr. J.-M. COSTANTINI	as	Examiner
Dr. A. JANKOWIAK	as	Invited

A mi familia, LLorenç, Grace, Cris y Patri, por vuestro amor constante e incondicional.

A mis viejas amistades, por compartir mis alegrías y penas aun en la distancia.

A mis nuevas amistades, por llenar París de música, risas y color.

Y, sobre todo, a la mujer de mi vida. Irene, por ti hay un yo; sin ti, ni soy.

Acknowledgements

Perhaps the most important lesson I have learned during my period as PhD student is that science is a matter of collaboration. I am much obliged to all who helped me and shared with me this experience. Without any doubt, the work here presented would not have been possible without the aid of my advisers and colleagues.

First person to acknowledge is, Dr. A. Jankowiak, for his guidance, "savoir-faire" and patience—even when things did not worked as expected. Also, my acknowledgments go to Dr. S. Miro, who played an important role during all the PhD period, specially during the ion-irradiation and Raman spectroscopy campaigns, and to Dr. J.M. Costantini, whose vast knowledge impressed me since the beginning and was source of many good hints. I would like to thank P. Chapelot and L. Nicolas for they welcome to the SRMA/LC2M and their endorse to this research project.

Also, my acknowledgments go to all those who helped me during the experimental procedures: To E. Bordas, F. Lepretre, H. Martin, Y. Serruys and L. Beck from JANNUS-Saclay, A. Debelle and L. Thomé from JANNUS-Orsay, and I. Monnet, C. Grygiel and T. Madi from GANIL for their support during the irradiation campaigns. To P. Bonnaillie, R. Podor and E. Meslin for their support with the SEM, E-SEM and TEM characterization. To T. Vandenberghe, for his support in multiple tasks—specially those concerning long nights side by side running the *in situ* tensile tests and, finally, to D. Troadec and Mr. B. Arnal for the preparation of the samples for TEM observations.

Last but not least, my acknowledgments go to my colleagues of the SRMA, specially to F. Bernachy-Barbé, F. Ouaki, Y. Chen, L. Gélébart, D. Menut and D. Gosset. It has been a real pleasure to share these three years at the CEA with you.

"Se convencerán de que la ciencia, se entiende toda la ciencia de cosas, sean éstas corporales o espirituales, es tanto obra de imaginación como de observación, que esta última no es posible sin aquélla —en suma, que la ciencia es construcción. Este carácter, en parte al menos, imaginativo de la ciencia, hace de ella una hermana de la poesía."

—José Ortega y Gasset, *Entorno a Galileo.*

Contents

List of Figures

LIST OF FIGURES

List of Tables

Glossary

μRs Micro-Raman spectroscopy; a spectroscopic technique based in the inelastic scattering of a monochromatic incident light

AFM Atomic Force Microscope; a very high-resolution type of scanning probe microscopy with resolution on the order of fractions of a nanometer

CMC Ceramic Matrix Composite; a composite materials consisting of ceramic fibers embedded in a ceramic matrix

CVD Chemical Vapor Deposition; a chemical process where a substrate is exposed to volatile precursor which react on the substrate surface to produce the desired compound

CVI Chemical Vapor Infiltration; a ceramic engineering process whereby matrix material is infiltrated into fibrous preforms by the use of reactive gases at elevated temperature to form fiber-reinforced composites

dpa Displacement per atom; the standard damage level measure. 1 dpa is equivalent to the displacement of every target atom from its lattice site

E-SEM Environmental Scanning Electron Microscopy; a type of scanning electron microscope that can be operated from vacuum to atmospheric pressures

GB Grain Boundary; the interface between two grains, or crystallites, in a polycrystalline material

HNS Hi Nicalon type S; a nuclear grade SiC fiber manufactured by Nippon Carbon (Japan)

LRO Long-Range Order; orderliness of lattice atoms repeated over great distances

LWR Light Water Reactor; a current type of nuclear reactor that uses normal water as coolant

NPP Nuclear Power Plants; a thermal power station in which the heat source is a nuclear reactor

ODS Oxide Dispersion Strenghtened alloys; alloys that contain a high density of small oxide particles dispersed in their matrix

PCS PolyCarboSilane; a polymeric precursor used in the fabrication of Nicalon SiC fibers

PKA Primary Knock-on Atom; the first lattice atom that is displaced from its equilibrium site by an incident particle

PTCS PolyTitanoCarboSilane; PCS doped with Ti used in the fabrication of Tyranno SiC fibers

SEM Scanning Electron Microscopy; a microscopy technique in which an image of the sample is produced by the backscattered electrons of an incident electron beam

SiC Silicon Carbide; chemical formula

SiC/SiC SiC-based composite; a type of CMC consisting of SiC fibers densified with a CVI-SiC matrix

SRO Short-Range Order; orderliness of lattice atoms over distances comparable to interatomic distances

TEM Transmission Electron Microscopy; a microscopy technique in which a beam of electrons is transmitted through an ultra-thin specimen

TSA3 Tyranno SA3; a nuclear grade SiC fiber manufactured by Ube Industry (Japan)

1

Introduction

One of the main challenges humankind will face in the years to come is to satisfy the ever-increasing energy demand. In a global warming scenario, where running out fossil fuels are the major greenhouse effect gas sources, renewable energy sources together with future fusion and Generation IV fission nuclear power plants (NPPs)[1] are potential candidates to overcome the energy supply challenge.[1,2]

Nowadays nuclear reactors, so-called Generation II and III, are among the most extreme environments for structural materials as they are exposed to high temperatures, corrosive environments and severe mechanical loadings while exposed to neutron and ion-irradiation. For instance, neutron exposure displaces numerous atoms from their lattice sites inducing material degradation. Such degradation may limit the material in-pile lifetime and is manifested in several forms: irradiation hardening and embrittlement, phase instabilities, precipitation, irradiation creep and volumetric swelling.[3] Future nuclear applications include the deployment of the so-called Generation IV fission reactors and fusion reactors. Indeed, as it can be observed in Figure 1.1, their nominal operating temperatures and doses[2] are significantly higher than in current nuclear reactors.

[1] For all abbreviations see the glossary on page xviii.

[2] 1 dpa (displacement per atom) is the standard damage level measure and is equivalent to the displacement of every target atom from its lattice site.

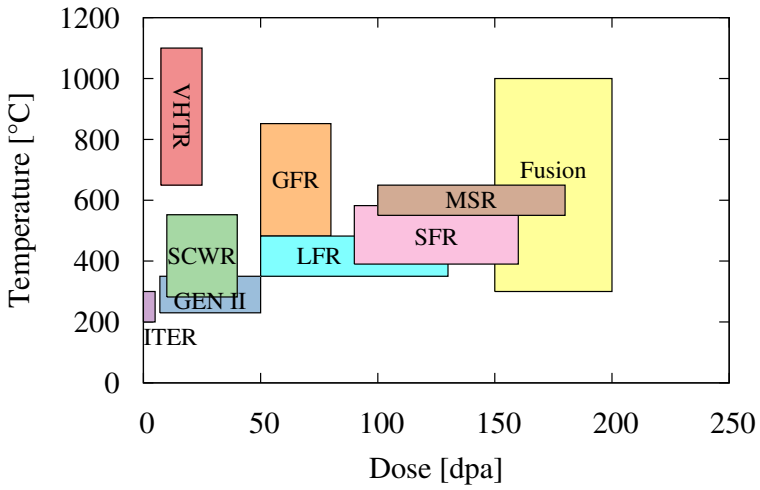

Figure 1.1: Operating temperatures and displacement damage dose regimes for structural materials in current (Gen II) and future nuclear applications - VHTR: Very High Temperature Reactor, SCWR: Super Critical Water Reactor, LFR: Lead Fast Reactor, GFR: Gas Fast Reactor, SFR: Sodium Fast Reactor and MSR: Molten Salt Reactor. Adapted from Ref.[3]

Intensive research is currently carried out at the French Atomic Energy and Alternative Energies Commission (CEA) concerning the development of high-performance structural materials. Such materials must withstand extreme environments while ensuring the safety and reliability of future nuclear applications therefore becoming crucial for their successful development.

Candidate materials for Generation IV NPPs depend on the reactor design. For instance, ferritic/martensitic and oxyde dispersion strenghtened (ODS) steels are suitable for sodium and lead cooled fast reactors. On the other hand, ceramic matrix composites (CMCs) are considered as structural materials for high temperature designs such as the gas cooled fast reactor (GFR) and the very high temperature reactor (VHTR).[4]

Silicon carbide based composites—a fabric of SiC fibers densified via CVI with a SiC matrix (SiC_f/SiC_m)—are among the most promising CMCs for nuclear applications. For instance, Figure 1.2, shows a prototype of a SiC_f/SiC_m fuel cladding for the GFR. In addition, it is a promising structural material for fusion reactors.[5] More recently,

SiC_f/SiC_m has been proposed as candidate for replacing nowadays zirconium-based nuclear fuel cladding of current light water reactors (LWRs) in order to improve both fuel cycle efficiency and safety margins under accidental conditions.[6–8]

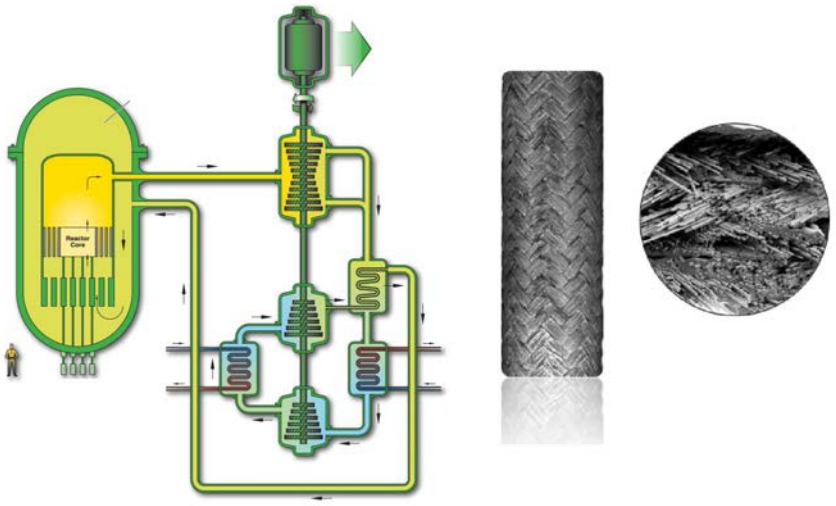

Figure 1.2: Gas cooled fast reactor (GFR) scheme, SiC_f/SiC_m fuel pin for GFR and detail of the composite microstructure - The goal manufacturing measures are: length=3 m, inner radius=5 mm and thickness=1 mm.[4] SiC_f/SiC_m fuel pin reproduced from Ref.[9]

There are potential benefits in terms of efficiency and safety issues inherent to the unique physico-chemical properties of SiC. The properties and stability under nuclear environments of this composite material directly depend on the irradiation behavior of its different components—not only individually but also on how they interact. Indeed, it is not until the development of third generation SiC fibers that SiC_f/SiC_m can be considered as an irradiation-stable material.[10] The availability of these nuclear-grade SiC fibers triggered out intensive research on the composite behavior under irradiation during the last decade.[11] Even though the significant advances in the understanding of the composites irradiation behavior, limited information is directly concerned to the irradiation behavior of third generation SiC fibers hence requiring further research and characterization.

During service, SiC_f/SiC_m, and thus its fiber reinforcement, will be subjected to different types of irradiation whose detrimental effects on the material may limit its in-core lifetime. Fast neutrons crossing materials lose energy by elastic collisions creating

cascades of displaced atoms which may result in defects in the atomic lattice of the material. Also, charged particles, such as fission fragments, may interact with the material. The interaction of these particles with the target is not straightforward due to their electrical charge. The Coulombic nature of the interactions between the incoming ion and the target atoms allow to consider the ion energy loss within the material as two different processes with different associated phenomena. Ion inelastic collisions with electrons in the medium deal to energy dissipation mainly as heat and are characterized by the electronic stopping power. Also, elastic collisions with target atoms will take place resulting in large displacement cascades and are characterized by the nuclear stopping power. Finally, in ceramic materials, both interactions may cause the modification of the material lattice structure, hence modifying the original material properties.

The objective of the present work is to study the irradiation effects in third generation SiC fibers. There are two SiC fibers which can be considered suitable for nuclear applications: Hi-Nicalon type S manufactured by Nippon Carbon (Japan), hereafter HNS, and Tyranno SA3 manufactured by Ube Industry (Japan), hereafter TSA3. Two crucial aspects in their use as reinforcement for ceramic composites for nuclear applications are investigated: their microstructural stability and their mechanical behavior under irradiation.

This manuscript is structured as follows. After the actual introduction chapter, chapters 2 and 3 introduce respectively the fundamental properties of SiC and the different generations of SiC fibers and the state of the art of their irradiation behavior. The materials and methods used during this research project are detailed in chapter 4 to finally discuss the obtained results in chapters 5, 6 and 7. For the experiments presented in the last chapters, two different irradiation temperature regimes have been differentiated according to the already mentioned possible nuclear applications.

On the one hand, the use of SiC_f/SiC_m as advanced cladding for LWRs will imply the exposure of the material to irradiation in a temperature range where it is sensitive to ballistic damage. It is known that irradiation in elastic energy loss regimes at low temperatures induces the amorphization of SiC single crystals. This phenomenon causes significant degradation of the physico-chemical properties of SiC[12] hence being detrimental for its use under low temperature nuclear environments. Even though the amorphization process is well understood for SiC single crystals, it has not been yet

studied whether the microstructure of the third generation SiC fibers have a significant influence on the amorphization threshold conditions and kinetics. In order to give some insights to the amorphization phenomenon in SiC fibers, HNS and TSA3 have been irradiated with 4 MeV Au^{3+} in order to simulate the neutron induced damage in the low irradiation temperature regime as it creates large cascades of displaced atoms. Chapter 5 presents the characterization of the ion-amorphization of these fibers in terms of micro-Raman spectroscopy (μRs) and transmission electron microscopy (TEM). It is reported that there is no significant difference in the ion-amorphization threshold conditions—dose and temperature—of these fibers as compared to the model material, i.e. 6H-SiC single crystals.

It has been also pointed out that thermal annealing of ion-amorphized SiC single crystals induces not only recrystallization but also mechanical failure, i.e. cracking and delamination, of the irradiated layer.[13,14] Nevertheless, the origin of the stress source remained unclear due to the possibility of the presence of thermal stresses resulting from the experimental settings. Also, these studies did not specified if the cracking phenomenon was exclusive for amorphous layers over single crystals substrates. In order to understand this phenomenon, chapter 6 is devoted to the investigation of the annealing effects in the ion-amorphized SiC fibers and single crystals via *in situ* environmental scanning electron microscope (E-SEM) and TEM. The *in situ* nature of the experimental setting allows to avoid thermal shock stresses originated by abrupt temperature changes. It has been found that independently of their microstructure, SiC fibers will also suffer thermal annealing induced mechanical failure. Also, the kinetics of the cracking process in single crystals are presented and compared to those of the recrystallization. Finally, it is reported that the recrystallization of the ion-amorphized samples is the underlying stress source that causes cracking and delamination of the annealed irradiated layer.

On the other hand, the use of SiC composites as cladding material for the GFR will imply its exposure to irradiation in a temperature range where dynamic annealing would neutralize the damage created by the elastic collisions[15] hence hindering the amorphization process. However, other phenomena associated to the inelastic interactions would be worth to study. The superior mechanical properties of SiC composites over brittle-bulk SiC allow they use as structural materials. When subjected to mechanical loadings matrix micro-cracking and the crack deviation through the matrix-fiber

interface allows the composite to accommodate the stresses while crack-bridging SiC fibers grant the composite integrity. Under this configuration, the operation lifetime of the composite will be determined by the sub-critical growth of the matrix cracks which, in turn, is controlled by creep of the crack-bridging SiC fibers.[16]

It is known that irradiation may cause time-dependent strain under conditions where thermal creep is negligible. This phenomenon, so-called irradiation creep, has been observed in both metals[17] and ceramics.[18] It is a major importance phenomenon as it can directly affect to the material performance under nuclear environments and even limit the in-core lifetime of the material. Though irradiation creep has been observed in bulk SiC[19] and in the first and second generation of SiC fibers[20,21] there is a lack of characterization of this phenomenon in third generation SiC fibers.

In this work, irradiation creep of TSA3 fibers has been investigated using a dedicated experimental facility coupled to different ion-accelerators. This machine, so-called MiniMecaSiC, allows to perform mono-axial tensile tests to single TSA3 fibers while being ion-irradiated under in-core-like conditions. Chapter 7 presents the *in situ* characterization of these phenomenon. In order to simulate the interaction with energetic fission fragments, TSA3 fibers have been irradiated with 12 MeV C^{4+} and Xe^{92+} ions. These ions have projected ranges in SiC larger than the mean diameter of the selected TSA3 fibers, which implies an irradiation regime where electronic energy loss is dominant. Under this irradiation conditions, irradiation creep of TSA3 fibers has been observed and characterized. This phenomenon is highly temperature dependent as TSA3 fibers present higher strain rates and residual strains when irradiated at low temperatures. Also, when irradiated at high temperatures, the irradiation creep strain rate is characterized by a linear correlation with the ion flux and a square root correlation with the applied tensile stress. In addition, irradiation creep in dominant electronic energy loss regimes appears to be higher than neutron-irradiation creep reported in the literature. At the sight of this results, an energy degrader has been used in order to reduce the electronic energy loss contribution and increase ballistic damage. *In situ* tests with the energy degrader reveal a high sensitivity of TSA3 fibers to the ion energy loss regime as the measured irradiation creep strain rates are higher for ion-irradiations under dominant electronic energy loss regimes.

2

SiC, SiC fibers and SiC_f/SiC_m composites

SiC physico-chemical properties are interesting for nuclear applications. However, its use as structural material is limited by its brittle nature, typical of ceramic materials. SiC-based composites, SiC_f/SiC_m, allow to overcome bulk SiC mechanical limitations while retaining its properties, hence placing themselves as one of the few realistic candidates for high temperature and nuclear structural applications. The achievement of high temperature resistant composites is indebted to the development of near-stoichiometric and highly crystalline SiC fibers. In this chapter, SiC fundamental properties as well as the properties of the successive generations of SiC fibers and their influence on the behavior of the composites are described.

2.1 SiC

Silicon carbide is a non-oxide covalent ceramic compound with chemical formula SiC. Figure 2.1 shows an assessed equilibrium phase diagram of the Si-C system. The diagram shows a peritectic transformation at 2545 ± 40 °C and an eutectic transformation at 1404 ± 5 °C that involve the intermediate compound SiC.[22]

Natural SiC is rare in earth. For instance, though it was first observed in 1824 by J.J. Berzelius[23] and first synthesized in 1891 by A.G. Acheson,[24] it was not until 1904 that H. Moissan first reported its presence in rocks from a meteor crater in Arizona.[25]

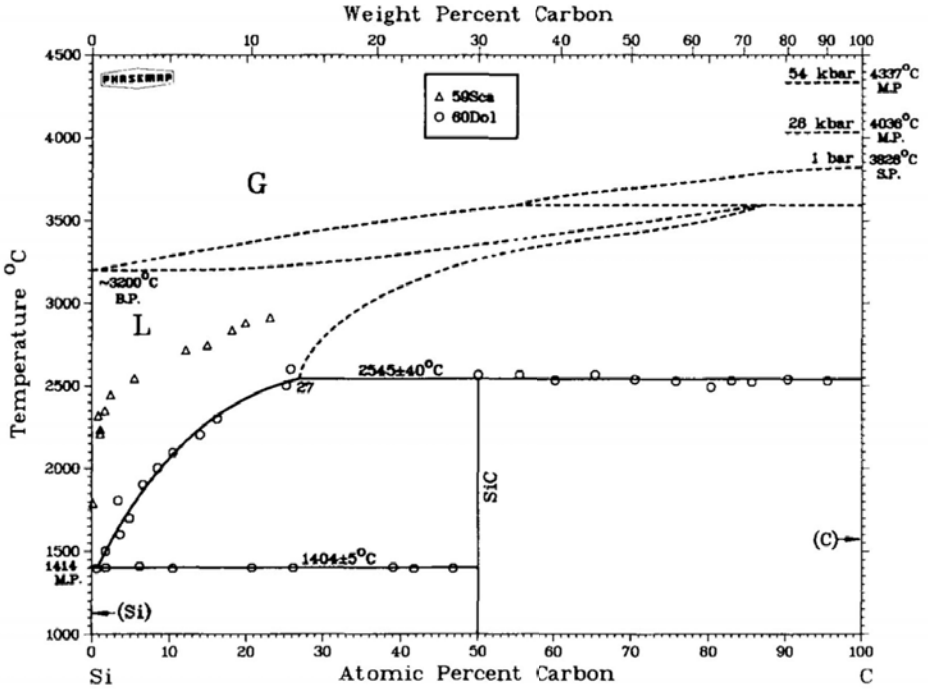

Figure 2.1: The Si-C system - Assessed equilibrium phase diagram.[22]

The process to obtain SiC followed by Acheson was rather simple. By combining silica sand and petroleum coke into a high temperature electric furnace, he was able to obtain the reaction $SiO_2 + 3C \rightarrow SiC + 2CO$.[24] Since then, more refined manufacturing methods such as sintering, direct conversion, gas phase reaction and polymer pyrolysis, appeared to cover the incrementing needs of SiC with high crystallinity levels for different purposes.[26] For instance, chemical vapor deposition (CVD) is one of the most familiar gas phase reaction methods for the synthesis of high crystallinity, stoichiometric and high purity β-SiC whereas polymer pyrolysis is often used in production of continuous SiC fibers. The CVD process can produce SiC in solid form by epitaxial growth from a gas phase reactant at relatively low temperatures, between 900 °C and 1100 °C, without the use of sintering aids. Either methyltrichlorosilane (CH_3SiCl_3) or ethyltriclorosilane ($C_2H_5SiCl_3$) are commonly used as gas reactants and hydrogen as carrier gas. Depending on the reactant, CVD-SiC is typically synthetized by Eq. 2.1 or 2.2:[12]

$$CH_3SiCl_3 \longrightarrow SiC + 3HCl \tag{2.1}$$

$$C_2H_5SiCl_3 + H_2 \longrightarrow SiC + 3HCl + CH_4 \tag{2.2}$$

The methane produced by using ethyltriclorosilane as reactant easily decomposes in free C with hydrogen generation producing undesirable C-rich phases or C layers in CVD-SiC.[12]

The basic structural unit of this compound is a C atom surrounded by four Si atoms forming a covalent-bonded tetrahedron. One of the characteristics of SiC is its remarkable number of different stable stoichiometric solid crystalline phases. Each of these phases, known as polytypes, can be achieved by altering the stacking sequence of the basic SiC tetrahedron. Figure 2.2 shows the fundamental tetrahedron as well as different stacking sequences. Among the more than 200 reported polytypes,[27] the most common are those which present cubic, hexagonal and rhombohedral structures with repetition sequences of 3, 4, 6 and 15 Si-C pairs.[28] Following the Ramsdell notation,[29] SiC polytypes are denoted as nX-SiC , where n designs the repetition period of the stacking sequence and X the crystallographic structure, these structures are commonly known as 3C-, 4H-, 6H-, 15R-SiC. The 3C-SiC polytype, also known as β-SiC, results to be the only stacking sequence that has cubic symmetry. The remaining polytypes, which show hexagonal or rhombohedral symmetry, are known as α-SiC. The occurrence and stability of different SiC polytypes primarily depend on the temperature. For instance, the 3C-SiC polytype is a metastable phase and will transform into α-SiC at very high temperatures, above 1900–2000 °C.[30] In addition, the presence of impurities and the deviation from strict Si:C stoichimetry play a role in polytype stability.[12]

Each of the polytypes exhibits unique physico-chemical properties which make SiC an attractive material for industrial applications ranging from heat engines and electronic devices to nuclear systems. Table 2.1 shows some characteristics of the most common SiC polytypes. Despite all SiC polytypes have almost the same Si–C bond length of 1.89 Å and a bilayer height along the c-axis of 2.52 Å, each of them have different lattice constants as well as different electronic band structures—hence the optical and electronic properties—due to their different crystalline structures. All the polytypes have indirect band structures with band gaps increasing monotonically with the polytype hexagonality (h). For instance, typical band gap values for 3C (h=0), 6H (h=0.33) and 4H (h=0.5) yield 2.4, 3 and 3.2 eV respectively. The density of the

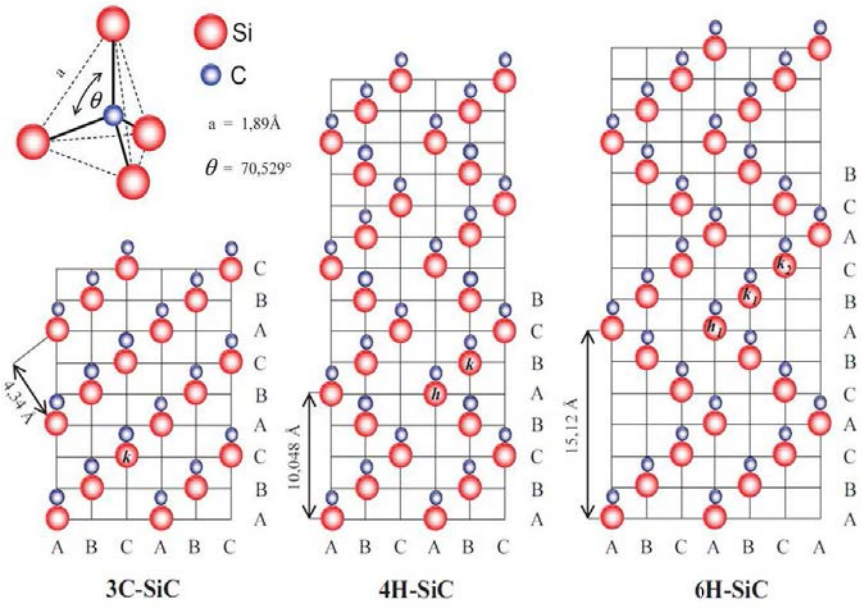

Figure 2.2: Fundamental SiC tetrahedron and its most common polytypes - All atoms are located in the $(11\bar{2}0)$ plane. The polytypes differ by the stacking sequence along one direction.[28,31]

Table 2.1: Most common SiC polytypes and their properties[1]

Polytype	ρ [g cm^{-3}]	a [Å]	c [Å]	h^2	Band gap [eV]	α [10^{-6} K^{-1}]	κ [W cm^{-1} K^{-1}]
3C (Zinc blende)	3.215	4.3589	-	0	2.4	3.8	3.6
4H (Wurtzite)	3.215	3.081	10.061	1/2	3.2	-	3.7
6H (Wurtzite)	3.215	3.081	15.092	1/3	3	4.3 $\perp_c$ 4.7 $\parallel_c$	4.9

[1] Refs.[12,30]

[2] hexagonality.

different polytypes can be considered constant in the temperature range of interest due to the low thermal expansion of SiC. Also, thermal conductivity is not sensitive to the SiC polytype but depends on the crystal direction and on the doping density and has typical values of 4×10^{-6} W cm^{-1} K^{-1}. It is reasonable to assume that the single-crystal form of SiC exhibits the highest thermal conductivity. However, high purity and dense polycrystalline CVD-SiC exhibits practically the same conductivity (3.87 W cm^{-1}K^{-1}) as the single crystal at room temperature (RT). Also, in the case of polycrystalline SiC, thermal conductivity monotonically increases with increasing grain size below RT.[12]

On the other hand, different polytypes have similar elastic modulus and fracture toughness due to the similarity of the Si–C bonds. Regarding the elastic modulus at RT, E_{RT}, SiC single crystals and CVD-SiC exhibit high values ranging from 390 to 690 GPa.[30] For the latter, grain size is considered to have a negligible effect on E_{RT} whereas it decreases with increasing porosity or impurity concentration.[12] In addition, the elastic modulus slightly decreases with temperature with typical values of $0.9 \times E_{RT}$ at 2000 °C. Despite the small impact of the temperature on SiC mechanical properties, it is remarkable the low fracture toughness of SiC, which typical values are between 2.4 and 5.1 MPa m$^{1/2}$ and are at least ten times lower than for steel alloys.[12] Such a brittle behavior makes bulk SiC not suitable for its use as structural material.

Thermal creep is also a relevant mechanical property for structural nuclear applications. Primary and steady state creep strains have been reported in the literature for CVD-SiC. The former occurs immediately upon loading and tends to saturate with time. In severe loading conditions, primary creep strain in CVD-SiC can reach as high as ∼1% at 1923 K depending on the quality of the material. Steady state or secondary creep rates for CVD-SiC have been only measured above ∼1650 K as they are typically too small to be measured under this temperature.[12] CVD-SiC creep rates for temperature ranging from 1655 to 1743 K are reported to be proportional to the applied flexural strength with an activation energy of 6.6±0.9 eV.[12] Also, the underlying creep mechanisms are related to grain boundary (GB) diffusion of C atoms and dislocation glide below 1923 K. Over this temperature, creep seems controlled by a climb-controlled glide mechanism.[12,32]

2.2 SiC based composites

Reinforcing SiC with continuous SiC fibers allows overcoming the brittle failure of bulk SiC inadequate for structural applications.[33] Indeed, the composite obtained is lightweight, damage tolerant, tough, and strong and exhibit a much greater resistance to high temperature environments than metals or other conventional engineering materials.[10] The chemical vapor infiltration (CVI) method can produce high crystalline SiC_f/SiC_m composites with excellent properties. The composite is made by the densification of a coated SiC fiber preform by infiltration of gaseous reactants, commonly methyltrichlorosilane (CH_3SiCl_3) and hydrogen.[33] The resulting high purity SiC matrix provides good irradiation resistance to the composite, necessary for nuclear applications.[11] Despite the quality of the achieved SiC matrix, CVI produced composites have a residual porosity of 10–15%. The porosity level not only affects the composite properties, such as thermal conductivity and mechanical behavior, but also its leak-tightness.[34] For nuclear structural applications, total leak-tightness is mandatory to contain gaseous fission products so different solutions to prevent SiC_f/SiC_m leakage have been proposed. For instance, covering the inner surface of the composite with a layer of high density monolithic SiC[7] or with a metallic liner[35] would allow fission gas retention.

The mechanical behavior of CMCs displays features that differentiate them from the other composites, such as polymer matrix composites or metal matrix composites, and from homogeneous (monolithic) materials. These features are due to heterogeneous and multiscale composite microstructure and the respective properties of the constituents—fibers, matrix and fiber-matrix interphase.[33] SiC_f/SiC_m pseudo-ductile behavior is achieved by micro-crack formation and propagation across the SiC matrix and crack deflection in the fiber-matrix interphase. The latter consist of a thin film of a compliant material, normally a single layer of pyrocarbon (PyC) or successive layers of PyC/SiC, with low shear stress deposited on the fiber surface prior to the matrix infiltration. In addition to deflect the matrix cracks, the interphase acts as a mechanical fuse and grants a good load transfer between the fiber and the matrix.[34,36] For composites with negligible matrix creep, subcritical crack growth is controlled by the time dependent elongation of crack-bridging fibers.[16] Finally, the ultimate failure

of the composite generally occurs after crack saturation of the matrix and fiber overload. This phenomenon is highly influenced by stochastic features as SiC fibers are brittle ceramics sensitive to present randomly distributed flaws which may act as stress concentrators.[37]

2.3 SiC fibers[1]

In the early 80' s, first generation SiC fibers developed by Prof. Yajima[39] caught the interest from the aerospace and aeroengine industries. The availability of small diameter ceramic fibers meant the possibility of producing structural ceramic materials capable to work at temperatures where metallic alloys could not operate. Nevertheless, the characteristics of these fibers were not the expected in terms of elastic modulus and creep resistance hence triggering out an intensive R&D process that eventually led to the so-called third generation of SiC fibers whose properties approach to those of high-purity SiC.[38]

The approach adopted to obtain SiC fibers is indebted to the production road of C fibers, which were obtained from polyacrylonitrile (PAN, $(C_3H_3N)_n$) as polymeric precursor.[40] In the case of SiC fibers the chosen polymeric precursor was polycarbosilane (PCS; $(SiH_2CH_2)_n$), as it included both C and Si and the cyclic arrangement of its atoms was similar to the 3C-SiC structure.[38] Once the precursor was identified, next step was to be able to produce a form of PCS that could be spun. The chosen production route was to decompose polydimethylsilane (PDS) in an autoclave at 470 °C for 14 h obtaining a precursor which, although difficult to spin, could be converted to ceramic fibers.[38] Finally, as it can be observed in Figure 2.3, it was found that the cross-linking stage that turned the PCS infusible was crucial in the obtention of high quality SiC fibers.

[1]This section is an updated summary of the comprehensive review of the development of SiC fibers by Bunsell et al.[38]

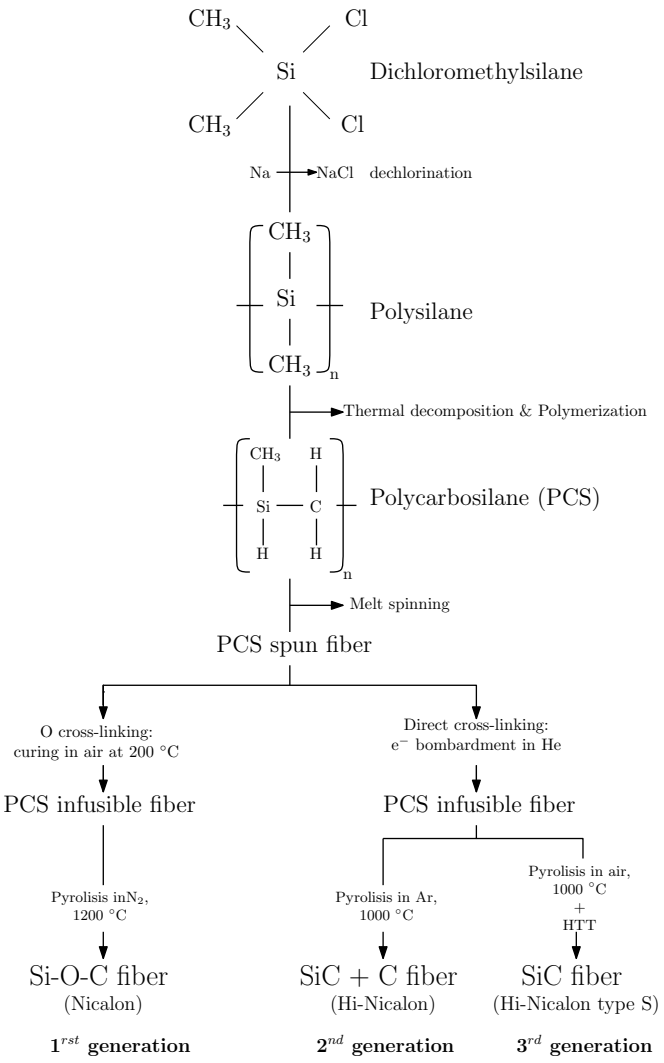

Figure 2.3: Elaboration processes - Manufacturing routes for different generations of Nicalon SiC fibers.

2.3.1 First generation SiC based fibers

First generation fibers were fabricated by making infusible the PCS by cross-linking in air between 145 °C and 200 °C. After cross-linking, PCS fibers were pyrolyzed to induce the evaporation of low weight components and the reaction of C with Si. The resultant fiber was composed by nano-sized β-SiC surrounded by a disordered $Si-O-C$ phase due to the O introduced during the cross-linking stage.[38]

The two first SiC fibers available were Nicalon, commercialized by Nippon Carbon in 1982, and Tyranno, commercialized by Ube industries in 1987. The difference between these fibers was found in the fabrication process. The PCS precursor of Tyranno fibers was doped with titanium (polytitanocarbosilane, PTCS) as sintering aid.[38]

Both fibers had a very similar chemical composition; however, despite the denomination of SiC fibers, the poor stoichiometry and the presence of free C resulted in poor mechanical properties at high temperatures when compared to bulk SiC. First generation SiC fibers had a low elastic modulus and crept above 1000 °C. Also they exhibited a poor chemical stability. Superficial silica layers appeared when heated in air above 1200 °C and CO formation induced the apparition of pores which caused the decohesion of the $SiO_2 - SiC$ interphase. Table 2.2 gathers the main characteristics of first generation fibers.[38]

Table 2.2: First generation SiC based fibers main characteristics[1]

Fiber	Nicalon 200	Tyranno LOX-M
Producer	Nippon Carbon	Ube Industries
Precursor	Polycarbonsilane (PCS)	Polytitanocarbosilane (PTCS)
Cured by:	Oxidation	Oxidation
Si [wt %]	56.6	54
C [wt %]	31.7	31.6
O [wt %]	11.7	12.4
Ti [wt %]	-	2
C/Si	1.31	1.36
Elastic Modulus [GPa]	200	185
Density [g cm-3]	2.55	2.37
Average Diameter [μm]	14	11

[1] Ref.[38]

2.3.2 Second generation SiC fibers

First generation SiC fibers poor characteristics were generally caused by their poor stoichiometry and the presence of the $Si-O-C$ amorphous phase.

On the one hand, the O content of Nicalon fibers was introduced during their cross-linking stage. Therefore, a new O-free cross-linking method using e^- irradiation was used to break the $Si-CH_3$, $Si-H$, $C-H$ chemical bonds allowing the formation of Si and C bonds. After the irradiation stage, the remaining free radicals trapped withing the fiber were removed by submitting the cross-linked fibers to a short heat treatment at 327 °C. The resultant SiC fibers, called Hi-Nicalon and produced by Nippon Carbon, presented an O content as low as the 0.5 wt.%.[38]

On the other hand, the successor of the Tyranno, the Tyranno LOX-E, still exhibited high O content as it was not only introduced during the cross-linking stage but also due to the presence of Ti on the polymeric precursor. Ti addition to the PCS precursor was via the alkoxide $Ti(OR)_4$, with $R = C_nH_{2n+1}$, hence introducing O despite the O-free cross-linking stage. In order to reduce the O content, the metallic additive to the PCS precursor shifted from Ti to Zr resulting in two types of fibers, Tyranno ZE and Tyranno ZM.[38]

O reduction resulted in improved physical properties for Hi-Nicalon fibers. For instance, the elastic modulus was increased by a 35% with respect Nicalon fibers and thermal creep below 1000 °C was negligible. However, the improvement of Tyranno fibers was not so significant though their reduced O content. Table 2.3 gives the main characteristics of second generation SiC fibers.[38,41]

2.3.3 Third generation SiC fibers

Low-O SiC fibers showed in general improved properties with respect first generation fibers. However, second generation SiC fibers still had a poor stoichiometry due to the excess of free C, causing a poor stability at high temperatures (cf. Table 2.3). As their properties remained insufficient to fulfill the requirements for their devised applications, efforts were directed towards achieving near-stoichiometric fibers which implied the reduction of the C excess present in Hi-Nicalon fibers. In order to do so, the pyrolysis of PCS fibers was carried out under a H_2 atmosphere. The presence of H_2 favored the departure of the methyl groups ($R-CH_3$) by forming CH_4 during the

Table 2.3: Second generation SiC based fibers main characteristics[1]

Fiber	Hi-Nicalon	Tyranno LOX-E	Tyranno ZM	Tyranno ZE
Producer	Nippon Carbon	Ube Industries		
Precursor	Polycarbosilane (PCS)	Polytitanocarbosilane (PTCS)		
Cured by	e^- irradiation	e^- Irradiation	Oxidation	e^- Irradiation
Si [wt%]	62.5	55	57	58.5
C [wt%]	37	37.5	34.5	38.5
O [wt%]	0.5	5	7.5	2
Ti [wt%]	0	2	0	0
Zr [wt%]	0	0	1	1
C/Si	1.39	1.64	-	-
Elastic Modulus [GPa]	270	200	200	235
Density [g cm^{-3}]	2.74	2.39	2.48	2.55
Average Diameter [μm]	13	11	11	11

[1] Ref.[38]

organic→inorganic transition. This new route resulted in the so-called Hi-Nicalon type S (HNS) fibers: near-stoichiometric fibers characterized by a low-O content and high crystallinity levels (cf. Figure 2.3).[38]

In the case of Tyranno fibers, the path followed to improve their stoichiometry was to change the chemical composition of the polymeric precursor. The metallic sintering aid shifted from Zr and Ti to Al compounds. Also, the polymeric precursor, polyaluminocarbosilane (PACS), was cured by a two-stage pyrolysis process. First stage allowed oxide phases to decompose and CO to outgas above 1200 °C. In the second stage, the Al content aided sintering the SiC grains between 1600 °C and 1800 °C. The resulting SiC fibers, called Tyranno SA 3 (TSA3), contained up to 2 wt.% of Al.[38] In addition, these fibers presented higher thermal stability and better properties than previous Tyranno fibers (LoxM, LoxE, ZMI and ZE).[42] Table 2.4 gathers the main characteristics of third generation SiC fibers.

Table 2.4: Third generation SiC fibers main characteristics[1]

Fiber	Hi-Nicalon type S	Tyranno SA3
Producer	Nippon Carbon	Ube Industries
Precursor	Polycarbosilane (PCS)	Polyaluminocarbosilane (PACS)
Cured by	e^- Irradiation	Oxidation
Si [wt%]	69	68
C [wt%]	31	32
O [wt%]	0.2	-
Ti [wt%]	-	-
Al [wt%]	-	0.6
C/Si	1.04	1.03 (edge) 1.2 (core)
Elastic Modulus [GPa]	400	375
Density [g cm^{-3}]	3.05	3.1
Average Diameter [μm]	12	7.5
Grain Size [nm]	20	200

Refs.[38,43,44]

As it is shown in Figure 2.4, these fibers exhibit unique microstructures as a result of their fabrication process. Both fibers consist of highly faulted β-SiC grains surrounded with free turbostratic C, i.e. unmatched graphene layers, and very low oxygen content.[43,44] As it is shown in Figure 2.5, the diametrical free C distribution in HNS fibers is rather constant whereas TSA3 fibers present a decreasing free C concentration from the core to the surface. The heterogeneous C concentration of the latter is a result of the reactions occurring during the two-step thermal treatment and the presence of the metallic sintering aid.[45]

The main microstructural differences between these fibers is found in their grain size with mean values of 20 nm for the HNS fibers and 200 nm for the TSA3 fibers. The smaller grain size of the former implies the smoother surface roughness of HNS fibers shown in Figure 2.6 which in turn produce composites with superior mechanical properties due to lower shear stresses between fiber and matrix.[45]

Finally, the development of third generation SiC fibers marked an inflexion point in the development of SiC composites. The properties of these fibers approach those of CVD-SiC due to their near-stoichiometry, high crystallinity and low O content. Also, these fibers overcome the degradation of the mechanical and physical properties at

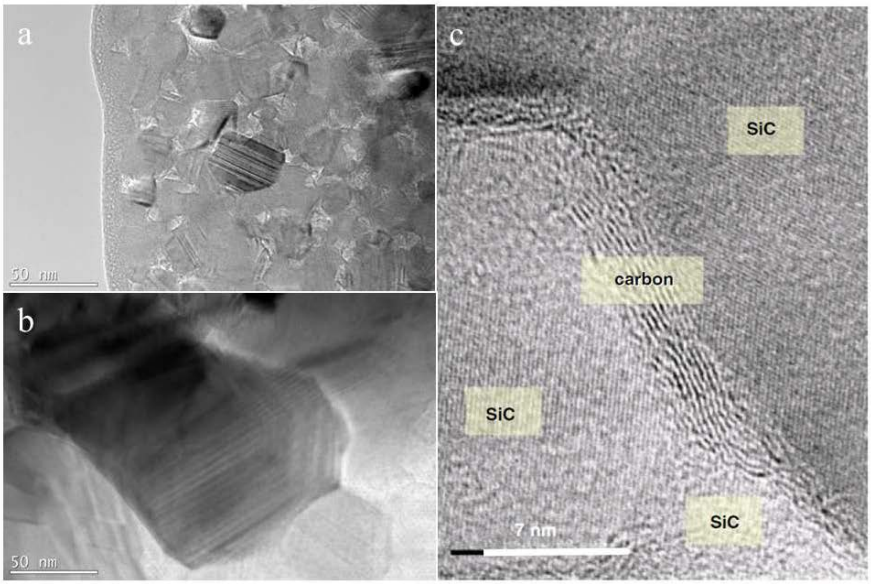

Figure 2.4: Detail of the microstructure of third generation SiC fibers - (a) Hi-Nicalon type S, (b) Tyranno SA3 and (c) detail of the intergranular turbostratic carbon. The stripped intragranular patterns in (a) and (b) are attributed to stacking faults.[43,44]

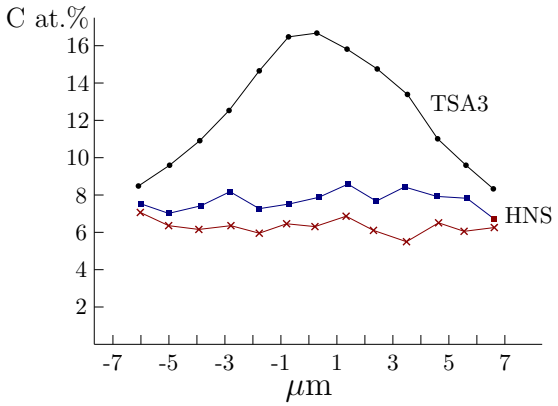

Figure 2.5: Free C distribution of third generation SiC fibers - Tyranno SA3 fibers present a decreasing radial distribution from the core to the surface.[45]

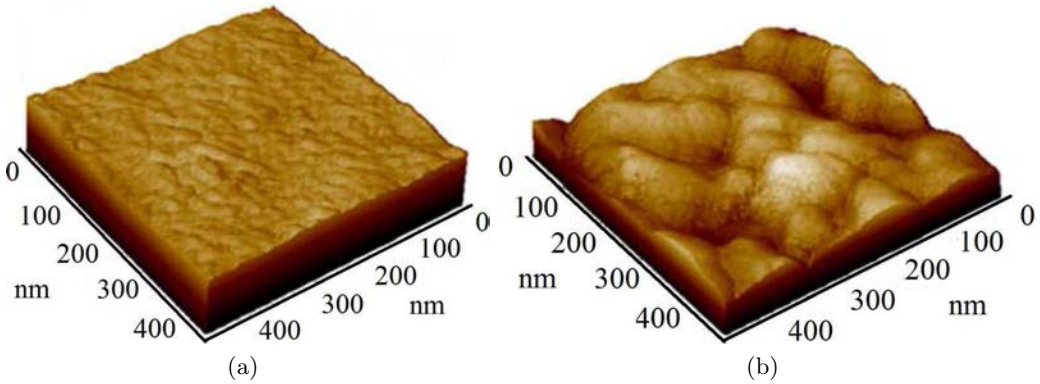

Figure 2.6: Atomic force microscopic images of the surface of (a) Hi Nicalon type S and (b) Tyranno SA3 fiber - The roughness of SiC fibers affects directly to the mechanical behavior of the composite.[45]

high temperatures characteristic of the previous generations of SiC fibers. Indeed, it is not since the development of third generation SiC fibers that SiC_f/SiC_m is considered suitable for high-temperature applications.

3

Ion and neutron irradiation effects in SiC and SiC fibers

SiC-based composites are referred frequently as the most promising structural materials for nuclear applications. Whereas there is an extensive characterization of the irradiation effects on single and polycrystalline SiC among the literature, including comprehensive bibliographic reviews,[11,12] the characterization of the irradiation effects in SiC fibers still requires further investigation. In this chapter, a bibliographic review of the irradiation effects in bulk SiC and in the different generations of SiC fibers is presented.

3.1 Irradiation damage creation

Before detailing the irradiation effects in SiC, it is necessary to recall the different processes that produce the displacement of the target lattice atoms and how to quantify irradiation damage.[1]

When an energetic incident particle elastically interacts with a lattice atom there is a kinetic energy exchange between them. If this transmitted energy is higher than the threshold displacement energy of the knocked lattice atom, E_d, it will be ejected from its equilibrium site leading to a Frenkel pair formation: a vacancy and an interstitial atom. Also, as schematized in Figure 3.1, if the kinetic energy transfer is high enough, the displaced atom may have enough kinetic energy to displace not only one but many

[1] A detailed description of the displacement process and a full derivation of the different models of irradiation damage quantification can be found in Ref.[17]

atoms of the lattice which, in turn, will cause other displacement processes. Displacement cascades depend on the energy given to the primary knock-on atom (PKA) by the incident particle and the displacement cascade process will continue until the kinetic energies of the displaced atoms are below the E_d. As a result of the displacement cascade, after thermal recombination of some of the displaced lattice atoms, a wide variety of stable lattice defects, ranging from isolated Frenkel pairs to large defect clusters (cf. Figure 3.1), can induce changes in the microstructure and properties of the host material.[46]

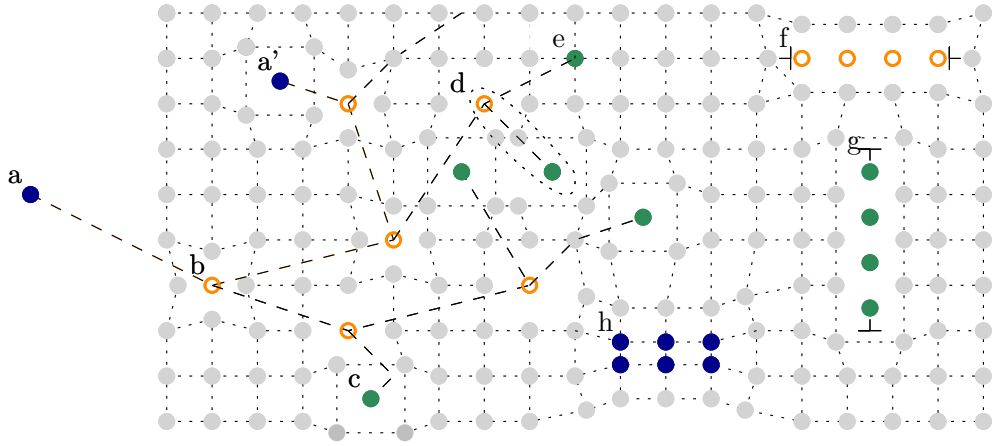

Figure 3.1: Schematic representation of a collision cascade and various crystal defects - a: incident particle, a': impurity, b: vacancy, c: interstitial atom, d: a Frenkel pair, e: replacement collision, f: vacancy dislocation loop, g: interstitial dislocation loop and h:precipitate of impurity atoms.

Normally, the changes observed in a material exposed to irradiation will depend on the amount of stable defects which, in turn, will vary according to the total number of displaced atoms or dose. The most extended model to calculate the total number of displaced atoms by an indicent particle is the model proposed by Norget, Robinson and Torrens,[47] (NRT) based on the initial work by Kinchin and Pease.[48] The NRT model (Eq. 3.1) gives the total relative number of atomic displacements, ν_{NRT}, produced by a PKA with kinetic energy E_{PKA}:

$$\nu_{NRT}(E_{PKA}) = 0.8\frac{T_{dam}(E_{PKA})}{2E_d} \tag{3.1}$$

Where $T_{dam}(E_{PKA})$ corresponds to the energy available by the PKA to generate

atomic displacements by elastic collisions and 0.8 is the displacement efficiency. Therefore, given an incident particle flux, the rate of atomic displacements, R_d, will be proportional to the target atom density, N, and the integration of the NRT damage function over the incident particle energy spectrum taking into account the interaction probability, thus:[17]

$$R_d = N \iint \phi(E)\nu_{NRT}(E_{PKA})\sigma(E, E_{PKA})\, dE_{PKA}\, dE \tag{3.2}$$

Where $\phi(E)$ is the incident particle flux of energy E, and the product $\sigma(E, E_{PKA})\, dE$ is the interaction probability of producing a PKA with energy E_{PKA}. Finally, the total number of times an atom has been displaced on average, dpa_{NRT}, will be given by:

$$dpa_{NRT} = \frac{R_d}{N} t \tag{3.3}$$

One of the advantages of this model is that it is independent of the incident particle and thus allows the comparison of the damage obtained with different types of irradiation such as neutrons, ion or electron irradiation. On the other hand, dpa_{NRT} unit does not take into account defect recombination thus overestimating the number of total displaced atoms. Indeed, when a displaced target atom fills the vacancy left by another displaced it has no effect on the lattice configuration of the material.

With the NRT model, the problem to quantify the damage generation in a target material is reduced to the quantification of the PKA production by an incident flux of particles. It is at this moment when the nature of the incident of particle influences the damage process. In contrast to the straightforward neutron-nucleus elastic interactions due to their null electric charge, the interaction of charged particles with the target lattice cannot be simplified to a hard-sphere collision and needs to be otherwise described.

The energy loss of an incident charged particle is also due to Coulomb interactions between the incident particle and the target electron cloud. Therefore, the energy loss process of a charged particle within a material can be considered as two separated processes according to the type of interaction. The different processes are known as the electronic stopping (S_e) and the nuclear stopping (S_n) powers, which refer respectively to the inelastic and the elastic processes that causes the gradual energy loss on the particle. The former can be described as inelastic collisions that result in small energy

losses in which the target electrons are excited or ejected from their shells and dissipate their energy through thermal vibration of the target. The latter can be described as ion-atom and atom-atom collisions due to repulsive Coulomb potentials.[46]

Figure 3.2 shows the morphology of the damage produced by different charged particles with an energy of 1 MeV as well as the damage profile of different particles with different energies as compared to the neutron flat energy deposition and damage profile. Also, areas with dominant electronic and nuclear energy regimes are highlighted in red and blue respectively.[46]

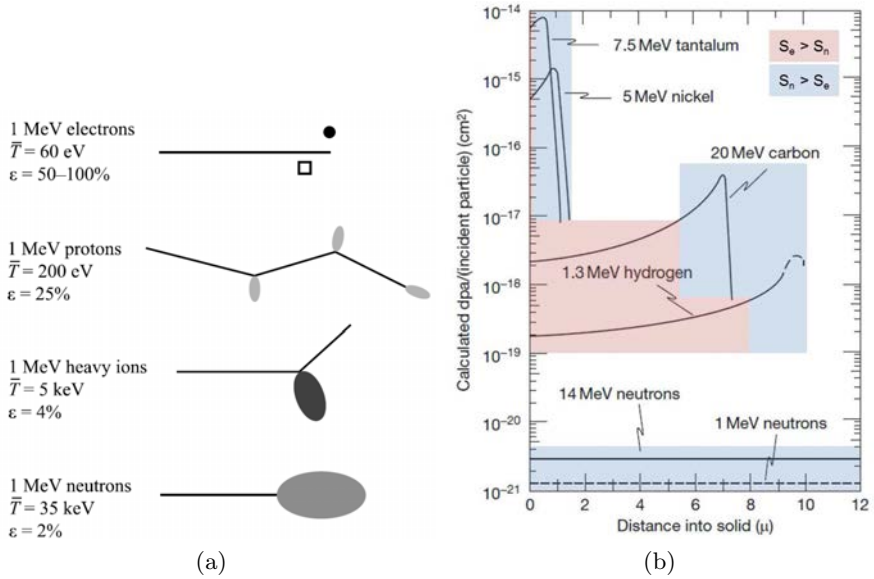

Figure 3.2: Difference interaction of different particles in Ni - (a)$\bar{T}$ is the average recoil energy and ϵ the displacement efficiency. (b) Neutrons present flat damage distribution whereas for charged particles damage spatial distribution will depend on both the energy and mass. Areas with dominant electronic and nuclear energy regimes are highlighted in red and blue respectively.[46]

As it can be observed, damage profiles and the contribution of the S_e and S_n to the stopping of the particle will depend on the type of particle and its energy. For light charged particles, such as electrons or protons, only isolated Frenkel pairs or small clusters are likely to be produced due to their small mass. For heavy ions, at the beginning of the interaction the energy loss of the charged particle will be mainly by electronic processes. As the incident particle moves on through the target, its energy

will gradually decrease until a level where nuclear processes become the main cause of energy loss. For electronic dominant energy loss regimes ($S_e > S_n$) the particle will follow a linear course in the material with heat deposition. On the other hand, for nuclear dominant energy loss regimes ($S_n > S_e$) the particle will follow a random course with large deflections until its implantation in the material. In the nuclear interaction regime, energy is dissipated mainly by the creation of large displacement cascades hence being the most damaging between the two processes. Therefore, the spatial distribution of the damage created by heavy ions will notably depend on the particle' s energy. The higher the energy, the larger the projected range in the material, the larger the range with dominant electronic energy losses, and the deeper the damage peak near the implantation zone of the ions.[46]

3.1.1 Monte Carlo simulations for irradiation damage estimation

As discussed above, the interaction of charged particles is not straightforward thus making the estimation of the induced damage difficult.

SRIM (Stopping and Range of Ions in Matter) is a binary-collision Monte Carlo simulation code that allows to compute the ion-implantation profile and the number of vacancies per ion and unit length, $V(E_{ion})\ \left[\frac{Vac}{ion\,\text{Å}}\right]$, created in a target irradiated with ions of energy E_{ion} while taking into account the electronic and nuclear contributions to the energy loss of the incident ion.[49] Figure 3.3 shows displacement cascades created by 6 incident 4 MeV Au ions in SiC. Necessary input data are E_{ion}, the E_d for each target sublattice and the target density.

Finally, this software allows ion-fluence to dpa-dose conversion in a simple manner. Using the SRIM output $V(E_{ion})$ and considering that ion-irradiation is usually performed with monoenergetic ions, equations 3.2 and 3.3 can be simplified to:

$$dpa_{SRIM} = \frac{V(E_{ion})\left[\frac{Vac}{ion\,\text{Å}}\right] \times 10^8}{N[\frac{atoms}{cm^3}]}\,\phi(E_{ion})[\frac{ions}{cm^2\,s}]\,t[s] \tag{3.4}$$

With $\times 10^8$ being the conversion factor from Å to cm, N the density of the target, $\phi(E_{ion})$ the fluence of ions with energy E_{ion} in and t the time. Respective units are given in the brackets.

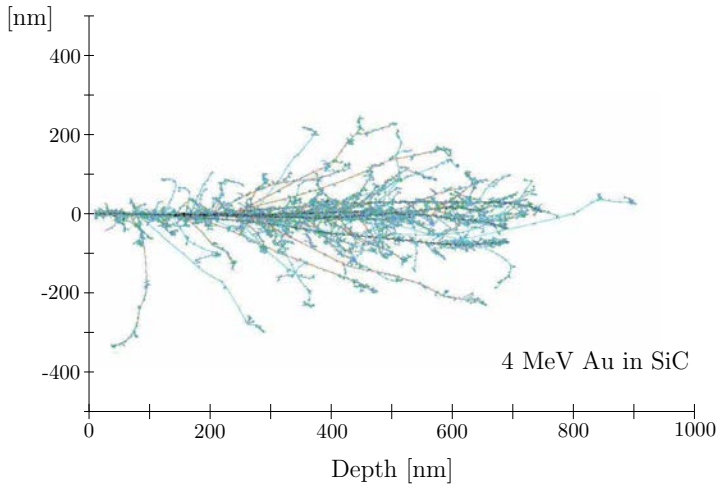

Figure 3.3: Displacement cascades created by 4 MeV Au ions in SiC - In red the created vacancies by collisions between the ion and the target atoms, in blue the displacement cascades created by the target atom recoil simulated with SRIM-2013 for 6 incident ions.[49]

3.2 Irradiation effects in SiC single crystals and CVD-SiC

3.2.1 Irradiation induced amorphization

Under certain conditions, ballistic damage created by electron, ion and neutron irradiation may induce the loss of crystallinity in SiC.[50,51] Figure 3.4 shows a HR-TEM image of the resultant loss of the crystalline structure of a 6H-SiC single crystal irradiated with 560 keV Si ions. This amorphization process is attributed to several mechanisms including direct amorphization within collision cascades, an increase in the free energy due to point defect accumulation and disordering processes. Also, amorphization has been described as a two-step process where the relaxation of the elastic energy introduced in the lattice by initial point defects and small defect clusters relax by the amorphization of defective crystalline regions.[52]

Crystal-to-amorphous transition highly depends on the irradiation temperature as the irradiation induced amorphization (RIA) depends on the mobility of self-interstitial atoms (SIAs). Figure 3.5 shows the evolution of the amorphization dose as a function of the irradiation temperature. Dose to amorphization of the samples under Si^+ and Xe^+ was the dose at which TEM-SAED patterns show concentric halos.[53,54] As it can be observed, dose to amorphization exponentially increases as irradiation temperatures

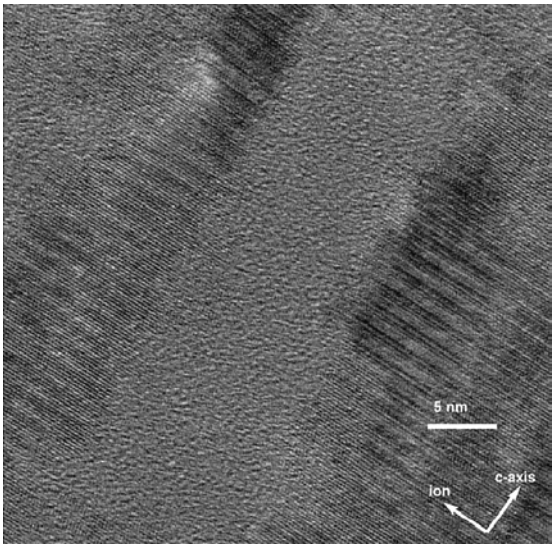

Figure 3.4: HR-TEM image of the crystalline to amorphous transition in 6H-SiC - Amorphous areas forming isolated island structures which eventually link and grow.[50]

increase. Following this tendency, it is possible to reach a temperature where RIA is virtually impossible. Indeed, when irradiated over this critical amorphization temperature, T_c, SiC will remain partially crystalline as SIAs have enough mobility to allow dynamic anneal of irradiation induced damage processes.[15] For instance, 6H-SiC irradiation with 4 MeV Au^{3+} and 4 MeV Xe^{+} ions at RT leads to full amorphization at a dose of about 0.4 dpa, with no significant influence of the incident particle on the process, whereas at 400 °C full amorphization was still not achieved even at 26 dpa.[15] In addition, it has been reported that no significant differences in the amoprhization kinetics at RT have been found between 6H-SiC and 3C-SiC polytypes as full amorphization at RT was observed for doses of 0.45 dpa under 100 keV Fe .[55] In the latter works, dose to amorphization was determined from RBS-C spectra and full amorphization of the samples was considered when the yield of the spectra at the position of maximum damage reached the random level.

In addition, the amorphization threshold conditions are dependent on the incident particle. Even though no master curve as a function of ballistic damage is available, attempts to rationalize these data have been done by including the electronic excitation effects. It has been reported that at temperatures below T_c, dose to amorphization at a certain temperature increases with the ratio of ionization to displacement rates.[56]

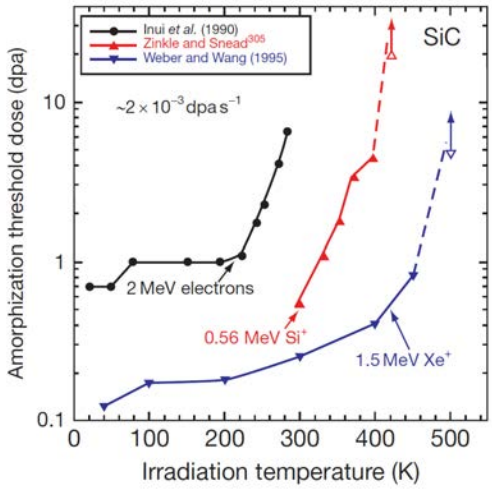

Figure 3.5: Dose to amorphization as a function of the irradiation temperature and incident particle for SiC - Closed symbols are for full amorphization.[53]

3.2.2 Irradiation induced swelling

Together with the amorphization process, irradiation swelling, i.e. a volumetric expansion caused by the irradiation, is observed in SiC. Figure 3.6 shows the neutron-irradiation induced swelling in high purity CVD-SiC as a function of the irradiation temperature. Swelling saturation values may be divided in three different regimes depending on the irradiation temperature and the associated swelling mechanisms.

First regime is for irradiation temperatures below ∼200 °C where amorphization of the sample is the source of the volumetric expansion. The amorphization swelling is described as the lattice expansion introduced by single interstitials or small interstitial clusters and the lattice contraction around immobile vacancies and antisite defects.[57] As temperature increases between ∼200 °C and 1000–1200 °C, SiC enters to the saturable point-defect swelling regime. In this temperature range, the number of defects surviving the post-cascade thermally activated recombination is reduced due to the thermally enhanced mobility of both Si and C interstitials hence reducing the swelling saturation value.[15] At these temperatures, swelling has an exponential dependence with dose until saturation. There is an inflexion point near 1000–1200 °C above which swelling increases again. Over these temperatures vacancies start to be mobile enough to cluster

and form cavities thus leading to a non-saturable void swelling regime.[12] In this regime, swelling increases almost linearly with neutron doses although it remains unclear how it will evolve for doses above 10 dpa.[11]

Irradiation swelling has been also reported for ion-irradiation. Threshold dose of saturation swelling for β-SiC by 4 MeV Ni^{3+} ions is 0.3–1 dpa at 400–600 °C whereas it is 0.1–0.5 dpa at 300–600 °C for neutrons indicating that ion-irradiation induced swelling may need a little higher dose to saturate than neutrons at the same irradiation temperatures.[10,58]

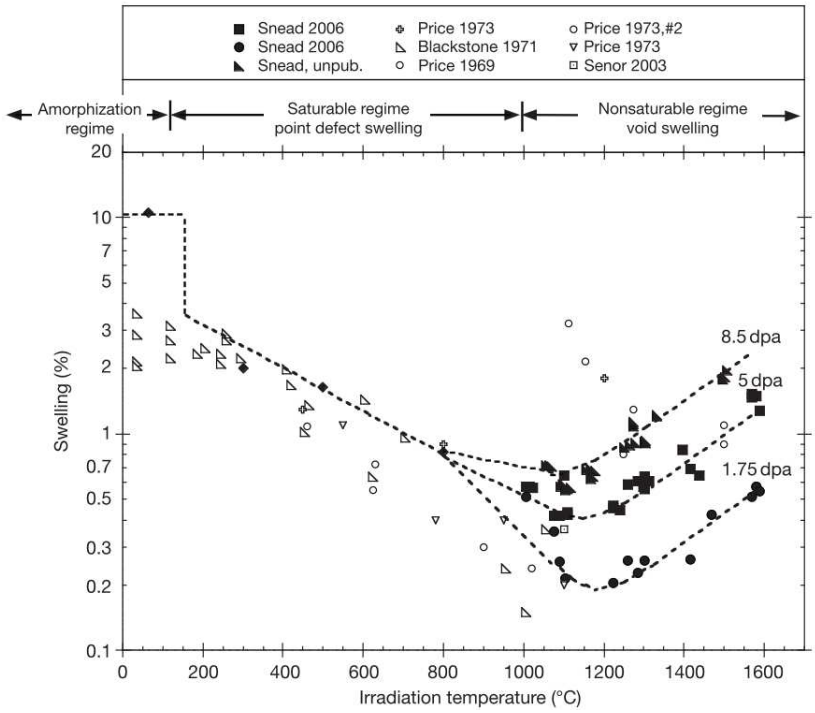

Figure 3.6: Radiation swelling of SiC as a function of the temperature - Swelling saturation value decreases with temperature until 1000–1200 °C.[12]

3.2.3 Degradation of physical properties

Ion and neutron irradiation in the amorphization temperature range causes the degradation of SiC physical properties. For instance, hardness and elastic modulus of amorphized SiC have been reported to decrease respectively to 54% and 55% of their initial values after neutron irradiation. This tendency has been also observed for ion-irradiation, after which hardness and elastic modulus yield the 45–70% and 70–76% of

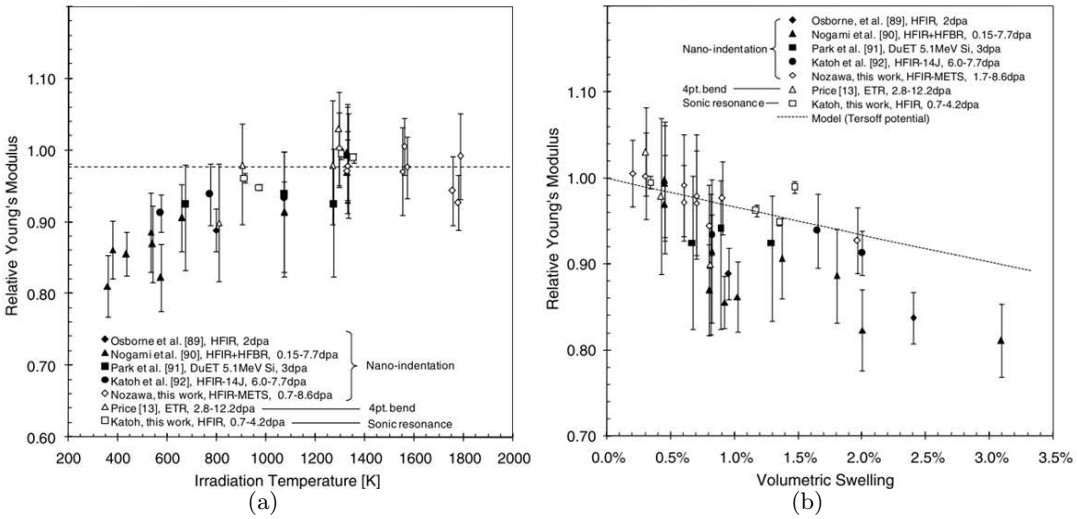

Figure 3.7: SiC elastic modulus evolution as a function of the (a) irradiation temperature and (b) swelling - The lower the irradiation temperature the higher the elastic modulus degradation.[12]

their initial values.[50] On the other hand, as shown in Figure 3.7, the degradation of the elastic modulus is not significant for irradiation at high temperatures. In addition, the correlation between the evolution of the elastic modulus and the irradiation swelling suggests lattice expansion as the main cause for the elastic modulus degradation.[12]

Figure 3.8 shows the evolution of SiC thermal conductivity with dose for neutron irradiation at low temperatures. The steep degradation of the thermal conductivity at low doses reflects its high sensitivity to point defects as defect-phonon scattering increases thermal resistivity of the crystal.[59,60]

3.2.4 Thermal annealing of irradiation effects

Numerous studies reveal that thermal annealing induces partial or complete recovery of the physical properties of ion and neutron amorphized SiC.[13,14,50,51,61–65] However, it has been highlighted that, together with the recovery process, thermal annealing may induce severe mechanical failure of the irradiated layer. For now, the mechanical failure shown in Figure 3.9 has been only observed for completely ion-amorphized SiC layers over 6H-SiC single crystals and the underlying mechanism remains uncertain.[13,14]

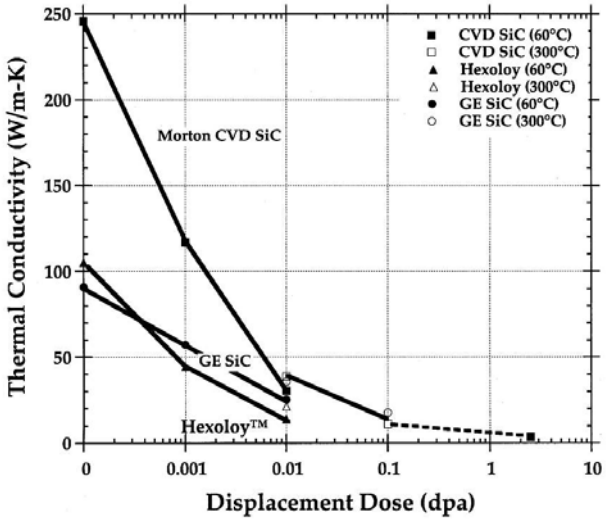

Figure 3.8: SiC thermal conductivity as a function of the neutron dose - The lower the irradiation temperature the higher the thermal conductivity degradation.[60]

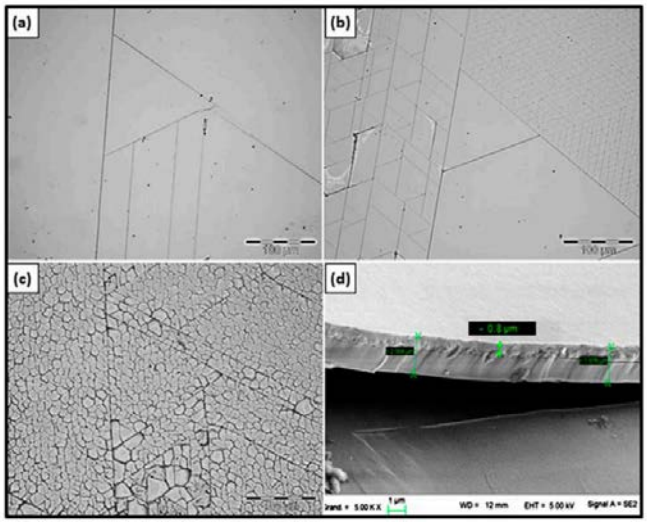

Figure 3.9: Thermal annealing induced cracking and delamination - Optical microscopy images, (a),(b) and (c), show fractures formed along the cleavage planes of the 6H-SiC crystalline substrate.SEM image, (d), show that delamination of the annealed sample below the irradiated thickness.[14]

3.3 Irradiation effects in SiC fibers

As stated in section 3.2, irradiation damage induces detrimental physico-chemical changes in high purity SiC. Also, as ultimate performance of SiC_f/SiC_m depends on the different evolution of its components, many studies have been carried out to characterize the evolution of different SiC fibers generations under irradiation. Near stoichiometry and high crystallinity levels are key features for the irradiation stability of SiC fibers as successive SiC fibers generations show improving irradiation behavior.

3.3.1 Irradiation induced surface degradation

Figure 3.10 shows the surface evolution of first and second generation SiC based fibers irradiated with neutrons at 250 °C to doses ranging from 1 to 3 dpa. As it can be observed, after irradiation Nicalon fibers show highly degraded surface as a result of its poor stoichiometry and the presence of a Si-O-C non-crystalline phase. Tyranno fibers showed the highest degradation of these fibers. Due to their low crysallinity, they disintegrated into mostly powder with only small fragments remaining after irradiation. On the contrary, Hi-Nicalon fiber presents little modification of its surface state as they become slightly rougher after irradiation.[66] The improvement on the Hi Nicalon surface stability under irradiation in front of its predecessor highlights the crystallinity and stoichiometry role on the irradiation tolerance of SiC fibers.

For instance, Figure 3.11 shows the evolution of third generation SiC fibers after neutron irradiation at 900 °C and to 5 dpa. Though the high irradiation temperature may also prevent surface degradation, neither TSA3 nor HNS fibers present any substantial degradation due to their high crystallinity and low O content.[67]

3.3.2 Irradiation induced amorphization, densification and swelling

The high O content and poor crystallinity of first and second generation of SiC fibers not only caused surface degradation but also induced dimensional changes under irradiation at variance with the observed in CVD-SiC.[20,68–70] For instance, irradiation induced densification has been reported for Nicalon fibers. The irradiation induced densification is dependent to the irradiation temperature. For doses over 40 dpa, density increment values yield +5% for irradiation temperatures ranging from 100 °C to 500 °C.

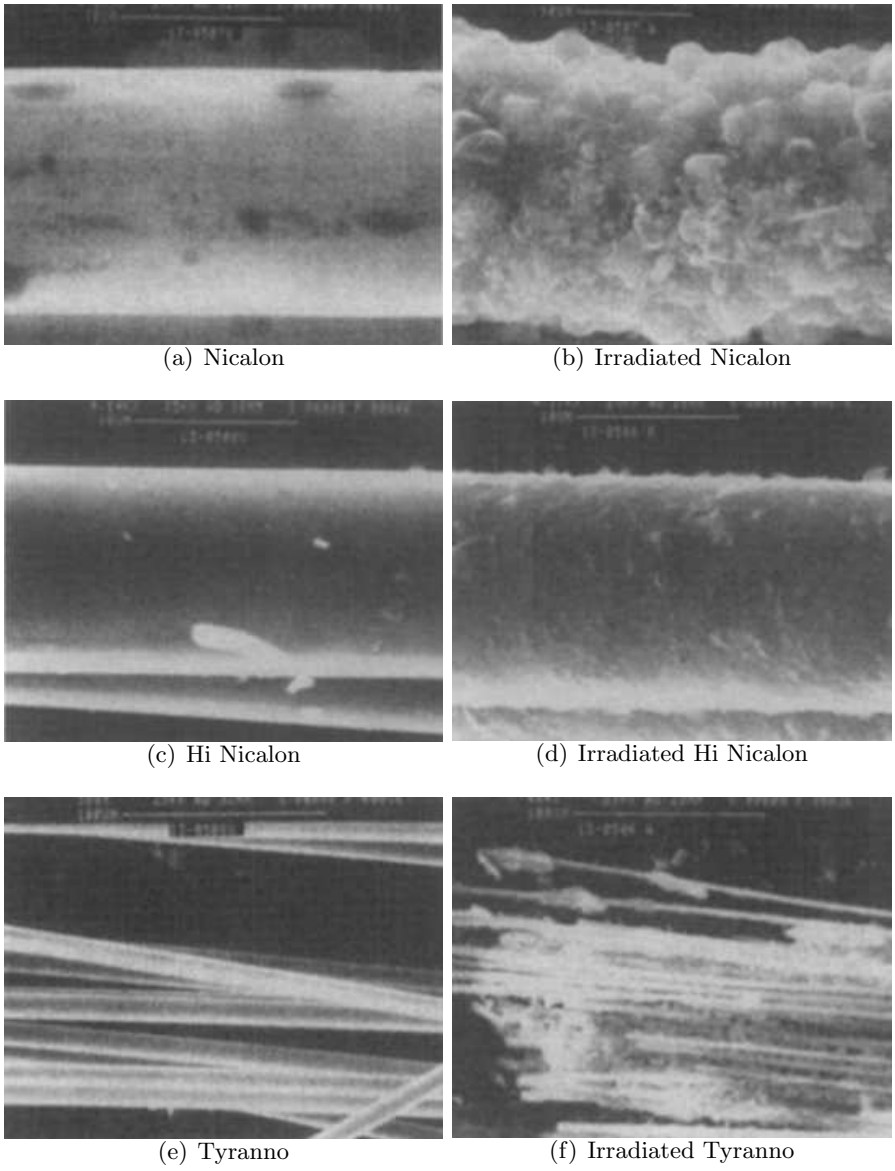

(a) Nicalon (b) Irradiated Nicalon

(c) Hi Nicalon (d) Irradiated Hi Nicalon

(e) Tyranno (f) Irradiated Tyranno

Figure 3.10: Neutron irradiation (250 °C, 1–3 dpa) induced surface degradation in first and second generation SiC fibers - First generation fibers, (a,b) Nicalon and (c,d) Tyranno, show high surface degradation as compared to second generation fibers, (c,d) Hi Nicalon.[66]

On the other hand, densification values decrease to +1% for irradiations at 800–1000 °C. The responsible mechanisms are also temperature dependent. When irradiated at 1000 °C and 43 dpa, Nicalon densification is attributed to crystallization of the

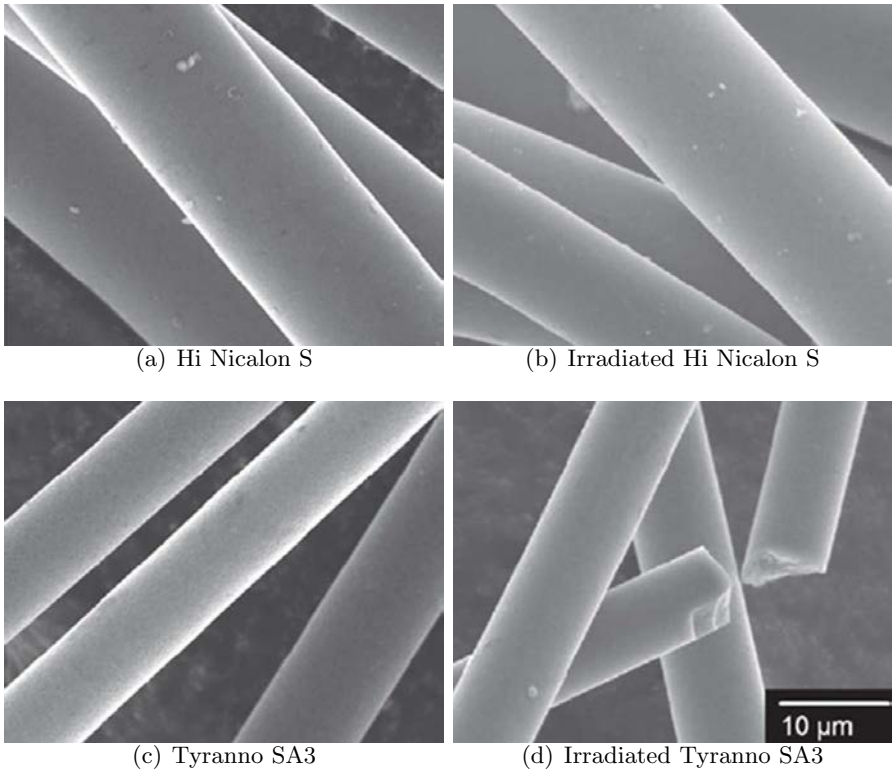

(a) Hi Nicalon S (b) Irradiated Hi Nicalon S

(c) Tyranno SA3 (d) Irradiated Tyranno SA3

Figure 3.11: Surface of third generation SiC fibers after neutron irradiation at 900 °C - No substantial surface degradation is observed.[67]

amorphous phases as the measured mean crystallite size grows from 1 to 5 nm. On the other hand, after irradiation at 100 and 500 °C irradiation induces densification of the Si-O-C non-crystalline phases. In both cases, this processes hides the amorphization process of SiC.[71]

Irradiation induced densification has been also observed for Hi Nicalon fibers. At low irradiation temperatures, irradiation also induces a +2–4% densification due to the presence of non-negligible free C (cf. Table 2.3).[69] However, at high temperatures, this phenomenon is subjected to some controversy as different densification values have been reported for similar irradiation conditions. For instance, reported values vary from +0.7%[70] to +6%[68] for irradiations to 43 dpa at 1000 °C. For the latter, densification increased with dose as a +10% increment was found for irradiations to 80 dpa at the same temperature.[68] Decreasing densification values with increasing irradiation temperature have been also reported for Hi Nicalon. For instance, densification at 2

dpa decreases from +4% to +2% for irradiation temperatures of 100–150 °C and 500–550 °C.[69] If this decreasing tendency can be extrapolated to higher temperatures, the reported densification of +0.7% would be closer to the expected values.

The irradiation induced densification mechanisms are also subjected to some controversy. On the one hand, TEM observations of the crystallite evolution have reported constant crystallite sizes after ion-irradiation at 1000 °C.[72] On the other hand, X-ray diffraction (XRD) investigations, supported by surface scanning electron microscope (SEM), point out the increase of crystallite size due to irradiation as responsible for the densification of the fiber.[68] However, despite the apparent controversy, both studies suggest that the crystallization process is not in the core but in the surface of the fiber.

Regarding third generation SiC fibers, both HNS and TSA3 behave as CVD-SiC under irradiation. Their density slightly decreases due to swelling. As in CVD-SiC, swelling values decrease with increasing irradiation temperatures.[68] Figure 3.12 shows the normalized density evolution of Tyranno SA fibers in comparison with first and second generation SiC fibers and CVD-SiC after similar irradiation conditions.[73] HNS fiber showed 0.41% swelling after 3 MeV He^+ implantation up to 0.2 dpa (5000 apm).[72] Recent investigations agree with these features. Chaabane et al.[74] irradiated SiC composites reinforced with HNS and TSA3 reporting similar irradiation swelling behavior and amorphization between the fiber reinforcement and the CVI-SiC matrix. Also, Shimoda et al.[75] reported fiber densification after submitting to cyclic heat treatments ion-irradiated TSA3 fibers. Shrinkage values yield 0.45% and 0.7% for TSA3 fibers irradiated at RT and 0.05 and 0.2 dpa respectively in agreement with the residual strain of TSA3 fibers reported by Jankowiak et al.[76] after *in situ* tensile tests irradiated with 92 MeV Xe^{23+} at 42 °C to 0.3 dpa and irradiation swelling reported by Katoh et al.[58] for CVD-SiC irradiated with 4 MeV Ni^{3+} at 60 °C.

Though the major agreement in the CVD-SiC-like behavior of these fibers, a recent paper by Kondo et al.[77] reports different dimensional evolution for TSA3 and HNS fibers under 5.1 MeV Si ion-irradiation to 100 dpa at 300 °C. Figure 3.13 shows a 3D image of a HNS reinforced SiC composite after irradiation where the HNS fibers are dimpled with respect to the surrounding CVI-SiC matrix. HNS radial and axial shrinkage values yield 0.7% and 0.8% respectively. On the contrary, TSA3 did not present significant differences with the CVI-matrix. In this case, both exhibited a volumetric swelling of 2.5%. The different dimensional evolution is attributed to mixing

and diffusion of C atoms between the SiC grain and the intergranular free C (cf. Figure 2.4). Indeed, TEM microstructural evaluation of HNS fibers irradiated with neutrons over 70 dpa at 300 °C showed size increase and amorphization of the intergranular turbostratic carbon.[78]

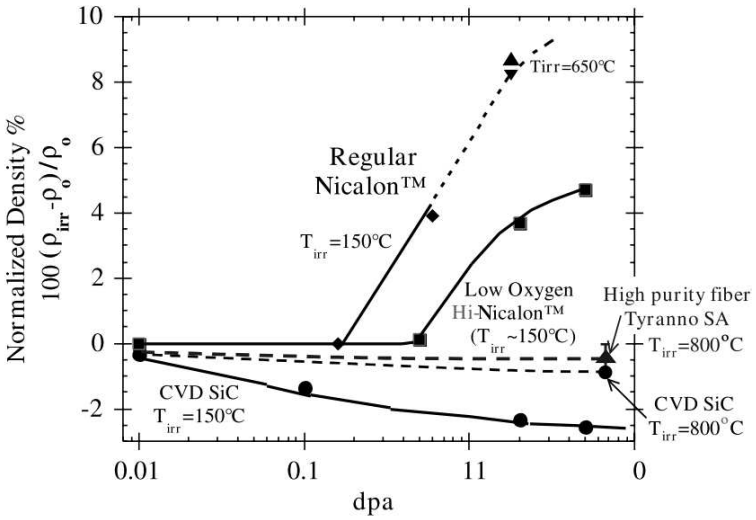

Figure 3.12: Normalized density evolution of SiC fibers as a function of the neutron dose - Only crystalline and near stoichiometric SiC fibers behave as CVD-SiC.[73]

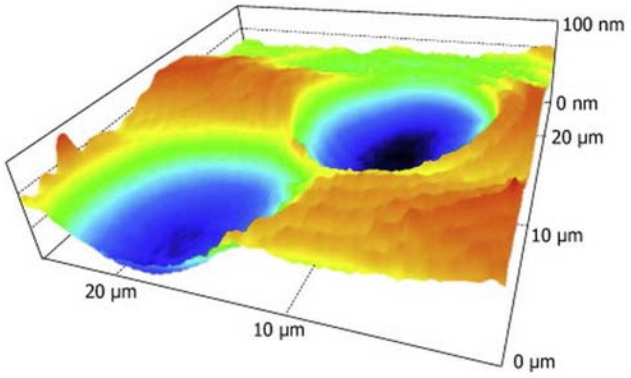

Figure 3.13: 3D-AFM profile image of an ion-irradiated SiC composite reinforced with HNS fibers - The irradiated surface of the HNS was dimpled with respect to the surrounding CVI-SiC matrix, especially at the fiber center.[77]

3.3.3 Irradiation induced degradation of physical properties

As discussed in sections 3.3.1 and 3.3.2, the poor stoichiometry and the presence of amorphous phases are responsible of the low irradiation stability of first and second generation SiC fibers.

In addition, as for CVD-SiC and single crystals, the irradiation induced morphological changes imply the degradation of the physical properties of SiC fibers. For instance, Figure 3.14 shows the evolution of the mechanical properties of Nicalon and Hi Nicalon fibers as a function of the neutron fluence for irradiations different temperatures. For both fibers the elastic modulus and the mean failure stress increases with dose, probably due to the fiber densification. Also, the changes observed in the Weibull modulus[1] suggest the redistribution or creation of fiber flaws. For Sylramic fibers, the decrease of the elastic modulus is related to the irradiation induced swelling.[69] The evolution of the failure characteristics of Sylramic fibers is particular. Its mean failure stress remains without significant changes at low irradiation temperatures whereas at moderated temperatures it decreases to the 50%. This evolution was discussed to be due to the damage caused by the B transformation into Li with He production through the nuclear reaction $B^{10}(n,\alpha)Li^{7}$.[69]

Regarding the evolution of the mechanical properties of third generation fibers, Katoh et al.[67] reported the mean tensile strength of HNS and TSA3 fibers as a function of the neutron dose and the irradiation temperature. Data shown in Figure 3.15 indicate that neutron irradiation below 800 °C causes minor strengthening for both HNS and TSA3 fibers, though significant strength degradation is observed for HNS fibers irradiated at higher temperatures, i.e. 910 °C. On the other hand, it is also remarked that HNS fibers strength was maintained when irradiated as reinforcement of a SiC composite pointing out substantially different behavior when irradiated alone or under a composite form.

[1] The Weibull modulus relates the strength variability of a brittle material to the presence and distribution of physical flaws.

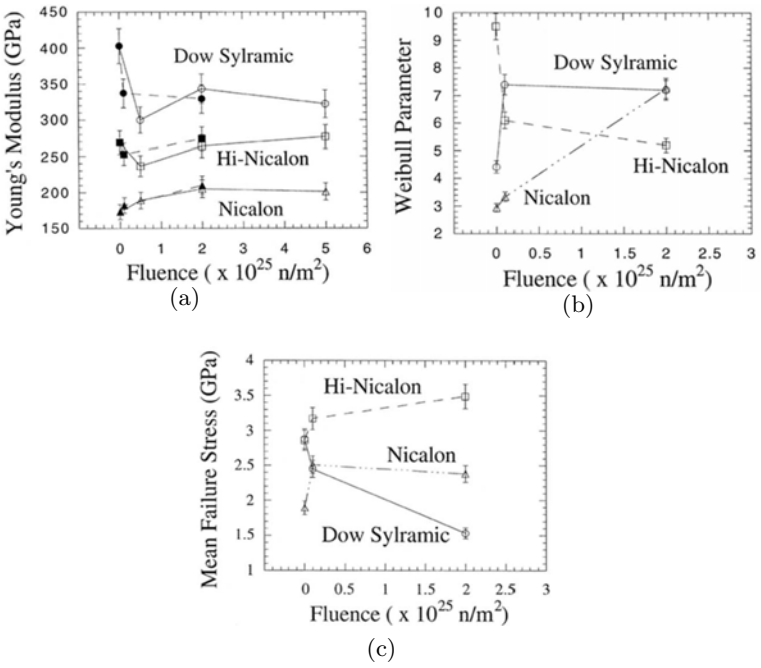

Figure 3.14: Evolution of first (Nicalon) and second generation (Hi Nicalon, Dow Sylramic) SiC fibers mechanical properties as a function of neutron fluence - Void and full symbols are for irradiation temperatures of 100–150 °C and 500–550 °C respectively.[69]

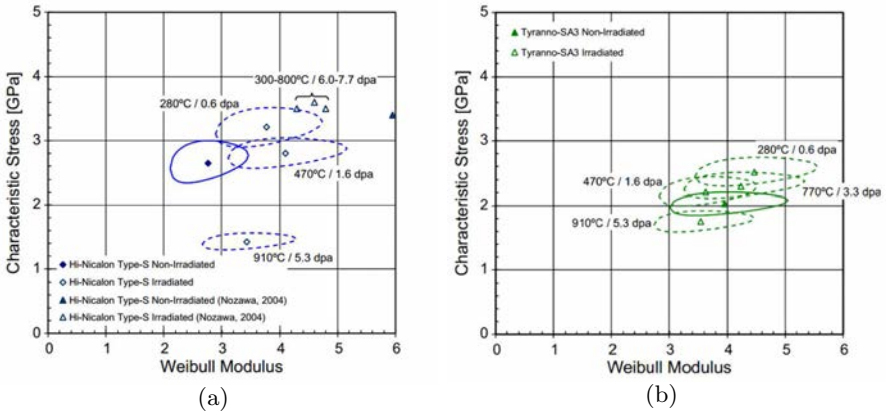

Figure 3.15: Evolution of (a) HNS and (b) TSA3 mechanical properties after neutron irradiation at different temperatures and doses - Rings represent the 95% confidence ratio bound.[67]

3.3.4 Influence of the fiber in SiC_f/SiC_m irradiation stability

As it has been commented in the previous sections, only third generation SiC fibers can be considered as irradiation and high temperature stable materials. In parallel with the SiC fibers evolution, the performance at high temperatures and under irradiation of SiC_f/SiC_m composites has improved with each new fiber generation apparition.

From a nuclear structural application point of view, early studies of SiC_f/SiC_m composites reinforced with first and second generation SiC fibers pointed out the fiber performance under irradiation as the key to achieve nuclear grade SiC composites.

For instance, Figure 3.16 illustrates the above stated by plotting the strength of irradiated composites with different fiber reinforcement normalized to pre-irradiation values.[79] Composites reinforced with Nicalon and Hi-Nicalon fibers displayed a decrease on the failure stress of 40–50% and 20–30% respectively under neutron irradiation to 1 dpa. The poor stoichiometry and low crystallinity of these fibers caused a differential behavior between the fibers and the high purity CVI-matrix: SiC fibers densified whereas SiC matrix swelled. The high stresses arising from the different density evolution in the fiber-matrix interphase translated into multiple fiber-matrix debonding causing the loss of mechanical properties. On the contrary, composites reinforced with third generation SiC fibers retain behave under irradiation similarly to CVI-SiC. This similar irradiation behavior avoids the differential swelling between the fibers and the matrix hence hindering the high degradation of the mechanical properties.

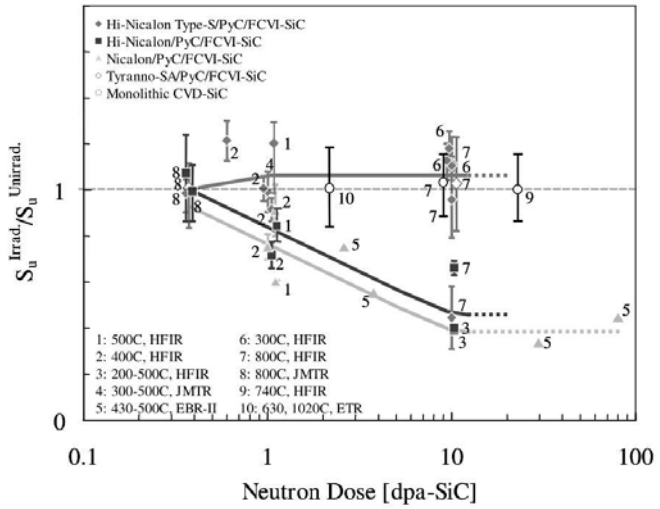

Figure 3.16: Relative strength of irradiated/unirradiated SiC composites for different SiC fiber generations - Only composites reinforced with third generation SiC fibers retain the mechanical properties after irradiation.[79]

Regarding the composites reinforced with third generation SiC fibers, those elaborated with HNS fibers display a slight decrease in the mechanical properties when compared to TSA3 reinforced ones as shown in Figure 3.17.[67] Also, a recent study highlights the temperature dependence of high neutron dose effects in HNS reinforced SiC composites. To now, the retention of strength properties of nuclear grade SiC composites has been only stated for low irradiation doses. However, as shown in Figure 3.18, HNS-SiC composites elastic modulus and proportional limit stress degrade when irradiated at high doses (>40 dpa). In addition, the mechanical properties degradation of HNS-SiC composites decreases for irradiation at high temperatures. Finally, the decrease of the ultimate tensile stress of the composite is due to the high degradation of the HNS fibers at high doses as it depends solely in the statistical strength of the fibers.[80]

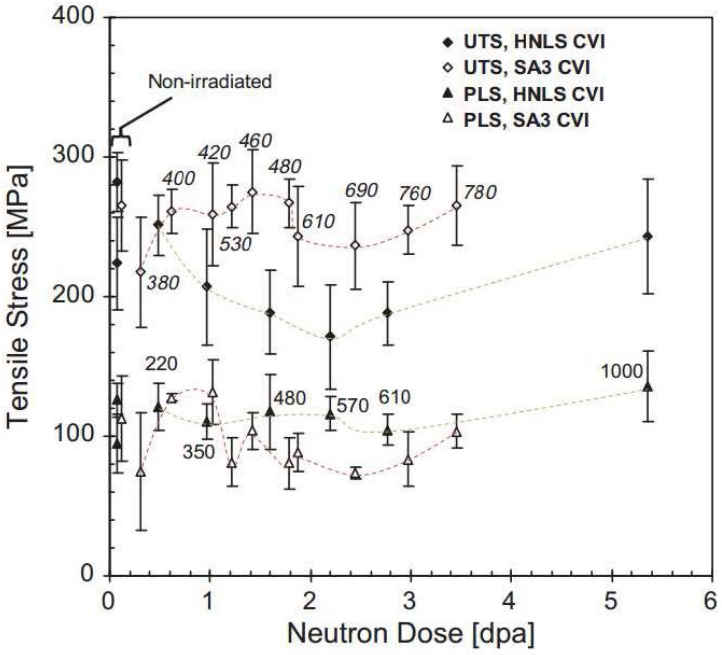

Figure 3.17: Mechanical properties evolution of SiC composite reinforced with third generation SiC fibers as a function of the neutron dose - Data labels indicate the nominal irradiation temperature.[67]

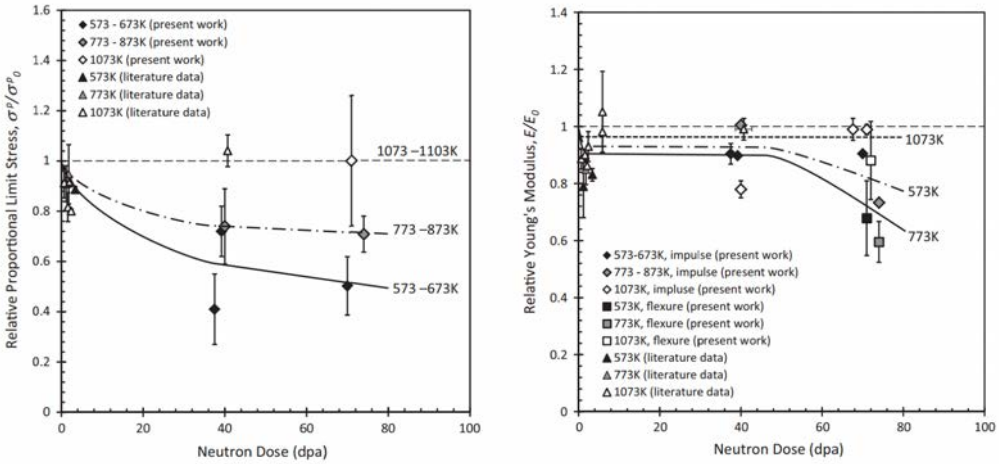

Figure 3.18: Mechanical properties evolution of SiC composite reinforced with HNS fibers as a function of the neutron dose and irradiation temperature - The higher the irradiation temperature the lower the mechanical properties degradation[80]

3. ION AND NEUTRON IRRADIATION EFFECTS IN SIC AND SIC FIBERS

Summary of the state of the art and scope

SiC_f/SiC_m composites are among the most promising materials devised for future nuclear applications. Their characteristics will be highly related to the fibers used as reinforcement. As it has been discussed, first generations of SiC-based fibers (Tyranno, Nicalon and Hi-Nicalon) suffer severe dimensional and properties changes under irradiation due to their content in glassy $Si-O-C$ phases. In turn, SiC composites formed by these fibers resulted to be unstable under irradiation. The different dimensional evolution under irradiation of the CVI-SiC matrix and SiC fibers caused fiber-matrix debonding therefore the degradation of the composite mechanical properties. Further development of SiC fibers led to the apparition of near-stoichiometric high crystallinity SiC fibers suitable for nuclear applications, the HNS and TSA3. These third generation SiC fibers show a CVD-SiC-like behavior at high temperatures and under irradiation. Finally, as CVI-SiC matrix and SiC fibers behave similarly, the mechanical properties of the composite are fairly retained hence deserving the radiation tolerant material appellation.

Despite of the substantial advances in SiC composites, further investigation must be carried out in order to fully understand the benefits of this material as well as its limitations. One major concern for its use as nuclear structural material is the operation temperature of the devised applications as the lower the irradiation temperature the higher the material degradation.

The general scope of this work is to gain further knowledge in the radiation behavior of third generation SiC fibers. More precisely, the objective is to focus on the phenomena affecting the fibers properties at irradiation temperatures relevant for the devised applications. With this purpose, HNS and TSA3 fibers have been irradiated

using ion-accelerators. These facilities allow fine tuning of the irradiation conditions in order to reproduce in-core-relevant conditions in terms of irradiation damage and temperature.

On the one hand, applications such as advanced cladding for Generation II NPP imply the exposure to irradiation in a temperature regime where SiC is susceptible to amorphize, i.e. RT to ∼300 °C. Therefore, the efforts have been directed towards studying the amorphization process on SiC fibers as well as the thermal annealing effects on amorphous samples.

On the other hand, devised applications for future Generation IV NPP and fusion reactors imply the exposure to irradiation at high temperatures, i.e. from 600 °C to 1000 °C. As at this temperatures amorphization is no longer a concern, the efforts have been directed towards studying the impact of irradiation in the mechanical properties of the fibers, focusing on the irradiation creep as it would imply the time-dependent strain of the fibers under conditions where thermal creep is negligible.

4

Materials & Methods

The study of the ion-irradiation effects on materials requires the deployment of different experimental techniques. For instance, ion-accelerators are needed to irradiate the sample. Once irradiated, different material characterization techniques are needed in order to evaluate the induced microstructural changes. With this purpose, widely adopted techniques, such as TEM, SEM and micro-Raman spectroscopy (μRs), have been used throughout this work. In addition, an innovative approach is taken in order to evaluate the impact of ion-irradiation on the mechanical behavior of single TSA3 fibers using a dedicated *in situ* tensile test machine. In this chapter, the different materials and experimental methods used in this work are presented.

4.1 Materials

SiC single crystals used in this work were machined from N-doped (0001)-oriented 6H-SiC single crystal wafers with a thickness of 246 μm grown by CREE Research using a modified Lely method.[81] Crystals are n-type with a net doping density (n_D-n_A) of 10^{17} cm^{-3}. All samples were polished to achieve a microelectronics epiready quality.

Fibers used in this work are as-received commercially available HNS and TSA3 SiC fibers. The main characteristics of these fibers have been already presented in section 2.3.3 and summarized in Table 2.4.

4.2 Ion-irradiation facilities

Ion-irradiation allows to simulate neutron damage in nuclear materials taking advantage of the versatility and precise control of the irradiation conditions—particle,

dose, dose rate and irradiation temperature. Also, the high-efficiency in damage creation allows to achieve accumulated doses equivalent to those experimented during 4–5 years of in-pile residence in a nuclear reactor in a matter of several hours.[1] In addition, post-irradiation characterization benefits from avoiding residual high-radioactivity of the sample inherent to neutron irradiation as no special handling of the ion-irradiated samples is needed.

However, ion-irradiation presents some challenges in order to establish an equivalence between the radiation damage created by charged particles or by neutrons. The differences between ion and neutron interaction with matter (cf. section 3.1) obliges to carefully select the irradiation conditions in order to focus on the effect to observe. The irradiated volume is considerably small as the projected range of ions is about few micrometers and the damage profile not spatially flat as the damage peak is located near the ion-implantation zone. Finally, ion-irradiation is a powerful technique to gain fundamental knowledge in the mechanisms involved in radiation damage, though neutron irradiation will always be required to qualify materials for their use in nuclear reactors.[46]

4.2.1 JANNUS

JANNUS (Joint Accelerators for Nanosciences and NUclear Simulation) project, is a unique experimental facility in Europe devoted to the study and characterization of the irradiation effects and ion-beam modification of materials. Figure 4.1 shows the two experimental facilities deployed with these means, a triple-beam irradiation facility, located at the CEA (Saclay, France), and a dual-beam coupled to an *in situ* TEM located at the CNRS-CSNSM (Paris-Sud University, Orsay, France).[82,83]

The JANNUS-Saclay facility consists of:[83]

- a 3 MV single-ended electrostatic accelerator (3-UH-2 Pelletron, NEC, Middleton,Wisconsin.), called Épiméthée, with an electron cyclotron resonance (ECR) source (Pantechnik, Nanogan type).
- a 2.5 MV Tandem (6SDH-2 Pelletron, NEC, Middleton,Wisconsin.)), called Japet, with cesium sputtering source.

[1] Typical nuclear reactors can accumulate damage at a rate of 3–5 dpa per year whereas in fast neutron reactors the dose rate can be on the order of 20 dpa per year.

- a 2.5 MV single-ended electrostatic accelerator (Pelletron, NEC, Middleton,Wisconsin.), called Pandore, with a radio frequency ion source.

These three beams converge in a triple chamber at 15° from both sides of the vertical plane and at 15° beneath the horizontal plane. Each beam-line is equipped with an energy degrader able to homogenize the irradiation damage along the whole ion range. The sample holder, mounted on the rear part of the chamber, allows temperatures ranging from liquid nitrogen to 800 °C. During irradiation, current measures are performed by multiple Faradays cups for accurate measurement of the ion fluxes and fluences. Also, two different beam lines end in two different ion beam analysis (IBA) vacuum chambers.

The JANNUS-Orsay facility consist of:[82]

- a 2 MV Tandem, called Aramis, equipped with both an external negative ion source and a Penning source inside the terminal.
- a a 190 kV implanter, called IRMA, with an external Bernas–Nier source producing ions from almost any chemical element.
- a 200 kV TEM (FEI Co., Hillsboro, OR, USA) with LaB_6 electron gun with <0.3 nm resolution.

The TEM is coupled to the beam-lines coming from ARAMIS and IRMA allowing *in situ* observations of the structural evolution of materials under irradiation in single or dual ion-beam modes.

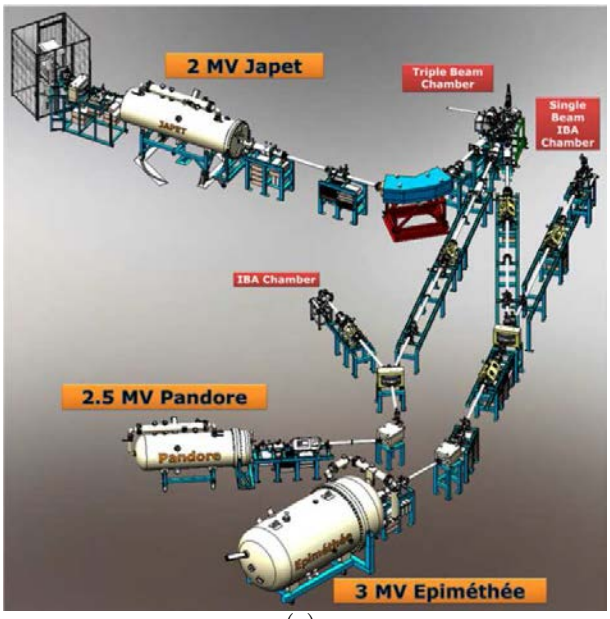

(a)

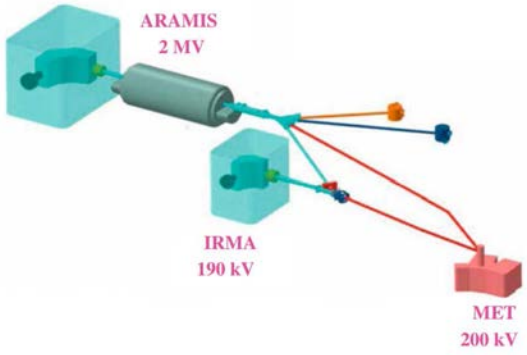

(b)

Figure 4.1: JANNUS ion-irradiation facilities - (a) JANNUS-Saclay[83] and (b) JANNUS-Orsay[82]

4.2.2 GANIL

Located at Caen (France), GANIL (Grand Accélérateur National d'Ions Lourds, National Large Heavy-Ions Accelerator in English) is one of the four largest laboratories in the world dedicated to ion-beam research. The research conducted at GANIL is varied with experimentation fields ranging from radiotherapy to condensed matter and astrophysics.[84]

Figure 4.2 shows an schematic plan of the irradiation facility. The acceleration starts

with the ionization of the ion-source, then the produced ions are slightly accelerated by compact cyclotrons (C01 or C02) and finally injected to the large separated sector cyclotrons (CSS1 and CSS2) and accelerated to energies ranging from 5 to 95 MeV/u, depending on the selected ion. A detailed description of the facility and an updated list of the available ion-beams can be found in Refs.[85,86]

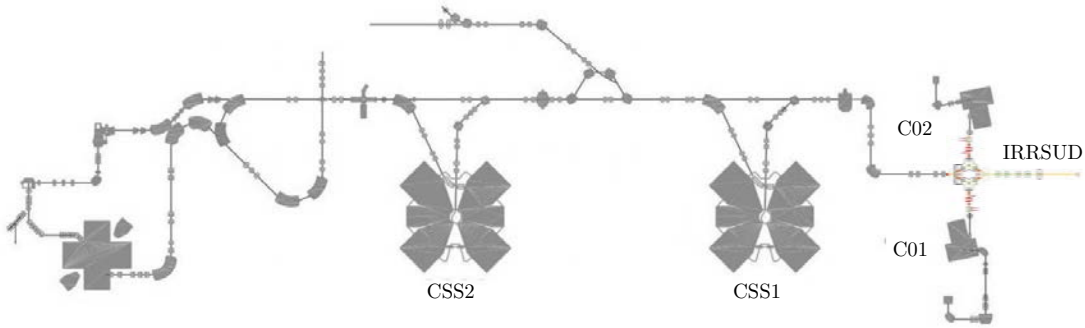

Figure 4.2: GANIL and SPIRAL acceleration systems and IRRSUD irradiation line - C01 and C02 are the cyclotron injectors and CSS1 and CSS2 are the large separated sector cyclotrons. Adapted from Refs.[85,87]

Among the different irradiation lines available at GANIL, the one used in this work is IRRSUD. It is located at the exit of C0 and is widely used by materials scientists as it provides low energy ions (0.4–1 MeV/u) up to high fluences.

4.3 *In situ* tensile test device: MiniMecaSiC

MiniMecaSiC is an experimental facility used in this work devoted to *in situ* axial tensile creep testing of single SiC fibers in a wide range of temperatures and loads and under ion-irradiation. With this purpose, it is devised to be coupled to irradiation lines allowing the access to a broad range of ions, fluxes and energies. Also, a specially designed energy degrader allows to study the impact of the different ion-irradiation stopping regimes.

The device is structured in two independent parts: the core, which is the tensile machine itself, and the vacuum chamber, which allows the core to be coupled to the irradiation lines as shown in Figure 4.3. Figure 4.4 shows in detail the machine core

consisting of a displacement table in which the fiber is mounted over two graphite supports.

(a) (b)

Figure 4.3: MiniMecaSiC coupled to the irradiation lines - Coupled to (a) GANIL/IRRSUD and (b) JANNUS-Saclay/E3 (Épiméthée IBA chamber line) lines shown in Figures 4.1 and 4.2.

The displacement table imposes the strain and a load membrane cell measures the stress. A Newport MFA CCV6 (Newport Co., Irvine, CA, USA) motorized linear stage permits accurate fiber strain with a maxim applicable axial load of 5 N under secondary vacuums ($<10^{-6}$ mbar) designed for compactness and mobility needs. It is remarkable that the measured strain takes into account the whole fiber-load cell membrane-clamps system. Thus it is necessary to consider the system compliance factor and correct the introduced error. The applied load to the fiber is measured by a HBM-U1A force transducer associated with an HBM-AB22A (HBM, Darmstadt, Germany) control and display. This sensor is fixed to the core and is attached to the superior graphite support that grips the fiber.

The energy degrader shown in Figure 4.5 consist of an umbrella-shaped support with capacity for six different foils coupled to a Phytron VSS-32.200.1,2 (Phytron Inc., Williston, VT, USA) stepper motor suitable for operation under high vacuum. The motor is controlled by a Phytron-MCC-1 and the used foils are high-purity Al of different thicknesses provided by Goodfellow, SARL.

The fiber can be heated by Joule effect with a Keithley 2410 High-Voltage SourceMeter system (Keithley Instruments, Inc., Cleveland, OH, USA). Nevertheless, as ion-irradiation may be a significant heat source besides the Joule heating, temperature

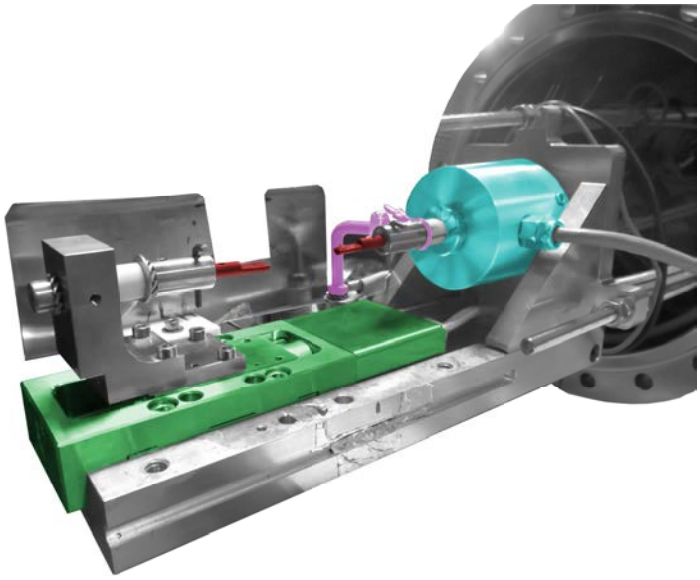

Figure 4.4: Core of the *in situ* tensile test machine - In green the displacement table, in blue the force transducer, in purple the heat-source connector and in red the graphite grips

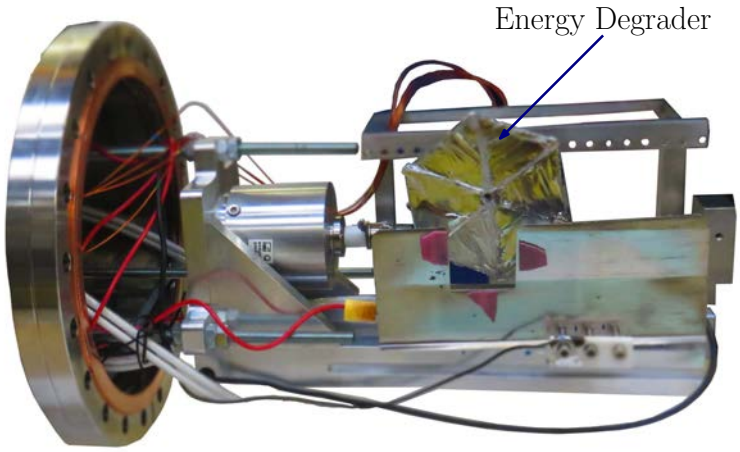

Figure 4.5: Energy degrader coupled to MiniMecaSiC' s core - The motor allows the six Al foils to turn to homogeneously displace the implantation peak of the selected ion within the fiber.

monitoring can be performed using an infrared sensor. The temperature of the fibers is then deduced from their spectral emission as the fiber can be assumed as quasi-isothermal with the only heat exchange being due to an irradiative process. The measuring system consists in a parabolic mirror collimator (RCO8FC) coupled to an infrared sensor placed out of the vacuum chamber connected by an optic fiber. The infrared sensor is a Thorlabs PDF10C (Thorlabs, Inc., Newton, NJ) which contains a low-noise photodiode InGaAs delivering a signal between 0 to 10 V as a function of the incident radiation in the 800–1800 nm range. The delivered signal is proportional to $e^{-\frac{hc}{k\lambda_2}\frac{1}{T}}$, with $\lambda_2 = 1800$ nm, and to a fourth order temperature polynomial function. Also, even though the delivered signal saturates at high temperature, it is possible to obtain a signal in the range 400 °C to 1200 °C by regulation of the distance between the fiber and the sensor. Finally, in order to regulate the fiber temperature, a control interface has been designed in a LABVIEW environment. The temperature regulator can compensate the heat contribution of the ion flux by decreasing the given electric intensity thus keeping the fiber at the target temperature. However, for the irradiation conditions of this study, flux variations resulted in temperature variations lower than the sensitivity of the temperature control system.

4.4 Characterization techniques

4.4.1 Micro-Raman spectroscopy

When photons interact with matter most part of them will be elastically scattered, hence changing their direction of propagation without modifying its kinetic energy. Such process is known as Rayleigh scattering. However, a small amount of them, approximately 1 out of 10^7, will be inelastically scattered, hence not only changing their direction of propagation but also changing their kinetic energy. Such process is known as Raman scattering.

Figure 4.6 schematically represents the different possibilities of light scattering and their associated spectrum. Raman scattering can be divided in two different scattering processes, Stokes and anti-Stokes. The former happens when the material absorbs energy from a photon with energy $h\nu_0$ by phonon creation whereas the latter happens when the material losses energy by phonon annihilation. If the energies of the incident photon and the created/annihilated phonon are denoted as $h\nu_0$ and $h\nu_v$ respectively,

the frequency of the scattered photon will be shifted by $\pm\nu_v$, thus having an energy of $h(\nu_0 \pm \nu_v)$.

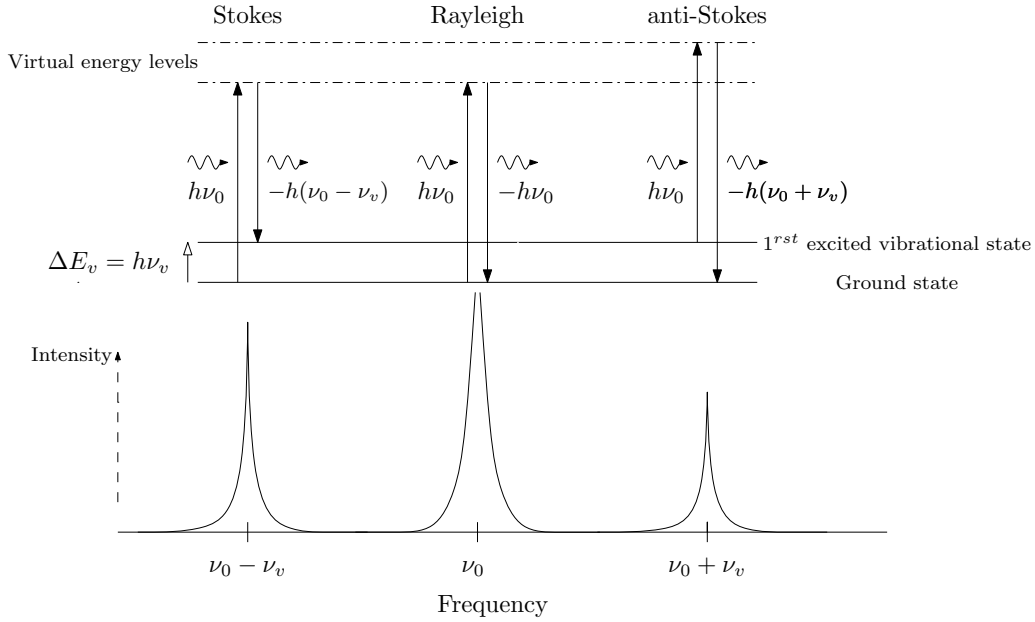

Figure 4.6: Light scattering processes and spectrum of photon transition from elemental ground states to virtual states - The energy differences of the Stokes and anti-Stokes Raman photons with respect to the excitation energy give information about molecular vibrational levels.

Micro-Raman spectroscopy (μRs) is a non-destructive characterization technique based in the Raman scattering of a monochromatic light, usually a laser. Since Raman scattering depends on the vibrational states of a given material, the energy shifts in the scattered light will be directly related to the atomic arrangement of the material, hence providing useful information that allows phase distribution and chemical bonding identification. Figure 4.7 shows the general scheme of a conventional micro-Raman spectrometer. A laser produces a monochromatic light which is focused over the sample through a microscope objective, which allows to limit the analyzed area. Then, the scattered light is collected through the microscope, focused, filtered and send to a spectrograph in order to separate it into a frequency spectrum. Finally, the spectrum is collected by a CCD and send to a computer.

The Raman spectrometer used at this work is an Invia Reflex Renishaw (Renishaw plc, Gloucestershire, UK) available at JANNUS-Saclay facility. All spectra were col-

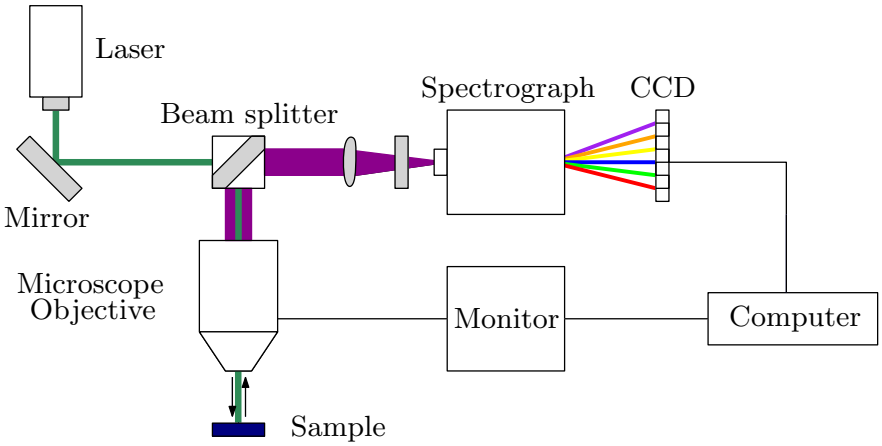

Figure 4.7: General scheme of a conventional micro-Raman spectrometer - The scattered light is collected and separated into a frequency spectrum which gives a chemical fingerprint of the analyzed sample.

lected using a 532 nm line of a frequency-doubled Nd-YAG laser. The laser was focused on a 0.5 μm^2 spot and collected through a 100× objective. The laser output power was kept around 2 mW to avoid sample heating.

4.4.2 Transmission electron microscopy

Visible-light wavelengths range from 400 to 700 nm limiting the practical magnification of optical microscopes to ∼1500× and a resolution of ∼200 nm. In order to study the microscopic effects of ion-irradiation on materials, this limit is simply not sufficient. Transmission electron microscopy (TEM) overcomes this limitation by using the ondulatory nature of electrons, which for the right conditions have wavelengths on the order of a fraction of an Å. Figure 4.8 shows the general scheme of a common TEM. In short, electrons are emitted by the source and accelerated thanks to a high voltage source. The electrons are focused onto the sample and then the transmitted electrons are projected on a phosphor screen or collected through a CCD camera. Normal voltage operation conditions are 200 kV which give an electron wavelength of 0.025 Å.

TEM observations have been conducted indistinctly with:

- a conventional CM20 TWIN-FEI (Philips, Amsterdam, Netherlands) operated at 200 kV equipped with a LaB_6 crystal as electron source and a Gatan Orius 200 CCD camera (Gatan Inc, Warrendale, PA, USA). Also, this microscope is

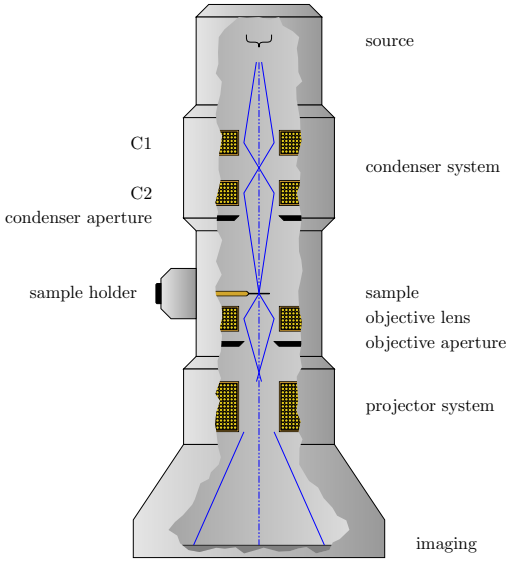

Figure 4.8: Transmission electron microscope system - Electrons emitted by the source are focused onto the sample, transmitted electrons are then projected on a phosphor screen or collected through a CCD camera.[88]

equiped with a heating specimen holder (25–1000 °C) with manual temperature control.

- a conventional JEOL FEG STEM 2010F (JEOL Ltd., Tokyo, Japan) operated at 200 kV and a GATAN CCD slow scan camera.
- a conventional JEOL FEG STEM 2100F (JEOL Ltd., Tokyo, Japan) operated at 200 kV and a GATAN CCD slow scan camera.

4.4.2.1 TEM thin foils preparation

TEM samples of the material to analyze must be thin enough, usually around 150–250 nm, to be transparent to electrons. To obtain such thin foils, also called specimens, is technically challenging and focused ion beams (FIB) coupled to SEM are one of the most powerful techniques available for such purpose. This technique has been successfully used for thin foil preparation of irradiated materials despite its tendency to introduce radiation damage in the samples as an ion-beam is used for milling and polishing the TEM specimen.[89]

In this work, thin foils have been prepared using a Helios Nanolab 650 (FEI Co.,Hillsboro, OR., USA) equipped with electron and *Ga* ion beams. Figure 4.9 shows the different steps for specimen preparation from ion-irradiated SiC samples. A layer of *Pt* was deposited over the area of interest to prevent damage of the cross-sectional surface of the TEM specimen. Initial milling was carried out with 30 keV *Ga* ions. Final polishing was carried out with successive decreasing *Ga* ion energies of 5, 2 and 1 keV to remove the implanted *Ga* ions and to produce a damage-free TEM specimen.

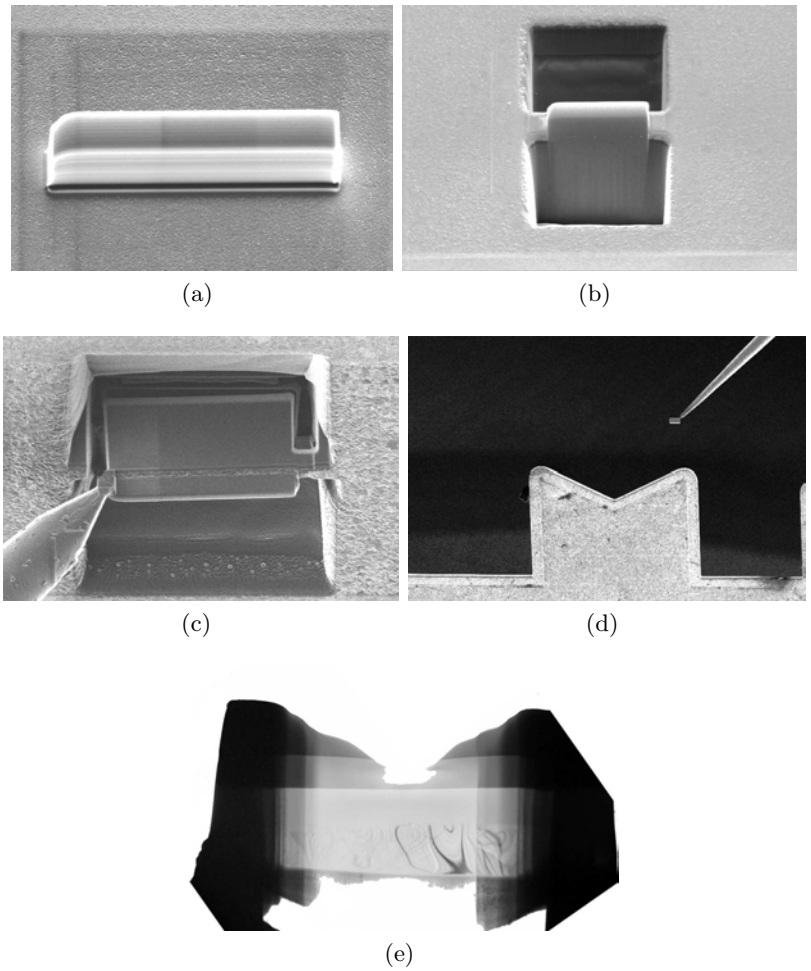

Figure 4.9: FIB thin foil extraction process - (a) Pt layer deposition, (b) ion-milling and G-cut, (c) foil extracion, (d) thin-foil welding to sample holder and (e) TEM image of the thin-foil.

4.4.3 Environmental scanning electron microscopy

As in the TEM, scanning electron microscopes (SEM) take profit of the short wavelengths of accelerated electrons. In SEM the electron beam is accelerated at voltages ranging from 200 eV to 40 keV and focused over the sample. Figure 4.10 depicts schematicaly the different effects of the electron beam interaction with the analyzed sample. The elastically backscattered electrons are used to detect areas with different chemical composition and secondary electrons, which are the result of inelastic scattering, are the most common imaging mode and allow image resolutions of ∼0.5 nm. Also, Auger electrons, X-ray photons and cathodeluminiscence arising from the electron beam interaction can be collected and used for detecting the composition of the material.

Environmental-SEM (E-SEM) can operate at a wider range of pressures than conventional SEM, from high vacuum to the pressure required to observe liquid distilled water. This allows to observe a wide variety of samples such as non-coated samples and "wet" tissues, such as organic matter, wool fibersand and phenomena like the crystallization and rewetting of salts.[90]

The E-SEM observation was conducted in a FEI QUANTA 200 E-SEM FEG equipped with a heating plate (25–1500 °C), operated at 30 kV. Precise sample temperature measurement is ensured by a homemade sample holder containing a Pt-Pt-Rh10 thermocouple.[91] H_2O pressure was kept constant at 120 Pa.

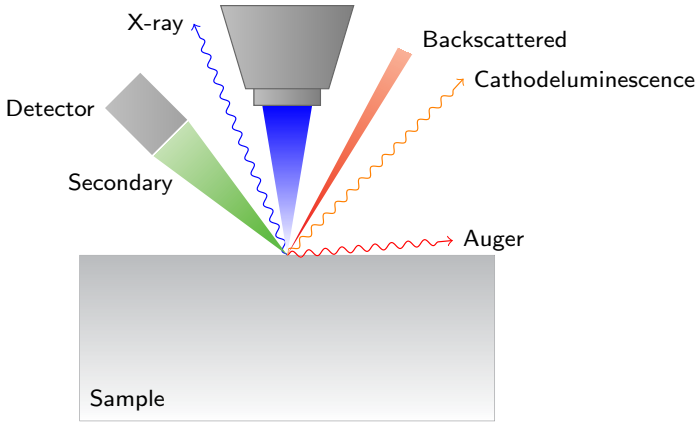

Figure 4.10: Scanning electron microscope system - When the primary electrons impact the surface they generate secondary electrons, backscattered electrons, Auger electrons, X-ray photons and cathodeluminescence.[92]

5

Characterization of the ion-amorphization threshold conditions of third generation SiC fibers

Amorphization is one of the most detrimental SiC characteristics for its use under nuclear environments at low temperatures. In order to study the amorphization threshold conditions of third generation SiC fibers, HNS and TSA3 fibers have been ion-irradiated with 4 MeV Au^{3+} ions at RT to increasing fluences. Also, for the highest fluence, i.e. 2×10^{15} cm^{-2}, different samples have been irradiation at temperatures ranging from RT to 300 °C. Irradiation effects have been characterized in terms of μRs and TEM and compared to the response of the as-irradiated model material, i.e. 6H-SiC single crystals. It is reported that the ion-amorphization kinetics of these fibers and 6H-SiC single crystals are similar despite their different microstructures and polytypes. Critical amorphization dose at RT yields $\sim2\times10^{14}$ cm^{-2} ($\sim$0.4 dpa) and critical amorphization temperature is in the 100–200 °C range.

5.1 Introduction

Among other nuclear structural applications, SiC_f/SiC_m has been proposed to replace nowadays zirconium-alloy based fuel cladding for light water reactors (cf. chapter 1).[6–8] In-pile conditions of these reactors are, in terms of damaging dose and temperature, less demanding for structural materials than those in future GEN-IV fission

and fusion reactors (cf. Figure 1.1). However, whereas the previous statement may hold for metallic structural materials —susceptible to fail mechanically or melt at high temperatures— it may not be the case for SiC-based composites which are high temperature stable materials.[38] However, it has been reported that irradiation induced degradation is higher at low temperatures.[93] For instance, as it has been previously described in sections 3.2 and 3.3, one of the most detrimental features of SiC for its use under nuclear environments at low temperatures is the degradation of its physico-chemical properties due to irradiation induced amorphization. Amorphization threshold conditions are fairly well known for SiC single crystals and CVI-SiC under ion and neutron irradiation and fall near the operating conditions of LWRs. However, at the knowledge of the author, there are not comprehensive studies of the amorphization threshold conditions of nuclear grade SiC fibers, which are necessary in order to determine whether if SiC composites are suitable or not for such applications.

In order study the effects of the microstructure on the behavior of these ceramic fibers under irradiation, HNS and TSA3 fibers have been ion-irradiated under in-pile relevant conditions. Then, irradiation effects have been characterized in terms of μRs and TEM and compared to the response of the as-irradiated model material, i.e. 6H-SiC single crystals.

5.2 Ion-irradiation conditions

Ion-irradiations have been performed at JANNUS-Saclay and JANNUS-Orsay facilites, both described in section 4.2.1. 6H-SiC single crystals and both HNS and TSA3 fibers have been irradiated simultaneously using 4 MeV Au^{3+} ions at RT to increasing fluences: 5×10^{12}, 10^{13}, 5×10^{13}, 10^{14}, 2×10^{14}, 3×10^{14} and 10^{15} cm^{-1}. Also, samples have been irradiated 2×10^{15} cm^{-2} at RT, 100 °C, 200 °C and 300 °C using a heating sample holder. Ion-flux was set at $\sim10^{-11}$ cm^{-2}s^{-1} and the irradiation temperature was continuously monitored by both a thermocouple located on the sample holder and *in situ* infrared (IR) imaging. The IR camera is a FLIR A325 SC controlled by the ThermaCAM Researcher software. The temperature gradient between the sample holder and the surface of the SiC single crystal sample can be neglected due to its small thickness, high thermal conductivity, and good thermal contact conductance. Also,

to achieve the contact with the sample holder and minimize the temperature gradient within the fibers, the fiber tows were flattened and fixed with conductive silver paint. Furthermore, the ion-irradiation effects were characterized in the area where the contact between the fibers and the sample holder was kept during the irradiation.

To evaluate the damage induced to the target and the contribution of the electronic (S_e) and nuclear (S_n) stopping powers, full damage cascade and Kinchin-Pease[94] simulations were performed using SRIM-2013.[49] Fluence to dose conversion has been calculated as described in Eq. 3.4. In both cases, threshold lattice displacement energies (E_d) were set to 35 eV for Si and 20 eV for C[95] and the theoretical density of SiC to 3.21 g cm^{-3}. Finally, the highest ion-fluence yields a mean dose of ∼4 dpa and the ion-flux a mean dose rate of ∼1.9×10^{-4} dpa s^{-1}.

Figure 5.1 shows the damage and the energy loss profiles of the incident ion in SiC as a function of depth. As it can be seen, the estimated dose is higher than the 6H-SiC dose to amorphization (DTA) at RT, i.e. 0.4 dpa, for an irradiated thickness of 0.8 μm.

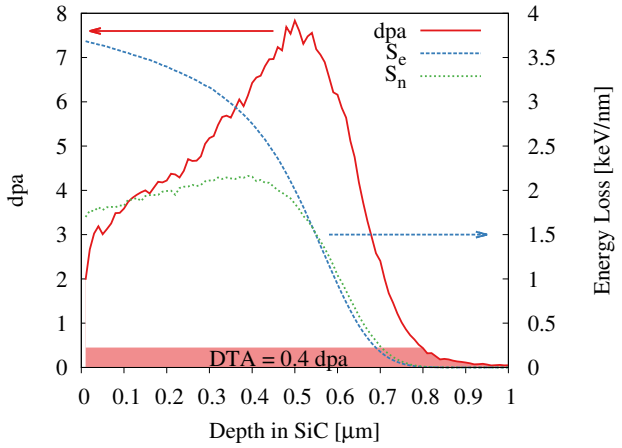

Figure 5.1: Damage profile (dpa) and electronic (S_e) and nuclear (S_n) stopping powers for 4 MeV Au^{3+} ions in SiC - Dose estimation for a fluence of 2×10^{15} cm^{-2} is calculated with full-cascade mode and the stopping powers with Kinchin-Pease mode using SRIM-2013.[49] Displacement energies were set to 35 and 20 eV for Si and C sublattices respectively.[95]

5.3 Results

5.3.1 Microstructural characterization of as-received materials

Figure 5.2 shows TEM images of the microstructures of both fibers. Stacking faults (SFs) in SiC grains are clearly observed for both fibers as striped patterns inside the grains. SF linear density (ρ_{SF}) was determined by counting the number of stripes per unit length in the perpendicular direction using ImageJ image analysis software.[96] Mean ρ_{SF} values are 0.29±0.1 nm^{-1} for HNS fibers and 0.18±0.1 nm^{-1} TSA3 fibers. Also, mean maximum and minimum Feret diameters—which correspond to the shortest and the longest distances between any two points along the GB—were determined. These values yield, respectively, 26 and 36 nm for the HNS fibers and 141 and 210 nm for the TSA3 fibers.

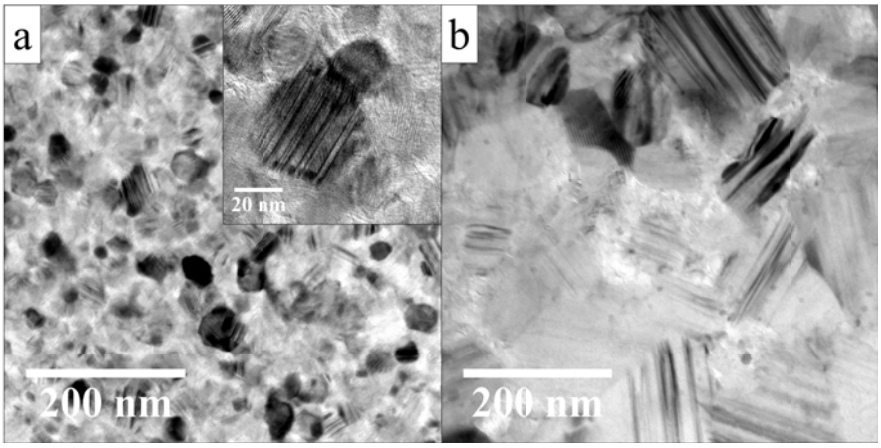

Figure 5.2: TEM image of the microstructure of as-received (a) HNS and (b) TSA3 - Stripped patterns inside the grains indicate the presence of high densities of stacking faults. Brighter contrasts correspond to intergranular free C.

As commented in section 4.4.1, μRs is a powerful characterization that provides a chemical fingerprint of the analyzed material. Raman peak parameters such as intensity, bandwidth and wavenumber provide useful information related to the polytype, phase distribution and chemical bonding that compose SiC and SiC fibers.[97] Table 5.1 gathers the characteristic Raman peak wavenumber of the folded modes for 3C- and 6H-SiC polytypes.[98]

Figure 5.3 shows the Raman spectrum collected from the as-received 6H-SiC single crystal. Group-theoretical analysis indicates that the Raman-active modes of the

Table 5.1: Raman shift of the folded modes for 3C- and 6H-SiC polytypes[1]

Polytype	χ=q/q_B[2]	Raman shift [cm^{-1}]			
		Planar acoustic TA	Planar optic TO	Axial acoustic LA	Axial optic LO
3C-SiC	0	-	796	-	972
6H-SiC	0	-	797	-	965
	2/6	145,150	789	-	-
	4/6	236,241	-	504,514	889
	6/6	266	767	-	-

[1] Ref.[98]

[2] χ denotes the folded modes, i.e. the reduced wave vector of the phonon modes in the Brillouin zone

wurtzite structure (C_{6v} symmetry for hexagonal polytypes) are the A_1, E_1 and E_2 modes. In turn, A_1 and E_1 phonon modes are split into longitudinal (LO) and transverse (TO) optical modes. Also, the high quality of the sample allows the observation of second order Raman bands as several weaker peaks located at 500 cm^{-1} and between 1400–1850 cm^{-1}.[98–100]

Figures 5.4 and 5.5 show the Raman spectra collected from the as-received HNS and TSA3 fibers. Raman spectra collected from these fibers differ notably from the single crystal spectrum. Their polycrystalline microstructure and the intergranular free *C* noticeable in Figure 5.2 induce the apparition of several peaks related to their chemical fingerprint. For instance, peaks located between the 700 cm^{-1} and 1000 cm^{-1} are related to the cubic SiC polytype. The unit cell of 3C-SiC contains one formula unit and there are longitudinal and doubly degenerate transversal modes in the optical branches located at 796 cm^{-1} (TO) and 972 cm^{-1} (LO). Satellite peaks around 766 cm^{-1} are attributed to disordered SiC consisting of a combination of simple polytype domains and nearly periodically distributed stacking faults.[97,101] This explanation is also consistent with the high SF density observed in Figure 5.2.

High-intensity peaks located between 1200 cm^{-1} and 1800 cm^{-1} are attributed to the intergranular free *C* despite the little free *C* content of both fibers. The high contribution of these peaks to the spectra is due to the high Raman cross-section of *C-C* bonds which is up to ten times higher than the *Si-C* bonds one.[97,102] Regarding

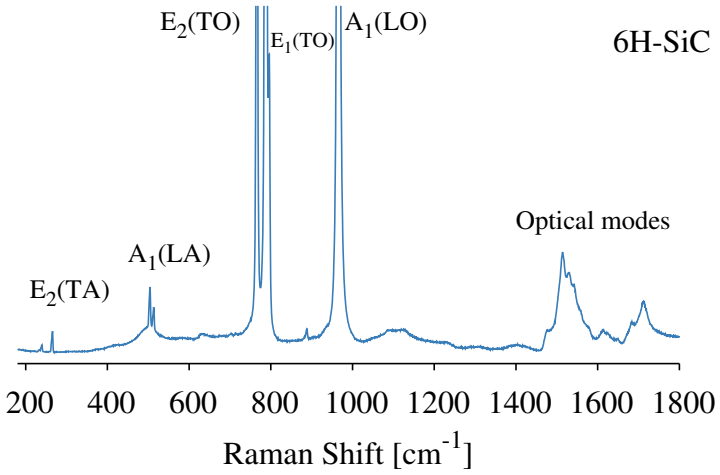

Figure 5.3: Raman spectrum collected from the as-received 6H-SiC - The absence of native defects allows to observe second order Raman bands.

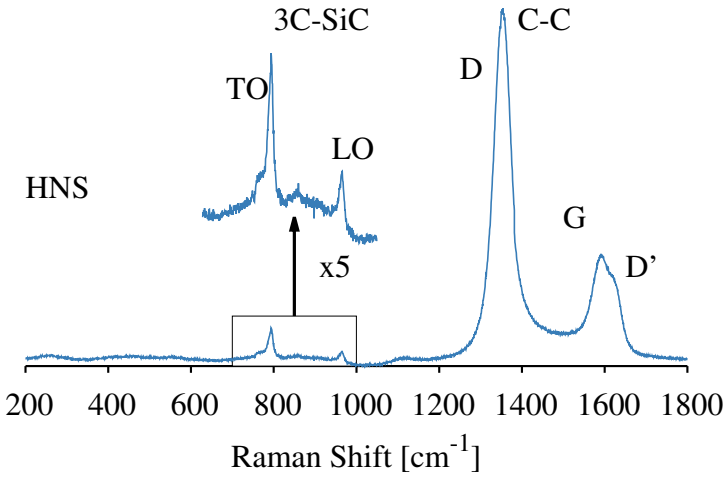

Figure 5.4: Raman spectrum collected from the as-received HNS fiber - The free C signal masks the Si-C bonds signal and the low intensity of the G band is attributed to small free C pockets.

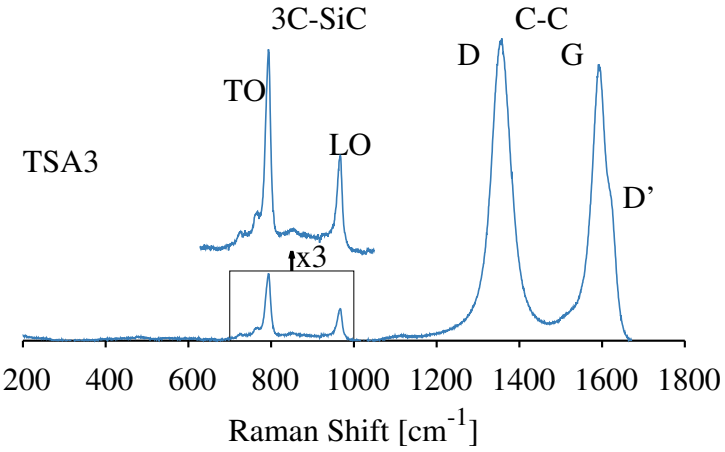

Figure 5.5: Raman spectrum collected from the as-received TSA3 fiber - The free C signal masks the Si-C bonds signal.

the C chemical fingerprint, G peak centered around 1581 cm^{-1} is related to graphitic structures as a result of the sp^2 stretching modes of C bonds and the D peak centered around 1331 cm^{-1}, according to Colomban et al.[97] should be attributed to vibrations involving sp^3-$sp^{2/3}$ bonds. The shouldering (D') on the G band in both fibers results from a folding of the graphite dispersion branch corresponding to G at Γ point. This shouldering is characteristic of the disorder of the crystallographic planes around the c-axis of the turbostratic C.[97]

Finally, there is a remarkable difference in the G peak intensity between TSA3 and HNS fibers. This difference can be related to the different crystallite size of the intergranular free C found in these fibers. For instance, Eq. 5.1, developed by Cançado et al.,[103] based on the studies by Tuinstra and Koenig[104] and Knight and White,[105] can be used to determine the in-plane graphitic crystallite size (L_a) from the D and G intensity ratios, $\left(\frac{I_D}{I_G}\right)$, and a given excitation laser energy (λ_l). As a result, the estimated graphite crystallite sizes yield 7 and 14 nm for HNS and TSA3 fibers.

$$L_a(nm) = 2.4 \times 10^{-10} \lambda_l^4 \left(\frac{I_D}{I_G}\right)^{-1} \tag{5.1}$$

5.3.2 Ion-amorphization kinetics at RT

As commented in section 4.2, ion-irradiation is widely used by the nuclear materials community to simulate neutron damage due to the tunability of the irradiation parameters (dose, dose rate, temperature) and the similarity of the defect production in terms of displacement cascade creation (cf. Figure 3.2).

Figures 5.6, 5.7 and 5.8 show, respectively, the evolution of the Raman spectra as a function of the dpa-dose for 6H-SiC single crystals and HNS and TSA3 fibers under irradiation at RT.

For 6H-SiC single crystals ion-irradiation induces sequential broadening of the Si-C bond related peaks in all samples until they combine in a unique low-intensity broad peak. Also, it is noticeable the appearance of new low-intensity broad peaks at ∼500 cm^{-1} and ∼1400 cm^{-1}. These changes in the Raman spectra imply a significant modification of the local structure and correspond respectively to the dissociation of the *Si-C* bonds and the creation of *Si-Si* and *C-C* homonuclear bonds. Also, the intensity of the Raman signal decreases exponentially with dose due to the modification of the SiC optical properties.[99]

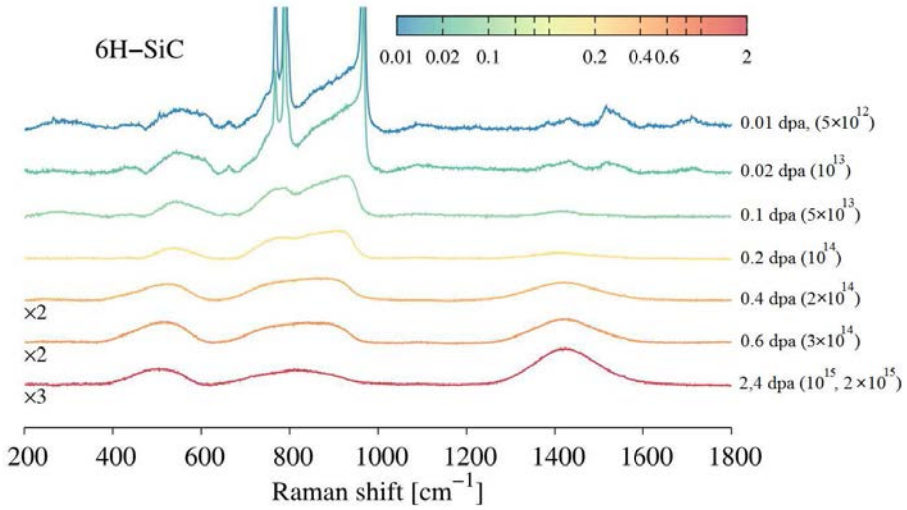

Figure 5.6: Raman spectra evolution for ion-irradiated (4 MeV Au^{3+}, RT) 6H-SiC single crystals as a function of the dose - Si-C peaks fade with dose until their complete randomization. Ion fluences are in cm^{-2}.

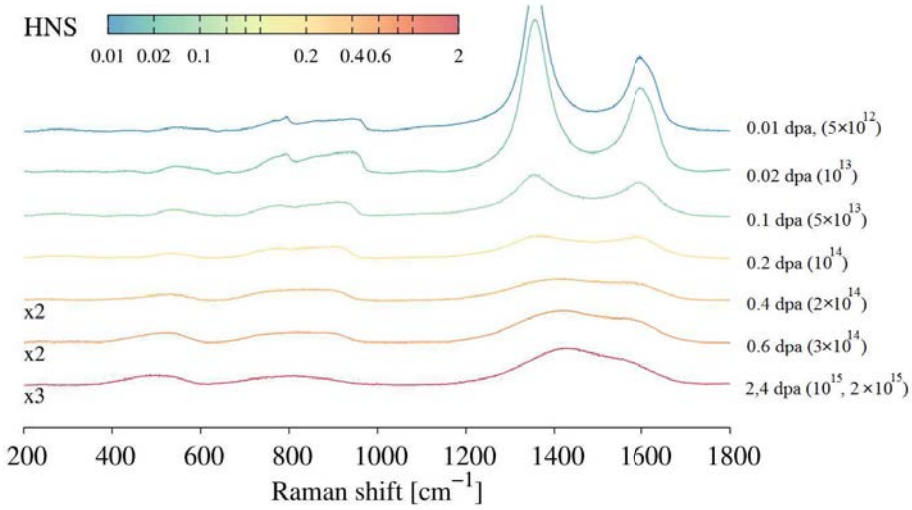

Figure 5.7: Raman spectra evolution for ion-irradiated (4 MeV Au^{3+}, RT) HNS fibers as a function of the dose - Si-C peaks fade with dose until their complete randomization.Ion fluences are in cm^{-2}.

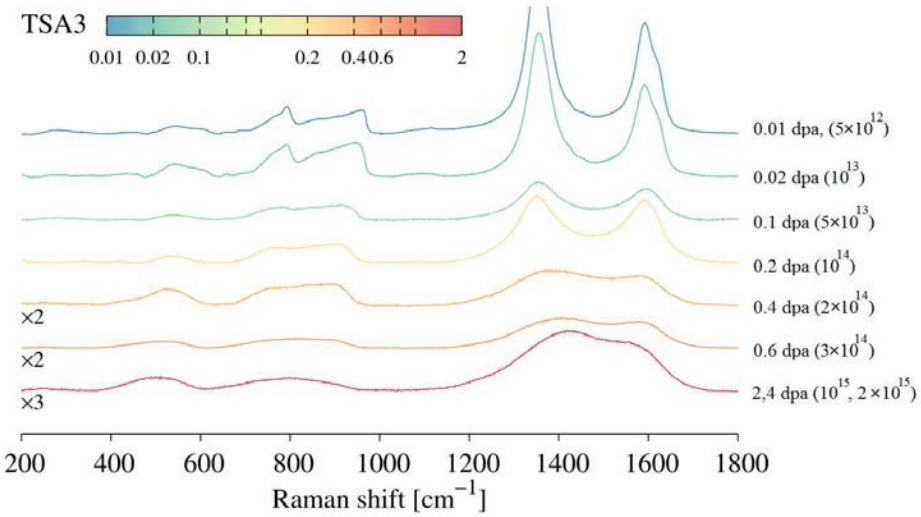

Figure 5.8: Raman spectra evolution for ion-irradiated (4 MeV Au^{3+}, RT) TSA3 fibers as a function of the dose - Si-C peaks fade with dose until their complete randomization.Ion fluences are in cm^{-2}.

Both SiC fibers present similar behavior. As for 6H-SiC, ion-irradiation causes the dissociation of their Si-C bonds giving rise to *Si-Si* and *C-C* homonuclear bonds. Nevertheless, irradiation at low doses increases the intensity of the Si-C related peak despite its randomization. As commented, there is a remarkable influence of the free *C* in the SiC fibers Raman spectra due to the high Raman cross-section of *C-C* bonds. Under irradiation, the rupture of these bonds will imply the drop of its cross-section allowing the SiC Raman signal to emerge over the free *C* one. Finally, the spectra show similar low-intensity broad peaks at ~800 cm^{-1} characteristic of amorphous SiC.

Finally, Figure 5.9 presents the evolution of the chemical disorder in terms of the ratio of the intensities associated to *Si-Si* to *Si-C* bonds ($\Theta_{(Si-Si)}$) for the single crystal and the two kinds of SiC fibers.

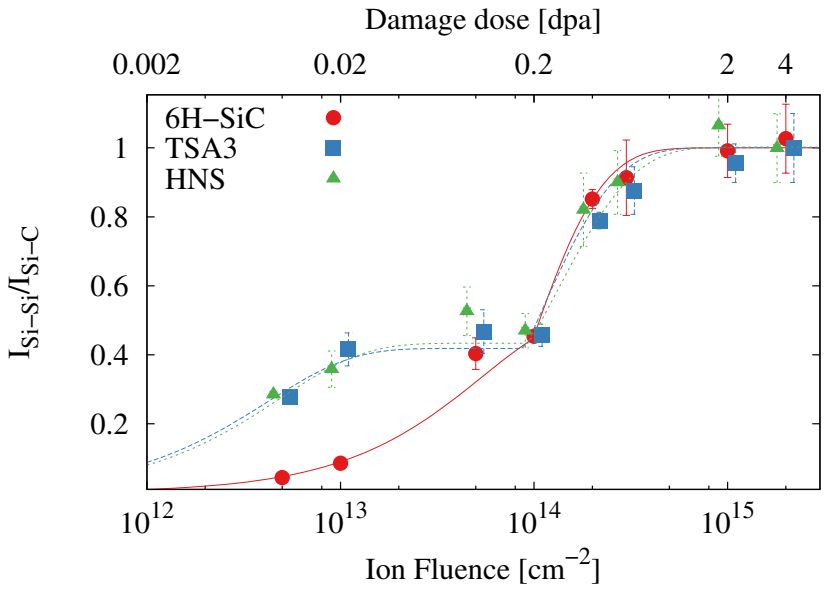

Figure 5.9: Intensity of the Raman peaks associated to homonuclear *Si-Si* bonds normalized to the intensity of the Raman peaks associated to *Si-C* bonds - I_{Si-Si}/I_{Si-C} is the chemical disorder denoted $\Theta_{(Si-Si)}$ in the text. Experimental data is horizontally offset for the sake of clarity. Data has been fitted with the MSDA model (n=2).

Data in Figure 5.9 has been fitted with the multi-step damage accumulation (MSDA)

model given by:

$$f_d = \sum_{i=1}^{n} \left[\left(f_{d,i}^{sat} - f_{d,i-1}^{sat} \right) \left(1 - e^{-\sigma_i (\varphi - \varphi_{i-1})} \right) \right] \tag{5.2}$$

Where n is the number of steps in damage accumulation, $f_{d,i}^{sat}$ the level of damage saturation for the step i, σ_i the damage cross section for the step i, and φ and φ_{i-1} the dose and the saturation dose of the i^{th} step.[106] This model assumes that damage accumulation is a sequence of distinct transformations of the current structure of the irradiated material and that reduces to a direct impact (DI) model for n=1 meaning that amorphization is achieved in a single cascade.[106] Table 5.2 gathers the best-fit parameters for n=2 of the $\Theta_{(Si-Si)}$ evolution. Fit has been performed using a non-linear least-squares Marquardt-Levenberg algorithm. As it can be observed, an inflection point and saturation of the curve is reached for doses of 0.2 and 0.6 dpa, respecively.

Table 5.2: Best-fit parameters for modeling the evolution of $\Theta_{(Si-Si)}$ with dose using the MSDA model

Sample	MSDA with n=2			
	i=1		i=2	
	f_d^{sat}	σ_1 [1]	f_d^{sat}	σ_2 [1]
6H-SiC	0.53	0.54	1	0.82
TSA3	0.44	0.046	1	0.94
HNS	0.43	0.049	1	1.18

[1] σ_i in 10^{-14} cm^{-2} units.

5.3.3 Ion-amorphization as a function of the irradiation temperature

Ion-amorphization is highly dependent on the irradiation temperature. As commented in section 3.2, there is a threshold temperature over which amorphization is virtually impossible as thermal dynamic annealing processes take place during irradiation.

Figures 5.10, 5.11, 5.12 and 5.13 show the Raman spectra for samples irradiated to 2×10^{15} cm^{-2} (4 dpa) at RT, 100 °C, 200 °C and 300 °C. This dose is up to ten times the amorphization threshold dose determined above for 4 MeV Au^{3+} ion-irradiation at RT.

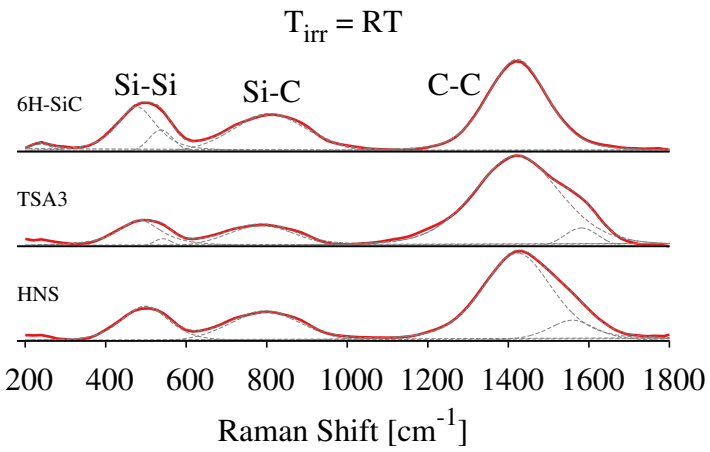

Figure 5.10: Raman spectra collected from samples irradiated at RT to 2×10^{15} cm^{-2} - All samples show completely randomized SiC related peaks.

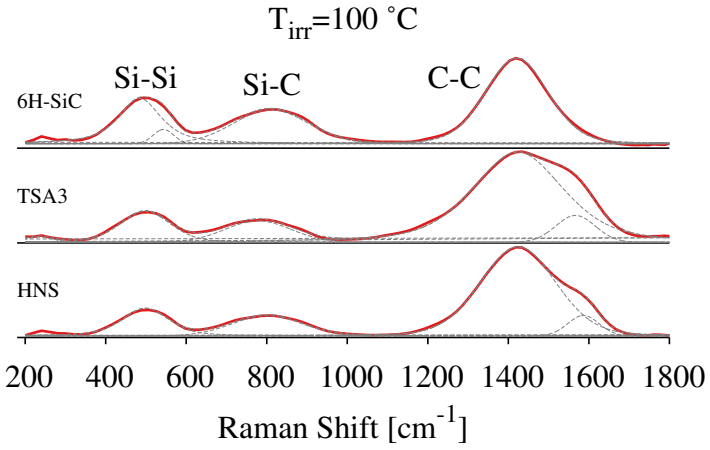

Figure 5.11: Raman spectra collected from samples irradiated at 100 °C to 2×10^{15} cm^{-2} - All samples show completely randomized SiC related peaks.

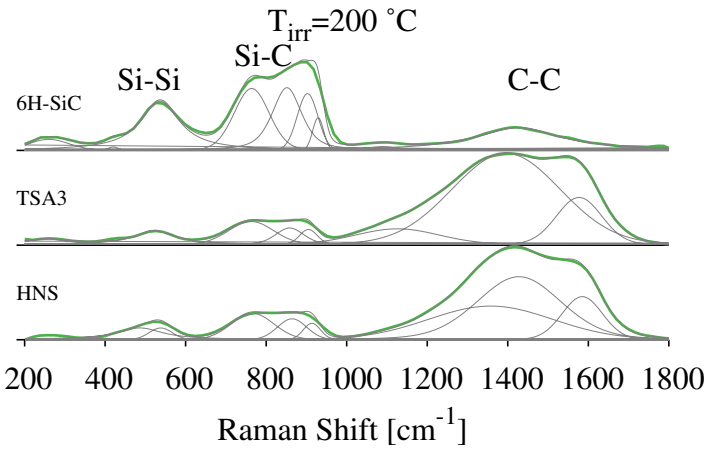

Figure 5.12: Raman spectra collected from samples irradiated at 200 °C to 2×10^{15} cm^{-2} - All samples show the deconvolution of the SiC related peak characteristic of residual crystallinity.

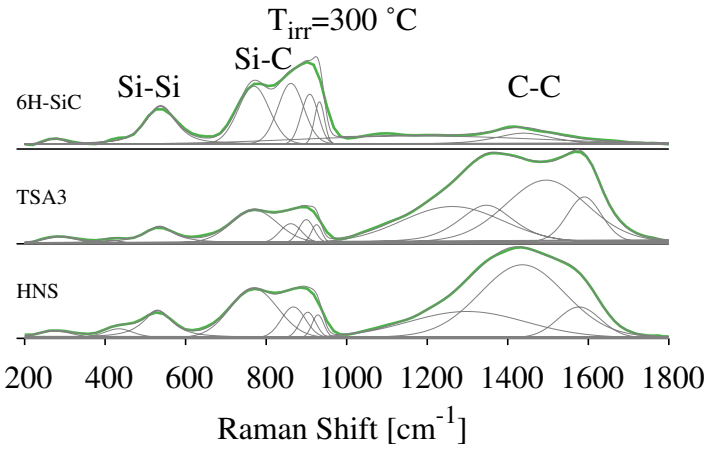

Figure 5.13: Raman spectra collected from samples irradiated at 300 °C to 2×10^{15} cm^{-2} - All samples show the deconvolution of the SiC related peak characteristic of residual crystallinity.

All samples irradiated at RT and 100 °C are amorphous as the crystalline peaks have completely disappeared. However, Raman spectra obtained from the samples irradiated at 200 °C and 300 °C exhibit the deconvolution of the Si-C related peak into several components which are characteristic of residual crystallinity. From direct comparison of the spectra from irradiation at 200 °C with Figures 5.6, 5.7 and 5.8, the damage level of the samples irradiated at 200 °C seems to be equivalent to 0.1–0.2 dpa for irradiations at RT, i.e. below the threshold amorphization dose at RT. Also, calculated values of $\Theta_{(Si-Si)}$ are in the 0.4–0.6 range for all samples. Therefore, the disorder level achieved at 4 dpa at 200 °C is equivalent to the disorder achieved at ∼0.2 dpa at RT (cf. Figure 5.9).

In order to give more details about the microstructural state of the samples after irradiation, cross-sectional thin foils have been extracted from the irradiated samples and observed through TEM as described in section 4.4.2.

Figures 5.14, 5.15 and 5.16 show TEM images and selected area electron diffraction patterns (SAED) obtained respectively from the 6H-SiC, TSA3 and HNS fibers irradiated at (a) RT and (b) 200 °C. As it can be observed, at RT, the incident particles induce the amorphization of the samples as indicated by the concentric rings of the SAED. The thickness of the amorphous SiC (a-SiC) band is 1.3 μm for the 6H-SiC and TSA3 fiber and 1.13 μm for the HNS fiber. Also, the spotted SAED patterns obtained from the non-irradiated substrates indicate that no amorphization was induced during the preparation of the samples. For the samples irradiated at 200 °C, it is possible to clearly identify two different zones in the irradiated layers: a partially amorphized band near the surface (irr.-SiC), as satellite spots appear in the SAED pattern, and an in-depth band of a-SiC. Irr.-SiC and a-SiC thicknesses yield respectively 0.6 μm and 0.5 μm for the single crystal, 0.2 μm and 0.8 μm for the TSA3 fiber and 0.6 μm and 0.4 μm for the HNS fiber. Also, in Figure 5.15, brighter-contrast zones embedded can be noticed in the a-SiC band of the irradiated TSA3 fibers. Direct comparison of the contrast and shape of these zones with the polycrystalline microstructure of the TSA3 fiber (Figure 5.2) indicates that these brighter-contrast zones correspond to irradiated C arising from the intergranular free C. Finally, in Figure 5.17 isolated dispersed nanocrystalline SiC (nc-SiC) grains can be found embedded in the in-depth a-SiC band of the HNS fibers irradiated at 200 °C.

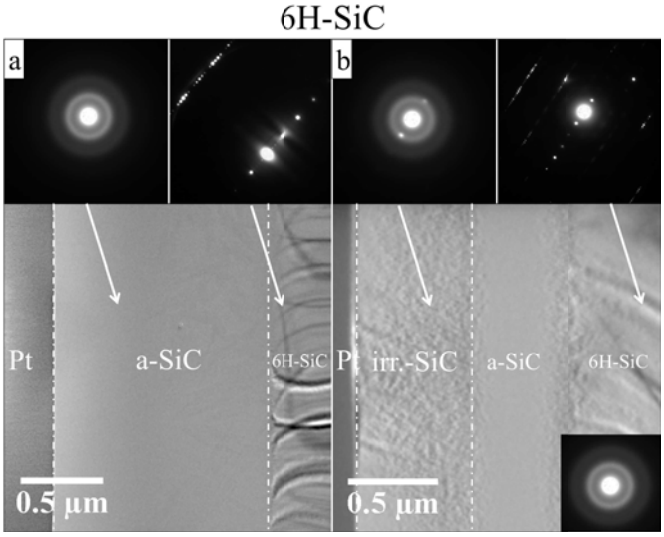

Figure 5.14: TEM images and SAED patterns obtained from 6H-SiC irradiated with 4 MeV Au^{3+} to 2×10^{15} cm^{-2} (4 dpa) at (a) RT and (b) 200 °C - SAED pattern in bottom right corner corresponds to a-SiC, which stands for amorphous SiC. Also, irr.-SiC stands for irradiated SiC.

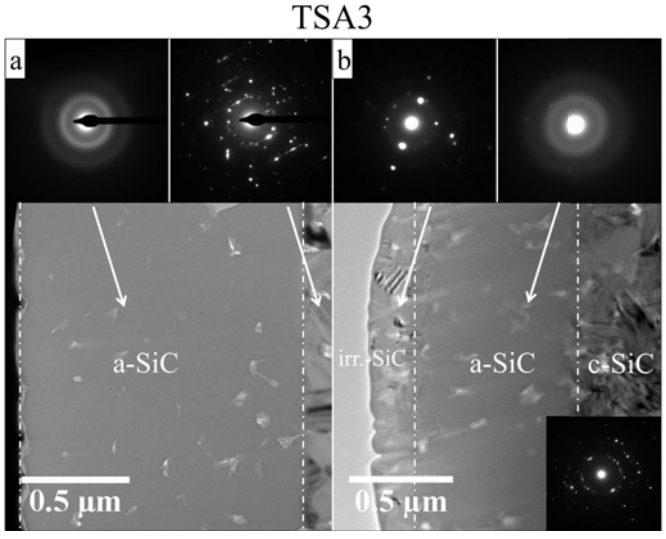

Figure 5.15: TEM images and SAED patterns obtained from TSA3 fibers irradiated with 4 MeV Au^{3+} to 2×10^{15} cm^{-2} (4 dpa) at (a) RT and (b) 200 °C - a-SiC stands for amorphous SiC and c-SiC stands for crystalline SiC.

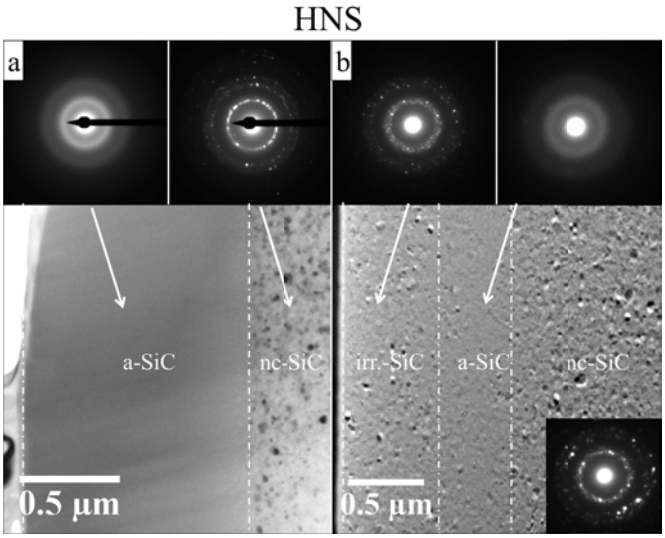

Figure 5.16: TEM images and SAED patterns obtained from HNS fibers irradiated with 4 MeV Au^{3+} to 2×10^{15} cm^{-2} (4 dpa) at (a) RT and (b) 200 °C - a-SiC stands for amorphous SiC, nc-SiC stands for nanocrystalline SiC and irr.-SiC stands for irradiated SiC.

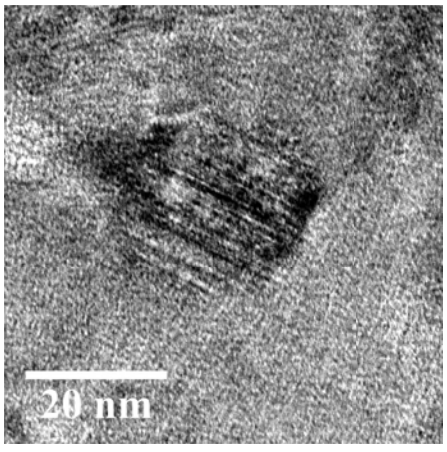

Figure 5.17: Detail of the amorphous SiC band of irradiated HNS fibers - Nanocrystalline faulted SiC grains can be found embedded in the a-SiC band

5.4 Discussion

In this work, heavy ion-irradiation is used to simulate the damage occurring in SiC fibers as a consequence of the neutron flux exposure. It has been pointed out that ion-irradiation with high S_e values may have synergetic effects in SiC as the electronic energy deposition may heal the damage produced by elastic collisions.[52,107,108] Also, partial ion-induced annealing in pre-damaged SiC has been observed for S_e values as low as 5 keV/nm for 21 MeV Si ion-irradiations.[94] However, for this energy, the S_n contribution is negligible to the energy loss process as indicated by the high S_e/S_n ratio (∼500). As it can be observed in Figure 5.1, for 4 MeV Au^{3+} ion-irradiation, S_e is ∼4 keV/nm at the surface. However, as indicated by the low S_e/S_n ratio (∼2 at the surface), only a small part of the kinetic energy will be lost due to inelastic interactions, thereby minimizing the dynamic annealing effects by electronic excitations.

Raman depth of field depends not only in the experimental conditions, such as laser wavelength or numerical aperture, but also on the optical properties of the material. For instance, a rough estimation of the Raman depth of field for the experimental conditions of this work yields ∼0.5 μm,[109] though it is sensitive to be overestimated for irradiated samples as SiC light absortion increases with irradiation damage.[99] In any case, the analyzed depth will be smaller than the thickness of the irradiated SiC layer thus limiting the Raman analysis to the surface of the sample.

Ion-amorphization kinetics for 6H-SiC single crystals has been previously studied by μRs in terms of the total disorder parameter and the chemical disorder. The former is defined as $\xi = (1 - A/A_{cryst})$, being A the total area under the principal first-order SiC peaks normalized to the value A_{cryst} of the crystalline material. This parameter accounts for the loss of long-range order (LRO), and ranges from 0 for completely crystalline to 1 for completely amorphized SiC. The latter has been defined as the ratio of C-C homonuclear bonds to Si-C bonds and denoted as $\Theta_{(C-C)}$, ranging from zero for perfect short-range order (SRO) to unity for random short-range disorder. SRO describes the degree of the chemical state with respect to the local arrangement of atoms, which can be partially preserved even when the LRO is completely lost.[14,99] However, the use of these parameters to study the ion-amorphization of SiC fibers is limited by two factors. First, the Si-C bond signal increases at low doses, hence invalidating ξ as an indicator of the loss of LRO, and second, the enormous impact

of the free C in the Raman spectra, hence invalidating also $\Theta_{(C-C)}$ as an indicative of the loss of SRO. In order to overcome these limitations, chemical disorder has been calculated as the ratio of Si-Si homonuclear bonds to Si-C bonds ($\Theta_{(Si-Si)}$), under the assumption that the intensity of the Raman peaks is proportional to the concentration of the related atomic bond.[99]

MSDA parameters for 6H-SiC amorphization kinetics are consistent with previous reported ones based in RBS and μRs data[14,15] hence confirming $\Theta_{(Si-Si)}$ as a relevant indicative for the amorphization level of the sample. According to the fit parameters, there is a significant difference in the first stage of the amorphization process between SiC fibers and 6H-SiC. However, this difference may arise from the difficulty of processing Raman spectra of SiC fibers due to their C signal so it cannot be directly attributed to a prompt amorphization. More experimental data is needed to determine whether there exists a difference in the amorphization kinetics at low doses. However, all irradiated samples show an inflexion point around 10^{14} cm^{-2} (0.2 dpa) and reach the saturation value over 3×10^{14} cm^{-2} (0.6 dpa) at RT.

In agreement to the μRs characterization, TEM images show complete amorphization of the samples irradiated at the highest dose at RT as indicated by the concentric rings of the SAED patterns. As it can be observed, ion-irradiation at RT induces the formation of a homogeneous a-SiC layer all across the irradiated zone for the HNS fibers and 6H-SiC. This homogeneity is not found for the TSA3 fibers case, as zones with brighter-contrast appear embedded in the a-SiC band. These brighter-contrast zones are associated to C clusters which remain after the ion-irradiation. Even though both fibers have comparable C/Si ratios, i.e. $\sim$1.03 for TSA3 fibers and $\sim$1.07 for HNS fibers, the free C distribution is different as TSA3 fibers exhibit larger C clusters than HNS fibers. Free C cluster sizes before irradiation obtained from TEM images yield minimum and maximum Feret diameters of 12 nm and 28 nm for the HNS fibers and 61 and 138 nm for TSA3. These values are higher than the determined in-plane graphite crystallite sizes of 7 nm for HNS and 14 nm for TSA3 fibers suggesting that the free C consists in graphite crystallites with several orientations. Graphite amorphizes when irradiated at RT for doses in the range of 0.2–0.5 dpa.[110] As shown in Figure 5.18, the smaller size of the C clusters in HNS fibers may ease the ballistic mixing of the damaged SiC with the free C inducing the cluster disappearance. By contrast, the

larger size of the free C clusters in TSA3 fibers may limit their complete disappearance hence explaining the C clusters embedded in the a-SiC band.

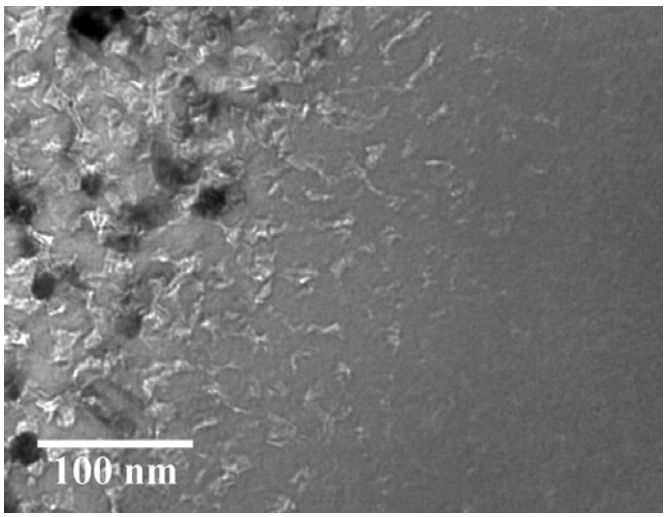

Figure 5.18: Detail of the amorphous-crytalline interphase of the HNS fiber irradiated at RT to 2×10^{15} cm^{-2} (4 dpa) - The small size of the free C pockets at grain boundaries eases their ballistic mixing with the surrounding SiC.

Regarding the samples irradiated at 200 °C and 300 °C, the deconvolution of the *Si-C* related peak of the Raman spectra indicate the presence of residual crystallinity after irradiation. In compliment to the surface μRs information, TEM images of the samples irradiated at 200 °C reveal the in-depth profile of the irradiated samples. As it has been described, all samples present a double layered structure with an irradiated layer showing residual crystallinity followed by an amorphous SiC layer, as indicated by the satellite spots in their respective SAED patterns. However, slight differences in the thickness of the a-SiC bands of the samples irradiated at 200 °C can be noticed. As the damage profile caused by the incoming ions is not spatially flat (cf. Figure 5.1) and increases from the surface to near the implantation peak depth, it would be desirable to estimate the DTA at this temperature by determining the dose at which the SRIM damage profile and the irradiated-to-amorphous SiC interface intersect. However, differences observed between the SRIM damage profiles and the TEM images prevent this estimation. Indeed, the estimation of the a-SiC band thickness based on SRIM calculations for the irradiation at RT yields ~0.8 μm. This value corresponds to the zone where the evaluated dose is over the DTA at RT. Nevertheless, this value

is lower than the measured irradiated thickness of the samples making impossible direct comparison between the TEM images and the simulated damage profile. Actually, it has been shown that SRIM calculations underestimate the implantation profile of heavy ions in light targets, such as *Au* ions in SiC.[111,112] Moreover, 6H-SiC swells up to 11.5–25%[15,113] under Au-irradiation at RT. However, even taking into account the highest density decrease on the irradiated layer ($0.75\times\rho_{SiC}$), SRIM calculations yield an underestimated value of the irradiated thickness of $\sim$1 μm. It should also be mentioned that the amorphous layer created under heavy ion-irradiation broadens over the theoretical ion projected range once the dose is over the DTA.[114] Therefore, the combination of the SiC irradiation swelling and the SRIM underestimation of the irradiated thickness explain the observed differences between the SRIM prediction and the TEM measurements. In addition, small temperature differences due to the experimental setting cannot be discarded as the source of the small variations of the a-SiC thicknesses of the samples. Finally, T_c for HNS and TSA3 SiC fibers, considering it as the temperature at which SiC is prevented from complete amorphization of the irradiated layer, is estimated to be in the range of 100–200 °C in agreement with literature values for SiC single crystals.[50,53,115] Finally, Figure 5.19, show how the similar amorphization threshold conditions for 6H-SiC, TSA3 and HNS fibers found in this work are in good agreement with literature values for single crystals irradiated with different particles.

Ion-irradiation behavior of materials will depend on their intrinsic and extrinsic characteristics. Regarding their chemical purity, in spite of the appellation of near-stoichiometric and low-oxygen fibers both TSA3 and HNS fibers exhibit non-negligible but comparable amounts of *O* and *C*[43] with respect to the single crystal. In addition, TSA3 fibers have some *Al* content coming from its polymeric precursor used as a sintering aid in the manufacturing process.[38] As commented in section 3.3, previous generations of SiC fibers, characterized by their poor stoichiometry, high amounts of *O* and low crystallinity, were not dimensionally stable under neutron irradiation. For instance, high *O* content fibers have an inverse behavior as compared to CVD-SiC as they tend to densify under irradiation whereas CVD-SiC swells.[68,71] Nevertheless, HNS and TSA3 fibers behave as CVD-SiC under neutron- and ion-irradiation, as their density decreases due to irradiation induced swelling,[68,74] though a recent study have shown HNS densification when irradiated to high doses.[77] Though there is a lack of a comprehensive characterization of the impurity effects on the ion-amorphization behavior

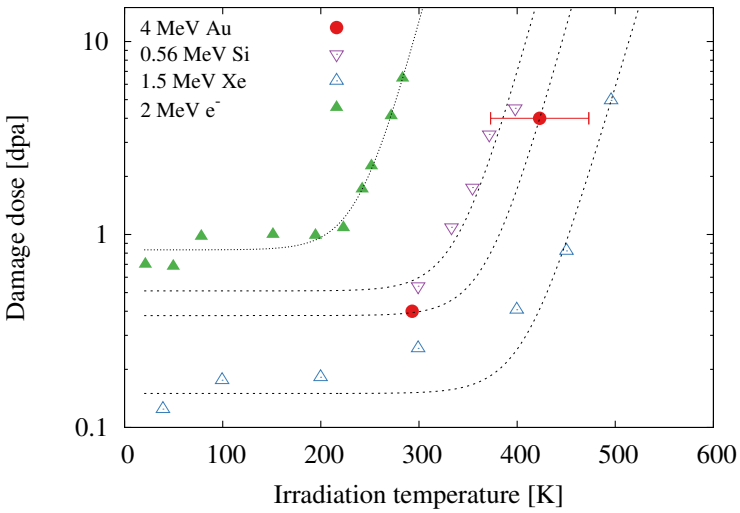

Figure 5.19: Comparison of the amorphization threshold conditions of SiC for different incident particles - Dot lines are exponential fits to data. Error bars correspond to the 100–200 °C range. 4 Mev Au, this work (6H-SiC/HNS/TSA3), other data adapted from Ref.[53]

of third generation SiC fibers, it seems that their C/Si ratio and O or Al contents do not have a significant effect in the amorphization kinetics under the conditions of this work.

Regarding the microstructure influence on the ion-amorphization behavior of the samples, it is widely accepted that GBs act as point defect sinks.[116] However, the grain size must be optimized because a small grain size has two opposing effects on the free energy of an irradiated material. Actually, a smaller grain size hinders intragranular point defects accumulation which, in turn, decreases the free energy resulting from irradiation-induced defects. However, a smaller grain size also may increase the free energy resulting from the increase on the GB density which can favor the path towards an amorphous phase.[117] Indeed, experimental studies reflect this issue as grain refinement results in an enhanced[118–121] or reduced[122,123] irradiation resistance depending on the studied material. Both experimental and simulation studies can be found concerning whether grain refinement in SiC enhances or reduces the RIA resistance. Jiang et al.[124] reported that nc-3C-SiC with a mean crystallite size of 4.6 nm and 6H-SiC single crystals had similar DTA under 2 MeV Au^{2+} ion-irradiation at RT. Later, they reported that nc-3C-SiC, with a crystallite size between 2 and 3.8 nm, had a smaller

DTA as compared to 3C-SiC single crystal when irradiated with 1 MeV Si^+ ions at RT and 127 °C[125] and 2 MeV Au^{2+} ions at 227 °C.[126] Also, Jamison et al.[127] reported DTA values of 1.3 dpa for 45–55 nm and 0.96 dpa for 10 nm 3C-SiC particles under 1 MeV Kr^+ ions at 100 °C. These experimental results point out that a highly refined microstructure has detrimental effects on the SiC irradiation tolerance in agreement with computational results.[128] However, nc-SiC with grains sizes in the range of 30–50 nm did not show significant differences with respect to single crystals under ion-irradiation at RT.[65] Also, even though in many materials GBs strongly interact with the displacement cascades,[129] many studies indicate that there is no direct effect of the GBs on the primary defect production in SiC.[130–132]

As discussed by Jiang et al.,[124] disorder accumulation in a crystalline grain cannot be avoided unless the point defects produced during irradiation are completely recovered before the next displacement event in the crystallite. A rough estimation of the mean diffusion length (l_D), for Si and C interstitials and vacancies at 200 °C can be calculated using the expression $l_D = \sqrt{2Dt}$, being D the diffusion coefficient for the desired point defect, and t the time between two consecutive displacement events. Diffusion coefficients can be calculated as $D = D_0 e^{\frac{-E_m}{kT}}$, where D_0 is the athermal pre-exponential factor, E_m is the migration energy, k is the Boltzmann constant, and T is the temperature in K. Using the energy migration and pre-exponential values given by Gao et al.,[133] diffusion coefficients for C and Si interstitials yield respectively 1.60×10^{-11} cm^2 s^{-1} and 1.64×10^{-19} cm^2 s^{-1}. The average time between two consecutive displacement events in a 20 nm spherical grain submitted to an ion flux of 10^{11} cm^{-2} s^{-1} is 3.18 s. Average mean diffusion lengths at 200 °C are respectively ∼100 nm and ∼0.01 nm for C and Si interstitials, in agreement with Jiang et al. for similar irradiation conditions.[125] Moreover, C and Si vacancies diffusion lengths are expected to be significantly smaller than for the interstitials due to their high migration energies. However, as the mean diffusion length will depend on the total cross-section of annihilation at microstructural sinks and reaction with other defects, such a long-range migration of C interstitial would be impossible due to the low mobility of the other defect types. Therefore, disorder accumulation may eventually lead to a possible amorphization within the grains for both HNS and TSA3. As a consequence, even if it has been shown that the grain size can have a significant influence on the irradiation be-

havior in SiC, in the case of study it is not sufficient to explain the presence of nc-SiC grains in the a-SiC band of the HNS fiber irradiated at 200 °C.

Both HNS and TSA3 fibers present high SF densities in comparison to the 6H-SiC single crystal. Estimated SF linear densities obtained from TEM observations before irradiation yield ∼0.29 nm^{-1} for HNS fibers and ∼0.18 nm^{-1} for TSA3 fibers. As it can be observed in Figure 5.17, the nc-SiC grains embedded in the a-SiC band of the as-irradiated HNS fibers retain a high SF density. Many authors have outlined that SFs may also play a major role in the stability of SiC under irradiation. For instance, Zhang et al.[134] reported that nano-engineered 3C-SiC samples with high SF densities display an enhanced DTA as a 3 dpa value under 2-MeV Si^{+} ions at RT was found. More recently, Jamison et al.[135] have shown that polycrystalline 3C-SiC, with a grain size of 90 nm and high SF density, exhibits a DTA of ∼2.5 dpa under 1.25 MeV electrons at -48 °C as compared to ∼0.5 dpa for the single crystals under 2 MeV electrons at the same irradiation temperature. Ab initio calculations suggest that the critical migration and reaction energies are reduced near the SFs. In turn, the probability of point defect recombination is increased. This phenomenon may hinder the accumulation of point-defects thus enhancing the RIA tolerance of the material.[135] Also, whereas interstitials recombine with vacancies following a 3D random walk in single crystals, SFs restrain the interstitial diffusion process which becomes a 2D-like motion between neighboring SFs. This 2D motion may ease the recombination of the interstitials with nearby vacancies or GBs which will also imply higher tolerance to RIA.[134] Finally, though small temperature variations near the threshold temperature may not have a negligible effect, the high SF density of the nc-SiC grains may explain the presence of these grains in the a-SiC layer of HNS fibers irradiated at 200 °C.

5.5 Conclusions

In order to study the amorphization process in TSA3 and HNS, both SiC fibers and 6H-SiC single crystals have been irradiated with 4 MeV Au^{3+} ions at RT to doses up to 4 dpa. In addition, in order to study the temperatures effects, samples where also irradiated to 4 dpa for temperatures ranging from RT to 300 °C. Irradiation effects were characterized by surface μRs and TEM imaging showing a good agreement between both techniques. All samples irradiated at RT showed complete amorphization for

irradiation doses over 0.4 dpa (2×10^{14} cm^{-2}). However, when irradiated at temperatures over 200 °C the irradiated layer of all samples consists in a partially amorphous band near the surface followed by an amorphous SiC band. In addition, nc-SiC grains with high stacking fault densities where found embedded in the amorphous SiC band of the HNS fiber. Finally, these investigation concludes that the microstructure of both TSA3 and HNS has a negligible effect on the ion-amorphization threshold conditions when as compared to 6H-SiC single crystals.

Finally, it is worthy to comment that amorphization under nominal PWR conditions should not be a concern to operation as SiC cladding temperature is meant to be >300 °C (cf. Figure 1.1) which is higher than the T_c of SiC and SiC fibers. However, during a reactor cold shutdown temperatures can reach value below 100 °C, i.e. below T_c. Under this conditions, amorphization due to neutron irradiation is not likely to happen. Indeed, since the fission chain reaction is stopped neutron population is highly decreased. Therefore, despite irradiation from fission fragment decay may also contribute, the received doses may fall below the amorphization dose. However, in-pile irradiation during such conditions would be necessary to determine whether SiC is suitable or not for such applications.

6

Characterization of the effects of thermal annealing on ion-amorphized 6H-SiC and third generation SiC fibers

In this work, the study of the annealing-induced cracking and recrystallization of ion-amorphized SiC fibers and single crystals are studied following an *in situ* approach. First, *in situ* E-SEM observations reveal that annealing-induced cracking is not exclusive for ion-amorphized single crystals as it has been also observed for as-irradiated HNS fibers. In addition, *in situ* observations allow discarding thermal shock and thermal expansion mismatch as the mechanical failure stress source. It is reported that cracking of the irradiated layer is a thermally driven mechanism with a characteristic activation energy of 1.05 eV. Cracking temperatures range from 850 °C to 1000 °C and cracking kinetics have been described in terms of a Johnson-Mehl-Avrami-Kolmogorov model with an exponent (n) ranging from 1.5 to 2.1. Secondly, *in situ* TEM observations of the annealing process reveal recrystallization temperatures of 870 °C, 900 °C and 930 °C for 6H-SiC, HNS and TSA3 fibers, respectively. Swelling recovery prior to recrystallization is reported for all three samples. Recrystallization of 6H-SiC starts by the epitaxial growth of the amorphous to crystalline interphase and is followed by the columnar grain growth of the irradiated layer resulting in a mixture of 6H and 3C polytypes. Concerning the SiC fibers, HNS recrystallization is via direct columnar growth arising from the a-c interphase; whereas for the TSA3 it results to be an spontaneaous phenomenon. No signs of different polytype coexistence has been observed in the recrystallized layers of the two SiC fibers.

6. CHARACTERIZATION OF THE EFFECTS OF THERMAL ANNEALING ON ION-AMORPHIZED 6H-SIC AND THIRD GENERATION SIC FIBERS

6.1 Introduction

As it has been shown in chapter 5, TSA3 and HNS do not exhibit significant differences in their ion-amorphization threshold conditions with respect to 6H-SiC single crystals. Though ion-amorphized SiC is highly stable due to the low mobility of point defects,[124] several studies have reported partial or complete recovery of the crystalline structure of the irradiated layer by means of thermal annealing.[13,14,50,51,61–65] In addition to recrystallization of the amorphous layer, thermal annealing has been reported to induce mechanical failure of the recrystallized layer in single crystals with amorphous layers of thicknesses over $\sim$1 μm.[13,14] Recrystallization induced stresses have been pointed out as a possible mechanism for the mechanical failure.[13] However, the experimental settings of the cited works do not allow discarding stresses arising from thermal shock and thermal expansion mismatch as a significant stress source for cracking and delamination.

In this work, the study of these two phenomena is carried out following an *in situ* approach. With this purpose, thermal annealing of ion-amorphized 6H-SiC and HNS and TSA3 fibers has been conducted and observed using E-SEM and TEM, both equipped with heating sample holders. *In situ* E-SEM and TEM thermal annealing of these samples allows avoiding thermal shock stresses while giving valuable insights about how cracking and recrystallization phenomena relate to each other.

6.2 Experimental conditions

6.2.1 Materials

Single crystals of 6H-SiC as well as HNS and TSA3 fibers have been ion-irradiated to 4 dpa (2×10^{15} cm^{-2}) at RT with 4 MeV Au^{4+} ions as described in section 5.2. As shown in Figures 5.14, 5.15, 5.16, this irradiation conditions lead to the formation of a homogeneous amorphous SiC layer of >1 μm in 6H-SiC and HNS samples. In the TSA3, the amorphous layer presents small inclusions attributed to irradiated intergranular free C.

6.2.2 *In situ* E-SEM

Cracking phenomenon has been investigated *in situ* in single HNS fibers and 6H-SiC single crystals using the E-SEM described in section 4.4.3. Despite the efforts, only one fiber has been successfully annealed. The ion-amorphized HNS fiber was heated from RT to 765 °C at 30 °C min^{-1} and to 970 °C at 10 °C min^{-1} to then keep the fiber at constant temperature. The small diameter of these fibers make proper handling of them difficult for its visualization with the E-SEM. In addition, for the annealed fiber, the non-regular contact between the sample and the heating sample holder introduces some error in the real temperature of the fiber with respect to the consign temperature.

In the light of these technical issues, the systematic study of the cracking phenomena has been conducted using ion-amorphized 6H-SiC single crystals. Several samples were annealed under different conditions as follows. First, two samples were annealed at constant temperature. For the first experiment, 6H-SiC sample was heated from RT to 785 °C at 30 °C min^{-1}, to 840 °C at 20 °C min^{-1} and finally to 855 °C at 10 °C min^{-1}. For the second experiment, 6H-SiC sample was heated from RT to 840 °C at 30 °C min^{-1}, to 905 °C at 20 °C min^{-1} and finally to 930 °C at 1 °C min^{-1}. Secondly, five experiments were conducted at constant linear heating rates of 1, 5, 10, 20 and 30 °C min^{-1}. All samples were heated from RT to 600–700 °C at 30 °C min^{-1} to then decrease the heat rate to the consign value. Cracking process was observed in a fixed area of the sample at constant magnification in all cases. Quantitative data on cracking kinetics has been obtained from image analysis using ImageJ software.[96]

6.2.3 *In situ* TEM

Recrystallization phenomenon has been investigated *in situ* in 6H-SiC as well as in HNS and TSA3 fibers. TEM annealings and observations have been conducted with the microscopes described in section 4.4.2. Thin foils for TEM annealing were extracted from the ion-amorphized samples using the FIB method described in section 4.4.2.1. The recrystallization process was recorded in real time and quantitative data have been obtained from images extracted from the recorded video using ImageJ software.[96]

Thermal treatments[1] were conducted as follows. The 6H-SiC was heated at high heating rate to 700 °C, then to 850 °C at 12 °C min^{-1} and finally at 4 °C to 870 °C. The

[1] The differences between the treatments are due to the manual control of the heating sample holder.

TSA3 fiber was heated at high heating rate to 550 °C, then to 810 °C at 16 °C min^{-1} and finally to 930 °C at 2 °C min^{-1}. Finally, the HNS fiber, after an initial heating to 810 °C, was heated to 900 °C at 15 °C min^{-1}. After a small excursion to 930 °C the temperature was stabilized at 920 °C.

6.3 Results

6.3.1 Thermal annealing induced cracking

Figure 6.1 shows the evolution of the irradiated HNS fiber during the thermal annealing. As it can be observed, (a) when temperature reaches ∼1090 °C annealing induces surface cracking of the fiber. As temperature increases, (b) crack grows with temperature reaching all the irradiated length of the fiber. Once the maximum temperature is achieved (c), 1113 °C, cracks perpendicularly to the fiber axis appear until (d) the eventual complete delamination of the irradiated layer in a crescent-shaped form.

As it can be observed, the crescent-shaped exfoliated layer is in good agreement with the theoretical cross-sectional damage distribution estimated with the aid of SRIM-2013 (cf. Appendice B).

Figure 6.2 shows an example of the surface evolution of the irradiated 6H-SiC during the *in situ* thermal annealing at constant heating rate (1 °C min^{-1}). Similar behavior was observed for all the annealed samples independently on the thermal treatment. As temperature increases with time, (a) cracks appear on the surface of the irradiated layer following the [1 1 $\bar{2}$ 0] direction of the crystalline substrate in agreement with literature experiments.[13,14] Subsequently, crack density increases with time and temperature (b,c) creating a patterned structure formed by annealed flakes delimited by the crossing cracks. Finally, (d) once crack density reaches a saturation value, these flakes start to bend from the free edges causing the delamination of the annealed layer.

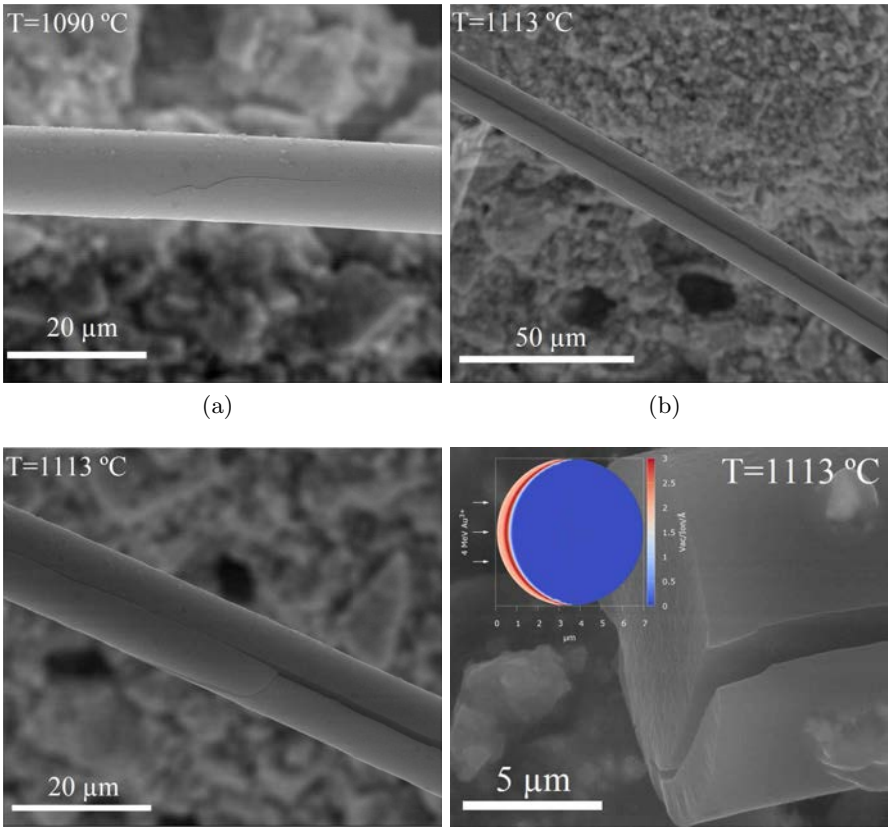

Figure 6.1: E-SEM images of the evolution of the thermal annealing induced cracks in a HNS fiber amorphized with 4 MeV Au^{4+} - (a) at 1090 °C surface cracking is observed, (b) crack grows with the increasing temperature. (c) Once temperature reaches 1113 °C, cracks perpendicular to the fiber axis appear until (d) the delamination of the irradiated layer. Inset in (d) corresponds to the cross-sectional damage profile of a fiber irradiated with 4 MeV *Au* ions.

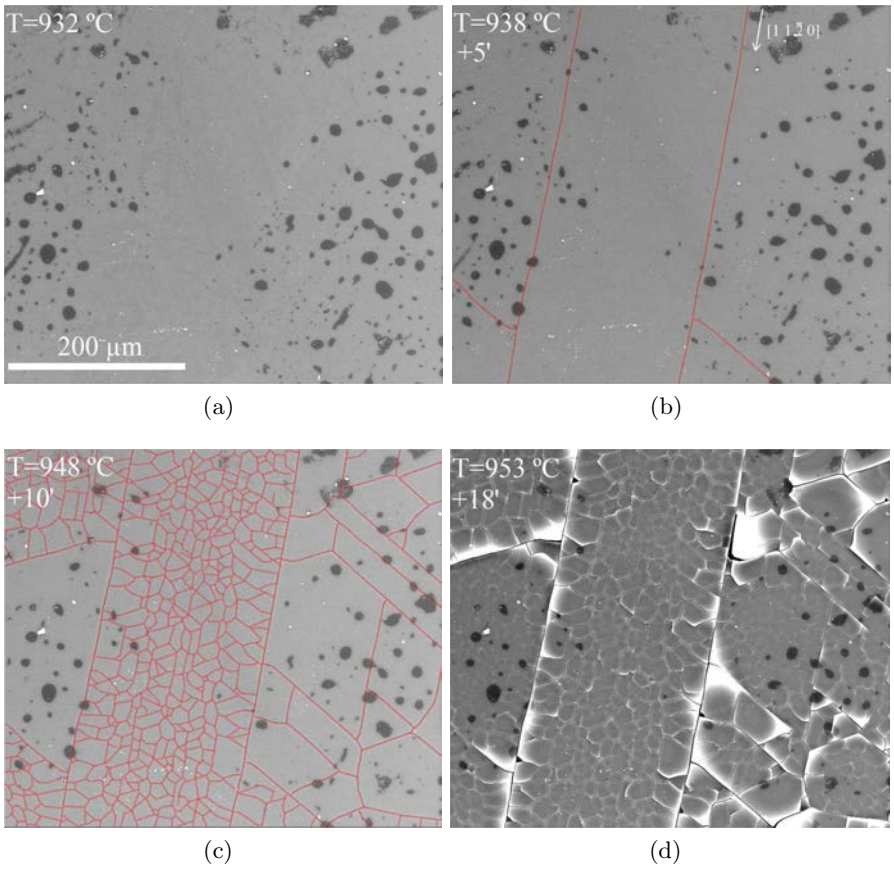

Figure 6.2: E-SEM images of the evolution of the thermal annealing induced cracks in a 6H-SiC single crystal amorphized with 4 MeV Au^{4+} - Scale bar is the same for all images. (a) Cracks appear and grow following the [1 1 $\bar{2}$ 0] direction at 932 °C and (b,c) crack density increases with time and temperature.(d) Once crack density saturation is achieved delamination of the resultant flakes starts.

Figure 6.3 shows the evolution of the crack density as a function of the annealing conditions. Experimental data have been modeled using the Johnson-Mehl-Avrami-Kolmogorov[136–140] (JMAK) equation. The usual expression is given by equation 6.1, where ρ_{fis} is the crack density as a function of time (t) and temperature (T), A is a normalizing factor and $K(T)$ and n are the JMAK constant and exponent respectively.

$$\rho_{fis}(t,T) = A(1 - e^{-(K(T)t)^n}) \tag{6.1}$$

$$ln(-ln(1 - \frac{\rho_{fis}(t,T)}{A})) = ln(K(T)) + nln(t) \tag{6.2}$$

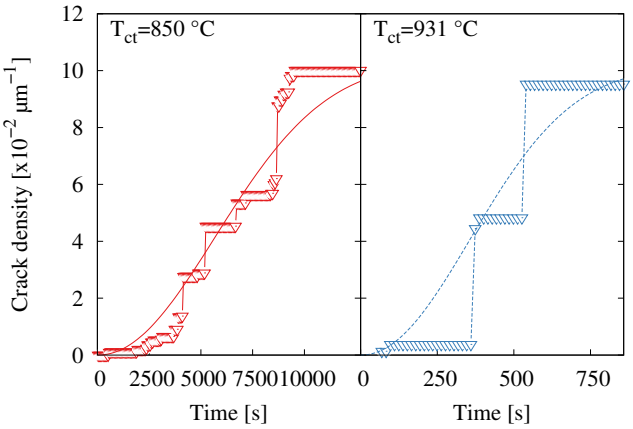

Figure 6.3: Time dependent evolution of the surface crack density of ion-amorphized 6H-SiC during the isothermal annealing tests - Data modeling has been done using the JMAK model (Eq. 6.1)

Figure 6.4 shows the determination of the JMAK exponent $n \sim 2$. Data have been fitted using the transformed JMAK equation (Eq. 6.2).

As isothermal experiments turned out to be highly time-consuming, non-isothermal controlled annealing experiments have been performed with linear heating rates.

Figure 6.5 shows the crack density evolution obtained from these tests as a function of time and the heating rate. As it can be observed, the temperature at which the first crack appears increases with increasing heating rates. In addition, the time elapsed since the appearance of the first crack to saturation decreases with increasing heating rates.

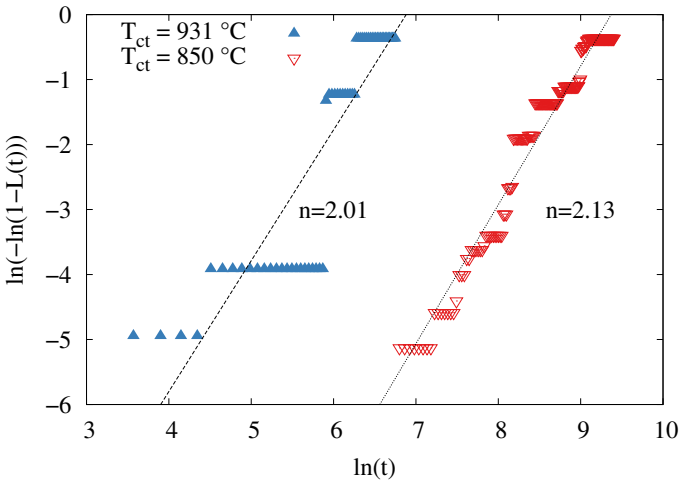

Figure 6.4: Logarithmic plot of the crack density evolution using the transformed JMAK equation (Eq. 6.2) - The slope of the linear fit yields the JMAK exponent n.

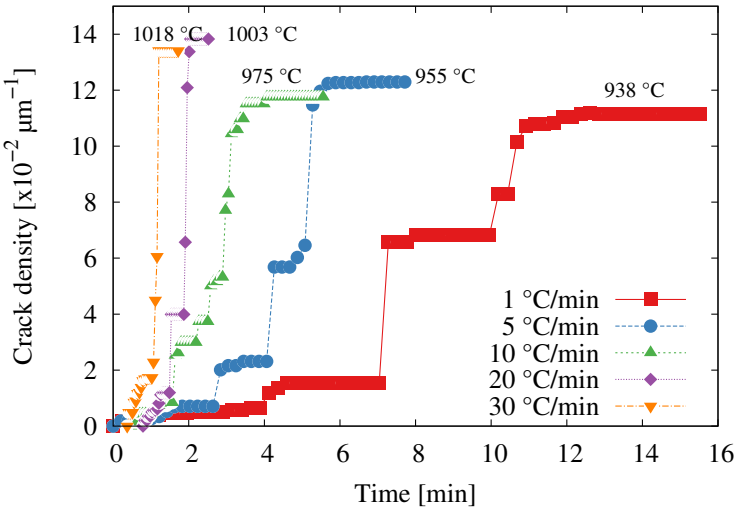

Figure 6.5: Time dependent evolution of the surface crack density and first crack appearance temperature of ion-amorphized 6H-SiC during the non-isothermal annealing tests - The higher the heating rate the higher the first crack temperature and the shorter the time to crack saturation.

Figure 6.6 shows the crack density evolution as a function of the test effective temperature. This temperature is defined as the difference between the current sample temperature and the temperature at which the first crack appeared. As it can be observed, apart from the test at 1 °C min^{-1}, the crack density curves overlap for the different annealing conditions.

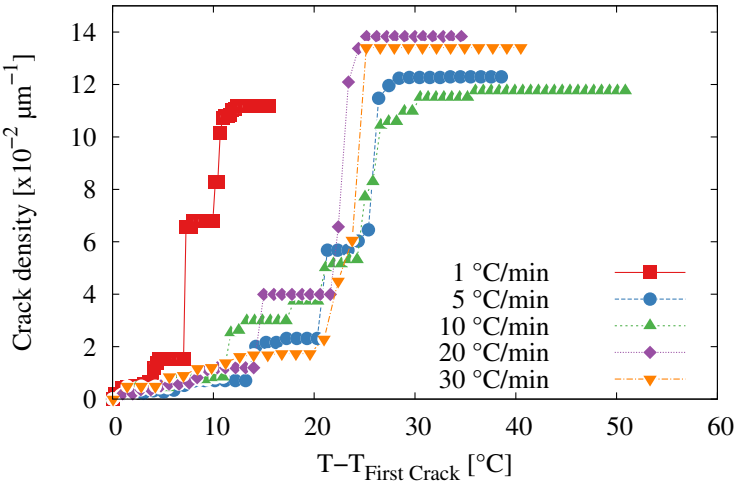

Figure 6.6: Temperature dependent evolution of the surface crack density of ion-amorphized 6H-SiC during the non-isothermal annealing tests - Once cracking starts, the crack density evolution as a function of the temperature is independent of the heating rate.

Table 6.1 gathers the saturation values for the crack density and the flake size. Obviously, there is an inverse proportionality between these two values; the higher the crack density the smaller the mean flake size. However, there is no correlation between the annealing conditions and the saturation values. Final state of the samples is rather constant showing a mean crack saturation value of 12.5±1.1×10^{-2} μm^{-1} and a mean final flake size of 153±29 μm^2.

Figure 6.7 shows the determination of the JMAK parameters for the non-isothermal annealing tests using equation 6.2. The JMAK exponents yield from ∼1.5 to ∼2 without direct correlation with the heating rate conditions.

As stated above, cracking is a thermally driven process for which heating rate has two major effects on its kinetics. First, to delay the temperature at which the first crack appears and, secondly, to decrease the time to reach crack saturation. In order

Table 6.1: Saturation values of crack density and flake size as a function of the heating rate.

Heating rate [°C min^{-1}]	Crack density [$\times 10^{-2}$ μm^{-1}]	Final flake size [μm^2]
1	11.2	192
5	12.3	153
10	11.8	171
20	13.8	119
30	13.4	132
Mean	12.5±1.1	153±29

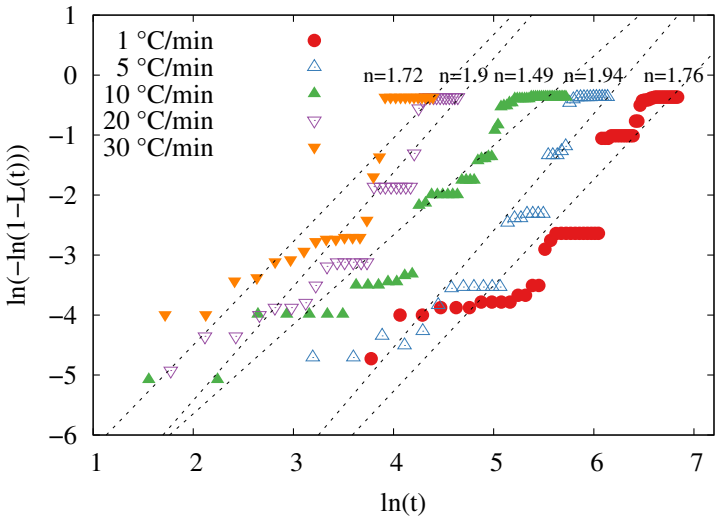

Figure 6.7: Logarithmic plot of the crack density evolution under non-isothermal conditions using the transformed JMAK equation (Eq. 6.2) - The slope of the linear fit yields the JMAK exponent n.

to determine the cracking activation energy E_a^{crack} that characterizes this process, two relevant quantities of the cracking kinetics have been supposed to follow an Arrhenius relation. Eq. 6.3 relates, under an Arrhenius form, the inverse of the time to reach the 50% of the cracking saturation value, $t_{50\%}$, and the temperature at that precise time, $T_{50\%}$. k_B is the Boltzmann constant.

$$ln(\frac{1}{t_{50\%}}) = C - (\frac{E_a^{crack}}{k_B})\frac{1}{T_{50\%}} \tag{6.3}$$

Experimental data has been plotted and fitted using Eq. 6.3 in 6.8 yielding a E_a^{crack} of 1.05±0.09 eV.

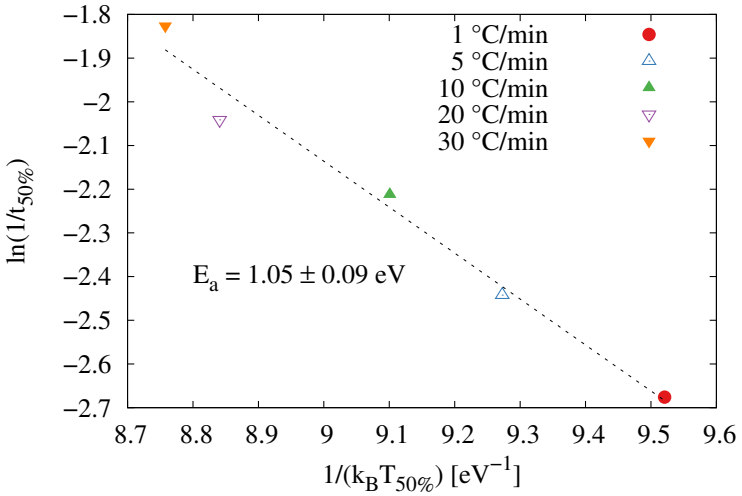

Figure 6.8: Arrhenius plot of the time to reach the 50% and sample temperature as a function of the heating rate - The slope of the linear fit yields the activation energy of the cracking process.

Figure 6.9 shows a cross-sectional TEM image of the final microstructure of one of the flakes of the sample annealed at a heating rate of 10 °C min^{-1}. It is found that the irradiated layer has been completely recrystallized. This layer is ∼1.05 μm thick and shows a polycrystalline microstructure. Though grain boundaries are diffuse, recrystallization appears to be columnar with preferential growing directions forming $\sim \pm 70°$ with the amorphous-crystalline (a-c) interphase. SAED pattern of this layer shows elongated and doubled spots due to the polycrystalline and faulted nature of

the recrystallized layer. Also, the SAED can be interpreted as a superposition of two different patterns, one corresponding to the pattern found for the 6H-SiC single crystal substrate and a central hexagonal pattern. This pattern superposition suggest the coexistence of different polytypes.

Cracks appear at the surface, grow along to the c axis and penetrate in the substrate. Once in the substrate, cracks eventually deviate and grow perpendicular to the c axis at ∼1.9 μm, where a high concentration of planar defects is found. The zones with high concentrations of planar defects can be noticed periodically distributed each ∼0.8 μm from the interphase and fade progressively with depth. SAED pattern of the highest faulted zone show a similar hexagonal pattern with the recrystallized layer but with sharper spots. Interplanar distances indicated in Figure 6.9 yield $d_{(hkl)_1}$=$d_{(hkl)_2}$=2.52 Å. These distances have been determined as the inverse of the distance in the reciprocal space between the highest intensity point of each spot with the central one.

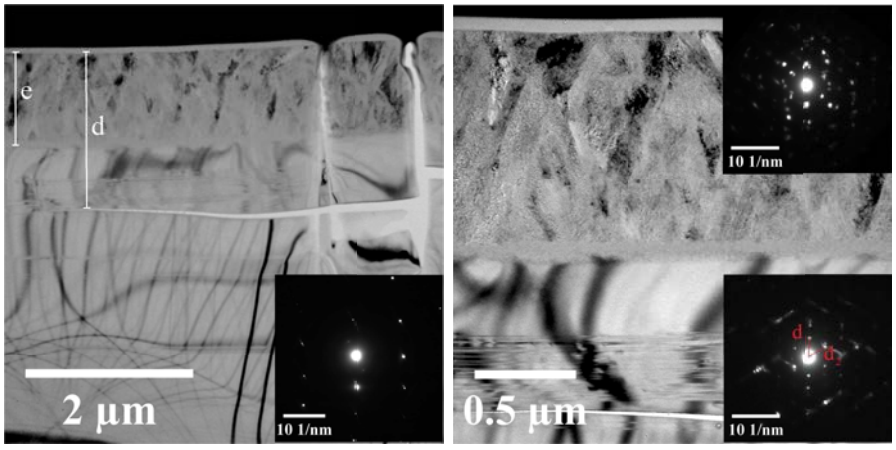

(a) (b)

Figure 6.9: Cross-sectional TEM image of the microstructure of the irradiated 6H-SiC sample after the annealing test at 10 °C min^{-1} - (a) General view showing cracks parallel and perpendicular to the surface and SAED of the crystalline substrate. e=1.05μm is the thickness of the irradiated layer and d=1.9μm is the delamination depth. (b) Detail of the recrystallized microstructure of the irradiated layer and SAED of the recrystallized layer and the faulted zone. Note that at d, where crack propagates parallel to the surface, the substrate presents the highest concentration of planar defects.

6.3.2 Thermal annealing induced recrystallization

In situ TEM annealing tests have been conducted on cross-sectional thin foils extracted from ion-amorphized 6H-SiC, TSA3 and HNS (Figures 5.14, 5.15 and 5.16).

6.3.2.1 Ion-amorphized 6H-SiC single crystal

Figure 6.10 shows the evolution of the thin foil during the thermal annealing described in section 6.2.3. As it can be seen, recrystallization of the amorphous layer is a two step process. During the first part of the annealing, the a-c interphase grows up to certain thickness. Once this thickness is reached, recrystallization of the amorphous layer starts from both the a-c interphase and the top surface via columnar grain growth. As can be observed, full recrystallization of the amorphous layer was not achieved due to the surface contamination of the sample during the test, probably due to the degradation of the *Pt* layer deposited on the surface.

A detail of the final microstructure of the recrystallized thin foil is shown in Figure 6.11. As it can be observed, the a-c interphase critical thickness yields ∼110 nm and grains grow forming ∼70°–120° with respect to it. Regarding the SAED, both patterns obtained from the recrystallized layer and the a-c interphase show new spots forming a hexagonal pattern not present in the non-irradiated substrate. Also, the substrate SAED pattern is characteristic of the hexagonal structure with a zone axis perpendicular to the c axis. Interplanar distances yield $d^{a}_{(hkl)_1}$=2.50 Å, $d^{b}_{(hkl)_1}$=2.51 Å, $d^{b}_{(hkl)_2}$=2.54 Å and $d^{c}_{(hkl)_1}$=2.52 Å. Finally, it is worth mentioning that the resultant microstructure of the recrystallized layers observed after both *in situ* E-SEM and TEM annealing experiments are in good agreement meaning that *in situ* experiments can reproduce the recrystallization process in bulk materials in agreement with similar experiments.[63]

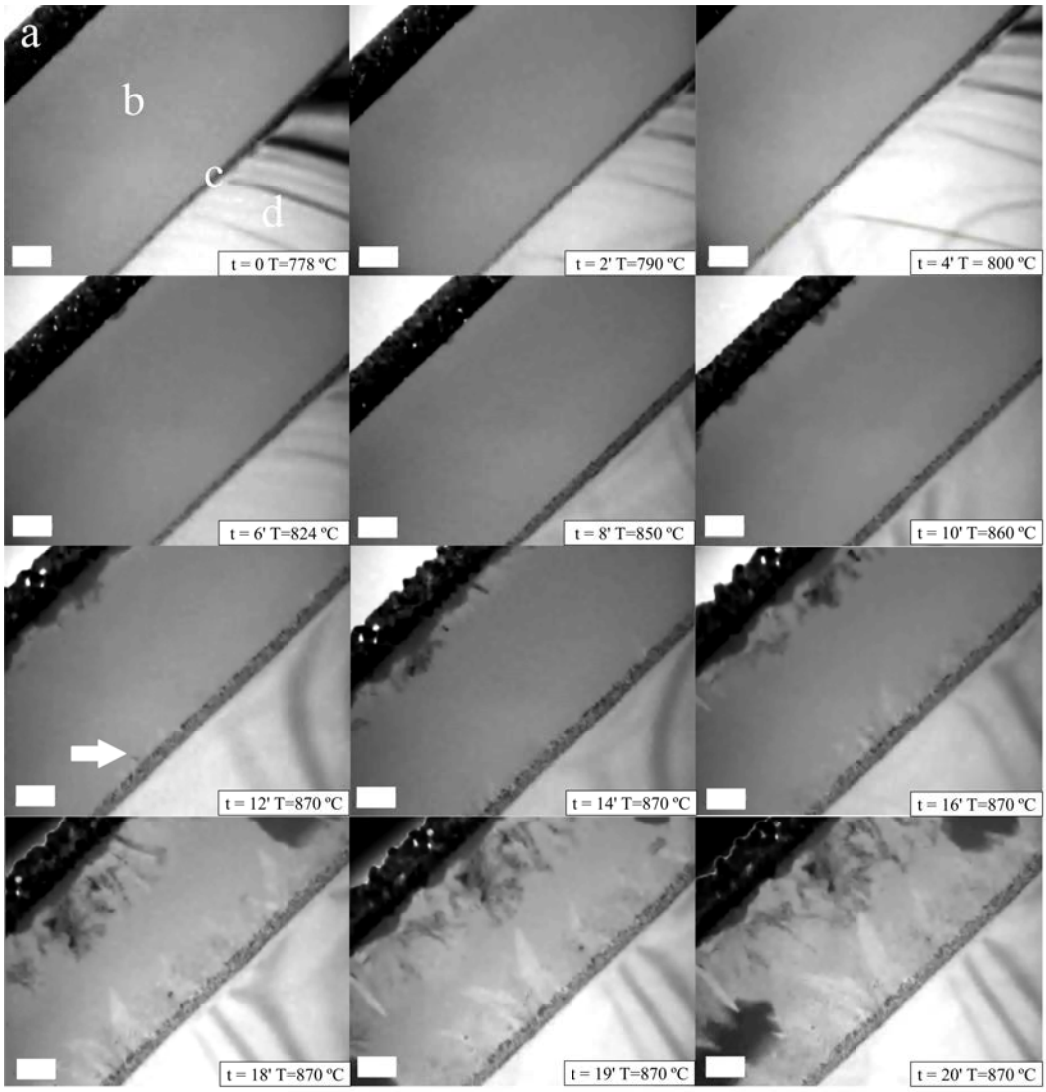

Figure 6.10: ***In situ*** **TEM observation of the recrystallization of an ion-amorphized 6H-SiC single crystal** - Scale bars are 2μm, (a) is the Pt deposit, (b) the irradiated SiC layer, (c) the amorphous-crystalline interphase and (d) the non-irradiated substrate. Recrystallization of the amorphous layer starts by the growth of the a-c interphase. Once it arrives to saturation, indicated by the arrow, it can be seen emergence of columnar grains at 70°.

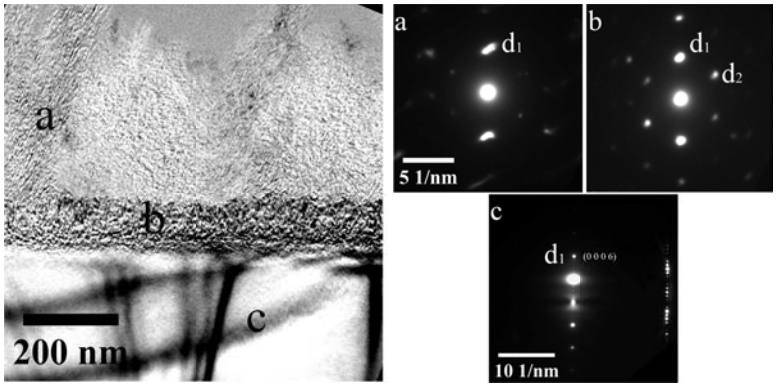

Figure 6.11: Detail of the final microstructure of the irradiated layer of 6H-SiC after the *in situ* annealing - The final microstructure and the SAED patterns are similar to those obtained for the E-SEM annealing of the bulk 6H-SiC. Interplanar distances are indicated in the text.

Real-time observation of the recrystallization process allows to determine its kinetics from image analysis. Figure 6.12 shows (a) the variation of thickness of the irradiated layer, (b) the a-c interphase growth and (c) the grain size as a function of time. Note that for convenience, the time counter has been set to zero when the recording started. As expected, the data reflects the observed recrystallization behavior. For instance, it has been possible to observe a progressive densification of the irradiated layer not previously noticed during the test and the growth of the a-c interphase prior to grain growth.

As it has been previously shown in Figure 5.14, at RT the initial thickness of the amorphous layer is 1.3 μm and there is no noticeable a-c interphase. However, the measured thickness of the irradiated layer at t=0 (T=778 °C) yields 1.09 μm and decreases at rate of 1.4 nm min^{-1}. In turn, there is a noticeable a-c interphase that grows from a initial thickness of 70 nm at a rate of 2.5 nm min^{-1}. Finally, once the a-c interphase growth saturates around 110 nm, columnar grain growth starts at a rate of 56 nm min^{-1} and densification rate increases to 4.2 nm min^{-1}.

6.3.2.2 Ion-amorphized HNS fiber

Figure 6.13 shows the recrystallization process of the ion-amorphized layer of the HNS fiber. At variance with the single crystal, there is no noticeable evolution of the a-c interphase. In addition, columnar grains emerging from the pristine nanocrystalline

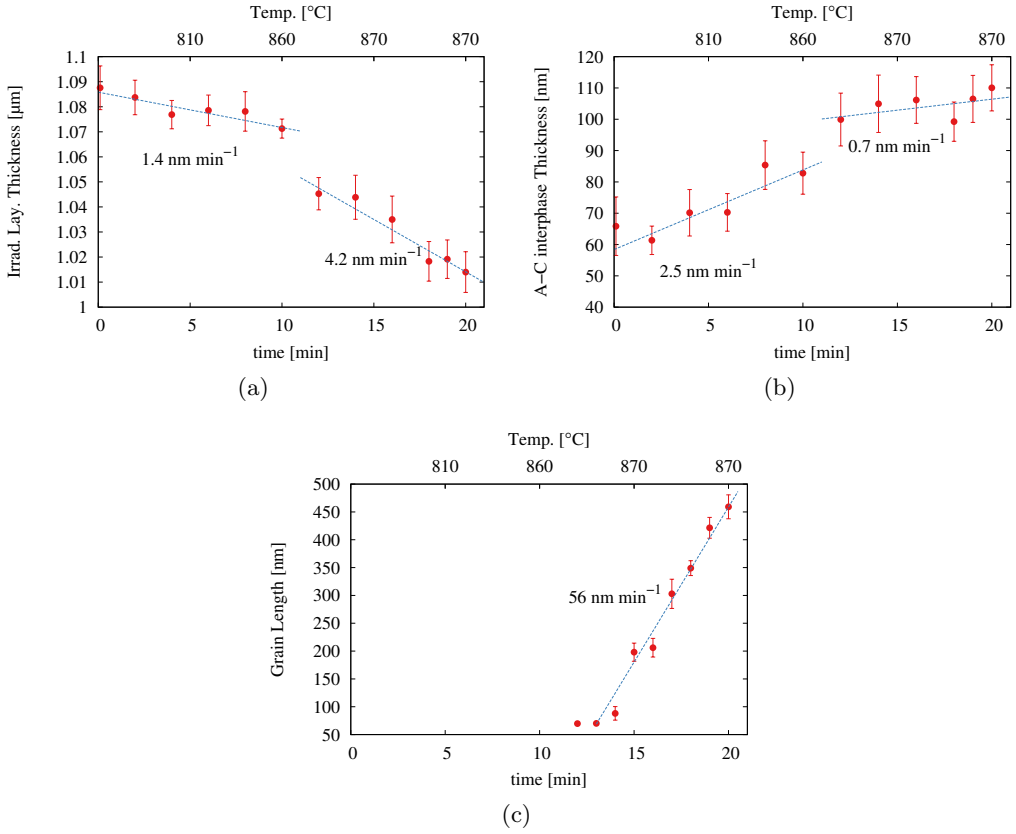

Figure 6.12: Kinetics of the thermal annealing induced recrystallization of ion-amorphized 6H-SiC - (a) Densification of the irradiated layer, (b) interphase growth and (c) grain length as a function of time.

substrate are perpendicular to the a-c interphase whereas grains arising from the surface show a certain inclination (∼60°). In this case, surface contamination during the test was not observed and the irradiated layer was successfully fully recrystallized.

The final microstructure as well as the respective SAED patterns are shown in Figure 6.14. The recrystallized layer is characterized by a polycrystalline microstructure formed by columnar grains with diffuse boundaries with grain sizes substantially larger than the substrate ones. In addition, there is no noticeable intergranular free C. Upper SAED pattern corresponds to the recrystallized layer. As it can be observed, the hexagonal pattern is similar to the reported for the recrysallized layer of the 6H-SiC. As before, the presence of doubled and elongated spots is due to the polycrystalline nature of the recrystallized layer. Interplanar distances yield $d_{(hkl)_1}$= 2.54 Å and $d_{(hkl)_2}$=2.57

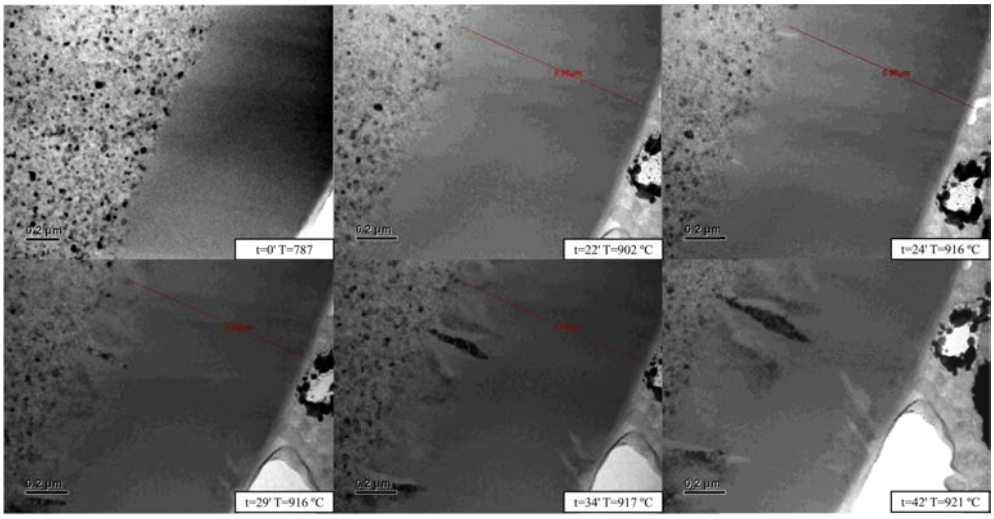

Figure 6.13: ***In situ*** **TEM observation of the recrystallization of an ion-amorphized HNS fiber** - Recovery of the amorphous layer starts by the densification of the amorphous layer followed by the emergence of columnar grains perpendicular to the substrate.

Å forming an angle of ∼55°. Lower SAED shows numerous bright spots disposed in concentric rings as a consequence of the nanophased microstructure. Radii of these rings yield $r_{(hkl)_1}$=2.55 Å, $r_{(hkl)_2}$=1.55 Å and $r_{(hkl)_3}$=1.33 Å and can be attributed to (1 1 1), (2 2 0) and (3 1 1) planes of 3C-SiC (cf. Appendice A)

Recrystallization kinetics of the HNS fiber are shown in Figure 6.15. As in the previous case, annealing of the irradiated layer can be considered as a two step process. The irradiated layer densifies at a rate of 6.5 nm min^{-1} during the first annealing stage previous to the recrystallization. Once the thickness of the irradiated layer has already reached the saturation value, columnar recrystallization starts at a constant rate of 21.2 nm min^{-1}.

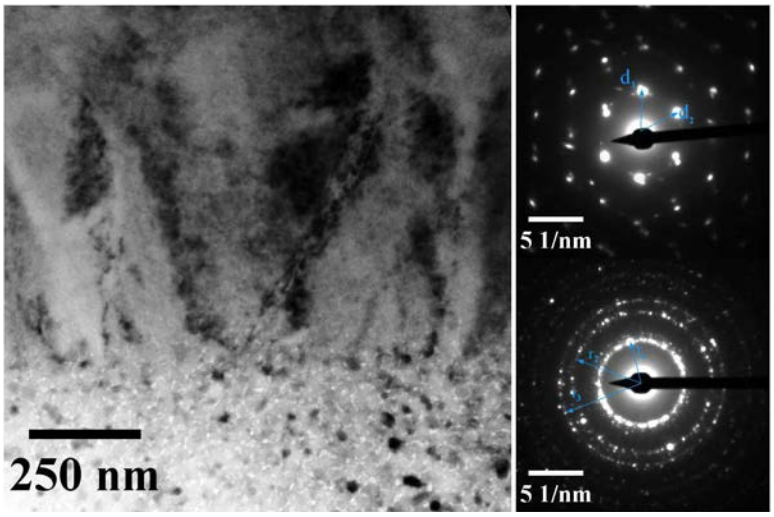

Figure 6.14: Detail of the final microstructure of the irradiated HNS fiber after the *in situ* annealing - The final microstructure and the SAED patterns substantially differ from the nanophased substrate. Also, there are no signs of intergranular free C in the recrystallized layer.

6.3.2.3 Ion-amorphized TSA3 fiber

Finally, Figure 6.16 shows the recrystallization process of the ion-amoprhized TSA3 SiC fiber. At variance with the previous cases, recrystallization of the amorphous layer appears to be a heterogeneous and a rather spontaneous phenomenon with no preferential growth direction. Also, no surface contamination was observed and recrysallization was fully achieved. As previously, a detail of the final microstructure of the recrystallized layer is presented in Figure 6.17 where grains are barely distinguishable. Also, it is remarkable the constant presence in the irradiated layer of what has been attributed to carbonaceous phases in section 5.4 during the annealing test. Upper SAED shows the already familiar hexagonal pattern with interplanar distances $d_{(hkl)_1}$= 2.55 Å and $d_{(hkl)_2}$=2.61 Å forming an angle of ∼56°. Lower SAED shows the pattern related to the non-irradiated microstructure. As before, though not as clear as for the HNS, concentric rings formed by different spots can be identified in the latter. Radii of these rings yield $r_{(hkl)_1}$=2.55 Å, $r_{(hkl)_2}$=1.53 Å and $r_{(hkl)_3}$=1.33 Å. This values are in agreement with those found for the HNS microstructure and are also characteristic of the 3C-SiC polytype. Also, it is noticeable the presence of a diffuse ring near the transmitted beam spot with radius r_c= 3.56 Å attributed to the intergranular free C.[141]

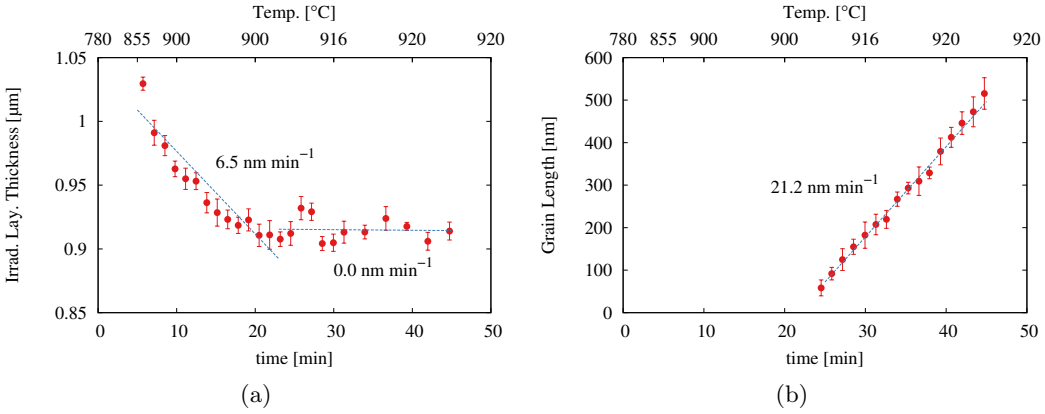

Figure 6.15: Kinetics of the thermal annealing induced recrystallization of ion-amorphized HNS fiber - (a) Densification of the irradiated layer and (b) grain length as a function of time.

Due to the spontaneous recrystallization only the kinetics of the densification of the irradiated layer can be measured. As it can be noticed in Figure 6.18, densification of the irradiated layer starts for temperatures as low as 250 °C. At the beginning, the irradiated layer densifies at rate of 6.8 nm min^{-1} to then almost saturate at 580 °C until reaching 860 °C. Once at this temperature, densification restarts at a rate of 4.2 nm min^{-1} until the spontaneous recrystallization.

6.4 Discussion

To the knowledge of the author, Höfgen et al.,[13] were the first to notice that thermal annealing of ion-amorphized 6H-SiC single crystals with 2 MeV Si^+ caused surface cracking and ultimate delamination of the samples. Surface cracking was observed for annealing temperatures over 800 °C and for samples with an irradiated layer of 1.75 μm. In addition, they reported that crack density increased with increasing annealing temperatures. For the higher annealing temperature, 1000 °C, delamination of the irradiated layer was reported with a ratio between the thickness of the irradiated layer, e_{irr}, and the thickness of the delaminated one, e_{exf}, of $\frac{e_{exf}}{e_{irr}} \sim 2.3$. Also, mechanical failure was attributed to tensile stresses arising from the crystallization of the amorphous layer. Since then, though intensive research has been carried on annealing induced recrystallization of ion-amorphized SiC, only two recent papers by Miro et al.[14,100] have

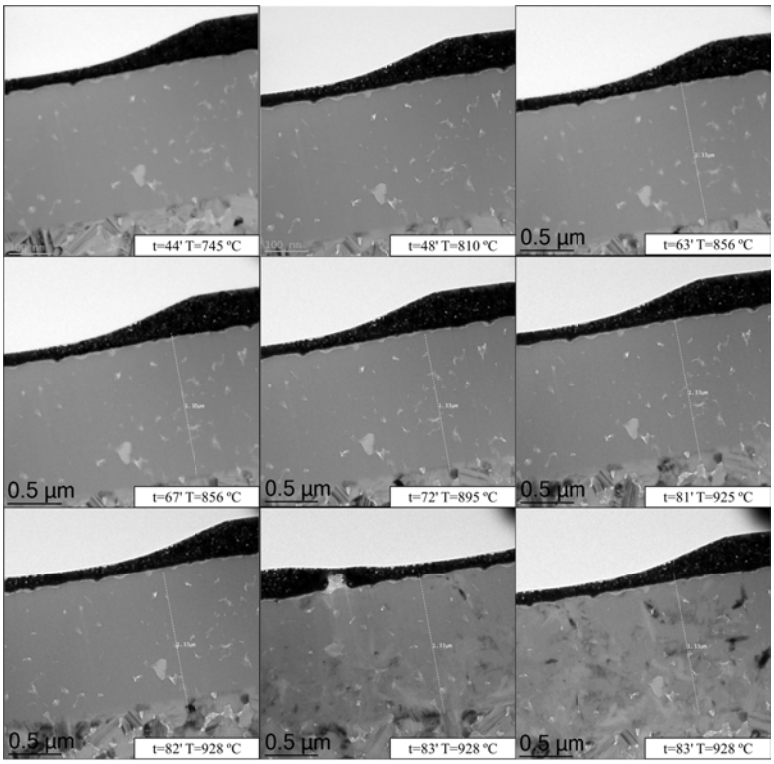

Figure 6.16: *In situ* TEM observation of the recrystallization of an ion-amorphized TSA3 fiber - Recovery of the amorphous layer starts by the densification of the amorphous layer followed by its spontaneous recrystallization.

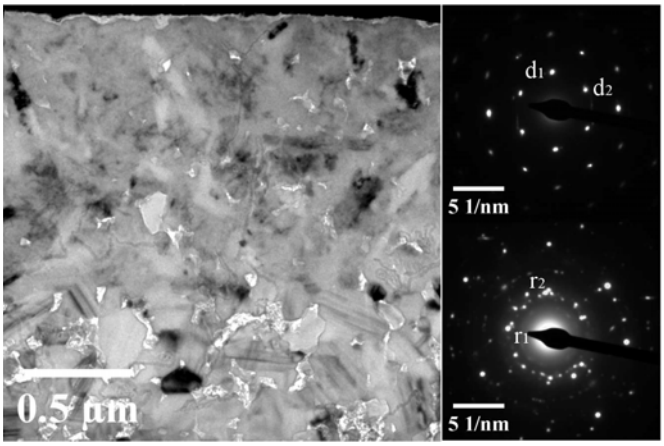

Figure 6.17: Detail of the final microstructure of the irradiated TSA3 fiber after the *in situ* annealing - The final microstructure and the SAED patterns substantially differ from the substrate. It is noticeable the presence of free C in the recrystallized layer.

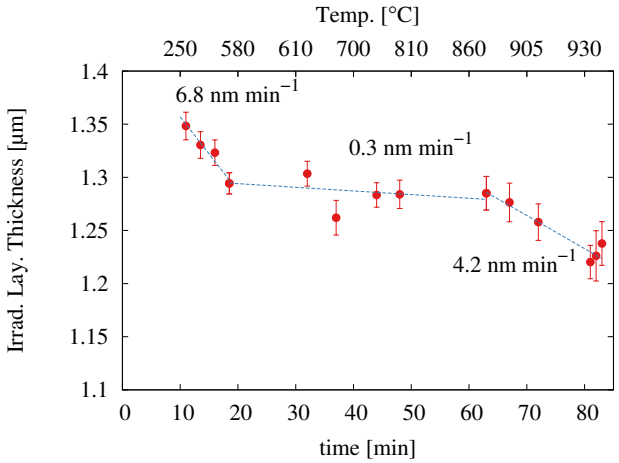

Figure 6.18: Kinetics of the thermal annealing induced densification of the ion-amorphized layer of TSA3 fiber - Strain recovery starts for temperatures as low as 250 °C and saturates once the layer spontaneously recrystallizes.

reported annealing induced mechanical failure of ion-amorphized samples. In their work, samples were amorphized using 4 MeV Au^{3+} and subsequently annealed. Under their experimental conditions, cracking was noticed for annealing temperatures over 1000 °C and delamination over 1500 °C. Crack density was reported to increase with increasing annealing temperatures and doses whereas the $\frac{e_{exf} \sim 2}{e_{irr} \sim 0.8} \sim 2.5$ remained constant for all irradiation and annealing conditions.

Major findings from the systematic *in situ* E-SEM observations presented in section 6.2.3 can be summarized as follows. First, annealing induced mechanical failure is not exclusive for single crystalline SiC as it has been also observed for HNS fibers, which have a nanophased microstructure. Secondly, surface cracking is a thermally driven dynamic phenomenon which kinetics depend on the annealing conditions. Thirdly, the final state of the annealed samples, i.e. crack density saturation and size of the annealed flakes, is rather constant and does not depend on the annealing temperature nor the heating rate. Finally, ultimate delamination has been observed even for the lowest annealing temperatures, i.e. 850 °C. These findings allow discarding the remarks stated by Höfgen et al. and Miro et al. about the dependence of crack density and delamination with the annealing temperature. In addition, the shift between the reported cracking and delamination temperatures shift between these papers can be easily explained by their different experimental configurations. Indeed, whereas Miro et al. conducted

isochronal thermal annealing of the samples at constant temperatures,[14] Höfgen et al. annealing tests were conducted following cyclic processes of heating to a certain temperature and cooling down to RT until the recrystallization of the sample.[13] As it can be observed in Figure 6.3, crack density evolution at constant temperature depends on the annealing time. Therefore, it is highly possible that Miro' s annealing time was not sufficient to trigger cracking during isochronal annealing tests at temperatures below 1000 °C.

As stated above, it has been discussed that cracking kinetics depend on the annealing conditions. Ion-amorphized 6H-SiC shows similar behavior for the two types of annaling tests, isothermal and non-isothermal with linear heating rates. For instance, the higher the temperature or the heating rate the shorter the time needed to trigger cracking and also to reach crack density saturation values. In addition, for the non-isothermal tests, the temperature at which cracking is triggered increases with increasing heating rates (cf. Figure 6.5). However, as shown in Figure 6.6, once cracking has started it does not seem to be affected by the thermal history of the sample as its dependence with the effective temperature does not depend on the heating rate. Cracking kinetics under both isothermal and non-isothermal annealing conditions have been described using the JMAK model (Eq. 6.1). This model was first derived to describe the kinetics of a certain phase transformation, such as crystallization of amorphous materials and growth, as a function of temperature and time under isothermal conditions.[136–140] Relevant JMAK equation parameters governing the kinetics of the phase transformation are the exponent, n, and the constant $K(T)$. The former is related to the nature of the phase transformation mechanism and the latter is considered to follow an Arrhenius law hence allowing to obtain the activation energy of the phase transformation. The JMAK exponent determined for the two isothermal tests is $n \sim 2$ (cf. Figure 6.4). It has been demonstrated that, if the kinetics of a certain isothermal transformation can be described by the JMAK model and the transformation rate does not depend on the thermal history, it is also possible to derive the JMAK parameters from non-isothermal annealing tests under linear heating conditions.[142,143] Indeed, for linear heating rates, the analytical expressions of non-isothermal and isothermal JMAK equations are equivalent simply by considering that the linear heating JMAK exponent is equal to 2 times the isothermal JMAK exponent, i.e. $n_{LinHeat} = 2n_{Iso}$.[143] Keeping in mind these considerations, cracking kinetics have been characterized under linear

heating conditions yielding a linear heating JMAK exponent of $2n$ ~1.5–2. Also, for non-isothermal conditions, the JMAK constant has been shown to be time-dependent under the form $K(t,\dot{T}) \propto \dot{T}^n exp(-\frac{E_a}{k_B \dot{T} t})$. This expression is explicitly and implicitly time dependent through $\dot{T}^n$ and $\dot{T}t$, respectively, and its physical validity is restricted to cases when the phase transformation is not governed by either nucleation or growth.[143] In order to avoid time dependency, the cracking activation energy has been determined using Eq. 6.3, which relates the inverse of the time to reach the 50% of the saturation value and the temperature at that certain moment, and yields E_a^{Crack}= 1.05 eV. It is worthy to note that this relation has been successfully used to determine the recrystallization activation energy of W filaments under annealing at constant heat rate.[144] Also, the JMAK equation has been succesfully used to model compressive strength evolution relating it to the degree of amorphous nucleation of certain gels in geopolymers.[145] Though the presented analysis of cracking kinetics is rather phenomenological and does not provide direct insights regarding the nature of the phenomenon controlling cracking, the agreement between the recrystallization and the cracking n values ($n_{recryst} \sim 2.25$)[13] and activation energies ($E_a^{recryst}$=0.65[14]–2.1[13] eV) suggests that its recrystallization which controls the cracking hence supporting Höfgen et al. argument. According to them, tensile stress should appear during recrystallization as compressive stresses generated in the initial stages of amorphization will no longer be compensated by volume swelling.[13] However, experimental data relating the recrystallization level and the cracking state is needed in order to confirm recrystallization as the cracking mechanism. Finally, it is remarkable that cracking directions are imposed by the cleavage planes parallel to the [1 1 $\bar{2}$ 0] of the crystalline substrate despite the polycrystalline microstructure and polytypism found in the recrystallized layer (cf. Figure 6.9). Cracks parallel to the surface causing delamination have been found to grow through highly faulted zones with $\frac{e_{exf}}{e_{irr}} \sim 2.1$, in good agreement with values discussed above.[13,14]

In order to study in detail the recrystallization process, a thin foil extracted from ion-amorphized 6H-SiC has been *in situ* TEM annealed, observed and compared to the final microstructure of the cracked sample. In addition, similar tests have been conducted in thin foils extracted from ion-amorphized HNS and TSA3 fibers in order to determine how different microstructures affect this process. Major findings from these tests are summarized in Table 6.2 and compared to the results obtained from the E-SEM tests.

Table 6.2: Summary of the *in situ* annealing tests

Sample	Cracking Temp. [°C]	Recryst. Temp. [°C]	Recryst. form	Densific. rate [nm/min]	Grain growth rate [nm/min]	$d_{(hkl)_1}$ [Å]	$d_{(hkl)_2}$ [Å]	α [°]	Polytypes
6H (E-SEM)	850–1020	-	-	-	-	2.52	2.52	56	3C/6H
6H (TEM)	-	870	Epitaxy + columnar (70°)[2]	1.4-4.2	56	2.51	2.54	57	3C/6H
HNS (E-SEM)	1090[1]	-	-	-	-	-	-	-	-
HNS (TEM)	-	900	Epitaxy + columnar (90°)[2]	6.5	21	2.54	2.57	55	3C
TSA3 (TEM)		930	Spontaneous (non oriented)	6.8-0.3-4.2	-	2.55	2.61	56	3C

[1] Heating sample holder thermocouple temperature

[2] with respect to the a-c substrate

In all cases, recovery of the amorphized layer can be considered a two step process. First stage is characterized by the densification of the irradiated layer with no noticeable crystallization. Regarding the 6H-SiC and HNS samples, there are strong indications that recovery started for temperatures lower than 800 °C as the measured thickness at this temperatures is already near the projected range of 4 MeV Au^{3+} in SiC, meaning that irradiation volume swelling has been almost completely recovered. This early recovery has been confirmed by the annealing test of the TSA3 sample, from which densification of the irradiated layer has been observed for temperatures as low as 250 °C. Second stage is characterized by the recrystallization of the amorphized layer with notable differences between the different samples. For instance, recrystallization of the thin foil extracted from 6H-SiC starts by the growth of the a-c interphase to a certain value and is followed by columnar recrystallization at ±70° with respect to the substrate; whereas the thin foil extracted from the HNS fiber presents direct columnar recrystallization at 90° without noticeable a-c growth. On the contrary, the thin foil extracted from the TSA3 presents a rather spontaneous and heterogeneous recrystallization. This difference may be caused by the presence of large carbonaceous

phases embedded in the amorphous layer of the TSA3 which hinder the columnar grain growth and in turn eases nucleation of SiC grains near the carbonaceous phases. Recrystallization temperatures, 850–930 °C, are in good agreement with the temperature range at which cracking is observed. These observations are consistent with reported structural relaxation of a-SiC upon prior to recrystallization. For instance, Bohn et al.[146] reported a constant decrease of the amorphous layer width with temperature for annealing of N-implanted 6H-SiC (8×10^{16} $\frac{62keVN}{cm^2}$) between RT and 1450 °C. In agreement with this observation, Snead et al.[51] observed linear densification with annealing temperature for neutron amorphized SiC between 150 °C and 885 °C. Also, Höfgen et al.[13] observed recovery in a temperature range in agreement with the one found for the TSA3 fiber, between 250 and 700 °C. Both, Snead et al.[51] and Bohn et al.,[146] attributed the structural relaxation to defect annealing processes with low activation energies. This argument is supported by Bae et al.,[62] who noticed the presence of a more chemically ordered atomistic structure in a-SiC after 1 h annealing at 890 °C. In a more recent paper, Ishimaru et al.[63] provided *in situ* TEM observations of a-SiC densification due to the structural relaxation during thermal annealing of ion-amorphized 6H-SiC (10^{15} $\frac{10MeVAu^{3+}}{cm^2}$) between 300 °C and 800 °C. In addition, they provided a detailed analysis pointing out that annealing of low energy and short Si-Si bonds (2.32 eV/bond, 2.3 Å) is faster than C-C ones (3.68 ev/bond, 1.5 Å). This unbalanced recovery reduces the average bond length justifying the densification of the a-SiC layer prior to recrystallization. Finally, Miro et al.[14] show that lattice damage fraction recovery and densification of the irradiated layer evolve similarly with the annealing temperature with an onset temperature of 200 °C. As in our case, once densification reaches a saturation value, recrystallization of the amorphous layer is triggered resulting in rather complex microstructures. For instance, Bohn et al.[146] reported an "explosive" epitaxial recrystallization from the crystalline substrate at 1500 °C from RBS analysis of the lattice damage evolution. However, they also reported recovery at temperatures as low as 650 °C from Raman spectroscopy, justifying the controversy between the two techniques due to a possible polycrystalline recrystallization which would align with the substrate at high temperatures. Harada et al.,[147] reported recrystallization of the amorphous layer by solid phase epitaxy (SPE) at 1000 °C. SPE started from the a-c interphase and saturated around 100 nm to continue by columnar growth resulting in

a polycrystalline layer composed by defected 6H-SiC and 3C-SiC. Höfgen et al.[13] reported that recrystallization epitaxial regrowth dominates for annealing temperatures over 1000 °C whereas for 800–850 °C recrystallization is governed by nucleated growth. Satoh et al.,[61] investigated the effect of the crystalline substrate orientation on the recrystallized polytype. They reported that during thermal annealing the amorphous layer regrows to the original polytype for $(11\bar{2}0)$ and $(1\bar{1}00)$ oriented 6H-SiC whereas it shows the appearance of 3C-SiC for (0 0 0 1) oriented 6H-SiC. Also, estimated regrowth rates at 850 °C yield ∼50 nm min^{-1} in good agreement with our experiments. On the contrary, Bae et al.[62] report complete SPE recrystallization for (0 0 0 1) oriented 6H-SiC with twin relationships between different domains. Ishimaru et al.,[63] in agreement with Harada et al.,[147] reported SPE from the a-c interphase to a saturation thickness of ∼160 nm and subsequent columnar growth without further discussion on the polytype nature of the resultant microstructure. However, Osterberg et al.[148] reported epitaxial recrystallization of ion-amorphized 3C-SiC at 725°C without signs of irradiated layer densification for temperatures below 800 °C. Finally, Miro et al.[14] reported full 6H polytype recrystallization of the annealed ion-amorphized after surface μRS analysis.

As summarized in Table 6.2, all recrystallized layers present similar SAED patterns with similar interplanar distances and angles of ∼2.5 Å and ∼56 °C. Interplanar spacings of (1 1 1) reflections of the 3C polytype are equivalent to (1 0 $\bar{1}$ 2) and (0 0 0 6) reflection of the 6H-SiC polytype (cf. Appendice A) and make crystal structure determination not straightforward. Regarding the delamination zone below the a-c interphase found for the E-SEM annealing tests, SAED patterns are consistent with highly faulted zones which can also be considered as polytypic transformations. For instance, SAED indexation of Figure 6.9 is consistent with a coexistence of (0 0 0 1) oriented 6H and (1 1 1) oriented 3C polytype. It has been reported that the presence of shear stresses can induce the alteration of the stacking sequence causing a 6H→3C polytypic transformation with a smooth interface between the $(1\ 1\ 1)_{3C}$ and the $(0\ 0\ 0\ 1)_{6H}$ interface.[149] Also, regarding the recrystallized layers of the 6H-SiC samples, similar polytypic transformation as discussed above can be obtained. For instance, it has been observed that epitaxial growth by atomic layer epitaxy of 3C-SiC over a (0 0 0 1)-6H-SiC substrate yields similar diffraction patterns to those of the recrystallized layer in Figures 6.9 and 6.11. The bright central hexagon overlapping the 6H pattern is explained by the overlap of two mirrored 3C diffraction patterns oriented by [0 1 $\bar{1}$] and

[0 $\bar{1}$ 1] zone axis.[150] Similarly, Harada et al.[147] reported SPE of 3C-SiC over 6H-SiC substrate in addition to the polycrystalline 3C-SiC in the middle of the recrystallized layer. In agreement with our experiments, they found an angle between the columnar grains and the substrate of 72°and proposed an atomic model for SPE recrystallization of a-SiC over (0 0 0 1)-oriented 6H SiC (cf. Figure A.1) which successes in explaining the observed microstructure. Regarding the recrysallized layers of HNS and TSA3 SiC fibers, SAED pattern indexation is consistent with (1 1 1) reflections of 3C-SiC, in agreement with Osterberg et al.[148] who did not observed recrystallization induced polytypism in a-SiC over polycrystalline 3C-SiC. Indeed, as polytypyc transformations have only been observed for SPE over 6H single crystalline substrates, it is believed that the nanostructure of the HNS fiber and the spontaneous recrystallization of the TSA3 fiber prevent polytypic transformation.

So far, we have discussed that thermal annealing induced mechanical failure is governed by the recrystallization of the irradiated layer. Taking into account that the recrystallized layer thickness is rather small with respect to the substrate, cracking and delamination can be reduced to a uniformily stressed thin film mechanical problem.[151] In this case, one of the main residual stress sources arise from thermal expansion mismatch between the film and the substrate. However, according to the E-SEM experiments, thermal shock can be discarded as for the test at constant temperature cracks were only observed after 2 hours at the consign temperature. At this moment, the difference between the CTE of the irradiated layer and the substrate is minimized with respect the beggining of the annealing due to initial recovery of SiC thermal properties. Another typical residual stress sources are often found in misfit stresses arising from film-substrate lattice or grain size mismatches. Whereas the former can be readily discarded as cracking has been also observed in HNS fibers, where no polytype transformation has been found, discarding the latter is not straightforward as in the HNS case SiC grains are larger in the recrystallized layer than in the substrate. To have a larger grain in the substrate would imply a film under compression, thus a substrate under tension, which is not compatible with the observed mechanical failure. Indeed, cracks in the recrystallized layer follow straight paths, hence discarding crack growth under compression as under this conditions cracks form wings with a certain angle with respect the initial crack direction.[152] In addtition, crack growth into the substrate

parallel to the surface is characteristic of substrates under compression and films in tension.[151]

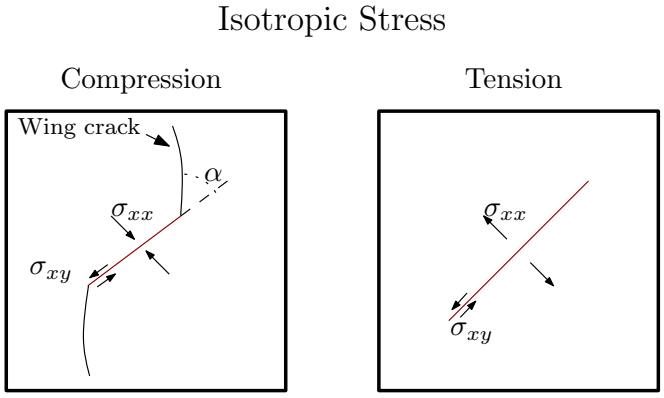

Figure 6.19: Crack growth evolution in brittle materials - Under compression, cracks tend to deviate from their initial direction forming wing cracks.[152]

One final residual stress source is related to point defect annihilation. For instance, stress arising from the annihilation of vacancies and interstitials is proportional to the excess defect concentration and can easily reach values on the order of GPa—e.g. a excess defect concentration of $\frac{C}{C_0} = 2$ can yield a stress of 2 GPa.[151] In addition, point defect annihilation stress is time and temperature dependent and may increase upon annealing. This stress source is likely to develop during annealing of ion-irradiated films and is in agreement with the faulted microstructure observed via TEM and the stresses competition pointed out by Höfgen et al.[13] during annealing.

In order to test the assumed stress distrubution of the sample, i.e. the recrystallized film under a tensional stress, a simplified mechanical approach under this assumption has been followed. Substrate delamination at a certain depth below the film-substrate interface can be reduced to the problem schematized in Figure 6.20. K_I and K_{II} denote the opening mode and the sliding mode fracture toughness, respectively. This mode are given by Eqs. 6.4 and 6.5, where σ denotes the applied stress and ω represents the relative proportion of mode II to mode I. Under the consideration that there is no elastic mismatch between the thin film and the substrate ω is meant to be $\sim 52°$.[151]

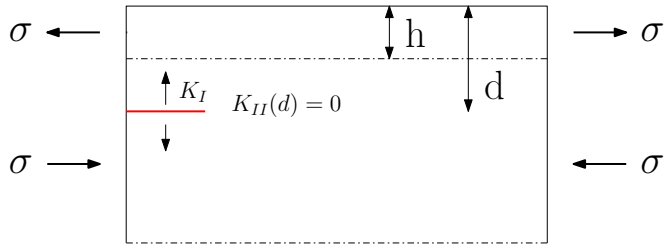

Figure 6.20: Reduced problem for substrate cracking parallel to the surface - Depth of delamination is given by imposing sliding crack equal to 0.[151]

$$K_I = \frac{\sigma h}{\sqrt{2d}}(\cos\omega + \sqrt{3}\left(\frac{d-h}{d}\right)\sin\omega) \tag{6.4}$$

$$K_{II} = \frac{\sigma h}{\sqrt{2d}}(\sin\omega - \sqrt{3}\left(\frac{d-h}{d}\right)\cos\omega) \tag{6.5}$$

Theoretically, the depth of the crack parallel to the surface will be given by $K_{II} = 0$. This condition, for an arbitrary depth d and $\omega = 52°$, is satisfied by Eq. 6.5 for a $\frac{d}{h}$ ratio of 3.68. Subsequently, using the obtained ratio, $\frac{d}{h}$, Eq. 6.4 can be reduced to the a simple expression as a function of the thickness of the film, i.e. $K_I = 0.586\sigma\sqrt{h}$. The latter expression evaluated for SiC limit values $K_{IC} = 2.8$ MPa m$^{1/2}$ and $\sigma_c = 3500$ MPa[12] yields a film thickness of 1.86 μm, which results to be higher than the theoretical value. However, the condition $K_{II} = 0$ with the measured values is satisfied by ω=40–46°, thus indicating that the initial assumption of no elastic mismatch may not be accurate for our case taking account for the differences with the expected value. However, normalization of the obtained theoretical thickness by the ratio between the measured $\frac{e_{exf}}{e_{irr}} \sim 2.1$ to the theoretical $\frac{d}{h} = 3.86$ yields 1.01μm in good agreement with the experimental value of 1.05 μm.

6.5 Conclusions

In situ thermal annealing experiments have been succesfully conducted in ion-amorphized 6H-SiC single crystals and TSA3 and HNS fibers. Thermal annealing induces cracking and delamination not only in 6H-SiC but also in HNS. Thermal expansion mismatches and thermal shocks have been discarded as stress sources. Cracking kinetics have been reported to be a thermally driven and have been modeled using a

JMAK equation with exponent of n=2. Also, cracking activation energy has been estimated to be 1.05 eV. The phenomenological description of the cracking process is in good agreement with the reported recrystallization phenomena, which, in addition with the good agreement between the cracking and recrystallization temperature range, points out recrystallization as the underlying mechanism governing cracking. Recrystallization characterization reveals a two stage recovery process. First stage consist in the densification of the irradiated layer for temperatures between 250–900 °C. Second stage concerns the irradiated layer recrystallization. Significant differences in the latter stage have been found between the different samples. On the one hand, 6H-SiC presents epitaxial and then columnar growth with coexistence of 3C and 6H SiC polytypes in the recrystallized layer. On the other hand, HNS presents columnar recrystallization with no polytype coexistence whereas TSA3 presents a rather spontaneous recrystallization due to the presence of carbonaceous phases embedded in the amorphous layer. Finally, a thin film mechanics approximation has been used in order to give some insights on the stress distribution that may lead to delamination.

7

In situ characterization of ion-irradiation creep of third generation Tyranno SA3 SiC fibers

Subcritical crack growth in SiC based composites is controlled by fiber creep processes. This lifetime limiting mechanism is of special concern under irradiation as it can enhance creep related mechanisms. To evaluate the impact of irradiation on the mechanical behavior of Tyranno SA3 fiber, *in situ* tensile tests were conducted on single fibers under conditions were thermal creep is negligible. First tests were conducted under 12 MeV C^{4+} irradiation to 0.07 dpa in a dominant electronic stopping regime at 300 MPa to determine the impact of the temperature on the irradiation strain. It is reported that irradiation strain and strain rate at low temperatures are higher than at high temperatures (∼1000 °C) due to a creep-swelling coupling mechanism. In order to minimize this coupling phenomena, irradiation creep has been characterized under 92 MeV Xe^{23+} at 1000 °C. It has been found that irradiation induces time-dependent strain under conditions where thermal creep is negligible. Finally, it is reported that irradiation creep rate shows a linear dependence with the ion flux and a square root dependence with the applied stress and an irradiation creep of 1.01×10^{-5} $MPa^{-1}dpa^{-1}$ under dominant electronic energy loss regimes. Similar experiments with an energy degrader, which allows a more uniform nuclear contribution for damage production across the sample, yield a linear dependence of the strain rate with the applied stress and an irradiation creep compliance of 10^{-6} $MPa^{-1}dpa^{-1}$ suggesting that the energy loss regime plays a major role on irradiation creep of SiC fibers.

7. *IN SITU* CHARACTERIZATION OF ION-IRRADIATION CREEP OF THIRD GENERATION TYRANNO SA3 SIC FIBERS

7.1 Introduction

Previously, in chapters 5 and 6, the effects of irradiation under nuclear energy loss regimes at low temperatures as well as the effects of thermal annealing at high temperatures have been investigated. As it has been discussed, high temperatures prevent SiC from radiation induced amorphization and degradation of its physico-chemical properties as dynamic annealing of the defects created by the displacement cascades takes place.[15] However, though the properties degradation is minimized with increasing temperatures to a certain value, other irradiation-related phenomena at the operation temperature range of the GFR (cf. Figure 1.1) may as well limit the in-pile lifetime of SiC composites. For instance, it is known that irradiation can enhance creep related mechanism, such as diffusion, and lead the time-dependent strain under loadings where thermal creep is negligible.

Irradiation creep (IC), has been the subject of intense research in metallic materials and several mechanisms are fairly well understood.[153–156] On the contrary, IC of ceramic materials, with the exception of nuclear graphite,[157–159] is rather rare. Indeed, only few studies can be found regarding IC in bulk SiC[19,160–164] and early generations of SiC fibers.[20,21,165] In addition, to date no data concerning IC of third generation SiC fibers is available with exception of a yet unpublished work by Koyanagi et al.[166]

SiC fibers play a key role in SiC_f/SiC_m pseudo-ductile mechanical behavior. When submitted to mechanical loadings, energy is released by matrix cracking and deflection of the cracks in the fiber-matrix interface.[33] SiC fibers are submitted to tensile stresses as they bridge the matrix cracks keeping the integrity of the composite beyond the elastic limit of bulk SiC. Sub-critical crack growth is controlled through fiber creep processes as matrix cracks grow and propagate due to the time-dependent strain of crack-bridging fibers.[167] This mechanism is of special concern for SiC composites devised for nuclear structural applications, as sub-critical crack growth may result in a lifetime limiting factor due to its acceleration by IC phenomenon.

The aim of this study is to evaluate the *in situ* mechanical behavior of third generation SiC fibers under in-pile relevant conditions. With this purpose, TSA3 fibers were tested at different stress loads and temperatures while ion-irradiated at different fluxes under mixed energy loss regimes using a dedicated tensile creep device.

7.2 Experimental conditions

The dedicated experimental facility used in this work is the tensile device described in section 4.3: MiniMecaSiC. The choice of the ion-irradiation conditions and SiC fibers have been made in order to simulate the interaction of the fibers with fission products while keeping an homogeneous damage profile.

It is worthy to mention that every step of the *in situ* tensile test is technically challenging due to the small size of the samples. In addition, the duration of the *in situ* tests are limited to the allocated ion-beam time in the experimental facilities described in section 4.2 obliging to a thoughtful selection of the experimental conditions.

7.2.1 Fiber selection and preparation

Selected TSA3 fibers for this work have mean diameters smaller than the projected range in SiC of the chosen ions in order to grant the non-implantation of the ions if the energy degrader is not used. In order to avoid stress hot spots due to possible diameter variations, TSA3 fibers were selected according to their cylindricity along the 25 mm sample fiber. To consider the fiber as suitable for the test, the measured diameter dispersion for the same fiber must be lower than 5% in all its length. The diameter measurements were performed every 3 mm using a Carl Zeiss Gemini 1525 Field Emission Gun Scanning Electron Microscope (FEG-SEM).

Once the fibers have been selected, they were fixed to two graphite grips using C-based cement C34 (from UCAR Co., Graftech International Ltd., Parma, OH) and submitted to a 12 hours heat treatment at 100 °C.[43] The graphite grips are then fixed to the displacement table and the force transducer with two copper pins as shown in Figure 7.1. After the traction bench is placed, the interface software resets the force transducer and allows inputting the parameters of the test.

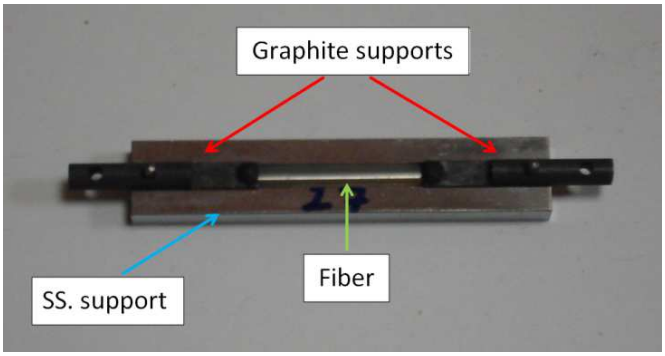

Figure 7.1: TSA3 SiC fiber fixed to the graphite grips - This fixation technique has been successfully applied to tensile testing of TSA3 at high temperatures with a similar device.[43]

7.2.2 Ion-irradiation conditions

Ideally, the study of irradiation creep would benefit from using neutron irradiation to simulate the nuclear reactor environment. However, the constraints inherent to neutron irradiation, e.g. irradiation time, precautions due to activation and time to radioactive decay,[46] together with the simplicity of the experimental approach necessary to its implementation in material test nuclear reactors, restrict the parametric study of SiC fibers irradiation creep.

On the other hand, together with neutron irradiation, SiC fibers will be subjeced to ion irradiation due to the non-negligible capture cross section of Si and C which lead to (n^0,α) nuclear reactions. This combination of neutron and ion-irradiation imply a rather complex radiation environment in which the fiber will be irradiated in a mixed energy loss regime.

In order to simulate the interaction of SiC fibers within different energy loss regimes, TSA3 fibers have been irradiated with 92 MeV Xe^{23+} and 12 MeV C^{4+}. These ions, which can be also used to simulate the interaction with fission products and alpha particles,[1] have the particularity of having a large projected range in SiC which, in combination with the energy degrader, allows to irradiation the fibers under an electronic and mixed energy loss regimes.

[1]In general, atomic numbers and energies of fission products fall near 42 (Mo) and 100 MeV or near 56 (Ba) and 70 MeV.[46] In addition, energetic He nuclei with mean energies of 5 MeV and 16 MeV arising from alpha decay[168] and ternary fission[169] respectively can also interact with the cladding material.

Table 7.1 summarizes the main characteristics of the interaction of these ions with the SiC fiber as calculated with SRIM 2013[49] with $E_d(C) = 20$ eV, $E_d(Si) = 35$ eV and $\rho_{SiC} = 3.21$ g cm^{-3}. Projected ranges (R_p) of these ions in SiC yield respectively 9.07 and 7.4 μm. These values are greater than the mean diameter of the selected SiC fibers. As it can be observed in Figure 7.2, since there is no ion-implantation a rather homogeneous damage profile with a small damage gradient with its maximum at the exit surface of the ion is created through the cross-section of the fiber. Mean damage values for dpa calculation with Eq. 3.4 yield 0.211 and 2.24×10^{-3} Vac/Ion/Å with electronic to nuclear stopping powers ratios ($\frac{S_e}{S_n}$) of 125 and 966 for 92 MeV Xe^{23+} and 12 MeV C^{4+} respectively.

Table 7.1: Damage creation, electronic (S_e) and nuclear (S_n) energy losses and projected range (R_p) of the selected ions for *in situ* tensile tests.

Ion	Vac/Ion/Å	S_e [keV nm^{-1}]	S_n [keV nm^{-1}]	$\frac{S_e}{S_n}$	R_p [μm]
12 MeV C^{4+}	2×10^{-3}	1.559	1.614×10^{-3}	966	7.4
92 MeV Xe^{23+}	0.2	17	0.136	125	9.1
93 MeV Xe^{23+} + E.D.	0.4	10.5	0.37	28	1.8-3.3-4.7-5.4-6.8-7.8

In addition, in order to increase the damage efficiency while keeping a homogeneous damage profile, 92 MeV Xe^{23+} *in situ* tests have been conducted with the energy degrader described in section 4.3. The thicknesses of the *Al* foils are 1.6, 3, 5, 6, 8 and 10 μm. In order to estimate the ions-SiC fiber interaction characteristics using the energy degrader, SRIM quick calculations have been conducted to estimate the output energy of the Xe ions after crossing the *Al* foils. Then, the output energy has been used as input for the calculation in SiC as described above. Estimated damage generation and energy losses have been calculated taking the arithmetic mean of the values calculated for each *Al* foil and are summarized in Table 7.1. Also, the cross-section damage profile estimation is shown in Figure 7.2. The use of the energy degrader displaces the implantation peak to different depths of the fiber. Implantation peak displacement increases the contribution of the nuclear stopping power as indicated by the higher $\frac{S_e}{S_n} = 28$. In turn, damage efficiency increases two times with respect the irradiation without the energy degrader.

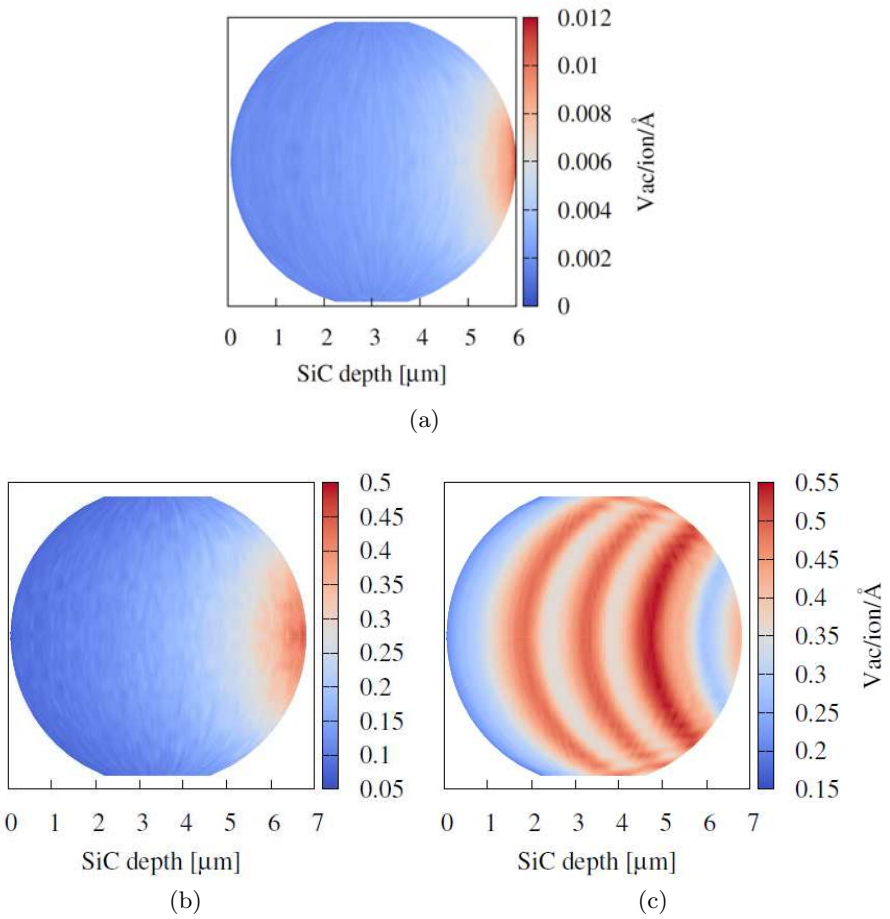

Figure 7.2: Cross-sectional damage profile of SiC fibers irradiated with 12 MeV C^{4+} and 92 MeV Xe^{23+} - No-implantation damage profile of (a) 12 MeV C^{4+} and (b) 92 MeV Xe^{23+}. (c) Various damage peaks with the energy degrader and 92 MeV Xe^{23+}.

Finally, in order to characterize the effect of ion-irradiation to the tensile behavior of TSA3 fibers, different *in situ* tests have been conducted under different experimental settings. Table 7.2 summarizes the experimental conditions chosen to determine the impact of the irradiation temperature on the tensile tests. Similarly, Table 7.3 summarizes the experimental conditions chosen to characterize the influence of the ion flux and the stress load in the IC phenomenon. Finally, Table 7.4 summarizes the experimental conditions in order to investigate whether the irradiation stopping regime may influence the IC phenomena.

Table 7.2: Ion-irradiation conditions for *in situ* tests under 12 MeV C^{4+}

Test	Low temp.		High temp.	
Irr. line	JANNUS-Saclay/Epimethee			
Stress [MPa]	300		300	
Temp. [°C]	RT[1]		1000	
Pressure [mbar]	2.1×10^{-6}		2.13×10^{-7}	
Diam. [μm]	6.02		6.27	
	Flux [$cm^{-2}s^{-1}$]	Dose rate [dpa s^{-1}]	Flux [$cm^{-2}s^{-1}$]	Dose rate [dpa s^{-1}]
12 MeV C^{4+}	1.68×10^{12}	3.9×10^{-6}	1.45×10^{12}	3.4×10^{-6}
	Fluence [cm^{-2}]	Dose [dpa]	Fluence [cm^{-2}]	Dose [dpa]
	3.03×10^{16}	0.07	3.08×10^{16}	0.071

[1] Free to heat under ion flux

Table 7.3: Ion irradiation conditions for *in situ* tests under 92 MeV Xe^{23+}

Test	$\dot{\phi}_{var}$ and σ_{ct}		$\dot{\phi}_{ct}$ and σ_{var}	
Irr. line	GANIL/IRRSUD			
Stress [MPa]	300		300-600-900	
Temp. [°C]	1000		1000	
Pressure [mbar]	6.7×10^{-7}		7×10^{-7}–10^{-6}	
Diam. [μm]	6.8		7.7	
	Flux [$cm^{-2}s^{-1}$]	Dose rate [dpa s^{-1}]	Flux [$cm^{-2}s^{-1}$]	Dose rate [dpa s^{-1}]
92 MeV Xe^{23+}	9.88×10^{7}	2.16×10^{-8}	5.22×10^{9}	1.14×10^{-6}
	9.67×10^{8}	2.12×10^{-7}		
	5.13×10^{9}	1.12×10^{-6}		
	9.73×10^{9}	2.13×10^{-6}		
	Fluence [cm^{-2}]	Dose [dpa]	Fluence [cm^{-2}]	Dose [dpa]
	5.34×10^{11}	1.17×10^{-4}	3.01×10^{14}	6.59×10^{-2}
	1.73×10^{13}	3.72×10^{-3}		
	1.13×10^{14}	2.47×10^{-2}		
	2.82×10^{14}	6.17×10^{-2}		

Table 7.4: Ion irradiation conditions for *in situ* tests under 92 MeV Xe^{23+} using the energy degrader

Test	$\dot{\phi}_{var}$ and σ_{ct}		$\dot{\phi}_{ct}$ and σ_{var}	
Irr. line	GANIL/IRRSUD			
Stress [MPa]	300		300-600-900	
Temp. [°C]	1000		1000	
Pressure [mbar]	$<10^{-6}$		$<10^{-6}$	
Diam. [μm]	7.4		7.5	
	Flux [cm^{-2}s^{-1}]	Dose rate [dpa s^{-1}]	Flux [cm^{-2}s^{-1}]	Dose rate [dpa s^{-1}]
92 MeV Xe^{23+} + E.D.	1×10^{9}	4.15×10^{-7}		
	5.02×10^{9}	2.08×10^{-6}	4.94×10^{9}	2.56×10^{-6}
	1.01×10^{10}	4.19×10^{-6}		
	Fluence [cm^{-2}]	Dose [dpa]	Fluence [cm^{-2}]	Dose [dpa]
	2.2×10^{13}	9.13×10^{-3}		
	1.44×10^{14}	5.97×10^{-2}	3.54×10^{14}	0.147
	3.39×10^{14}	0.141		

7.2.3 Ion-flux-induced temperature rise estimation

During the *in situ* experiments, the real temperature of the fiber will be the target temperature plus the ion-beam-induced temperature rise. Under the consideration of a negligible temperature gradient from the fiber core to the surface and a heat exchange only due to radiative processes,[43] the ion beam temperature rise will be given by Eq. 7.1

$$\Delta T_{irr}(\dot{\phi}) = \left(\frac{P_{irr}(\dot{\phi})}{S_r \epsilon \sigma_s} + T_0^4 \right)^{1/4} - T_0 \tag{7.1}$$

With $P_{irr}(\dot{\phi})$ being the radiated power by the fiber submitted to an ion flux $\dot{\phi}$, S_r the radiative surface of the fiber, $\epsilon = 1$ the emissivity of the fiber, σ_s the Stefan-Boltzmann constant and T_0 the room temperature. Under vacuum conditions, the radiated power is assumed equal to the ion-beam deposited power, $P_{dep}(\dot{\phi})$, which will be given by Eq. 7.2:

$$P_{dep}(\dot{\phi}) = E_{ion}^{tot} \phi S_{rect} \tag{7.2}$$

With E_{ion}^{tot} and S_{rect} being respectively the total energy deposited in the fiber by a trespassing ion and the fiber cross section perpendicular to the ion beam. $P_{dep}(\dot{\phi})$ can be estimated from the electronic energy deposition of the crossing ions in the fiber. Figure 7.3 shows how the ion path length vary as a function of the entry point of the ion ,y. The path length can be obtained as a function of y by Eq. 7.3.

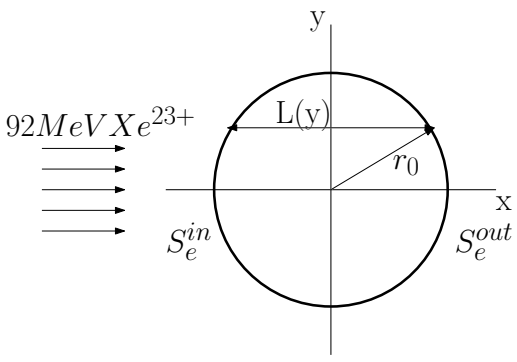

Figure 7.3: Schematic representation of the ion-path through the fiber - Maximum electronic energy deposition will be for y=0 and it will be 0 for y=r.

$$L(y) = 2\sqrt{r_0^2 - y^2} \tag{7.3}$$

The deposited energy by a crossing ion, $\Delta S_e(L)$, will depend on the ion path length. Therefore the total energy deposition, E_{ion}^{tot}, will be given by the integral of $\Delta S_e(L)$ over the entire fiber diameter, expressed as Eq. 7.4:

$$E_{ion}^{tot} = \int_{-r_0}^{+r_0} \Delta S_e(L(y))dy \tag{7.4}$$

Then, if a lineal variation of S_e with the ion path length $L(y)$ is assumed, the energy deposition $\Delta S_e(y)$ of a crossing ion in the fiber for a given y will be under the form of Eq. 7.5:[170]

$$\Delta S_e(L) = \left(S_e^{in} + \frac{S_e^{out} - S_e^{in}}{2r_0} L(y) \right) L(y) \tag{7.5}$$

With S_e^{in} and S_e^{out} in ev/ion/Å being the electronic stopping powers of the ion at the entry and exit point of the fiber for a path length equal to the fiber diameter as calculated by SRIM-2013.[49]

Finally, substituting Eq. 7.5 and Eq. 7.4 in Eq. 7.3 and in Eq. 7.2 yields a total deposited power given by Eq. 7.6:

$$P_{dep}(\dot{\phi}) = \dot{\phi} L r_0^2 \left(\pi S_e^{in} + \frac{4(S_e^{out} - S_e^{in})}{3} \right) \times 10^8 [\frac{\text{Å}}{cm}] \times 1.6 \times 10^{-19} [\frac{J}{eV}] \tag{7.6}$$

With L,r_0 being the gauge length and the radius of the fiber in cm. Also, conversion factors for cm-to-Å and J-to-eV are $10^(8)$ and 1.6×10^{-19} respectively.

Figure 7.4 shows the temperature rise as a function of the ion flux for (a) 12 MeV C^{4+} and (b) 92 MeV Xe^{23+}. The calculation parameters and the temperatures for the maximum fluxes used in this work are given in Table 7.5.

Table 7.5: Estimated temperature rise and associated thermal expansion for the maximum ion fluxes used in this work.

Ion	Diam. [μm]	S_e^{in} [eV/Ion/Å]	S_e^{out} [eV/Ion/Å]	Flux max. [cm^{-2} s^{-1}]	ΔT [°C]	$\Delta\epsilon_{\Delta T}$ [%]
12 MeV C^{4+}	6	156	172	1.5×10^{12}	285	0.057
92 MeV Xe^{23+}	7	1700	500	10^{10}	45	0.009

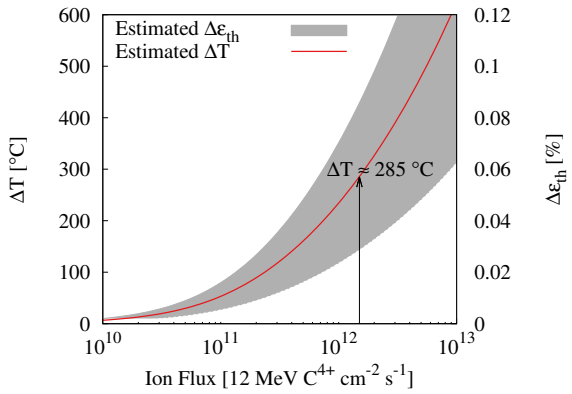

(a)

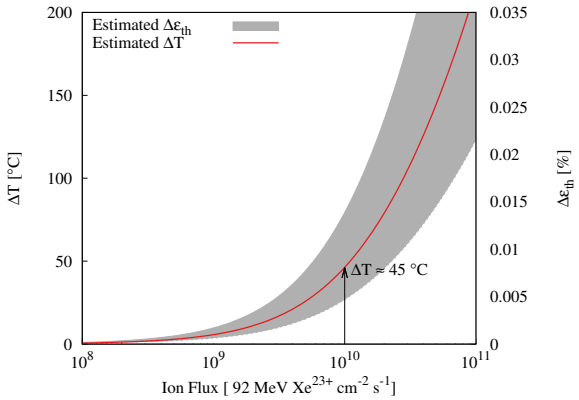

(b)

Figure 7.4: Estimation of the ion-flux induced temperature rise of TSA3 fibers during the *in situ* tests - The temperature rise caused by the highest ion fluxes yield (a) ∼285 °C with an associated mean thermal expansion of 0.057% for 1.5×10^{12} 12 MeV C^{4+} cm^{-2}s^{-1} and (b) ∼45 °C with an associated mean thermal expansion of 0.01% for 10^{10} 92 MeV Xe^{23+} cm^{-2}s^{-1}.

7.3 Results

7.3.1 Thermal creep

Thermal creep for TSA3 fibers has been determined for relevant mechanical and thermal loadings. Also, a tensile test was performed at 1350 °C and 850 MPa. As it can be seen in Figure 7.5, this test confirms the validity of the experimental facility results as the determined strain rate is in agreement with the reported strain rate for TSA3 fibers at the very same conditions.[43] Also, creep tests were performed for 300, 600 and 900 MPa at 1000 °C. As shown in Figure 7.5, TSA3 fibers are almost insensitive to thermal creep at 1000 °C. For instance, it was not possible to directly determine the strain rate at 300 MPa and 1000 °C from the experimental curve as it was lower than the sensitivity of the experimental facility. Upper and lower bounds for 300 MPa were estimated respectively by fitting the experimentally determined strain rates at 600 and 900 MPa with a linear and power law relationship, respectively. Then, the data was fitted with a power law using the upper and lower estimations at 300 MPa and the experimental strain rates at 600 and 900 MPa. As it can be observed in Figure 7.5, the power law exponent yields ∼2.1, in good agreement with reported values.[43] Finally, thermal creep rates at 300, 600 and 900 MPa yield respectively 6.2×10^{-11}, 2.8×10^{-10} and 5.3×10^{-10} s^{-1}.

7.3.2 Influence of the irradiation temperature on *in situ* tensile tests

Figures 7.6 and 7.7 show respectively the strain curves obtained for the *in situ* tests at RT, allowing the fiber to heat freely under the ion flux presence, and 1000 °C under 12 MeV C^{4+} at $\sim10^{12}$ ions cm^{-2} s^{-1}. Both tests were conducted at 300 MPa. As it can be observed, there is a clear influence of the ion-flux on the fiber tensile behavior. Both tests present time-dependent strain under conditions where thermal creep is negligible. There is also a notable impact of the irradiation temperature on the fiber behavior. For instance, the measured strain rate yields 7.13×10^{-8} s^{-1} for the test at low temperature and 4.22×10^{-9} s^{-1} for the test at 1000 °C. Residual strains at the end of the test yield ∼0.13% for the test at low temperature and ∼0.04% for the test at 1000 °C. The instantaneous strain observed in Figure 7.6 corresponds to the thermal expansion induced by the presence of the ion flux. The measurement of the latter is performed using a Faraday cup that intercepts the ion beam during 45

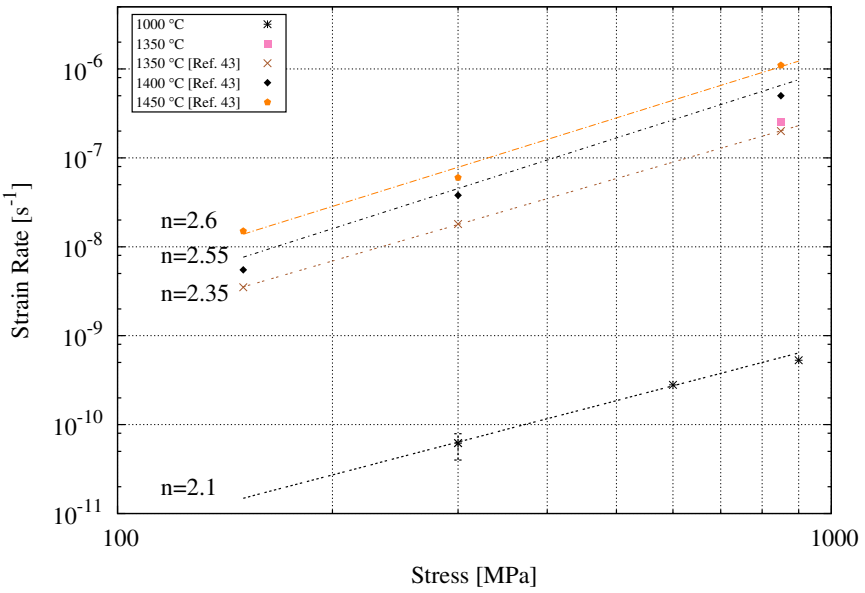

Figure 7.5: Thermal creep as a function of temperature and stress - Thermal creep determined at 1350 °C is in good agreement with literature values. TSA3 fibers exhibit low thermal creep rates at 1000 °C.

s. As the heat given by the ion flux disappears during the measurement, ion flux measurements cause the fiber to instantaneously contract 0.04–0.05%. Therefore, the temperature rise due to the ion beam presence can been estimated to be 200–250 °C using the thermal contraction during ion flux measurements and Eq. 7.7 with mean CTE, α, 2×10^{-6} K^{-1}.[75] It is remarkable that the estimation of the temperature rise and its associated thermal expansion in section 7.2.3 (cf. Table 7.5) are overestimated with respect the values here determined. On the contrary, ion flux heating for the tests at 1000 °C was prevented by the IR heat compensation system described in section 4.3.

$$\Delta T_{\dot{\phi}} = \frac{\Delta \epsilon_{th}}{\alpha} \tag{7.7}$$

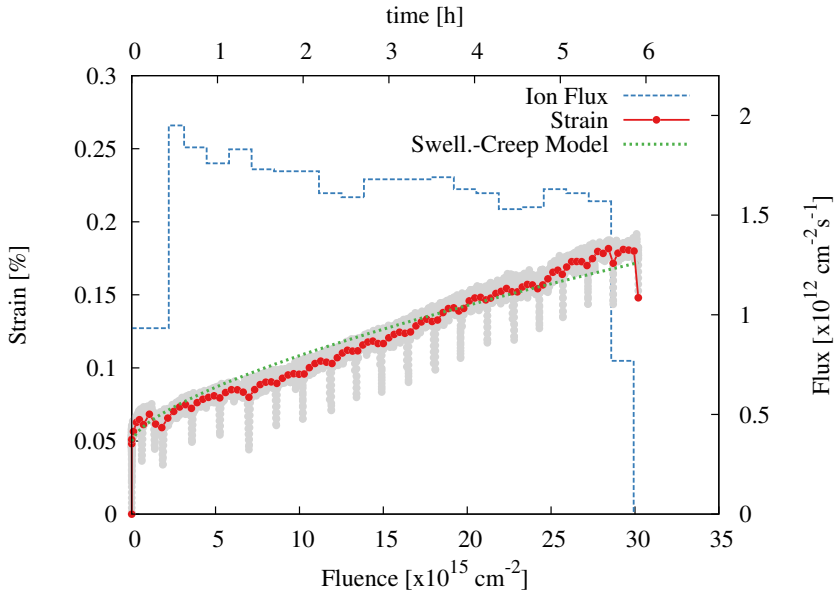

Figure 7.6: ***In situ*** **tensile test at RT and 300 MPa under 12 MeV** C^{4+} - The fiber was freely heated by the presence of the ion flux. The irradiation temperature of the fiber is estimated from the thermal contraction observed for each flux measurement with the Faraday cup.

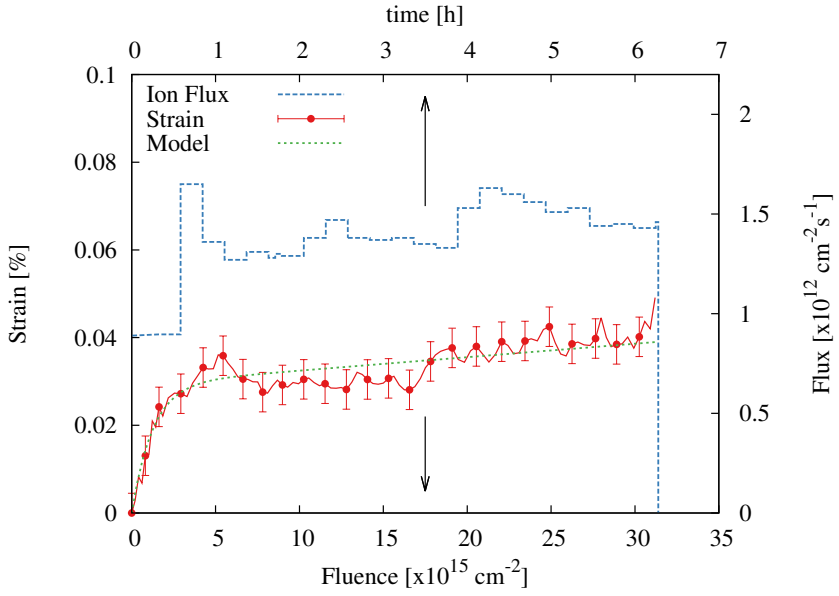

Figure 7.7: ***In situ*** **tensile test at 1000 °C and 300 MPa under 12 MeV** C^{4+} - Ion flux heating was prevented by using the IR heat compensation system.

7.3.3 Characterization of irradiation creep at high irradiation temperatures

Figure 7.8 shows the strain curve obtained for the tensile test at 1000 °C, allowing the fiber to heat freely under the ion flux, and 300 MPa stress under increasing 92 MeV Xe^{23+} ion fluxes of 10^8, 10^9, 5×10^9 and 10^{10} cm^{-2} s^{-1}. As it can be seen, the fiber appears to be unaffected by the ion beam presence for a flux of 10^8 ions cm^{-2} s^{-1}. Then, for every flux intensity increment the fiber shows a transient regime followed by a steady state regime. Once the ion beam was stopped, temperature and load where kept constant. During this last stage, a slow contraction of the fibers was observed until reaching a residual strain value of ∼0.055 %. Fiber contraction, ∼0.03%, is higher than the estimated thermal expansion due to the ion flux (cf. Table 7.5).

Figure 7.9 shows the strain curve obtained for the tensile test at 1000 °C and a 92 MeV Xe^{23+} ion flux of 5×10^9 cm^{-2}s^{-1} for tensile loads of (a) 300, (b) 600 (c) 900 MPa and (d) 300 MPa. The fiber shows a transient regime at the beginning of the irradiation. Also, there was an unexpected ion beam stop during the experiment. During the stop, the fiber was unloaded and loaded again once the ion beam was reset. As a consequence, the strain rates have been determined from sections (b), (c) and (d) to avoid ion beam fluctuations. As in the previous test, once the ion beam was stopped, the fiber contracted to a residual strain of ∼0.03%. At this flux, ion-beam induced temperature rise is estimated to be 25 °C and its thermal expansion 0.005%, which is lower than the observed contraction of ∼0.01%.

Under these experimental conditions, the total steady state strain rate ($\dot{\epsilon}_{tot}$) can be considered as the addition of the steady state IC ($\dot{\epsilon}_{IC}$) and thermal creep ($\dot{\epsilon}_{th}$) strain rates. Also, due to the non-implantation nature of the irradiation, the low doses and the tests temperature, ion-swelling has been neglected. This assumption is further developed in the discussion section. Finally, the steady state strain rate is given by Eq. 7.8:

$$\dot{\epsilon}_{tot} = \dot{\epsilon}_{IC} + \dot{\epsilon}_{th} \tag{7.8}$$

The steady state IC rate equation as a function of the stress and the flux intensity

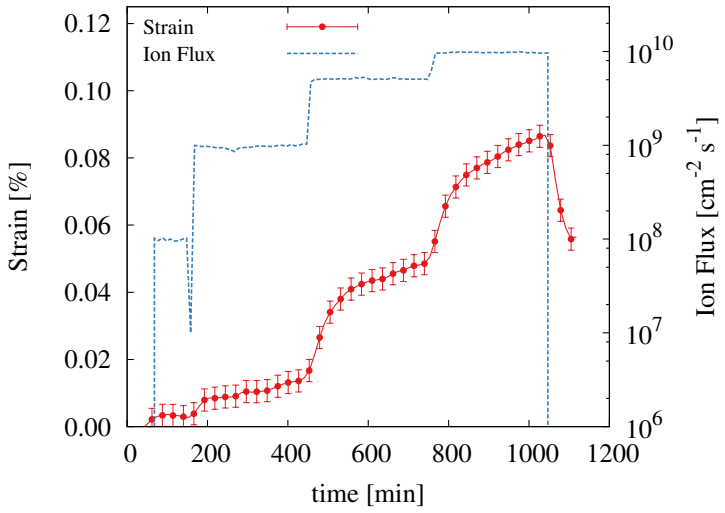

Figure 7.8: ***In situ*** **tensile test of a TSA3 fiber for determination of the ion flux impact on irradiation creep under dominant electronic energy loss regimes** - Experimental conditions: 1000 °C, constant stress 300 MPa and increasing 92 MeV Xe^{23+} ion flux.

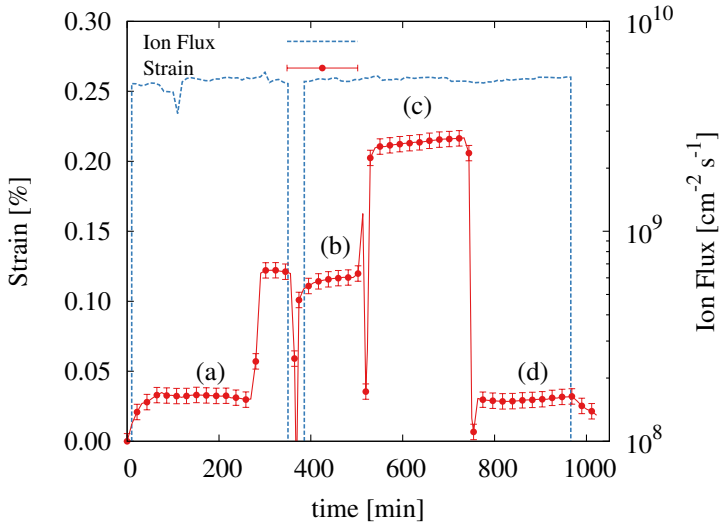

Figure 7.9: ***In situ*** **tensile test of a TSA3 fiber for determination of the stress load influence on irradiation creep under dominant electronic energy loss regimes** - Experimental conditions: 1000 °C under (a) 300 (b) 600, (c) 900 and (d) 300 MPa and constant 92 MeV Xe^{23+} ion flux.

is considered under the form of Eq. 7.9:

$$\dot{\epsilon}_{IC} = C(\dot{\phi}, \dot{\phi}_c) B_0 \sigma^n (\dot{\phi} - \dot{\phi}_c)^m \; ; \qquad C(\dot{\phi}, \dot{\phi}_c) = \begin{cases} 0 & \text{if } \dot{\phi} \leq \dot{\phi}_c \\ 1 & \text{if } \dot{\phi} > \dot{\phi}_c \end{cases} \tag{7.9}$$

Where B_0, $\dot{\phi}$ and $\dot{\phi}_c$ stand for the IC compliance , the flux intensity and the threshold ion flux intensity respectively. The n and m exponents determine the IC rate dependence with the applied stress and ion flux intensity respectively. Under the assumption of constant temperature and stress, Eq. 7.9 can be easily rewritten as Eq. 7.10 in order to determine m.

$$\ln(\dot{\epsilon}_{tot} - \dot{\epsilon}_{th}) = m \ln(\dot{\phi} - \dot{\phi}_c) + K_1 \tag{7.10}$$

Similarly, under constant temperature and the ion flux, n can be easily determined from Eq. 7.11:

$$\ln(\dot{\epsilon}_{tot} - \dot{\epsilon}_{th}) = n \ln(\sigma) + K_2 \tag{7.11}$$

Figure 7.10 shows the plot of Eqs. 7.10 and 7.11 using the experimental data shown in Figure 7.5. Best fit of the experimental data yield m and n values of 1.1 and 0.4 respectively. Table 7.6 gathers literature data for SiC irradiation creep under neutron and ion-irradiation. As it can be seen, the dependence of the strain rate with the ion flux is in agreement with reported m=1 values[19–21,165,171] whereas the determined dependence of the strain rate with the stress load is at variance with the reported n=1 values.[19,21] Also, Table 7.6 gathers the B_0 literature values for different experimental configurations. This parameter is defined as the ratio between the strain rate and the stress load and the flux intensity and is expressed in units of $MPa^{-1}dpa^{-1}$. Therefore, in order to be able to compare B_0 with reported values also a linear proportionality with the stress load has been assumed. Figure 7.10 shows how the experimental data also have a good agreement with the linear fit with an error of 9.2% with respect to the best fit. Finally, IC compliance B_0 yields 1.01×10^{-5} MPa^{-1} dpa^{-1}.

In order to model the behavior of the SiC fiber as a function of the ion fluence, IC is considered as the addition of a primary (ϵ_p) and steady state ($\epsilon_{s.s}$) creep regimes, thus Eq. 7.12. The former is considered to be under the form of a viscoelastic creep model[19] and the latter is given by Eq. 7.9. Taking in consideration the multi-step nature of

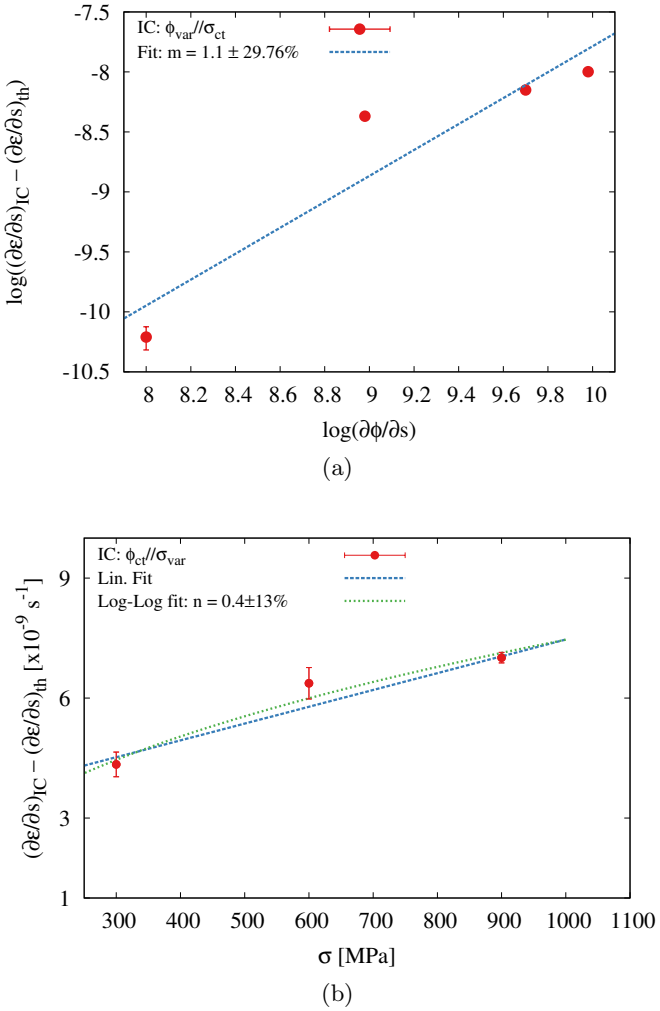

Figure 7.10: Determination of the m and n exponents of Eq. 7.9 for IC characterization under 92 MeV Xe^{23+} irradiation - Tests performed at 1000 °C under (a) variable ion flux, constant stress and (b) constant ion flux and variable stress.

the test, the total strain for a constant stress load and variable ion flux is given by Eq. 7.13.

$$\epsilon_{IC} = \epsilon_p + \epsilon_{s.s.} \tag{7.12}$$

Table 7.6: Irradiation creep of SiC and SiC fibers under ion and neutron irradiation

Sample	Form	Method	Stress[MPa]	Irr. Temp. [°C]	Dose [dpa]	Dose rate [$\times 10^{-6}$dpas^{-1}]	Particles [MeV]	m	n	B_0 [MPa^{-1}dpa^{-1}]
HD-SiC [161]	dog-bone	*in situ*	100	265	0.02	0.2	10.7 (H^+)	<1	-	5×10^{-4}
				505						
Text. SCS-6 [20,165]	CVD Fiber	Torsion	554	450	0.06	3	14 (H^{2+})	1	-	2.1×10^{-5}
			554	600	0.04	-	10 (H^+)			3×10^{-5}
Sylramic [20]	3rd gen. fiber	BSR[1]	-	600	0.04	-	10 (H^+)	1	-	4.7×10^{-6}
3C-SiC [20]	monolithic	BSR[1]	-	800	7.7	-	>0.1 (n^0)	-	-	4×10^{-7}
Text. SCS-6 [21]	CVD Fiber	Torsion	160	600	0.15	3.5	12 (H^+)	0.5	1	-
			320	600	0.15	3.5	12 (H^+)	0.5	1	-
			160	1000	0.12	3.5	12 (H^+)	1	-	-
CVD-SiC [163]	plate	BSR[1]	-	600–950	>0.7	-	>0.1 (n^0)	1	1	2.7×10^{-7}
				1080		-	>0.1 (n^0)	1	1	1.5×10^{-6}
				600/1080	<0.7	-	>0.1 (n^0)	1	1	$1\text{-}2\times10^{-6}$
CVD-SiC [162]	plate	*in situ*	18.5	910	0.12	1.6	2.8 (H^+)	3	1	8×10^{-5}
			97.8	910	0.13	1.5	3.2 (H^+)	3	1	2×10^{-4}
			97.8	910	0.13	2.4	3.2 (H^+)	3	1	2×10^{-4}
CVD-SiC [19]	plate	BSR[1]	-	380/540/790	0.1	-	>0.1 (n^0)	1	1	4×10^{-6}
			-	540/790	1	-	>0.1 (n^0)	1	1	4×10^{-7}
Sylramic [166]	3rd gen. fiber	BSR[1]	-	560	1–10	1.1	>0.1 (n^0)	1	1	3×10^{-7}
HNS [166]	3rd gen. fiber	BSR[1]	-	560	1–10	1.1	>0.1 (n^0)	1	1	2×10^{-7}
TSA3 (This work)	3rd gen. fiber	*in situ*	300–900	1000	0.06	0.021-2.13	92 (Xe^{23+})	1.1	0.4 (1)	1.01×10^{-5}
					0.14	0.04-4.16	E. Deg.	-	0.94	9.4×10^{-7}

[1] Bend Stress Relaxation

$$\epsilon_{IC} = \sum_i \left((p_i - p_{i-1}) \frac{\sigma}{E} \left(1 - e^{-\frac{\phi - \phi_i}{\phi_s^i}} \right) + B_0 \sigma (\phi - \phi_c) \right) + \epsilon_{th} \tag{7.13}$$

Where i is the current step of the test, p_i is a fraction of the elastic strain, σ is the applied stress, E the elastic modulus, ϕ the dose in dpa and ϕ_s^i the saturation dose of the i-th step. The resulting model is mathematically equivalent to the visco-elasto-plastic four-element model—a spring-dashpot model consisting in a Voigt model in series with a Maxwell model—. Finally, Figure 7.11 shows the good agreement between the model and the experimental curve. Nevertheless, it should not be considered as a model validation as the same test was used for the model calibration.

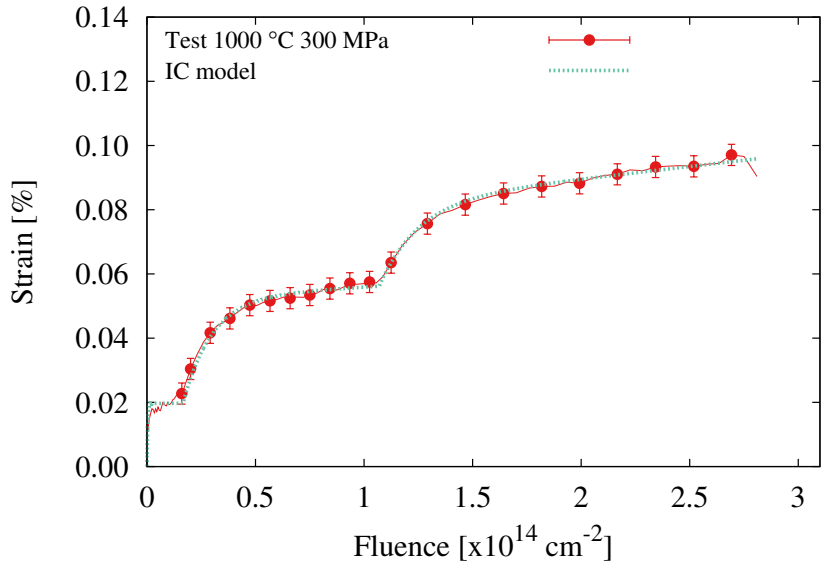

Figure 7.11: Irradiation creep of TSA3 fiber under constant temperature and increasing ion fluxes as a function of the ion fluence - Strain-fluence curve has been modeled with Eq. 7.13 with good agreement.

In addition, in order to investigate how the ion energy loss regime may influence irradiation creep, similar *in situ* tests have been conducted with the energy degrader. Ion-irradiation conditions are sumarized in Tables 7.1 and 7.4. Two main features should be highlighted. First, the efficiency in damage generation per ion doubles and, secondly, the implantation of ions at different depths imply the decrease of the electronic contribution to the ion energy loss.

Figure 7.12 shows the strain curve obtained for the test at 1000 °C and 300 MPa stress under increasing 92 MeV Xe^{23+} ion fluxes of 5×10^{9} and 10^{10} cm^{-2} s^{-1} with the energy degrader. As previously, for each flux increase the fiber undergoes through a transient which saturates to a linear plateau. Strain rates of both steady state regimes yield $\sim6\times10^{-10}$ s^{-1}. These similar values reflect a lower sensitivity to the flux than the tests without the energy degrader and prevent the experimental determination of the m exponent of Eq. 7.9 for irradiations with the energy degrader. Once the beam was stopped, the fiber contracted to a residual strain of $\sim$0.01 %, which is significantly lower than in previous tests.

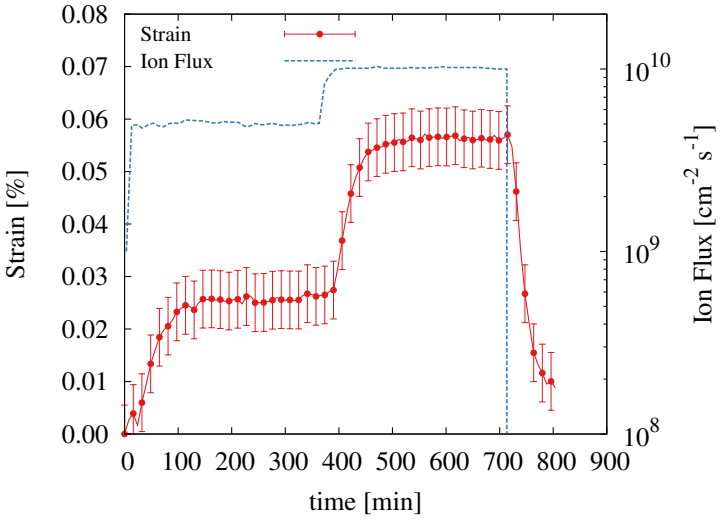

Figure 7.12: *In situ* tensile test of a TSA3 fiber for determination of the ion flux impact on irradiation creep under mixed energy loss regimes - Experimental conditions: 1000 °C, constant stress 300 MPa and increasing 92 MeV Xe^{23+} ion flux with the energy degrader.

Figure 7.13 shows the strain curve obtained for the test at 1000 °C under a constant 92 MeV Xe^{23+} flux with the energy degrader of 5×10^{9} $cm^{-2}s^{-1}$ for tensile loads of (a) 300, (b) 600 (c) 900 MPa. The fiber shows a transient regime at the beginning of the irradiation not observed for each load increase. Again, after the ion beam stopped the fiber contracted to ∼0.21%. This high residual strain with respect to the previous experiments is attributed to the higher applied load at the end of the test. Strain rates yield 9.3×10^{-10}, 7.7×10^{-9} and 1.1×10^{-8} $cm^{-2}s^{-1}$. Figure 7.14 shows the fit to the experimental data following Eq. 7.11 yielding a n exponent of 0.94.

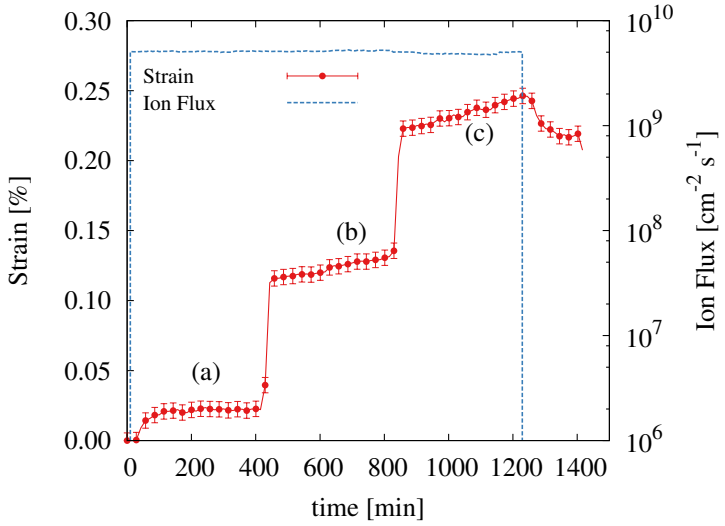

Figure 7.13: ***In situ*** **tensile test of a TSA3 fiber for determination of the stress load influence on irradiation creep under mixed energy loss regimes** - Experimental conditions: 1000 °C under (a) 300 (b) 600, (c) 900 MPa and constant 92 MeV Xe^{23+} ion flux with the energy degrader.

Finally, in order to compare the behavior of the TSA3 fiber under different ion-irradiation stopping regimes, fiber strains of the tests at constant temperature and stress load have been plotted as a function of the dpa-dose. As it can be observed in Figure 7.15, for similar fluences the test with the energy degrader shows higher dpa-dose. Fluence-to-dpa conversion has been calculated using the damage per ion specified in Table 7.1. Experimental curves have been fitted with Eq. 7.13 showing a good agreement. Finally, irradiation creep compliance for the test using the energy degrader, B_0=9.43×10^{-7} $MPa^{-1}dpa^{-1}$, is an order of magnitude lower than the determined for the test without the energy degrader.

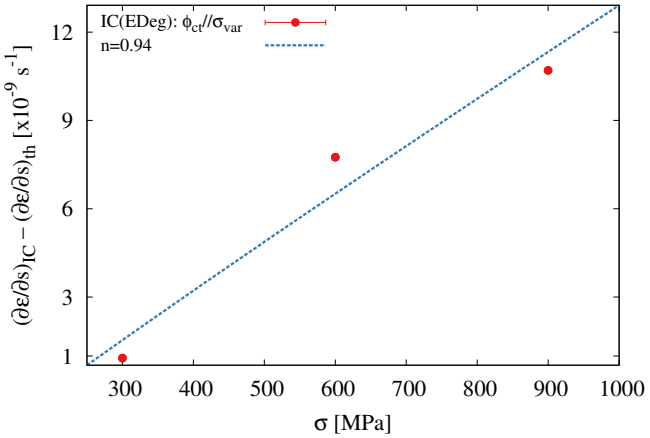

Figure 7.14: Determination of the n exponents of Eq. 7.9 for IC characterization under 92 MeV Xe^{23+} irradiation with the energy degrader - Test conducted at 1000 °C, constant flux and increasing stress loads.

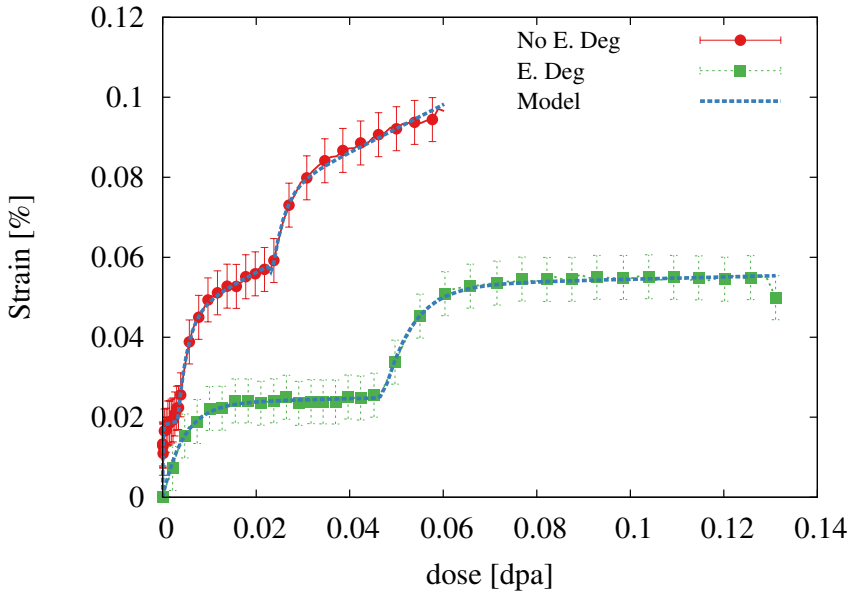

Figure 7.15: Influence of the energy loss regime on the fiber strain as a function of the dpa-dose - Tests were conducted at 1000 °C, constant 300 MPa and increasing ion fluxes. E. Deg. stands for energy degrader.

7.4 Post-mortem characterization

Table 7.7 shows the normalized elastic modulus of the tested fibers before and after irradiation. Measurements were made at RT and once secondary vacuum was reached. As it can be observed, irradiation in all experimental configurations of this work does not cause significant degradation of the mechanical properties.

Table 7.7: Elastic modulus of TSA3 fibers after the *in situ* tensile tests

	12 MeV C^{4+}	92 MeV Xe^{23+}	
		No E.Deg.	E.Deg.
E_{irr}/E_0	1±0.004	0.99±0.01	0.98±0.01

Figure 7.16 shows the evolution of the Raman spectra after the *in situ* tensile tests under 92 MeV Xe^{23} as compared to the as-received fiber. As it can be observed, both tested fibers present signs of irradiation as an incipient peak near the Raman bands associated to *Si-Si* homonuclear bonds. In addition, the fiber that has been irradiated with the energy degrader shows the higher degradation of the *Si-C* peak giving proof of the higher damaging efficiency.

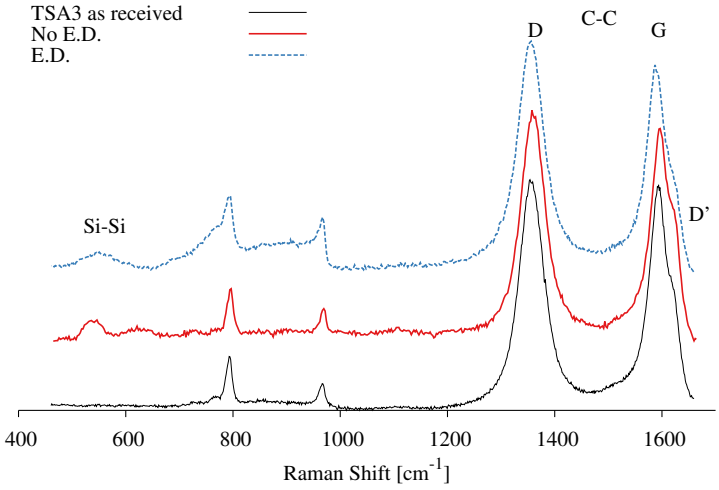

Figure 7.16: Comparison of the Raman spectra collected from the tested fibers under 92 MeV Xe^{23+} irradiation with and without the energy degrader - The fiber after irradiation with the energy degrader shows signs of low amorphization.

7.5 Discussion

Tensile creep behavior of TSA3 fibers at high temperatures has been previously characterized revealing a behavior similar to bulk SiC.[38,43] In this work, the reported steady state creep rate for relevant experimental conditions is 6.2×10^{-11} s^{-1}. This measurement is in agreement with bibliographic data[43] and reflects the low sensitivity of these fibers to thermal creep at these stress loads and temperatures. However, when stressed under ion-irradiation, TSA3 fibers have been reported to present time-dependent strain under conditions where thermal creep is negligible.[76,172]

IC in SiC has been mostly characterized following a post-mortem approach using the bend stress relaxation (BSR) method. This technique is the most extended one. It was first introduced by R.J. Price,[160] further developed by Morscher and DiCarlo[173] and recently used by Katoh et al[19,163] and Koyanagi et al.[166] for the study of irradiation creep in CVD-SiC and nuclear grade SiC fibers, respectively. The success of this method to evaluate IC is due to its simplicity hence allowing its implementation in nuclear reactors. Samples are elastically bend to a certain degree with a sample holder which is placed in the reactor to measure the stress relaxation rate by its correlation with a parameter m. If the sample recovers its initial form no stress relaxation has taken place during the irradiation and m equals unity. However, if stress relaxation associated to creep mechanisms takes place, m tends towards zero. However, it presents some difficulties at the time of evaluating the results as the stress load of the sample does not remain constant during the test. Also, *in situ* tests under ion-irradiation have been conducted to characterize IC of SiC. For instance, torsion methods have been used by Scholz et al.[20,21,165] with Textron SCS-6, a first generation fiber made of CVD-SiC deposited onto a C core filament,[38] and Sylramic fibers under deuteron irradiation. This method consists in measuring the time-evolution of the twist angle of the fiber after certain torque is applied to one end of the fiber. The major advantage of this method is that it minimizes the swelling influence as it does not affects to the torsional mechanical properties of the fibers. However, it needs transformation of the data to tensile equivalents to allow data interpretation. More recently, Shankar and Was[162] have adopted an *in situ* tensile characterization method to determine the effects of proton irradiation in polycrystalline CVD-β-SiC plates. It presents the advantage of independent monitoring of the different parameters involved in IC. Their experimental

facility is devoted to the study of IC of large size strips and under proton irradiation. The *in situ* facility used in this work allows *in situ* testing of micrometric SiC fibers individually under a wide range of irradiation conditions. However, the experiments need the deployment of large irradiation facilities with limited in-line time which in turn limits the possibility of a systematic characterization of IC in SiC fibers.

Despite this limitations, characterization of IC in TSA3 SiC fibers has been conducted for different irradiation, temperatures and stress loading conditions. First, the effect of the temperature on the time-dependent strain of the fibers has been investigated. The measured strain and strain rate of the fibers under ion-irradiation in Figures 7.6 and 7.7, are higher for irradiation at low temperatures, in agreement with Katoh et al.[19] Both, residual strain and strain rates are an order of magnitude higher for the *in situ* test at RT under ion-beam free heating. It is known that under neutron and ion-irradiation SiC swells. For temperatures near the critical amorphization temperature, i.e. ∼150 °C,[50,115,174] swelling is described as the strain introduced by the irradiation induced defects in the SiC lattice that remain after the post-cascade thermally activated recombination.[11,15,175] For instance, Katoh et al.[19] explain the time-dependent strain at low irradiation temperatures in terms of a coupled swelling-creep mechanism in which the applied stress may introduce anisotropy on the radiation volumetric swelling. SiC swelling has a decreasing saturation value with temperature until 1000–1200 °C due to the thermal recombination of the point defects. At these temperatures, the reported value under neutron irradiation is in the range of 0.2–0.36% for 1 to 2 dpa.[57] However, above this temperature range, the swelling saturation value begins to increase as the vacancies are sufficiently mobile to accumulate into vacancy clusters which induce void swelling.[11] To the knowledge of the author, SiC swelling under ion-irradiation at electronic energy loss regimes has not been characterized nor measured hence preventing direct comparison with literature values for neutron or ion-irradiation under nuclear energy loss regimes. For instance, swelling at 0.1 dpa under 4 MeV Ni^{+} at 200 °C has been reported to be ∼1%[58] which is up to eight times higher than the residual strain of 0.13% measured after the *in situ* test at RT (200 °C). As shown in Table 7.1, the projected range of the incident ion is greater than the fiber diameter. With this condition, the SiC fiber irradiation is under a dominant electronic regime. It has been pointed out that ion-irradiation in dominant S_e regimes may result in low damage creation as the electronic energy deposition may heal the damage produced by elastic

collisions.[94,107,108,176–178] These competing effects between the electronic and nuclear energy loss may justify the low residual strain observed for the 12 MeV C^{4+} test at low temperature. Swelling-creep has been reported to be proportional to 2/3 power of dose.[19,171] In Figure 7.6, the experimental curve shows a fair agreement with the mentioned relationship though it tends to diverge at the end of the irradiation.

In order to minimize swelling influence on the characterization of the IC phenomenon, *in situ* tensile tests under 92 MeV Xe^{23+} irradiation were performed at 1000 °C, which corresponds to the aimed nominal temperature for GFR.[4] Given that swelling at the irradiation temperature is near its minimum, fibers have been exposed to low doses and that irradiations with high $\frac{Se}{Sn}$ ratios imply low damage creation, swelling in the *in situ* tests conditions is considered to be negligible. During the *in situ* tests, ions crossing the fiber can be also considered as a supplementary heat source. In the case of 12 MeV C^{4+} irradiation at RT two different methods to estimate the temperature rise, $\Delta T(\dot{\phi})$ have been used. First estimation has been made from a radiative-heat transfer calculation yielding a $\Delta T(\dot{\phi}_C)_1$ of 285 °C for the used flux, $1.5{\times}10^{12}$ cm^{-2}s^{-1}. In addition, $\Delta T(\dot{\phi}_C)_2$ has been estimated from the thermal contraction measured during the beam current measures yielding 200-250 °C, pointing out the overestimation of the temperature-rise with the first method. For irradiations at 1000 °C, ion-flux heating of the fiber was prevented using the IR compensation system for the 12 MeV C^{4+} irradiation. However, for the 92 MeV Xe^{23+} the ion flux induced heating appeared to be not sufficient to be sensed by the IR captor. In this case, the $\Delta T(\dot{\phi}_{Xe})_1$ yields ∼45 °C for the highest ion flux, 10^{10} cm^{-2}s^{-1}. Such a temperature deviation from the consign value of 1000 °C will increment the contribution of thermal creep to the measured strain rate. However, as it can be observed in Figure 7.17, such a temperature rise, even though is overestimated, is not sufficient to justify the experimentally determined irradiation strain rates for all the irradiation conditions. The fiber contraction at the end of the tests in all cases cannot be attributed to thermal contraction. The contraction values are to high to correspond to a temperature decrease of the fiber once the ion-beam stops. Also, time-scale of the contraction is not compatible with thermal contraction as radiative processes rapidly cool down the fiber once the additional heat source disappears. Another possible explanation for this contraction would be the annealing of the irradiation defects created during the test as the fiber is kept at 1000 °C. However, Raman spectra of the tested fibers (cf. Figure 7.16) still exhibit features attributable

to irradiation damage. Finally, the most probable reason for this contraction is strain recovery of the transient regimes, which have been modeled as viscoelastic saturable transients (cf. Figures 7.11 and 7.15), originated for each flux increment.

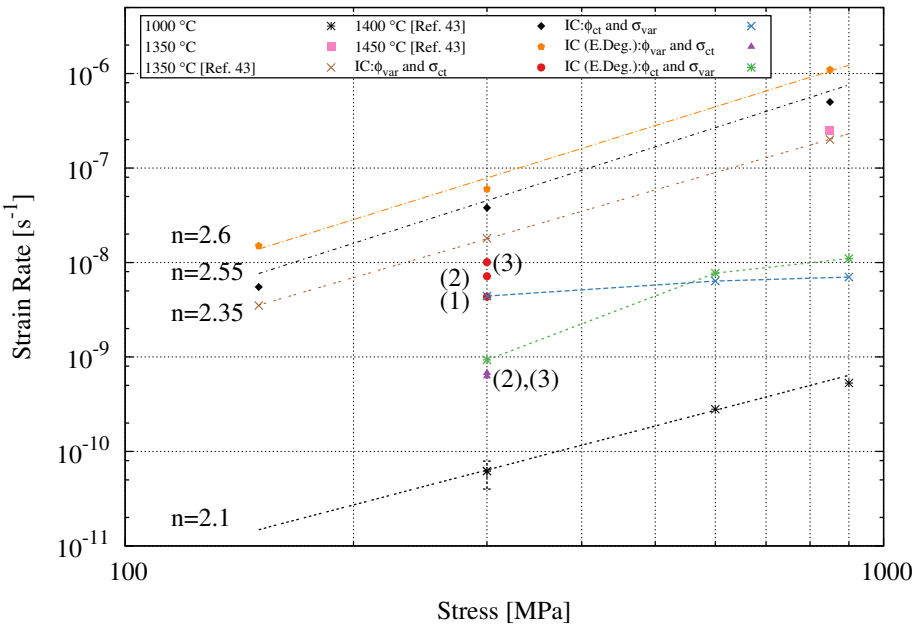

Figure 7.17: Thermal creep and irradiation creep rate as a function of temperature and stress - 92 MeV Xe^{23+} ion fluxes for IC tests at constant stress and 1000 °C are (1)10^9, (2) 5×10^9 and (3) 10^{10} $cm^{-2}s^{-1}$. Constant ion flux for tests at increasing stress is 5×10^9 $cm^{-2}s^{-1}$.

In order to ease the comparison, Table 7.6 gathers IC compliances extracted from different experimental configurations and irradiation conditions among the literature. It can be noticed that even though there is a large variability in the literature values, it seems fair to conclude that the testing temperature has a great impact on the fiber mechanical behavior under both, ion and neutron irradiation. Also, it is remarkable the technical complexity of the evaluation and comparison of the IC phenomena in micrometric SiC fibers. To reduce the uncertainty that may arise from differences in the testing configuration, both the flux influence and the stress influence on the strain rate of the fibers have been conducted in single tests for each irradiation. Two similar irradiation campaigns have been conducted: first without and secondly with the energy degrader. Regarding the former, determination of the flux influence on the stress rate

was performed at 300 MPa and 1000 °C for increasing ion fluxes. From the analysis of the experimental data shown in Figure 7.10, a linear relationship between the flux and the strain rate has been obtained in agreement with Scholz et al.[21,165] data for Textron SCS-6 SiC based fibers. Determination of the stress influence was conducted at constant ion flux of 5×10^{9} cm^{-2} s^{-1} for increasing stress loads. Best fit of data yields an almost square root relationship of the strain rate with the applied stress. This n exponent is at variance with the reported linear relationship in the literature for IC of SiC.[21,179] It is also at variance with typical thermal creep stress exponents, which normally take values equal to unity for diffusion processes and greater values for grain boundary sliding and has been reported to be $n \sim 2$ for TSA3 fibers.[43] Experimental curve in Figure 7.9 exhibits several features that difficult its analysis. For instance, negative strain rates values where obtained during the first part of the irradiation attributed to ion flux instabilities. Therefore, for the sake of comparing our experimental data with previous works, a linear relationship has been assumed between the strain rate and the applied stress. It is wise to mention that under this assumption only a ∼10% error with respect to the best fit is introduced, as shown in Figure 7.10. Determination of the IC compliance with $n = m = 1$ yields B_0=1.01×10^{-5} MPa^{-1}dpa^{-1}. Under the same assumptions, data from *in situ* tests under 12 MeV C^{4+} yield a IC of B_0=4.39×10^{-6} MPa^{-1}dpa^{-1}. As shown in Table 7.6, the obtained IC compliance values are respectively ∼25 and ∼10 times higher than value of 4×10^{-7} MPa^{-1}dpa^{-1} for β-SiC under neutron irradiation at 800 °C.[19,160] More recently, Koyanagi et al.[166] have reported third generation SiC fibers (TSA3, HNS and Sylramic) to have an IC compliance of ∼10^{-7} under neutron irradiation to 6 dpa at 500 °C in agreement with those of CVD-SiC. On the other hand, B_0 values found in this work are in the order of magnitude of those IC compliances obtained in torsion by Scholz et al.[21], i.e. 3×10^{-5} MPa^{-1}dpa^{-1} 10 and *in situ* by Shankar and Was[162], i.e. 8×10^{-5}–2×10^{-4} MPa^{-1}dpa^{-1}, both under proton irradiation. It is highly remarkable that all these experiments have in common that they are irradiated under non-implantation conditions suggesting irradiation under dominant electronic energy loss regime as responsible of the increased IC compliances. In order to investigate possible effects of the irradiation slowing down regime, *in situ* tests have been conducted under similar irradiation conditions, 1000 °C and 92 MeV Xe^{23+}, but forcing the implantation of the ions homogeneously distributed

in the fiber with the energy degrader. Under this mixed energy loss regime, experimental determination of the m exponent of Eq. 7.10 was not possible as measured strain rates were not significantly different for the different ion fluxes. On the contrary, as plotted in Figure 7.14, n exponent is close to 1, in agreement with the literature values gathered in Table 7.6. Finally, also under the assumption of a linear correlation with the flux, IC compliance of TSA3 fibers have been found to decrease nearly one order of magnitude, i.e. 9.43×10^{-7} $MPa^{-1}dpa^{-1}$. In addition, despite being the irradiation conditions with the energy degrader more damaging as estimated with SRIM and confirmed by μRs of the irradiated fibers, TSA3 fibers seem to be insensitive to IC under stress loadings where it is already present without the energy degrader.

Even though the phenomenological description of the IC process is rather simple, the real underlying mechanisms responsible of the IC phenomena remain unclear. It is wise to recall that dislocation motion contribution to SiC plastic deformation is limited for temperatures above 1700 °C[43] thus being negligible in our experimental configuration. IC under dominant nuclear stopping range irradiation with stress exponents of n=1 may be explained by enhanced volume (Nabarro-Herring) or grain boundary (Coble) diffusion creep mechanisms due to the increase of interstitials and vacancies produced by displacement cascades.[156] Thermal creep in TSA3 fibers has been described in terms of grain boundary sliding due to the intergranular free C compliance.[43] Therefore, irradiation enhanced diffusion processes can lead to an enhanced grain boundary motion by crystallographic slip at C basal planes under the applied stress. For instance, even though experimental data is needed to confirm these hypotheses under relevant conditions, Koyanagi et al.[180] have found a linear correlation between the grain size and the creep strain normalized to the applied stress meaning a contribution of grain boundary sliding to IC of nano-powder sintered SiC under neutron irradiation for doses between 0.01 and 0.11 dpa. These samples showed a TSA3-like microstructure with an average grain size of 226 nm and free carbon at grain boundaries. However, taking into consideration the differences between the IC compliances obtained in this work with and without the energy degrader, as well as the literature values concerning neutron and ion-irradiation under electronic stopping regimes, it seems reasonable to presume that energy loss regime play a role on the mechanical behavior of SiC fibers under irradiation. The high IC compliances obtained for ion-irradiation under dominant electronic energy regime suggest that inelastic interactions between the incident particle and the

lattice atoms are more effective than elastic interactions to accelerate the strain of the fiber under irradiation. Also, the difference in the n exponent between the tests with and without the energy degrader may indicate a change in the IC creep mechanism. For instance, many authors have described IC in terms of stress relaxation in the volume of the thermal spikes created by swift heavy ions, i.e. highly energetic charged particles with high S_e. According to this model, the target material would locally melt along the ions path due to the high electronic energy deposition as heat. This melted zone would deform relaxing shearing stresses to then freezing-in due to fast cooling-down.[181–183] Though this model has shown a fair agreement for amorphous SiO_2, a systematic characterization of IC under different irradiation regimes would be necessary to establish the correlation between IC and the stopping regime in SiC. Finally, as remarked by Scholz et al.,[20] it is wise to comment that high IC compliance values may be an important life-time limiting factor for structural nuclear applications.

7.6 Conclusions

Despite its inherent difficulty, TSA3 SiC fibers have been successfully *in situ* mechanically tested under ion-irradiation with different energy loss regimes. These experiments revealed time-depending strain of TSA3 fibers at loadings where thermal creep is negligible. This phenomenon is highly temperature dependent: the lower the temperature the higher the irradiation strain and strain rate. The decreasing trend with temperature is associated to the decrease of SiC swelling which is minimal between 1000–1200 °C. For irradiations under dominant electronic energy loss and at 1000 °C IC presents a two stage creep process consisting in a saturable transient regime that leads to a steady state IC creep. Irradiation strain rate shows a linear dependence with the ion beam flux and square root dependence with the applied stress proportional to a IC compliance of 1.01×10^{-5} $MPa^{-1}dpa^{-1}$. The latter value is higher than reported values for similar fibers and CVD-SiC under neutron irradiation suggesting that the ion energy loss regime may play a role in IC. Further tests have been conducted with an energy degrader to achieve a rather homogeneous damage profile while increasing the nuclear contribution to the energy loss. Under this configuration, IC rate depends almost linearly with the applied stress and, assuming a linear correlation with the ion

flux, a IC compliance of $\sim 10^{-6}$ $MPa^{-1}dpa^{-1}$ confirming that the energy loss regime plays an important role on IC of SiC fibers.

8

Summary Conclusions & Future Work

SiC composites reinforced with third generation SiC fibers, Tyranno SA3 (TSA3) and Hi Nicalon S (HNS), are promising materials for future nuclear applications. As a key component of a structural nuclear material, these fibers will be exposed to neutron and fission products fluxes which can modify their properties ultimately affecting the in-pile composite lifetime. In order to study the irradiation behavior of these fibers, the effects of ion-irradiation, used to simulate nuclear environments, have been studied by means of *ex situ* and *in situ* characterization techniques.

It is well established that SiC amorphizes when irradiated over a certain dose and below certain temperature with particles—neutrons, ions and electrons—with dominant energy losses due to elastic interactions with the target lattice. These interactions displace Si and C atoms from their equilibrium sites creating defects that eventually pile up and induce the loss of crystallinity the material. Damaging dose and temperature dependence of ion-amorphization are well known for different particles in single crystalline SiC. On the contrary, the characteristics of ion-amorphization in these fibers have not been studied to date. One of the interests of studying ion-amorphization threshold conditions of TSA3 and HNS fibers relies on the influence of their microstructure to this process. Despite both fibers are composed of highly faulted 3C-SiC grains with free C located at grain boundaries and triple points, their microstructures are rather different

as grain sizes are around 200 nm for TSA3 and 20 nm for HNS fibers. In this work, ion-amorphization kinetics of TSA3 and HNS fibers under 4 MeV Au^{3+} irradiation have been studied using μRs and TEM and compared to the response of as-irradiated 6H-SiC single crystals. A good agreement has been found between μRs and TEM imaging and electron diffraction. It is reported that there is no significant influence of the fibers mictrostructure on their amorphization kinetics and temperature depencence with respect to the 6H-SiC single crystal. Indeed, amorphization kinetics at RT have been well described using a multi-step damage accumulation (MSDA) model showing a two step process with an amorphization threshold dose ∼0.4 dpa. In addition, no complete amoprhization was found for irradiation temperatures over 200 °C. Despite the general agreement between the fibers and the single crystals, slight differences in the amorphization kinetics at RT have been observed. Indeed, the quantitative analysis of the Raman spectra indicates a prompt amorphization of these fibers at very low doses (<0.2 dpa). Future work should be directed to a TEM study of the amorphization level for each dose in order to clarify if this prompt amorphization reflects the actual physical evolution of the fibers microstructure or if it is the result of incertitude related to the quantitative Raman analysis.

One of the main features of amorphous SiC is its thermal stability due to the low mobility of point defects. Recrystallization of amorphized SiC has been reported after thermal annealing at temperatures ranging from 700 to 1500 °C. More interestingly, it has been reported that if the amorphous layer of SiC on top of the non-irradiated SiC substrate exceeds a certain thickness, thermal annealing induces also the mechanical failure of the recrystallized layer. In this work, thermal annealing effects on fully amoprhized SiC fibers and single crystals have been investigated by *in situ* E-SEM and TEM. It has been reported that thermal annealing induced cracking and delamination is observed also for SiC fibers. The systematic study of the cracking process have been conducted in ion-amorphized SiC single crystals. It has been reported that cracking is a thermally driven phenomenon with an activation energy of 1.05 eV. In addition, cracking kinetics have been modeled with a JMAK equation with n exponents yielding from 1.5 to 2. Both, the activation energy and the JMAK parameters are in good agreement with those found for recrystallization of amorphous SiC, thus pointing the latter as the controlling mechanism for the mechanical failure. In order to give further insights on how these two phenomena relate, *in situ* TEM thermal annealing of

amorphous SiC fibers and 6H-SiC single crystals have been conducted. Recrystallization temperatures for all samples are in good agreement with the temperatures found for the mechanical failure. Also, though different recrystallization processes have been found depending on the microstructure of the non-irradiated substrate, all samples present a two stage annealing process. For all samples, densification of the amorphous layers has been observed previous recrystallization and for temperatures as low as 250 °C. However, though annealing of defects is pointed out as the ultimate stress source that causes cracking, no direct evidence between the cracking density state and the degree of recovery or recrystallization has been given. Further work should be directed to investigate such relation by means of a systematic TEM study of the annealed samples for different cracking densities and their related recovery states.

At temperatures where ion-amorphization of SiC is virtually impossible due to dynamic annealing of the irradiation defects, other phenomena may as well affect the fibers properties. Special attention has been given to irradiation creep of TSA3 fibers under ion-irradiation simulating the interaction of the fibers with fission fragments. This high energetic charged particles can induce high energy deposition. By means of a devoted experimental facility, different *in situ* tests have been conducted in order to characterize irradiation creep at different temperatures, loads and irradiation conditions. It has been reported that TSA3 fibers under ion-irradiation show time-dependent strain under temperatures and stress loads where thermal creep is negligible. This strain is higher at low temperatures due to a coupling between irradiation swelling and irradiation creep, in agreement with literature. At higher temperatures and under dominant electronic energy loss regimes, where swelling is negligible, irradiation creep rate has been reported to depend linearly with the ion flux and to the square root of the applied stress with an irradiation creep compliance of $\sim 10^{-5}$ MPa^{-1} dpa^{-1}. This value is higher than reported ones for similar fibers under neutron irradiation. However, when irradiated under mixed energy loss regimes, irradiation creep has been reported to linearly depend with the applied stress with an irradiation creep compliance of $\sim 10^{-6}$ MPa^{-1} dpa^{-1}. By this experiments it has been demonstrated that energy loss regime plays an important role on the irradiation creep phenomenon. Further efforts should be addressed to a complete microstructural characterization of the tested fibers in order to give insights on the irradiation creep mechanisms. Finally, the approach followed to characterize irradiation creep in TSA3 fibers should be also applied to HNS fibers. By so, relevant

information concerning the role of the grain size in the irradiation creep phenomenon could be obtained.

List of publications

1. **J. Huguet-Garcia** A. Jankowiak, S. Miro, T. Vandenberghe, C. Grygiela, I. Monnet and J.-M. Costantini, In situ characterization of ion-irradiation enhanced creep of third generation Tyranno SA3 SiC fibers, Journal of Materials Research, Vol. 30, Iss. 9, pp. 1572–1582, 2015.

2. **J. Huguet-Garcia**, A. Jankowiak, S. Miro, D. Gosset, Y. Serruys, and J.-M. Costantini, Study of the ion-irradiation behavior of advanced SiC fibers by Raman spectroscopy and transmission electron microscopy, Journal of the American Ceramic Society, Vol. 98, Iss. 2, pp. 675–682, 2015.

3. **J. Huguet-Garcia**, A. Jankowiak, S. Miro, R. Podor, E. Meslin, Y. Serruys, and J.-M. Costantini, *In situ* E-SEM and TEM observations of the thermal annealing effects on ion-amorphized 6H-SiC single crystals and nanophased SiC fibers, physica status solidi (b), Vol. 252, Iss. 1, pp. 149–152, 2015.

4. S. Miro, J.-M. Costantini, **J. Huguet-Garcia**, L. Thomé, Recrystallization of hexagonal silicon carbide after gold ion-irradiation and thermal annealing, Philosophical Magazine, Vol. 94, Iss. 34, pp. 3898–3913, 2014.

5. **J. Huguet-Garcia**, A. Jankowiak, S. Miro, Y. Serruys, and J.-M. Costantini, Ion irradiation effects on third generation SiC fibers in elastic and inelastic energy loss regimes, Nuclear Instruments and Methods in Physics Research Section B: Beam Interactions with Materials and Atoms, Vol. 327, pp. 93–98, 2014.

6. **J. Huguet-Garcia**, A. Jankowiak, S. Miro, R. Podor, E. Meslin, L. Thomé, Y. Serruys, and J.-M. Costantini, Characterization of ion-irradiation effects and thermal annealing on third generation SiC fibers and 6H-SiC,The European Journal of Physics N, 2015. (Accepted)

References

[1] *World energy outlook 2014*. IEA, Paris, 2014. 1

[2] B.W. Brook and C.J.A. Bradshaw. **Key role for nuclear energy in global biodiversity conservation**. *Conservation Biology*, **0**(0):1–11, 2014. 1

[3] S.J. Zinkle and J.T. Busby. **Structural materials for fission and fusion energy**. *Materials Today*, **12**(11):12 – 19, 2009. 1, 2

[4] P. Yvon and F. Carré. **Structural materials challenges for advanced reactor systems**. *Journal of Nuclear Materials*, **385**(2):217 – 222, 2009. 2, 3, 139

[5] A. Iveković, S. Novak, G. Dražić, D. Blagoeva, and S. de Gonzalez de Vicente. **Current status and prospects of SiCf/SiC for fusion structural applications**. *Journal of the European Ceramic Society*, **33**(10):1577–1589, 2013. 2

[6] D.M. Carpenter. *An assessment of Silicon Carbide as a cladding material for light water reactors*. PhD thesis, Massachussetts Institute of Technology, 2010. 3, 59

[7] J.D. Stempien, D.M. Carpenter, G. Kohse, and M.S. Kazimi. **Characteristics of composite Silicon Carbide fuel cladding after irradiation under simulated PWR conditions**. *Nuclear Technology*, **183**(1):13–29, 2013. 12

[8] K. Yueh and K.A. Terrani. **Silicon carbide composite for light water reactor fuel assembly applications**. *Journal of Nuclear Materials*, **448**(1–3):380–388, 2014. 3, 59

[9] F. Bernachy-Barbe. *Caractrisation des mcanismes d'endommagement et modlisation du comportement mcanique sous chargements multi-axiaux de tubes composites SiC/SiC*. PhD thesis, Materials and structures in mechanics. Ecole Nationale Superieure des Mines de Paris, 2014. 3

[10] L.L. Snead, T. Nozawa, M. Ferraris, Y. Katoh, R. Shinavski, and M. Sawan. **Silicon carbide composites as fusion power reactor structural materials**. *Journal of Nuclear Materials*, **417**(1-3):330–339, 2011. 3, 12, 29

[11] L.L. Snead, Y. Katoh, and T. Nozawa. **Radiation Effects in SiC and SiC-SiC**. In R. Konings, editor, *Comprehensive Nuclear Materials*, chapter 4.07, pages 215–240. Elsevier Inc., Oxford, 2012. 3, 12, 21, 29, 138

[12] L.L. Snead, T. Nozawa, Y. Katoh, T.-S. Byun, S. Kondo, and D.A. Petti. **Handbook of SiC properties for fuel performance modeling**. *Journal of Nuclear Materials*, **371**(1-3):329–377, 2007. 4, 8, 9, 10, 11, 21, 29, 30, 111

[13] A. Hofgen, V. Heera, F. Eichhorn, and W. Skorupa. **Annealing and recrystallization of amorphous silicon carbide produced by ion implantation**. *Journal of Applied Physics*, **84**(9):4769, 1998. 5, 30, 84, 86, 101, 104, 105, 107, 108, 110

[14] S. Miro, J.-M. Costantini, J. Huguet-Garcia, and L. Thomé. **Recrystallization of hexagonal silicon carbide after gold ion irradiation and thermal annealing**. *Philosophical Magazine*, **94**(34):3898–3913, 2014. 5, 30, 31, 75, 76, 84, 86, 101, 104, 105, 107, 108

[15] X. Kerbiriou, J.-M. Costantini, M. Sauzay, S. Sorieul, L. Thome, J. Jagielski, and J.-J. Grob. **Amorphization and dynamic annealing of hexagonal SiC upon heavy-ion irradiation: Effects on swelling and mechanical properties**. *Journal of Applied Physics*, **105**(7):073513, 2009. 5, 27, 28, 76, 78, 114, 138

[16] C.H. Henager. **Subcritical crack growth in Hi-Nicalon type S fiber CVI-SiC/SiC composites**. *Ceramic Engineering and Science Proceedings*, **27**(5):127–144, 2007. 6, 12

[17] G.S. Was. *Fundamentals of radiation materials science*. Springer-Verlag, Berlin, 2007. 6, 21, 23

[18] T.D. Burchell. **Radiation Effects in Graphite**. *Comprehensive Nuclear Materials*, pages 299–324, 2012. 6

[19] Y. Katoh, L.L. Snead, C.M. Parish, and T. Hinoki. **Observation and possible mechanism of irradiation induced creep in ceramics**. *Journal of Nuclear Materials*, **434**(1-3):141–151, 2013. 6, 114, 129, 131, 137, 138, 139, 141

[20] R. Scholz and G.E. E Youngblood. **Irradiation creep of advanced silicon carbide fibers**. *Journal of Nuclear Materials*, **283-287**:372–375, 2000. 6, 32, 114, 131, 137, 143

[21] R. Scholz, R. Mueller, and D. Lesueur. **Light ion irradiation creep of Textron SCS-6 silicon carbide fibers**. *Journal of Nuclear Materials*, **307-311**:1183–1186, 2002. 6, 114, 129, 131, 137, 141

[22] R.W. Olesinski and G.J. Abbaschian. **The C-Si (Carbon-Silicon) system**. *Bulletin of Alloy Phase Diagrams*, **5**(5):486–489, 1984. 7, 8

[23] J.J. Berzelius. **Unterfuchungen uber die Flufsfpathfaure und deren merkwrudig Verbindungen**. *Annalen der Physik und Chemie*, **1**:169–230, 1824. 7

[24] E.G. Acheson. **Production of artificial crystalline carbonaceous materials**, 1893. 7, 8

[25] H. Moissan. **Nouvelles recherches sur la météorite de Cañon Diablo**. *Comptes rendus hebdomadaires des séances de l'Académie des sciences*, **139**:773–780, 1904. 7

REFERENCES

[26] O. Kordina and S.E. Saddow. **Silicon Carbide Overview**. In S.E. Saddow and A. Agarwa, editors, *Advances in Silicon Carbide Processing and Applications*, chapter 1, pages 1–4. Artech House, Inc, 2004. 8

[27] G. R. Fisher and P. Barnes. **Towards a unified view of polytypism in silicon carbide**. *Philosophical Magazine Part B*, **61**(2):217–236, 1990. 9

[28] F. Bechstedt, P. Kackell, A. Zywietz, K. Karch, B. Adolph, K. Tenelsen, and J. Furthmuller. **Polytypism and Properties of Silicon Carbide**. *Physica status solidi (b)*, **202**(1):35–62, 1997. 9, 10

[29] L.S. Ramsdell. **Studies on silicon carbide**. *American Mineralogist*, **32**(1-2):64–82, 1947. 9

[30] T. Kimoto and J.A. Cooper. *Fundamentals of Silicon Carbide Technology: Growth, Characterization, Devices, and Applications*, chapter Physical Properties of Silicon Carbide, pages 11–38. John Wiley & Sons, Singapore, 2014. 9, 10, 11

[31] J. Lefevre. *Etude des effets dirradiation dans le polytype cubique du carbure du silicium par les techniques spectroscopiques de photoluminescence et de resonance paramagnetique elecronique*. PhD thesis, Ecole Polytechnique, 2008. 10

[32] C. H. Carter, R. F. Davis, and J. Bentley. **Kinetics and Mechanisms of High-Temperature Creep in Silicon Carbide: II, Chemically Vapor Deposited**. *Journal of the American Ceramic Society*, **67**(11):732–740, 1984. 11

[33] J. Lamon. **Properties and Characteristics of SiC and SiC/SiC Composites**. In R. Konings, editor, *Comprehensive Nuclear Materials*, chapter 2.12, pages 323 – 338. Elsevier, Inc., Oxford, 2012. 12, 114

[34] R. Naslain. **Design, preparation and properties of non-oxide CMCs for application in engines and nuclear reactors: an overview**. *Composites Science and Technology*, **64**(2):155–170, 2004. 12

[35] M. Zabiego, C. Sauder, C. Lorrette, and P. Guedeney. **Multilayer tube in ceramic matrix composite material, resulting nuclear fuel cladding and associated manufacturing processes**, 2014. 12

[36] R.R. Naslain. **The design of the fibre-matrix interfacial zone in ceramic matrix composites**. *Composites Part A: Applied Science and Manufacturing*, **29**(9-10):1145–1155, 1998. 12

[37] V. Calard and J. Lamon. **A probabilistic-statistical approach to the ultimate failure of ceramic-matrix composites—part I: experimental investigation of 2D woven SiC/SiC composites**. *Composites Science and Technology*, **62**(3):385 – 393, 2002. 13

[38] A.R. Bunsell and A. Piant. **A review of the development of three generations of small diameter silicon carbide fibres**. *Journal of Materials Science*, **41**(3):823–839, 2006. 13, 15, 16, 17, 18, 60, 78, 137

[39] S. Yajima, K. Hasegawa, and T. Matsuzawa. **Development of high tensile strength silicon carbide fibre using an organosilicon polymer precursor**. *Nature*, **273**(5663):525–527, 1978. 13

[40] M.S.A. Rahaman, A.F. Ismail, and A. Mustafa. **A review of heat treatment on polyacrylonitrile fiber**. *Polymer Degradation and Stability*, **92**(8):1421 – 1432, 2007. 13

[41] N. Hochet, M. H. Berger, and A. R. Bunsell. **Microstructural evolution of the latest generation of small-diameter SiC-based fibres tested at high temperatures**. *Journal of Microscopy*, **185**(2):243–258, 1997. 16

[42] K. Kumagawa, H. Yamaoka, M. Shibuya, and T. Yamamura. **Fabrication and Mechanical Properties of New Improved Si-M-C-(O) Tyranno Fiber**. *Ceramic Engineering and Science Proceedings*, **19**(3):65–72, 1998. 17

[43] C. Sauder and J. Lamon. **Tensile Creep Behavior of SiC-Based Fibers With a Low Oxygen Content**. *Journal of the American Ceramic Society*, **90**(4):1146–1156, 2007. 18, 19, 78, 115, 116, 121, 124, 137, 141, 142

[44] D. Gosset, C. Colin, A. Jankowiak, T. Vandenberghe, and N. Lochet. **X-ray Diffraction Study of the Effect of High-Temperature Heat Treatment on the Microstructural Stability of Third-Generation SiC Fibers**. *Journal of the American Ceramic Society*, **96**(5):1622–1628, 2013. 18, 19

[45] E. Buet, C. Sauder, S. Poissonnet, P. Brender, R. Gadiou, and C. Vix-Guterl. **Influence of chemical and physical properties of the last generation of silicon carbide fibres on the mechanical behaviour of SiC/SiC composite**. *Journal of the European Ceramic Society*, **32**(3):547–557, 2012. 18, 19, 20

[46] G.S. Was and R.S. Averback. **Radiation damage using ion beams**. In R. Konings, editor, *Comprehensive Nuclear Materials*, chapter 1.07, pages 195–221. Elsevier, Oxford, 2012. 22, 24, 25, 46, 116

[47] M.J. Norgett, M.T. Robinson, and I.M. Torrens. **A proposed method of calculatind displacement dose rates**. *Nuclear Engineering and Design*, **33**:50–54, 1975. 22

[48] G.H. Kinchin and R.S. Pease. **The displacement of atoms in solids by radiation**. *Reports on Progress Physics*, **18**(1), 1955. 22

[49] J.F. Ziegler, M.D. Ziegler, and J.P. Biersack. **SRIM–The stopping and range of ions in matter (2010)**. *Nuclear Instruments and Methods in Physics Research Section B: Beam Interactions with Materials and Atoms*, **268**(11-12):1818–1823, 2010. 25, 26, 61, 117, 122

[50] L.L. Snead, S.J. Zinkle, J.C. Hay, and M.C. Osborne. **Amorphization of SiC under ion and neutron irradiation**. *Nuclear Instruments and Methods in Physics Research Section B: Beam Interactions with Materials and Atoms*, **141**(1-4):123–132, 1998. 26, 27, 30, 78, 84, 138

[51] L.L. Snead and S.J. Zinkle. **Structural relaxation of amorphous silicon carbide.** *Nuclear Instruments and Methods in Physics Research Section B: Beam Interactions with Materials and Atoms*, **191**:497–503, 2002. 26, 30, 84, 107

[52] A. Debelle, A. Boulle, A. Chartier, F. Gao, and W. J. Weber. **Interplay between atomic disorder, lattice swelling, and defect energy in ion-irradiation-induced amorphization of SiC**. *Physical Review B*, **90**:174112, 2014. 26, 75

[53] S.J. Zinkle and L.L. Snead. **Influence of irradiation spectrum and implanted ions on the amorphization of ceramics**. *Nuclear Instruments and Methods in Physics Research Section B: Beam Interactions with Materials and Atoms*, **116**(1-4):92–101, 1996. 26, 28, 78, 79

[54] S.J. Zinkle. **Radiation-Induced Effects on Microstructure**. In R. Konings, editor, *Comprehensive Nuclear Materials*, chapter 1.03, pages 65–98. Elsevier, Oxford, 2012. 26

[55] A. Debelle, L. Thomé, D. Dompoint, A. Boulle, F. Garrido, J. Jagielski, and D. Chausende. **Characterization and modelling of the ion-irradiation induced disorder in 6H-SiC and 3C-SiC single crystals**. *Journal of Physics: Applied Physics*, **43**:455408, 2010. 27

[56] W. J. Weber, L. Wang, Y. Zhang, W. Jiang, and I.-T. Bae. **Effects of dynamic recovery on amorphization kinetics in 6H-SiC**. *Nuclear Instruments and Methods in Physics Research Section B: Beam Interactions with Materials and Atoms*, **266**(12–13):2793 – 2796, 2008. 27

[57] L.L. Snead, Y. Katoh, and S. Connery. **Swelling of SiC at intermediate and high irradiation temperatures**. *Journal of Nuclear Materials*, **367-370**(2007):677–684, 2007. 28, 138

[58] Y Katoh, H Kishimoto, and a Kohyama. **The influences of irradiation temperature and helium production on the dimensional stability of silicon carbide**. *Journal of Nuclear Materials*, **307-311**:1221–1226, 2002. 29, 35, 138

[59] J. Li, L. Porter, and S. Yip. **Atomistic modeling of finite-temperature properties of crystalline β-SiC: II. Thermal conductivity and effects of point defects**. *Journal of Nuclear Materials*, **255**(2):139–152, 1998. 30

[60] L.L. Snead, S.J. Zinkle, and D.P. White. **Thermal conductivity degradation of ceramic materials due to low temperature, low dose neutron irradiation**. *Journal of Nuclear Materials*, **340**(2–3):187 – 202, 2005. 30, 31

[61] M. Satoh, Y. Nakaike, and T. Nakamura. **Solid phase epitaxy of implantation-induced amorphous layer in (1100)- and (1120)-oriented 6H-SiC**. *Journal of Applied Physics*, **89**(3):1986, 2001. 30, 84, 108

[62] I.-T. Bae, M. Ishimaru, Y. Hirotsu, and K. E. Sickafus. **Solid phase epitaxy of amorphous silicon carbide: Ion fluence dependence**. *Journal of Applied Physics*, **96**(3):1451, 2004. 107, 108

[63] M. Ishimaru, A. Hirata, M.i Naito, I.-T. Bae, Y. Zhang, and W.J. Weber. **Direct observations of thermally induced structural changes in amorphous silicon carbide**. *Journal of Applied Physics*, **104**(3):033503, 2008. 95, 107, 108

[64] T. Sawabe, M. Akiyoshi, K. Ichikawa, K. Yoshida, and T. Yano. **Microstructure of heavily neutron-irradiated SiC after annealing up to 1500 °C**. *Journal of Nuclear Materials*, **386-388**:333–337, 2009.

[65] D. Gosset, A. Audren, Y. Leconte, L. Thomé, I. Monnet, and N. Herlin-Boime. **Structural irradiation damage and recovery in nanometric silicon carbide**. *Progress in Nuclear Energy*, **57**:52–56, 2012. 30, 80, 84

[66] G. A. Newsome. **The Effect of Neutron Irradiation on Silicon Carbide Fibers**. In *Proceedings of the 21st Annual Conference on Composites, Advanced Ceramics, Materials, and StructuresA: Ceramic Engineering and Science Proceedings*, pages 579–583. John Wiley & Sons, Inc., 1997. 32, 33

[67] Y. Katoh, L. L. Snead, T. Nozawa, S. Kondo, and J. T. Busby. **Thermophysical and mechanical properties of near-stoichiometric fiber CVI SiC/SiC composites after neutron irradiation at elevated temperatures**. *Journal of Nuclear Materials*, **403**(1-3):48–61, 2010. 32, 34, 37, 38, 40, 41

[68] G.E. Youngblood, R. H. Jones, A. Kohyama, and L. L. Snead. **Radiation response of SiC-based fibers**. *Journal of Nuclear Materials*, **258-263**:1551–1556, 1998. 32, 34, 35, 78

[69] M.C. Osborne, C.R. Hubbard, L.L. Snead, and D. Steiner. **Neutron irradiation effects on the density, tensile properties and microstructural changes in Hi-Nicalon and Sylramic SiC fibers**. *Journal of Nuclear Materials*, **253**(1–3):67 – 77, 1998. 34, 35, 37, 38

[70] C.H. Henager, G.E. Youngblood, D.J. Senor, G.A. Newsome, and J.J. Woods. **Dimensional stability and tensile strength of irradiated Nicalon-CG and Hi-Nicalon fibers**. *Journal of Nuclear Materials*, **253**(1–3):60 – 66, 1998. 32, 34

[71] L.L. Snead and O.J. Schwarz. **Advanced SiC composites for fusion applications**. *Journal of Nuclear Materials*, **219**:3–14, 1995. 34, 78

[72] A. Hasegawa, S. Nogami, T. Aizawa, K. Katou, and K. Abe. **Mechanical property change and swelling behavior of SiC fiber after light-ion irradiation**. *Journal of Nuclear Materials*, **307-311**:1152–1156, 2002. 35

[73] T. Hinoki, L.L. Snead, Y. Katoh, A. Hasegawa, T. Nozawa, and A. Kohyama. **The effect of high dose/high temperature irradiation on high purity fibers and their silicon carbide composites**. *Journal of Nuclear Materials*, **311**(2002):1157–1162, 2002. 35, 36

[74] N. Chaâbane, M. Le Flem, M. Tanguy, S. Urvoy, C. Sandt, P. Dumas, and Y. Serruys. **Au ion irradiation of various silicon carbide fiber-reinforced SiC matrix composites**. *Journal of Nuclear Materials*, **439**(1-3):123–130, August 2013. 35, 78

[75] K. Shimoda and C. Colin. **Thermo-physical, -mechanical, and -electrical behaviors of ion-irradiated Tyranno-SA SiC fibers at high temperatures (1473 K)**. *Journal of Nuclear Materials*, **442**(1–3, Sup.1):376 – 379, 2013. 35, 125

REFERENCES

[76] A. Jankowiak, C. Grygiel, I. Monnet, Y. Serruys, C. Colin, S. Miro, L. Gelebart, L. Gosmain, and J.-M. Costantini. **Advanced SiC fiber strain behavior during ion beam irradiation**. *Nuclear Instruments and Methods in Physics Research Section B: Beam Interactions with Materials and Atoms*, **314**:144–148, 2013. 35, 137

[77] S. Kondo, T. Hinoki, M. Nonaka, and K. Ozawa. **Irradation-induced shrinkage of hihgly crystalline SiC fibers**. *Acta Materialia*, **83**:1–9, 2015. 35, 36, 78

[78] A.G. Perez-Bergquist, T. Nozawa, C. Shih, K.J. Leonard, L.L. Snead, and Y Katoh. **High dose neutron irradiation of Hi-Nicalon Type S silicon carbide composites, Part 1: Microstructural evaluations**. *Journal of Nuclear Materials*, **xxx**(xx):xxx–xxx, 2014. (Article in press). 36

[79] R.H. Jones, L. Giancarli, A. Hasegawa, Y. Katoh, A. Kohyama, B. Riccardi, L.L. Snead, and W.J. Weber. **Promise and challenges of SiCf/SiC composites for fusion energy applications**. *Journal of Nuclear Materials*, **307-311**:1057–1072, December 2002. 39, 40

[80] Y. Katoh, T. Nozawa, C. Shih, K. Ozawa, T. Koyanagi, W. Portera, and L. L. Snead. **High-dose neutron irradiation of Hi-Nicalon Type S silicon carbide composites. Part 2: Mechanical and physical properties**. *Journal of Nuclear Materials*, **xxx**(xx):xxx–xxx, 2015. (Article in press). 40, 41

[81] Y.M. Tairov and V.F. Tsvetkov. **Investigation of growth processes of ingots of silicon carbide single crystals**. *Journal of Crystal Growth*, **43**(2):209–212, 1978. 45

[82] Y. Serruys, P. Trocellier, S. Miro, E. Bordas, M.O. Ruault, O. Kaïtasov, S. Henry, O. Leseigneur, Th. Bonnaillie, S. Pellegrino, S. Vaubaillon, and D. Uriot. **JANNUS: A multi-irradiation platform for experimental validation at the scale of the atomistic modelling**. *Journal of Nuclear Materials*, **386-388**:967–970, 2009. 46, 47, 48

[83] L. Beck, Y. Serruys, S. Miro, P. Trocellier, E. Bordas, F. Lepretre, D. Brimbal, T. Loussouarn, H. Martin, S. Vaubaillon, S. Pellegrino, and D. Bachiller-Perea. **Ion irradiation and radiation effect characterization at the JANNUS-Saclay triple beam facility**. *Journal of Materials Research*, **30**:1183–1194, 2015. 46, 48

[84] **Ganil webpage: http://www.ganil-spiral2.eu**. 48

[85] A.C.C. Villari, C. Eleon, R. Alves-Condé, J.C. Angelique, C. Barué, C. Canet, M. Dubois, M. Dupuis, J.L. Flambard, G. Gaubert, P. Jardin, N. Lecesne, P. Leherissier, F. Lemagnen, R. Leroy, L. Maunoury, J.Y. Pacquet, F. Pellemoine, M.G. Saint-Laurenta, C. Stodel, and J.C. Thomas. **SPIRAL at GANIL: Latest Results and Plans for the Future**. *Nuclear Physics A*, **787**:126c–133c, 2007. 49

[86] **Interactive chart of available nuclei at GANIL**. 49

[87] F. Loyer. **Projet IRRSUD-Rapport de fin de projet**, 2002. 49

[88] Image credits to Eric Jensen under CC BY 2.5. **Transmission Electron Microscope System**. 55

[89] H.-H. Jin, C. Shin, and J Kwon. **Fabrication of a TEM sample of ion-irradiated material using focused ion beam microprocessing and low-energy Ar ion milling**. *Journal of Electron Microscopy*, **59**(6):463–468, 2010. 55

[90] D. J. Stokes. **Recent advances in electron imaging, image interpretation and applications: environmental scanning electron microscopy**. *Philosophical Transactions of the Royal Society of London A: Mathematical, Physical and Engineering Sciences*, **361**(1813):2771–2787, 2003. 57

[91] R. Podor, D. Pailhon, H.P. Brau, and J. Ravaux. **Sample holder with integrated thermocouple**, 2013. 57

[92] Image credits to Eric Jensen under CC BY 2.5. **Scanning Electron Microscope System**. 58

[93] Y. Katoh, L.L. Snead, I. Szlufarska, and W.J. Weber. **Radiation effects in SiC for nuclear structural applications**. *Current Opinion in Solid State and Materials Science*, **16**(3):143–152, 2012. 60

[94] Y. Zhang, T. Varga, M. Ishimaru, P.D. Edmondson, H. Xue, P. Liu, S. Moll, F. Namavar, C. Hardiman, S. Shannon, and W.J. Weber. **Competing effects of electronic and nuclear energy loss on microstructural evolution in ionic-covalent materials**. *Nuclear Instruments and Methods in Physics Research Section B: Beam Interactions with Materials and Atoms*, **327**:33–43, 2014. 61, 75, 139

[95] R. Devanathan and W.J. Weber. **Displacement energy surface in 3C and 6H SiC**. *Journal of Nuclear Materials*, **278**(2-3):258–265, April 2000. 61

[96] C.A. Schneider, W.S. Rasband, and K.W. Eliceiri. **NIH Image to ImageJ: 25 years of image analysis**. *Nat Meth*, **9**(7):671–675, 2012. 62, 85

[97] P. Colomban, G. Gouadec, and L. Mazerolles. **Raman analysis of materials corrosion: the example of SiC fibers**. *Materials and Corrosion*, **53**(5):306–315, May 2002. 62, 63, 65

[98] S. Nakashima and H. Harima. **Raman Investigation of SiC Polytypes**. *physica status solidi (a)*, **162**(1):39–64, 1997. 62, 63

[99] S. Sorieul, J.-M. Costantini, L. Gosmain, L. Thomé, and J.-J. Grob. **Raman spectroscopy study of heavy-ion-irradiated α-SiC**. *Journal of Physics: Condensed Matter*, **18**(22):5235–5251, 2006. 66, 75, 76

[100] S. Miro, J.-M. JM Costantini, S. Sorieul, L. Gosmain, and L. Thomé. **Recrystallization of amorphous ion-implanted silicon carbide after thermal annealing**. *Philosophical Magazine Letters*, **92**(11):633–639, 2012. 63, 101

[101] G. Gouadec and P. Colomban. **Raman Spectroscopy of nanomaterials: How spectra relate to disorder, particle size and mechanical properties**. *Progress in Crystal Growth and Characterization of Materials*, **53**(1):1–56, March 2007. 63

[102] M. Havel and P. Colomban. **Rayleigh and Raman images of the bulk/surface nanostructure of SiC based fibres**. *Composites Part B: Engineering*, **35**(2):139–147, 2004. 63

[103] L.G. Cançado, K. Takai, T. Enoki, M. Endo, Y.A. Kim, H. Mizusaki, A. Jorio, L.N. Coelho, R. Magalhaes-Paniago, and M. A. Pimenta. **General equation for the determination of the crystallite size La of nanographite by Raman spectroscopy**. *Applied Physics Letters*, **88**(16):163106, 2006. 65

[104] F. Tuinstra and J.L. Koenig. **Raman Spectrum of Graphite**. *The Journal of Chemical Physics*, **53**(3):1126, 1970. 65

[105] D.S. Knight and W.B. White. **Characterization of diamond films by Raman spectroscopy**. *Journal of Materials Research*, **4**(02):385–393, 1989. 65

[106] J. Jagielski and L. Thomé. **Damage accumulation in ion-irradiated ceramics**. *Vacuum*, **81**(10):1352–1356, 2007. 69

[107] A. Audren, I. Monnet, Y. Leconte, X. Portier, L. Thomé, M. Levalois, N. Herlin-Boime, and C. Reynaud. **Structural evolution of SiC nanostructured and conventional ceramics under irradiation**. *Nuclear Instruments and Methods in Physics Research Section B: Beam Interactions with Materials and Atoms*, **266**(12-13):2806–2809, June 2008. 75, 139

[108] L. Thomé, A. Debelle, F. Garrido, S. Mylonas, B. Décamps, C. Bachelet, G. Sattonnay, S. Moll, S. Pellegrino, S. Miro, P. Trocellier, Y. Serruys, G. Velisa, C. Grygiel, I. Monnet, M. Toulemonde, P. Simon, J. Jagielski, I. Jozwik-Biala, L. Nowicki, M. Behar, W.J. Weber, Y. Zhang, M. Backman, K. Nordlund, and F. Djurabekova. **Radiation effects in nuclear materials: Role of nuclear and electronic energy losses and their synergy**. *Nuclear Instruments and Methods in Physics Research Section B: Beam Interactions with Materials and Atoms*, **307**:43–48, 2013. 75, 139

[109] G. Gouadec, L. Bellot-Gurlet, D. Baron, and Ph. Colomban. **Raman Mapping for the Investigation of Nano-phased Materials**. In Arnaud Zoubir, editor, *Raman Imaging*, **168** of *Springer Series in Optical Sciences*, pages 85–118. Springer Berlin Heidelberg, 2012. 75

[110] H. Abe, H. Naramoto, A. Iwase, and C. Kinoshita. **Effect of damage cascades on the irradiation-induced amorphization in graphite**. *Nuclear Instruments and Methods in Physics Research Section B: Beam Interactions with Materials and Atoms*, **127-128**:681–684, May 1997. 76

[111] Y. Zhang, I.-T. Bae, K. Sun, C. Wang, M. Ishimaru, Z. Zhu, W. Jiang, and W.J. Weber. **Damage profile and ion distribution of slow heavy ions in compounds**. *Journal of Applied Physics*, **105**(10):104901, 2009. 78

[112] K. Jin, Y. Zhang, H. Xue, Z. Zhu, and W.J. Weber. **Ion distribution and electronic stopping power for Au ions in silicon carbide**. *Nuclear Instruments and Methods in Physics Research Section B: Beam Interactions with Materials and Atoms*, **307**:65–70, 2013. 78

[113] W. Jiang, Y. Zhang, and W.J. Weber. **Temperature dependence of disorder accumulation and amorphization in Au-ion-irradiated 6H-SiC**. *Physical Review B*, **70**(16):165208, 2004. 78

[114] S. Pellegrino, L. Thomé, A. Debelle, S. Miro, and P. Trocellier. **Radiation effects in carbides: TiC and ZrC versus SiC**. *Nuclear Instruments and Methods in Physics Research Section B: Beam Interactions with Materials and Atoms*, **327**:103–107, 2014. 78

[115] W.J. Weber, N. Yu, L.M. Wang, and N.J. Hess. **Temperature and dose dependence of ion-beam-induced amorphization in α-SiC**. *Journal of Nuclear Materials*, **244**(3):258–265, 1997. 78, 138

[116] W.G. Wolfer. **Fundamental properties of defects in metals**. In *Comprehensive Nuclear Materials*, chapter 1.07, pages 1–45. Elsevier, 2012. 79

[117] T.D. Shen. **Radiation tolerance in a nanostructure: Is smaller better?** *Nuclear Instruments and Methods in Physics Research Section B: Beam Interactions with Materials and Atoms*, **266**(6):921–925, 2008. 79

[118] M. Rose, A.G. Balogh, and H. Hahn. **Instability of irradiation induced defects in nanostructured materials**. *Nuclear Instruments and Methods in Physics Research Section B: Beam Interactions with Materials and Atoms*, **127/128**:119–122, 1997. 79

[119] Y. Chimi, A. Iwase, N. Ishikawa, M. Kobiyama, T. Inami, and S. Okuda. **Accumulation and recovery of defects in ion-irradiated nanocrystalline gold**. *Journal of Nuclear Materials*, **297**(3):355–357, September 2001.

[120] N. Nita, R. Schaeublin, and M. Victoria. **Impact of irradiation on the microstructure of nanocrystalline materials**. *Journal of Nuclear Materials*, **329-333**:953–957, 2004.

[121] A.R. Kilmametov, D.V. Gunderov, R.Z. Valiev, A.G. Balogh, and H. Hahn. **Enhanced ion irradiation resistance of bulk nanocrystalline TiNi alloy**. *Scripta Materialia*, **59**(10):1027–1030, 2008. 79

[122] F. Djurabekova, M. Backman, O.H. Pakarinen, K. Nordlund, L.L. Araujo, and M.C. Ridgway. **Amorphization of Ge nanocrystals embedded in amorphous silica under ion irradiation**. *Nuclear Instruments and Methods in Physics Research Section B: Beam Interactions with Materials and Atoms*, **267**(8-9):1235–1238, May 2009. 79

[123] A. Meldrum, L.A. Boatner, and R.C. Ewing. **Size effects in the irradiation-induced crystalline-to-amorphous transformation**. *Nuclear Instruments and Methods in Physics Research Section B: Beam Interactions with Materials and Atoms*, **207**(1):28–35, 2003. 79

[124] W. Jiang, H. Wang, I. Kim, I.-T. Bae, G. Li, P. Nachimuthu, Z. Zhu, Y. Zhang, and W. Weber. **Response of nanocrystalline 3C silicon carbide to heavy-ion irradiation**. *Physical Review B*, **80**(16):161301, 2009. 79, 80, 84

[125] W. Jiang, H. Wang, I. Kim, Y. Zhang, and W.J. Weber. **Amorphization of nanocrystalline 3C-SiC irradiated with Si ions**. *Journal of Materials Research*, **25**(12):2341–2348, 2010. 80

REFERENCES

[126] W. Jiang, L. Jiao, and H. Wang. **Transition from Irradiation-Induced Amorphization to Crystallization in Nanocrystalline Silicon Carbide**. *Journal of the American Ceramic Society*, **94**(12):4127–4130, 2011. 80

[127] L. Jamison, P. Xu, K. Shrindharan, and T. Allen. **Advances in Materials Science for Environmental and Nuclear Technology II**. pages 161–168. John Wiley & Sons, Inc., Hoboken, NJ, USA, 2011. 80

[128] N. Swaminathan, D. Morgan, and I. Szlufarska. **Role of recombination kinetics and grain size in radiation-induced amorphization**. *Physical Review B*, **86**(21):214110, 2012. 80

[129] I.J. Beyerlein, A. Caro, M.J. Demkowicz, N.A. Mara, A. Misra, and B.P. Uberuaga. **Radiation damage tolerant nanomaterials**. *Materials Today*, **16**(11):443–449, November 2013. 80

[130] E. Jin, L.S. Niu, E. Lin, and X. Song. **Grain boundary effects on defect production and mechanical properties of irradiated nanocrystalline SiC**. *Journal of Applied Physics*, **111**(10):104322, 2012. 80

[131] N. Swaminathan, P.J. Kamenski, D. Morgan, and I. Szlufarska. **Effects of grain size and grain boundaries on defect production in nanocrystalline 3C-SiC**. *Acta Materialia*, **58**(8):2843–2853, 2010.

[132] N. Swaminathan, M. Wojdyr, D.D. Morgan, and I. Szlufarska. **Radiation interaction with tilt grain boundaries in β-SiC**. *Journal of Applied Physics*, **111**(5):054918, 2012. 80

[133] F. Gao, W.J. Weber, M. Posselt, and V. Belko. **Atomistic study of intrinsic defect migration in 3C-SiC**. *Physical Review B*, **69**(24):245205, June 2004. 80

[134] Y. Zhang, M. Ishimaru, T. Varga, T. Oda, C. Hardiman, H. Xue, Y. Katoh, S. Shannon, and W.J. Weber. **Nanoscale engineering of radiation tolerant silicon carbide.** *Physical chemistry chemical physics*, **14**(38):13429–36, 2012. 81

[135] L. Jamison, M.-J. Zheng, S. Shannon, T. Allen, D. Morgan, and I. Szlufarska. **Experimental and ab initio study of enhanced resistance to amorphization of nanocrystalline silicon carbide under electron irradiation**. *Journal of Nuclear Materials*, **445**(1-3):181–189, 2014. 81

[136] A.N. Kolmogorov. **A statistical theory for the recrystallisation of metals**. *Akad. Nauk. SSSR. Izv., Ser. Matem.*, **335**:1, 1937. 89, 104

[137] W.A. Johnson and R.F. Mehl. **Reaction Kinetics in Processes of Nucleation and Growth**. *Transactions of the American Institute of Mining, Metallurgical, and Petroleum Engineers*, **135**:416–418, 1939.

[138] M. Avrami. **Kinetics of Phase Change. I General Theory**. *Journal of Chemical Physics*, **7**(12):1103–1112, 1939.

[139] M. Avrami. **Kinetics of Phase Change. II Transformation-Time Relations for Random Distribution of Nuclei**. *The Journal of Chemical Physics*, **8**(2):212–224, 1940.

[140] M. Avrami. **Granulation, Phase Change, and Microstructure Kinetics of Phase Change. III**. *The Journal of Chemical Physics*, **9**(2):177–184, 1941. 89, 104

[141] Z. Czigany and L. Hultman. **Interpretation of electron diffraction patterns from amorphous and fullerene-like carbon allotropes**. *Ultramicroscopy*, **110**(7):815 – 819, 2010. 100

[142] E. Woldt. **The relationship between isothermal and non-isothermal description of Johnson-Mehl-Avrami-Kolmogorov kinetics**. *Journal of Physics and Chemistry of Solids*, **53**(4):521–527, 1992. 104

[143] G. Ruitenberg, E. Woldt, and A.K. Petford-Long. **Comparing the JohnsonMehlAvramiKolmogorov equations for isothermal and linear heating conditions**. *Thermochimica Acta*, **378**(1–2):97–105, 2001. 104, 105

[144] C.J.M Denissen, J. Liebe, and M. Van Rijswick. **Recrystallisation temperature of tungsten as a function of the heating ramp**. *International Journal of Refractory Metals and Hard Materials*, **24**(4):321–324, 2006. 105

[145] A. Nazari and J.G. Sanjayan. **Johnson-Mehl-Avrami-Kolmogorov equation for prediction of compressive strength evolution of geopolymer**. *Ceramics International*, **41**:3301–3304, 2015. 105

[146] H.G. Bohn, J.M. Williams, C.J. McHargue, and G.M. Begun. **Recrystallization of ion-implanted α-SiC**. *Journal of Materials Research*, **2**(1):107–116, 1987. 107

[147] S. Harada, M. Ishimaru, T. Motooka, T. Nakata, T. Yoneda, and M. Inoue. **Recrystallization of MeV Si implanted 6H-SiC**. *Applied Physics Letters*, **69**(23):3534, 1996. 107, 108, 109, 158

[148] Daniel D. Osterberg, John Youngsman, Rick Ubic, Ivar E. Reimanis, and Darryl P. Butt. **Recrystallization Kinetics of 3C Silicon Carbide Implanted with 400 keV Cesium Ions**. *Journal of the American Ceramic Society*, **96**(10):3290–3295, 2013. 108, 109

[149] P. Pirouz and J. W. Yang. **Polytypic transformations of SiC: the role of TEM**. *Ultramicroscopy*, **51**:189–214, 1993. 108

[150] M. Diani, L. Simon, L. Kubler, D. Aubel, B. Matko, B. Chenevier, R. Madar, and M. Audier. **Crystal growth of 3C-SiC polytype on 6H-SiC (0001) substrate**. *Journal of Crystal Growth*, **235**:95–102, 2002. 109

[151] A.G. Evans and Hutchinsonm J.W. **The thermomechanical integrity of thin films and multilayers**. *Acta Metallurgica et Materialia*, **43**(7):2507 – 2530, 1995. 109, 110, 111

[152] M.F. Ashby and S.D. Hallam. **The failure of brittle solids containing small cracks under compressive stress states**. *Acta Metallurgica*, **34**(3):497 – 510, 1986. 109, 110

[153] V. Fidleris. **The irradiation creep and growth phenomena**. *Journal of Nuclear Materials*, **159**(0):22 – 42, 1988. 114

[154] A. Soniak, N. L'hullier, JP. Mardon, V. Rebeyrolle, P. Bouffioux, and Ch. Bernaudat. **Irradiation creep behavior of Zr-base alloys**. In *Zirconium in the nuclear industry*. ASTM International, US., 2002.

[155] W. Schüle and H. Hausen. **Neutron irradiation creep in stainless steel alloys**. *Journal of Nuclear Materials*, **212–215, Part 1**(0):388 – 392, 1994.

[156] J.R. Matthews and M.W. Finnis. **Irradiation creep models: an overview**. *Journal of Nuclear Materials*, **159**(0):257 – 285, 1988. 114, 142

[157] Mark A Davies and Mark Bradford. **A revised description of graphite irradiation induced creep**. *Journal of Nuclear Materials*, **381**(12):39–45, 2008. 114

[158] Timothy D. Burchell. **Irradiation induced creep behavior of H-451 graphite**. *Journal of Nuclear Materials*, **381**(1-2):46–54, October 2008.

[159] Xiang Fang, Haitao Wang, Suyuan Yu, and Chenfeng Li. **The various creep models for irradiation behavior of nuclear graphite**. *Nuclear Engineering and Design*, **242**:19–25, January 2012. 114

[160] R.J. Price. **Properties of Silicon Carbide for nuclear fuel particle coatings**. *Nuclear Technology*, **35**(2):320–336, 1977. 114, 137, 141

[161] Zhiyong Zhu and Peter Jung. **Dimensional changes of Al2O3 and SiC, proton irradiated under tensile stress**. *Journal of Nuclear Materials*, **212-215**:1081–1086, 1994. 131

[162] Vani Shankar and Gary S. Was. **Proton irradiation creep of beta-silicon carbide**. *Journal of Nuclear Materials*, **418**(1-3):198–206, 2011. 131, 137, 141

[163] Y. Katoh, L.L. Snead, C.H. Henager, A Hasegawa, A Kohyama, B. Riccardi, and H. Hegeman. **Current status and critical issues for development of SiC composites for fusion applications**. *Journal of Nuclear Materials*, **367-370**(2007):659–671, 2007. 131, 137

[164] S. Kondo, T. Koyanagi, and T. Hinoki. **Irradiation creep of 3C–SiC and microstructural understanding of the underlying mechanisms**. *Journal of Nuclear Materials*, **448**(1):487–496, 2014. 114

[165] R Scholz. **Deuteron irradiation creep of chemically vapor deposited silicon carbide fibers**. *Journal of Nuclear Materials*, **254**(1):74–77, 1998. 114, 129, 131, 137, 141

[166] T. Koyanagi, K. Ozawa, T. Hinoki, and L.L. Snead. **Irradiation creep of near-stoichiometric SiC fibers**. *Unpublished*, 2014. 114, 131, 137, 141

[167] C.H. Henager Jr, C. Lewinsohn, and R. H. Jones. **Subcritical crack growth in CVI SiC_f/SiC composites at elevated temperatures: effect of fiber creep rate**. *Acta Materialia*, **49**:3727–3738, 2001. 114

[168] **Chart of Nuclides**. 116

[169] G. Farwell, E. Segre, and C. Wiegand. **Long Range Alpha-Particles Emitted in Connection with Fission. Preliminary Report**. *Physical Review*, **71**:327–330, Mar 1947. 116

[170] L. Gélébart, C. Colin, P. Trocellier, and Y. Serruys. **Étude des possibilités d'irradiation de fibres SiC sur MécaSiC/JANNUS**. *Document Technique DMN*, pages DMN/SRMA/LC2M/NT/2007–2865/A, 2007. 122

[171] Y. Katoh, L.L. Snead, and S. Golubov. **Analyzing irradiation-induced creep of silicon carbide**. *Mechanical Properties and Performance of Engineering Ceramics and Composites III*, pages 297–306, 2007. 129, 139

[172] J. Huguet-Garcia, A. Jankowiak, S. Miro, Y. Serruys, and J.-M. Costantini. **Ion irradiation effects on third generation SiC fibers in elastic and inelastic energy loss regimes**. *Nuclear Instruments and Methods in Physics Research Section B: Beam Interactions with Materials and Atoms*, **327**:93–98, 2014. 137

[173] G. Morscher and J.A. DiCarlo. **A Simple Test for Thermomechanical Evaluation of Ceramic Fibers**. *Journal of the American Ceramic Society*, **75**(1):136–140, 1992. 137

[174] J. Huguet-Garcia, A. Jankowiak, S. Miro, D. Gosset, Y. Serruys, and J.-M. Costantini. **Study of the Ion-Irradiation Behavior of Advanced SiC Fibers by Raman Spectroscopy and Transmission Electron Microscopy**. *Journal of the American Ceramic Society*, **98**(2):675–682, 2015. 138

[175] H. Zang, D. Guo, T. Shen, C. He, Z. Wang, L. Pang, C. Yao, and T. Yang. **Investigation of swelling induced by heavy ion and neutron irradiation in SiC**. *Journal of Nuclear Materials*, **433**(1-3):378–381, 2013. 138

[176] A. Debelle, M. Backman, L. Thomé, K. Nordlund, F. Djurabekova, W.J. Weber, I. Monnet, O.H. Pakarinen, F. Garrido, and F. Paumier. **Swift heavy ion induced recrystallization in cubic silicon carbide: New insights from designed experiments and MD simulations**. *Nuclear Instruments and Methods in Physics Research Section B: Beam Interactions with Materials and Atoms*, **326**:326–331, May 2014. 139

[177] M. Backman, M. Toulemonde, O.H. Pakarinen, N. Juslin, F. Djurabekova, K. Nordlund, A. Debelle, and W.J. Weber. **Molecular dynamics simulations of swift heavy ion induced defect recovery in SiC**. *Computational Materials Science*, **67**:261–265, February 2013.

[178] S. Sorieul, X. Kerbiriou, J.-M. Costantini, L. Gosmain, G. Calas, and C. Trautmann. **Optical spectroscopy study of damage induced in 4H-SiC by swift heavy ion irradiation**. *Journal of Physics: Condensed Matter*, **24**(12):125801, 2012. 139

[179] S. Zhu, M. Mizuno, Y. Kagawa, J. Cao, Y. Nagano, and H. Kaya. **Creep and fatigue behavior of SiC fiber reinforced SiC composite at high temperatures**. *Materials Science and Engineering: A*, **225**(1-2):69–77, 1997. 141

[180] T. Koyanagi, K. Shimoda, S. Kondo, T. Hinoki, K. Ozawa, and Y. Katoh. **Irradiation creep of nano-powder sintered silicon carbide at low neutron fluences**. *Journal of Nuclear Materials*, **455**(1-3):73–80, 2014. 142

REFERENCES

[181] H. Trinkaus. **Local stress relaxation in thermal spikes as a possible cause for creep and macroscopic stress relaxation of amorphous solids under irradiation**. *Journal of nuclear materials*, **223**:196–201, 1995. 143

[182] H. Trinkaus. **Thermal spike model for irradiation creep of amorphous solids: Comparison to experimental data for ion irradiated vitreous silica**. *Journal of Nuclear Materials*, **246**(2-3):244–246, 1997.

[183] W. Dienst. **Irradiation induced creep of ceramic nuclear fuels**. *Journal of Nuclear Materials*, **65**:1–8, March 1977. 143

Appendix A

Table of interplanar spacings of 3C- and 6H-SiC structures

Table A.1: 3C-SiC interplanar spacings for crystal structure identification

h	k	l	2θ [°]	d [Å]	I [rel.]	F(hkl)
1	1	1	35.647	2.51661	100	41.35
2	0	0	41.395	2.17945	18.07	23.95
2	2	0	59.978	1.5411	46.06	41.13
3	1	1	71.763	1.31426	34.94	30.66
2	2	2	75.493	1.25831	5.01	21.08
4	0	0	89.962	1.08973	7.54	33.62
3	3	1	100.761	1	17.23	25.86
4	2	0	104.429	0.97468	8.3	17.82
4	2	2	119.935	0.88976	26.36	28.98

A. TABLE OF SIC INTERPLANAR SPACINGS

Table A.2: 6H-SiC interplanar spacings for crystal structure identification

h	k	l	2θ [°]	d [Å]	I [rel.]	F(hkl)
0	0	4	23.561	3.773	21.37	22.46
1	0	0	33.56	2.66822	5.89	9.92
1	0	1	34.096	2.62748	31.93	16.62
1	0	2	35.662	2.51559	100	30.88
0	0	6	35.666	2.51533	34.35	44.34
1	0	3	38.148	2.35719	12.11	11.57
1	0	4	41.414	2.17851	18.21	15.55
1	0	5	45.327	1.99911	6.77	10.49
0	0	8	48.199	1.8865	2.66	17.29
1	0	6	49.778	1.83027	3.64	8.55
1	0	7	54.689	1.67697	13.76	18.52
1	1	0	60.004	1.5405	34.07	45.76
1	0	8	60.009	1.54038	25.04	27.74
1	1	2	61.374	1.50937	7.7	15.77

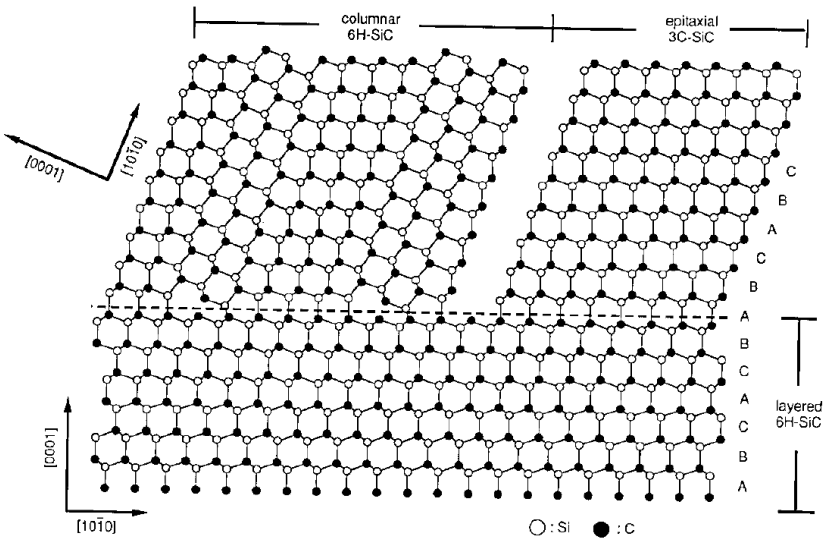

Figure A.1: Atomic model for 3C-SiC solid phase epitaxial growth - Proposed by Harada et al.[147] after their observations of recrystallization of ion-amorphized 6H-SiC.

Appendix B

Estimation of the cross-sectional damage profile of SiC fibers

A simple script using Python 2.7 has been developed in order to simulate the damage cross section of a SiC fiber submitted to ion irradiation with or without the energy degrader. The code takes advantage of the possibility of running SRIM-2013 automatically in batch mode. A detailed description on how to use it is available in SRIM documentation. It is divide in three main parts. First, the estimation of the SiC thickness that an ion will have to cross as a function entry point position with respect to the fiber axis and the creation of the input files for SRIM-2013. Secondly, the calculation of the different damage profile for each SiC and *Al* thick foils using SRIM-2013 in batch mode, and thirdly, the reconstruction of the cross section damage profile in a of a x, y, z file for the plot of the results. Here, map plot is performed with gnuplot for the sake of the manuscript graphical homogeneity though *matplotlib* python package could also be used with this purpose.

In order to run SRIM in batch mode, two input files are needed, one containing the discretized values of the fiber cross section and the other the thicknesses of the *Al* foils. Given the radius of the fiber, SiC thicknesses are given by Eq. B.1:

$$e_{SiC}(y) = 2\sqrt{r^2 - y^2} \tag{B.1}$$

Where r is the fiber radius and y is the vertical distance from the center of the fiber cross section.

```
import os
import numpy as np
import math

###
# Returns the input file for SRIM-2013 calculation in auto mode
#given an Al and SiC thickness
###

def InitTRIMIN(Al_Thick,SiC_Thick):
        with open('TRIM.IN', 'r') as file:
            data=file.readlines()
        #Plot Type (5=no plot), Min_plot,Max_plot
        data[10]='5 '+str(Al_Thick)+' '+str(SiC_Thick+Al_Thick)+'\n'
        #Al layer
        data[17]='1 "Al" '+str(Al_Thick)+' 2.702 1 0 0\n'
        #SiC layer
        data[18]='2 "SiC" '+str(SiC_Thick)+' 3.21 0 .5 .5\n'
        with open('TRIM.IN','w') as file:
            file.writelines(data)

###
#  Moves the SRIM output files of each calculation to dedicated folders
###

def MoveFilesToFolder(Path):
    os.rename('LATERAL.txt',Path+'/LATERAL.txt')
    os.rename('IONIZ.txt',Path+'/IONIZ.txt')
    os.rename('E2RECOIL.txt',Path+'/E2RECOIL.txt')
    os.rename('NOVAC.txt',Path+'/NOVAC.txt')
    os.rename('PHONON.txt',Path+'/PHONON.txt')
    os.rename('RANGE.txt',Path+'/RANGE.txt')
    os.rename('TDATA.txt',Path+'/TDATA.txt')
    os.rename('VACANCY.txt',Path+'/VACANCY.txt')

###
# Changes commas to points of SRIM output files
###
def CommaToPoint(file):
    with open(file,'r') as f:
        data=[]
        for line in f:
            data.append(line.replace(',','.'))
     with open(file,'w') as f:
        f.writelines(data)
```

```
###
#  Returns the input file with the discretized thicknesss of SiC
###

def writeSiCthickness(a):
    with open('SiC_Thickness','w') as f:
        for i in a:
            f.write(str(i)+'\n')

# Opens the file containing the Al thicknesses for the energy degrader
Al_thick=np.loadtxt('FiberDpa\init_Al.txt',dtype=int)

# Opens the file containing the SiC fiber diameter
Fiber_Diam=np.loadtxt('FiberDpa\init_SiC.txt')

# Calculation of the y values for cross section discretization
d=np.linspace(0,int(Fiber_Diam/2),num=15,endpoint=False)

# Calculation of the SiC thickness as a function of y
TRIM_SiCthicknes=[]
for i in range(np.size(d)):
    TRIM_SiCthicknes.append(int(round(math.sqrt(math.pow(Fiber_Diam/2,2)
    -math.pow(d[i],2))*2)))

# Initialization of the SRIM input file
writeSiCthickness(TRIM_SiCthicknes)

###
#  SRIM run in batch mode with the initialized input files
###
for i in range(np.size(Al_thick)):
    if not os.path.exists('FiberDpa/FiberDpa_Output/Al-'+str(Al_thick[i])):
        os.mkdir('FiberDpa/FiberDpa_Output/Al-'+str(Al_thick[i]))
    for j in range(np.size(TRIM_SiCthicknes)):
        Path='FiberDpa/FiberDpa_Output/Al-'+str(Al_thick[i])+'/SiC-'
        +str(TRIM_SiCthicknes[j])
        if not os.path.exists(Path):
            os.mkdir(Path)
        InitTRIMIN(Al_thick[i],TRIM_SiCthicknes[j])
        os.system("TRIM.exe")
        CommaToPoint('VACANCY.txt')
        CommaToPoint('IONIZ.txt')
        MoveFilesToFolder(Path)
```

```
###
# Reconstruction of the fiber cross section and
# creation of the xyz file for gnuplot
###
SiC_Thickness=np.loadtxt('SiC_Thickness',dtype=int)
All=[]
All_Neg=[]
for i in range(np.size(SiC_Thickness)):
    vac=np.zeros(100,)
    for j in Al_thick:
        Path='FiberDpa/FiberDpa_Output/Al-'+str(j)+'/SiC-' + str(SiC_Thickness[i])
        +'/VACANCY.txt'
        Si_Vac,C_Vac=np.loadtxt(Path,skiprows=35,comments='T',
        usecols=(3,4),unpack=True)
        vac+=(Si_Vac+C_Vac)
    Path='FiberDpa/FiberDpa_Output/Al-0/SiC-'+str(SiC_Thickness[i])
    + '/VACANCY.txt'
    e_SiC=np.loadtxt(Path,skiprows=35,comments='T',usecols=(0,))
    Origin=(SiC_Thickness[0]-SiC_Thickness[i])/2
    x=e_SiC+Origin
    y=np.zeros(100)+d[i]
    z=vac/np.size(Al_thick)
    Mean_Vac=np.array([x,y,z])
    Mean_Vac_Neg=np.array([x,-1*y,z])
    All.append(np.transpose(Mean_Vac))
    All_Neg.append(np.transpose(Mean_Vac_Neg))

All=np.array(All)
All_Neg=np.array(All_Neg)
Stack=np.vstack((All,All_Neg))
with open('FiberDpa/VacFileForGnuplot/VacIonFile-Xe92MeV-ED-75000.txt','w') as file:
    file.write('#e_SiC    y_SiC    Vac/ion/A \n')
    for i in range(np.size(Stack[:,0,0])):
        np.savetxt(file,Stack[i,:,:])
        file.write('\n')
```

Appendix C

Résumé: principaux résultats de la thèse

Caractérisation *in situ* et *ex situ* des effets d'irradiation dans les fibres de SiC de troisième génération

Résumé du manuscrit de thèse présenté par J. Huguet-Garcia pour l'obtention du titre de Docteur de l'Université Pierre et Marie Curie.

1. Introduction

Les composites céramiques SiC_f/SiC_m, font partie des matériaux les plus prometteurs pour les applications nucléaires du futur.[1] La Figure 1 montre un exemple de l'utilisation de ce type de matériau pour des concepts avancés de gaines de combustible nucléaire. La tenue sous irradiation de ces composites à matrice céramique est fortement liée au type de fibre utilisé comme renfort. Les composites SiC renforcés des fibres de SiC de première et deuxième génération (Tyranno, Nicalon et Hi-Nicalon) se sont révélés instables sous irradiation. En effet, ces fibres souffrent de variations dimensionnelles importantes par rapport à la matrice CVI-SiC en raison de leur teneur significative en phase vitreuse Si-O-C et d'une non-stœchiométrie induisant la dégradation des propriétés mécaniques du composite.[2]

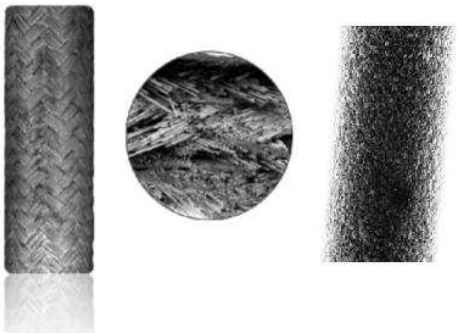

Fig. 1. Gaines de combustible nucléaire en composite SiC_f/SiC_m, détail du tressage et d'une fibre de SiC de troisième génération (Tyranno SA3)

Le développement continu des fibres de SiC a finalement donné lieu à l'apparition des fibres de SiC de troisième génération (Fig. 1). Les fibres Hi Nicalon S (HNS) et Tyranno SA3 (TSA3) sont caractérisées par leur haute cristallinité, leur bonne stœchiométrie et sont considérées comme utilisables pour des applications nucléaires. Sous irradiation, elles présentent un comportement similaire à celui de la matrice CVI-SiC du composite ce qui permet de préserver les propriétés mécaniques du composite.[2] Néanmoins, malgré les progrès substantiels des composites SiC depuis l'apparition des fibres SiC de troisième génération, il est encore nécessaire d'approfondir les connaissances sur leur comportement sous irradiation.

L'objectif général de ce travail a été d'acquérir de nouvelles connaissances dans le comportement des fibres de SiC de troisième génération sous irradiation à des températures d'irradiation pertinentes pour les applications visées. Pour cela, des fibres HNS et TSA3 ont été irradiées sur plusieurs plateformes d'irradiation aux ions. Ces installations permettent un ajustement fin des conditions d'irradiation afin de reproduire les conditions de dose et de température auxquelles ces fibres pourraient être exposées dans un réacteur nucléaire. L'une des principales applications envisagées est une gaine tolérante en situation accidentelle pour le parc nucléaire REP (Réacteur à Eau Pressurisée) actuel. Cette application implique l'exposition à

l'irradiation dans une gamme de température (de la température ambiante (T_a) à 300 °C) où le SiC est susceptible de s'amorphiser. Par conséquent, les premiers travaux ont porté sur l'étude du processus d'amorphisation de fibres de SiC, ainsi que les effets des recuits thermiques sur des échantillons amorphes. D'autre part, les réacteurs nucléaires refroidis à gaz (GFR) tout comme les réacteurs de fusion impliqueront des irradiations à des températures nominales élevées situées entre 600 °C à 1000 °C.[1] À ces températures l'amorphisation du SiC est impossible. Les travaux ont donc été orientés vers l'étude de l'impact de l'irradiation sur les propriétés mécaniques des fibres. En effet, en utilisant une machine de traction dédiée, le phénomène de fluage d'irradiation a pu être caractérisé de façon *in situ*. Ce phénomène implique la déformation des fibres en fonction du temps pour des conditions où le fluage thermique est négligeable. Ce phénomène est important car il peut constituer un facteur limitant pour la durée de vie des composites dans les réacteurs.

2. Résultats et discussion

2.1. Caractérisation des fibres HNS et TSA3

L'une des techniques les plus utilisées pour la réalisation de cette étude a été l'imagerie MET (Microscopie Electronique en Transmission).[1] Ainsi, la Figure 2 montre en détail la microstructure des fibres (a) HNS et (b) TSA3. Les fibres sont constituées de grains de SiC de structure cubique (3C-SiC). On note également la présence de zones blanches disposées aux joints de grain et points triples attribuées à l'accumulation de *C* libre turbostratique. On observe également la présence de défauts d'empilement (DE) en quantité significative sur les deux images. Les densités linéaires de DE (ρ_{DE}) ont été estimées en utilisant ImageJ,[3] un logiciel d'analyse d'image. Pour les fibres HNS, on obtient une ρ_{DE} de 0,29±0,1 nm^{-1} et 0,18±0,1 nm^{-1} pour les fibres de TSA3. En outre, la moyenne des diamètres de Féret minimales et maximales donnent respectivement, 26 et 36 nm pour les fibres HNS et 141 et 210 nm pour les fibres TSA3.

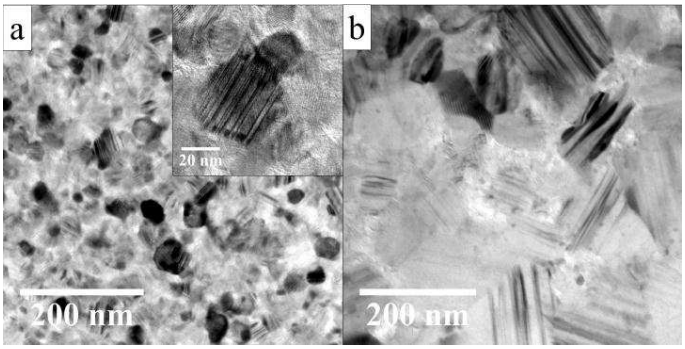

Fig. 2. Détail de la microstructure des fibres (a) Hi Nicalon s et (b) Tyranno SA3. Les motifs rayés intra-granulaires sont caractéristiques des densités de défauts planaires élevées.

Une autre technique de caractérisation largement utilisée dans ce travail a été la micro-spectroscopie Raman (μRS). Il s'agit d'une technique de caractérisation basée sur la diffusion inélastique de la lumière due à son interaction avec la matière à analyser. Les paramètres caractéristiques des spectres obtenus sont l'intensité, la largeur de bande ainsi que le nombre d'onde. Ces paramètres fournissent des informations utiles relatives à la distribution des phases et sur les liaison chimiques dans le SiC.[4] Le SiC est connu pour avoir de nombreux polytypes, les 3C-SiC et 6H-SiC étant les plus courants.[5] Le Tableau 1 montre les positions des pics Raman pour les deux polytypes et la Figure 3 les spectres Raman typiques des fibres HNS et TSA3 comparés

[1] Les démarches expérimentales en concernant la préparation des échantillons pour observation MET ainsi que la configuration des différents appareils utilisés (MET, MEB-E, Raman, etc…) sont détaillées dans le chapitre 4 du manuscrit original.

à celui du 6H-SiC monocristallin. Le spectre du monocristal montre de nombreux pics attribués aux différents modes actifs de la structure wurtzite, de symétrie C_{6v} pour les polytypes hexagonaux. On note également que l'absence de défauts permet l'observation de pics de deuxième ordre plus faibles situés autour de 500 cm^{-1} et entre 1400–1850 cm^{-1}.

Néanmoins, les spectres Raman des fibres SiC diffèrent sensiblement de celui du monocristal. En effet, leur microstructure polycristalline et le *C* libre observés sur la Figure 2 induisent l'apparition de différents pics. Les pics situés entre les nombre d'ondes 700–1000 cm^{-1} sont caractéristiques du SiC de structure cubique comme indiqué dans le Tableau 1. On peut également observer l'apparition de pics satellites autour de 766 cm^{-1}. Ces pics ont été attribués à une combinaison de domaines de différents polytypes et à une distribution quasi périodique de défauts d'empilement, [4,6] visibles sur la Figure 2. En outre, la présence de deux pics de haute intensité localisés entre 1200–1800 cm^{-1} est attribuée au *C* libre intra-granulaire. En effet, malgré la faible teneur en *C* dans les fibres (*C/Si*~1,03-1,2), ces pics masquent le signal provenant des liaisons *Si-C* en raison du rendement très important des liaisons *C-C*.[7] Finalement, concernant la signature Raman de ces liaisons, le pic G, centré autour 1581 cm^{-1}, est attribué à des structures graphitiques et le pic D, centré autour 1331 cm^{-1} à des liaisons mixtes sp^2-$sp^{2/3}$.[6]

Tableau 1 Pics Raman pour les polytypes 3C- et 6H-SiC[5]

Polytype	$h^1=q/q_B$	Raman shift [cm^{-1}]			
		TA	TO	LA	LO
3C-SiC	0	-	796	-	972
6H-SiC	0	-	797	-	965
	2/6	145,150	789	-	-
	4/6	236,241		504,514	889
	6/6	266	767	-	-

[1]hexagonalité

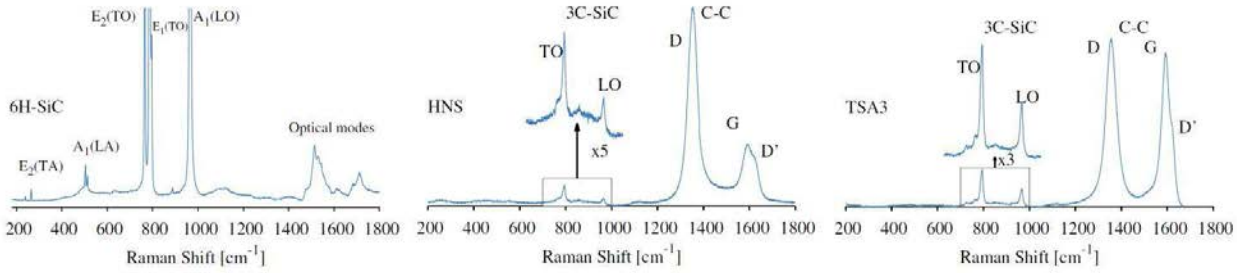

Fig. 3. Spectres Raman acquis en surface d'un monocristal 6H-SiC et de fibres SiC HNS et TSA3.

2.2. Amorphisation sous irradiation aux ions en régime de ralentissement nucléaire

Dans cette partie, la dégradation des propriétés physico-chimiques du SiC due à l'amorphisation sous irradiation en régime de ralentissement nucléaire a été étudiée. Ce processus de perte de l'ordre cristallin se produit suite à l'accumulation de défauts créés par collisions élastiques entre la particule incidente et les atomes du réseau cristallin. Les conditions d'amorphisation, bien caractérisées pour les monocristaux de SiC, n'ont jamais été étudiées pour les fibres de SiC de troisième génération et en particulier dans le cas des REP.

Ainsi, nous avons déterminé les conditions d'amorphisation des fibres HNS et TSA3 et nous les avons comparées à celles obtenues pour un matériau modèle tel que le 6H-SiC monocristallin. Pour étudier les effets de la microstructure sur le comportement de ces fibres, les fibres HNS et TSA3 ont été irradiées aux ions (4 MeV Au^{3+}) à plusieurs doses allant de 0,002 à 4 dpa à température ambiante (T_a) et à la plus forte dose pour des températures s'étendant de la T_a à 300 °C. Les fibres ainsi irradiées ont été caractérisées par µRs et imagerie MET.

La Figure 4 montre l'évolution des spectres Raman des monocristaux 6H-SiC et des fibres TSA3 et HNS après irradiation à T_a. Comme on peut le constater, il n'y a pas de différence significative entre les différents échantillons. Les pics Raman attribués aux liaisons *Si-C* subissent une perte d'intensité et un élargissement jusqu'à leur coalescence en un seul pic de basse intensité. En outre, la disparition progressive des liaisons *Si-C* conduit à de nouvelles liaisons homo-nucléaires *Si-Si* et *C-C* aboutissant à l'apparition de pics larges autour 500 cm^{-1} et 1400 cm^{-1}.

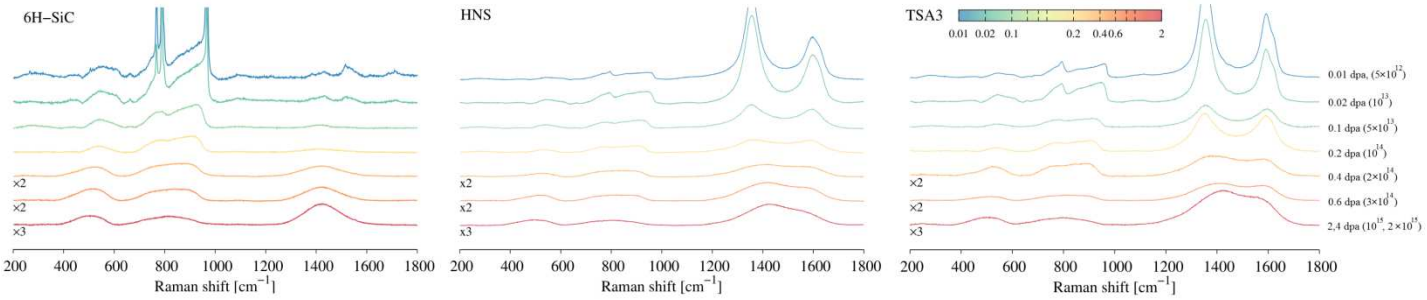

Fig. 4. Spectres Raman des monocristaux 6H-SiC et des fibres HNS et TSA3 après irradiation aux ions à T_a. La légende est en dpa et les doses entre parenthèses en cm^{-2} s^{-1}.

La Figure 5 montre les images MET et les clichés de diffraction aux électrons associés aux échantillons irradiés à plus forte dose, 4 dpa, (a) à T_a et (b) à 200 °C. Comme on peut le constater, les échantillons irradiés à T_a sont complétement amorphisés ce qui est en bon accord avec les spectres Raman.

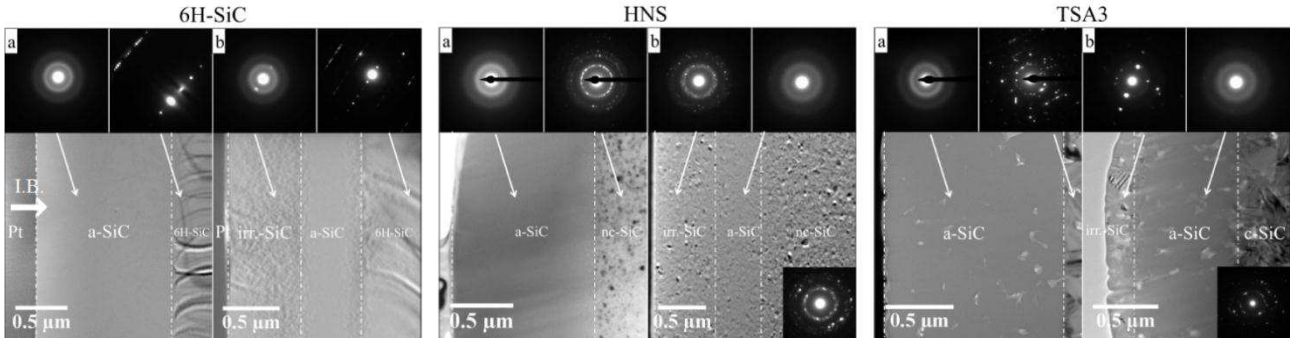

Fig. 5. Images MET de la section transverse des échantillons après irradiation à (a) T_a et (b) 200 °C.

A 200 °C, les échantillons présentent un certain niveau de cristallinité résiduel après irradiation ce qui situe par conséquent la température critique d'amorphisation totale (T_c) en dessous de 200 °C. T_c est définie comme la température au-dessus de laquelle le processus d'amorphisation est virtuellement impossible en raison de la recombinaison des défauts d'irradiation par agitation thermique.[8]

La cinétique d'amorphisation aux ions a été étudiée dans les monocristaux 6H-SiC en fonction du niveau de désordre chimique.[8,9] Ce paramètre, $\chi_{(C\text{-}C)}$, est obtenu à partir d'une analyse quantitative de l'évolution des spectres Raman et fait référence à l'ordre à courte distance. Il est défini par le ratio entre l'intensité des pics des liaisons homo-nucléaires *C-C* et celle des liaisons *Si-C*. $\chi_{(C\text{-}C)}$. Il prend la valeur 0 pour un ordre à courte distance parfait et 1 quand le désordre est total. L'ordre à courte distance décrit le niveau d'arrangement local des atomes qui peut être préservé même si l'ordre à longue distance n'est pas conservé.[9,10] Dans ce travail, l'utilisation de ce paramètre est limitée par le fort impact du *C* libre qui rend $\chi_{(C\text{-}C)}$ inexploitable. Le désordre chimique a donc été évalué à partir du ratio entre l'intensité des pics des liaisons *Si-Si* et *Si-C* ($\chi_{(Si\text{-}Si)}$), en faisant l'hypothèse que cette intensité est proportionnelle à la concentration des liaisons atomiques respectives.[9] La Figure 6.a présente l'évolution du $\chi_{(Si\text{-}Si)}$ en fonction de la dose pour les différents

échantillons. Ces données ont été modélisées à partir du modèle MSDA (Multi-Step Damage Accumulation en anglais) (Eq. 1) qui suppose que l'accumulation du dommage peut se produire en différentes étapes, caractéristiques de la irraditation.[11]

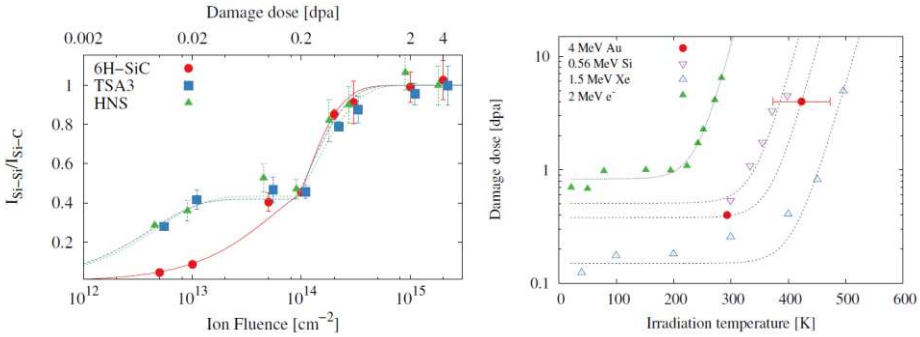

Fig. 6. (a) Evolution du processus d'amorphisation des échantillons irradiés à T_a en fonction de la dose. Les données expérimentales ont été modélisées avec le modèle MSDA (n=2). (b) Les conditions de seuil pour l'amorphisation des fibres de troisième génération (rouge) sont comparées aux valeurs trouvées dans la littérature pour des monocristaux irradiés avec différentes particules incidentes.

Les paramètres déterminés avec le modèle MSDA pour la cinétique d'amorphisation du monocristal 6H-SiC sont en bon accord avec les valeurs trouvées dans la littérature pour des expériences similaires.[8,10] Tous les échantillons présentent un point d'inflexion autour de 10^{14} cm^{-2} (0,2 dpa) et une amorphisation totale autour de 3×10^{14} cm^{-1} (0,6 dpa). Finalement, sur la Figure 6.b, on peut observer que les fibres HNS et TSA3 présentent une dose seuil à l'amorphisation aux ions similaire à celle du monocristal 6H-SiC indépendamment de leur microstructure, composition et polytype.

Il est admis que les joints de grain agissent comme des puits pour les défauts d'irradiation mais cela impose néanmoins une gamme de taille de grain optimisée. En effet, même si une taille de grain réduite facilite l'élimination des défauts ponctuels, l'énergie libre du système associée à une forte densité de joints de grain peut favoriser le processus d'amorphisation.[12] Dans le cas du SiC, le rôle de la microstructure sur la résistance à l'amorphisation est un sujet controversé. En effet, il est possible de trouver des études expérimentales et des simulations contradictoires en ce qui concerne la résistance à l'amorphisation du SiC comportant des microstructures fines.[13–16] Dans cette étude, la similarité des conditions de seuil à l'amorphisation du 6H-SiC, des fibres TSA3 et HNS suggère que la microstructure de ces fibres n'est pas suffisamment fine y compris pour les fibres HNS qui ont une taille de grain de 20 nm.

2.3. Effets du recuit thermique sur les fibres amorphisées aux ions

L'amorphisation du SiC aux ions est un facteur prépondérant de la dégradation de ses propriétés physico-chimiques.[17] Néanmoins, il a déjà été montré que la restauration de ces propriétés et la recristallisation du SiC amorphisé était possible par un processus de recuit thermique à hautes températures. Il faut cependant noter que ce processus de recuit thermique conduit également à la fissuration de la couche recristallisée dans le cas des monocristaux du SiC.[10,19] Afin d'approfondir ce sujet, des essais de recuit thermique *in situ* ont été réalisés en utilisant un MEB (Microscope Electronique à Balayage) environnemental disposant d'un porte-échantillon chauffant (25-1500 °C).

La Figure 7 montre un exemple des résultats obtenus lors de ces essais. On observe que la fissuration induite par le recuit thermique n'est pas spécifique au SiC monocristallin car ce phénomène est également observé dans les fibres. Néanmoins, en raison du faible diamètre des fibres TSA3 (~7,5 µm) et

HNS (~12 μm) l'étude systématique de ce phénomène a été réalisée en utilisant des monocristaux de 6H-SiC recuits avec différentes rampes de température (1–30 °C min^{-1}) et en observant une seule zone.

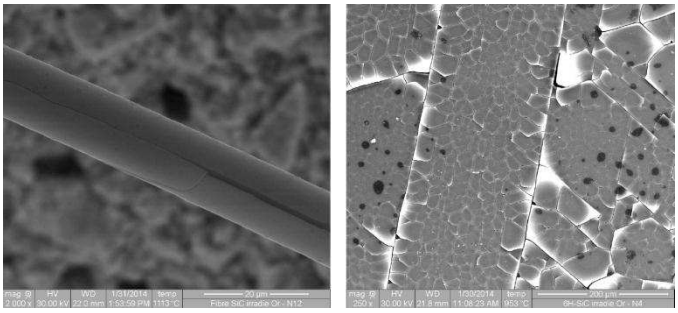

Fig. 7. Fissuration des fibres HNS (à gauche) et des monocristaux 6H-SiC (à droite) après recuit thermique à haute température.

Il a été montré que les contraintes qui donnent lieu à cette fissuration ne sont pas issues d'une différence du coefficient de dilatation thermique entre la couche irradiée et le substrat. Il s'agit en fait d'un processus contrôlé thermiquement. Comme le montre la Figure 8.a, lorsque l'on augmente la vitesse d'échauffement, la température à laquelle les fissures vont apparaître augmente et le temps entre le début de la fissuration et la saturation diminue. Les valeurs de saturation ne montrent pas de corrélation avec les conditions de recuit. La taille moyenne des fragments à saturation est de 150 μm^2.

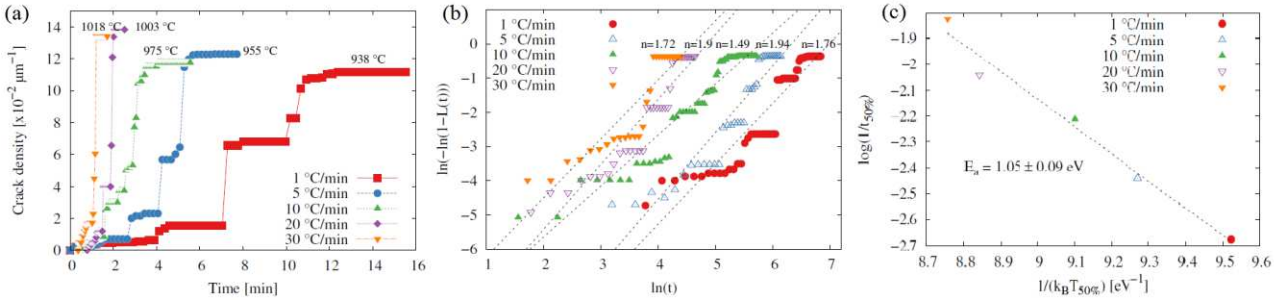

Fig. 8. Résultats obtenus à partir des expériences MEB-E *in situ* pour différentes rampes de température. (a) Evolution de la densité de fissures en fonction du temps, (b) détermination de l'exposant JMAK (Eq. 2) et (c) détermination de l'énergie d'activation du processus de fissuration.

La cinétique de fissuration a été modélisée en utilisant le modèle de Johnson-Mehl-Avrami-Kolmogorov (JMAK) (Eq. 1). Ce modèle a été initialement mis en œuvre pour décrire les cinétiques de transformation de phase en fonction de la température et du temps en conditions de recuit isothermes. Les paramètres *n* et *K(T)* fournissent une information sur le type de transformation et sa dépendance à la température. Il a également été montré que l'utilisation de ce modèle avec des conditions de chauffage linéaire conduit à une forme équivalente avec $n_{iso}=2n_{lin}$.[19] Comme on peut l'observer sur la Figure 8.b, cette équation permet de modéliser le processus de fissuration avec *n=1,5–2* et conduit à une énergie d'activation (E_a) 1,05 eV (Figure 8.c). Cette E_a a été déterminée en utilisant l'Eq. 2, où $t_{50\%}$ représente le temps nécessaire pour arriver à 50% de la valeur de saturation de fissuration et $T_{50\%}$ la température de l'échantillon à $t_{50\%}$.

$$\rho_{fis}(t,T) = A(1 - e^{-(K(T)t)^n}) \quad (1)$$

$$log(\frac{1}{t_{50\%}}) = C - (\frac{E_a^{crack}}{k_B})\frac{1}{T_{50\%}} \quad (2)$$

Même s'il s'agit d'une approximation phénoménologique du phénomène de fissuration et que les valeurs trouvées ne peuvent être directement reliées à des transformations physiques de la couche amorphisée, on peut noter le bon accord avec les valeurs représentatives du processus de recristallisation où n=2,25[18] et $E_{recryst}$ =0,65[10]–2,61[18] eV.

Dans la mesure où le phénomène de recristallisation a été identifié comme une cause potentielle de défaillance mécanique, des essais de recuit *in situ* ont été réalisés en utilisant un MET équipé d'un porte-échantillons chauffant. La Figure 9 montre une comparaison des microstructures observées au MET après des traitements thermiques (a) dans le MEB-E et (b) dans le MET pour les monocristaux de 6H-SiC. On constate que les deux microstructures obtenues sont similaires, ce qui indique que les processus de recristallisation sont bien identiques d'un essai à l'autre. Il est généralement admis que le processus de recristallisation peut être divisé en deux étapes. La première correspond à une étape de densification de la couche irradiée amorphe à mesure que l'interface amorphe-cristallin (a-c) croît par épitaxie. La deuxième étape concerne la recristallisation colonnaire de la couche amorphe une fois que l'épaisseur de l'interface a-c atteint 100 nm. La couche recristallisée présente une coexistence de polytypes 6H et 3C.

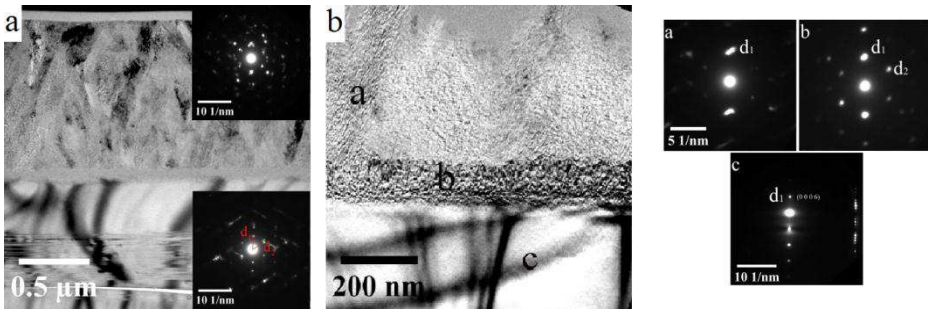

Fig. 9. Images MET du détail de la microstructure finale du monocristal 6H-SiC après traitements thermiques *in situ* (a) MEB-E et (b) MET.

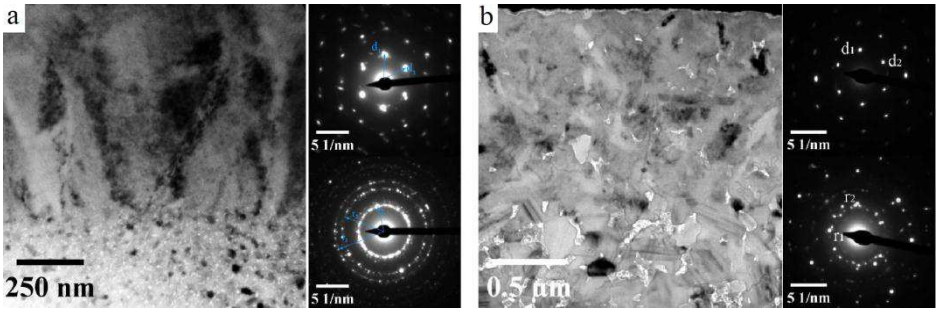

Fig. 10. Images MET du détail de la microstructure finale des fibres SiC (a) HNS et (b) TSA3 après le traitement thermique *in situ* MET.

La température de recristallisation de 900 ºC, est en bon accord avec la plage de températures pour laquelle la fissuration a lieu. Pour déterminer quelle est l'influence de la microstructure du substrat dans le processus de recristallisation, des essais de recuit *in situ* en MET ont été réalisés sur les fibres HNS et TSA3 amorphisées. La Figure 10 montre la microstructure finale des couches recristallisées des deux fibres. Dans ce cas, la couche recristallisée ne montre pas de changement de polytype par rapport au substrat et les températures de recristallisation sont respectivement de 900 ºC et 930 ºC pour la fibre HNS et TSA3. Comme dans le cas du monocristal 6H-SiC, ces températures sont en bon accord avec les températures de fissuration reportées. On observe enfin que le déroulement de la phase de recristallisation dépend fortement de l'état de la couche amorphe et du substrat. En effet, le substrat nanophasé de la fibre HNS évite la recristallisation par épitaxie et provoque une recristallisation colonnaire. Par contre, la présence de phases riches en *C* dans la

couche amorphe de la TSA3 génère une recristallisation spontanée avec des grains sans orientation préférentielle.

2.4. Caractérisation des propriétés mécaniques sous irradiation aux ions en régime de ralentissement électronique et mixte

L'intérêt de cette partie se situe dans le cadre des travaux menés sur des réacteurs refroidis à gaz de Génération IV. Ces réacteurs ont la particularité de fonctionner à températures nominales (600–1000 ºC)[1] où l'amorphisation n'est plus un facteur limitant. Néanmoins, à ces températures, d'autres phénomènes peuvent limiter la durée de vie des composites et doivent être étudiés. L'un des principaux phénomènes est le fluage d'irradiation. Dans ce contexte, différents essais de traction *in situ* en utilisant une machine de traction dédiée ont été réalisés sur des fibres TSA3 sous irradiation en régime de ralentissement électronique et mixte.

Il a été constaté que les fibres testées sous irradiation avaient subi des déformations significatives en fonction du temps pour un niveau de sollicitations mécanique et thermique où le fluage thermique est négligeable. En outre, à partir des essais d'irradiation aux ions 12 MeV C^{4+} présentés sur la Figure 10, il a pu être observé que la déformation sous irradiation était plus élevée à basse température. Ce comportement est dû au couplage des phénomènes de gonflement et de fluage d'irradiation. La déformation du SiC est alors due à une anisotropie du gonflement induite par la charge imposée.[20] La valeur à saturation du gonflement diminue avec la température et atteint une valeur minimale vers 1000 ºC[21].

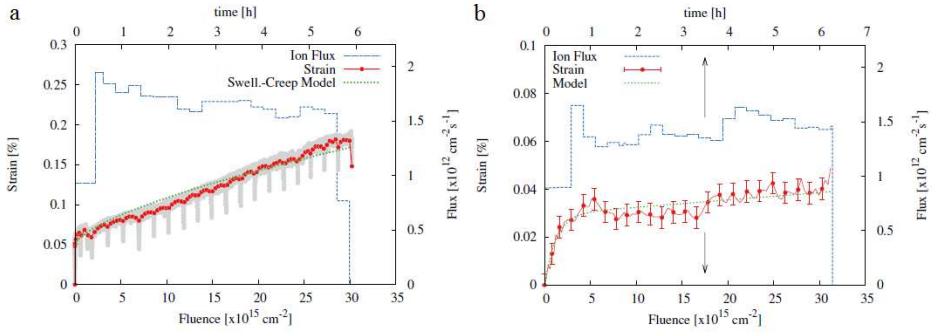

Fig. 10. Déformation des fibres TSA3 à une contrainte de 300 MPa et un flux d'ions constant (~1,5×10¹² cm⁻² s⁻¹) à (a) Ta et (b) 1000ºC.

La caractérisation de l'influence des conditions expérimentales sur le fluage d'irradiation a été réalisée à 1000 ºC avec des ions Xe^{23+} de 92 MeV. On considère que la vitesse de fluage d'irradiation, ε_{IC}, est définie par l'Eq. 3, avec B_0 la complaisance de fluage d'irradiation, σ la contrainte axiale, Φ le flux et Φ_c le flux de seuil. Deux types d'essais ont été réalisés. Le premier est destiné à la détermination de l'exposant n de la contrainte sous un flux constant (5×10^9 cm^{-2}s^{-1}) avec des paliers de contraintes croissants de 300, 600 et 900 MPa. De façon similaire, la détermination de l'exposant de flux m a été réalisée à partir d'essais à contrainte constante (300 MPa) et avec des paliers de flux croissants de 10^9, 5×10^9 et 10^{10} cm^{-2}s^{-1}.

$$\dot{\epsilon}_{IC} = C(\dot{\phi},\dot{\phi}_c)B_0\sigma^n(\dot{\phi}-\dot{\phi}_c)^m\ ; \qquad C(\dot{\phi},\dot{\phi}_c) = \begin{cases} 0 & \text{if } \dot{\phi} \le \dot{\phi}_c \\ 1 & \text{if } \dot{\phi} > \dot{\phi}_c \end{cases} \tag{3}$$

Avec ces conditions d'irradiation, il a ainsi pu être montré que la vitesse de déformation présente une dépendance linéaire (m~1.1) avec le flux en accord avec la littérature,[21,23] et en racine carrée (n~0,4) avec la contrainte. Ce dernier paramètre diffère des valeurs trouvées dans la littérature où une valeur n=1 est le plus souvent rencontré.[21,23] En faisant l'hypothèse d'une vitesse de déformation proportionnelle à la

contrainte, la complaisance B_0 est estimée à 10^{-5} $MPa^{-1}dpa^{-1}$. Cette valeur est cependant deux ordres de grandeurs supérieures à de celles rapportées pour le SiC polycristallin irradié aux neutrons.[20] Une valeur de B_0 aussi élevée suggère que le régime de ralentissement des ions peut jouer un rôle important sur le phénomène de fluage d'irradiation. C'est pourquoi, des essais similaires à ceux décrit précédemment ont été réalisés mais en utilisant un dégradeur d'énergie. Le dégradeur d'énergie permet de décaler les pics d'implantation des ions à différentes profondeurs dans la fibre, ce qui permet d'obtenir des conditions d'irradiations en régime de ralentissement mixte et d'accroître l'endommagement dans la fibre. Dans ces conditions d'essai, le paramètre *n* est proche de 1 (0,94), et B_0 chute à une valeur de 10^{-6} $MPa^{-1}dpa^{-1}$. Pour faciliter la comparaison entre les deux essais, la Figure 11.a présente les courbes de déformation, en fonction de la dose en dpa, à 300 MPa et 1000 °C des fibres irradiées pour une fluence équivalente avec et sans dégradeur. Il apparaît clairement que bien que l'endommagement de la fibre soit plus élevé dans le cas d'une irradiation avec le dégradeur d'énergie (Figure 11.b), c'est cependant avec les irradiations en régime de ralentissement électronique que le fluage d'irradiation est le plus important.

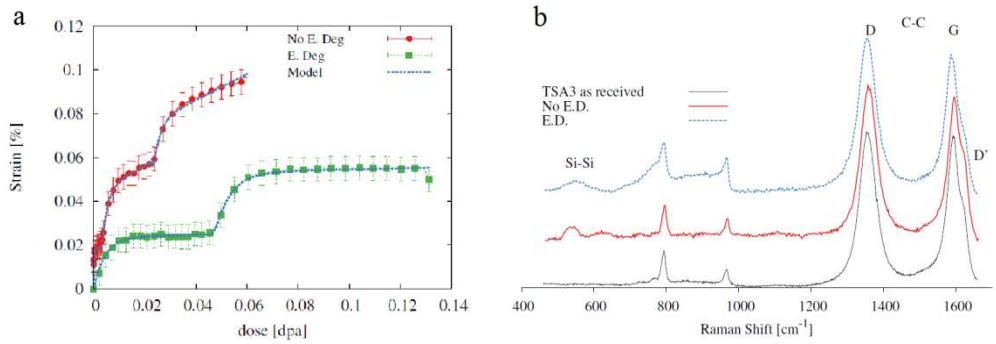

Fig. 11. (a) Modélisation des courbes expérimentales avec (E. Deg) et sans (No E. Deg.) dégradeur d'énergie en fonction de la dose avec l'Eq. 2. (b) Les spectres Raman des fibres TSA3 après les essais de traction *in-situ*.

Dans le cas du SiC, la contribution du mouvement des dislocations aux phénomènes liés à une déformation plastique ne sont présents qu'à des températures largement supérieures à celles de ces essais, c'est-à-dire 1700 °C[23]. Ce mécanisme peut donc être exclu. Pour le fluage thermique, les exposants de contrainte *n* prennent différentes valeurs en fonction des mécanismes de fluage impliqués. Ainsi, une valeur de n=1 correspond à des mécanismes de diffusion tandis que des valeurs n=2, 3 correspondent à des glissements aux joints de grain.[23] Dans le cas des fibres TSA3 sous irradiation en régime de ralentissement nucléaire, le fluage pourra être causé par un glissement de grains renforcé par un mécanisme de diffusion plus important, en raison de la présence d'importante quantité d'interstitiels et de lacunes produites par les cascades de déplacement.[24] Dans le cas d'irradiation en régime de ralentissement électronique, les différences obtenues entre les essais réalisés avec et sans le dégradeur d'énergie peuvent être expliquées par la relaxation de contraintes dans le volume de la pointe thermique créé par l'ion incident.[25]

3. Conclusion

L'utilisation des fibres SiC de troisième génération, Tyranno SA3 (TSA3) et Hi Nicalon S (HNS), pour le renforcement de composites céramiques dédiées aux applications nucléaires impose l'étude de leur stabilité microstructurale et de leur comportement mécanique sous irradiation. En ce qui concerne la stabilité sous irradiation, la cinétique d'amorphisation des fibres a été étudiée et comparée à celle d'un matériau modèle, 6H-SiC monocristallin, sans que des différences significatives puissent être observées. La dose seuil d'amorphisation totale a été évaluée à ~0,4 dpa à température ambiante. En outre, aucune amorphisation complète n'a pas être obtenue pour des températures d'irradiation supérieures à 200 °C. Les échantillons

amorphes ont ensuite été recuits thermiquement ce qui a conduit, pour des températures élevées, à leur recristallisation mais également à une fissuration et une délamination de la zone irradiée. L'analyse de ces résultats a permis de conclure que ce processus d'endommagement était activé thermiquement avec une énergie d'activation de 1,05 eV. En ce qui concerne le comportement mécanique, le fluage d'irradiation des fibres TSA3 a été étudié en utilisant une machine de traction *in situ* implantée sur deux plateformes d'irradiation aux ions. On montre que sous irradiation (12 MeV C^{4+} et 92 MeV Xe^{23+}) ces fibres se déforment en fonction du temps avec des chargements thermique et mécanique où le fluage thermique est négligeable. De plus, cette déformation est plus élevée pour les faibles températures d'irradiation en raison d'un couplage entre le gonflement et le fluage d'irradiation. Pour des températures plus élevées voisines de 1000°C, le gonflement devient négligeable ce qui permet l'étude spécifique du fluage d'irradiation dont la vitesse de déformation présente une dépendance linéaire au flux d'ions et en racine carrée avec la charge appliquée. Finalement, il a également été montré que le fluage d'irradiation croît lorsque la contribution du régime de ralentissement électronique augmente.

4. Références

1. Yvon, P. & Carré, F. Structural materials challenges for advanced reactor systems. *J. Nucl. Mater.* **385,** 217–222 (2009).

2. Snead, L. L. *et al.* Silicon carbide composites as fusion power reactor structural materials. *J. Nucl. Mater.* **417,** 330–339 (2011).

3. Schneider, C. A., Rasband, W. S. & Eliceiri, K. W. NIH Image to ImageJ: 25 years of image analysis. *Nat Meth* **9,** 671–675 (2012).

4. Gouadec, G. & Colomban, P. Raman Spectroscopy of nanomaterials: How spectra relate to disorder, particle size and mechanical properties. *Prog. Cryst. Growth Charact. Mater.* **53,** 1–56 (2007).

5. Nakashima, S. & Harima, H. Raman Investigation of SiC Polytypes. *Phys. status solidi* **162,** 39–64 (1997).

6. Colomban, P., Gouadec, G. & Mazerolles, L. Raman analysis of materials corrosion: the example of SiC fibers. *Mater. Corros.* **53,** 306–315 (2002).

7. Havel, M. & Colomban, P. Raman and Rayleigh mapping of corrosion and mechanical aging in SiC fibres. *Compos. Sci. Technol.* **65,** 353–358 (2005).

8. Kerbiriou, X. *et al.* Amorphization and dynamic annealing of hexagonal SiC upon heavy-ion irradiation: Effects on swelling and mechanical properties. *J. Appl. Phys.* **105,** 073513 (2009).

9. Sorieul, S., Costantini, J.-M., Gosmain, L., Thomé, L. & Grob, J.-J. Raman spectroscopy study of heavy-ion-irradiated α-SiC. *J. Phys. Condens. Matter* **18,** 5235–5251 (2006).

10. Miro, S., Costantini, J.-M., Huguet-Garcia, J. & Thomé, L. Recrystallization of hexagonal silicon carbide after gold ion irradiation and thermal annealing. *Philos. Mag.* **94,** 3898–3913 (2014).

11. Jagielski, J. & Thomé, L. Damage accumulation in ion-irradiated ceramics. *Vacuum* **81,** 1352–1356 (2007).

12. Shen, T. D. Radiation tolerance in a nanostructure: Is smaller better? *Nucl. Instruments Methods Phys. Res. Sect. B Beam Interact. with Mater. Atoms* **266,** 921–925 (2008).

13. Jiang, W. *et al.* Response of nanocrystalline 3C silicon carbide to heavy-ion irradiation. *Phys. Rev. B* **80,** 161301 (2009).

14. Jiang, W., Wang, H., Kim, I., Zhang, Y. & Weberb, W. J. Amorphization of nanocrystalline 3C-SiC irradiated with Si ions. *J. Mater. Res* **25,** 2341–2348 (2010).

15. Jamison, L., Xu, P., Shrindharan, K. & Allen, T. in (Sundaram, S. K., Fox, K., Ohji, T. & Hoffman, E.) 161–168 (John Wiley & Sons, Inc., 2011). doi:10.1002/9781118144527

16. Jamison, L. *et al.* Experimental and ab initio study of enhanced resistance to amorphization of nanocrystalline silicon carbide under electron irradiation. *J. Nucl. Mater.* **445,** 181–189 (2014).

17. Katoh, Y., Snead, L. L., Szlufarska, I. & Weber, W. J. Radiation effects in SiC for nuclear structural applications. *Curr. Opin. Solid State Mater. Sci.* **16,** 143–152 (2012).

18. Hoĭgen, A., Heera, V., Eichhorn, F. & Skorupa, W. Annealing and recrystallization of amorphous silicon carbide produced by ion implantation. *J. Appl. Phys.* **84,** 4769 (1998).

19. Woldt, E. The relationship between isothermal and non-isothermal description of Johnson-Mehl-Avrami-Kolmogorov kinetics. *J. Phys. Chem. Solids* **53,** 521–527 (1992).

20. Katoh, Y., Snead, L. L., Parish, C. M. & Hinoki, T. Observation and possible mechanism of irradiation induced creep in ceramics. *J. Nucl. Mater.* **434,** 141–151 (2013).

21. Snead, L. L., Katoh, Y. & Nozawa, T. in *Compr. Nucl. Mater.* 215–240 (Elsevier Inc., 2012). doi:10.1016/B978-0-08-056033-5.00093-8

22. Scholz, R., Mueller, R. & Lesueur, D. Light ion irradiation creep of Textron SCS-6™ silicon carbide fibers. *J. Nucl. Mater.* **307-311,** 1183–1186 (2002).

23. Sauder, C. & Lamon, J. Tensile Creep Behavior of SiC-Based Fibers With a Low Oxygen Content. *J. Am. Ceram. Soc.* **90,** 1146–1156 (2007).

24. Mathews, J. R. & Finnis, M. W. Irradiation creep models - an overview. *J. Nucl. Mater.* **159,** 257–285 (1988).

25. Trinkaus, H. Thermal spike model for irradiation creep of amorphous solids: Comparison to experimental data for ion irradiated vitreous silica. *J. Nucl. Mater.* **246,** 244–246 (1997).

Abstract

The use of third generation SiC fibers, Tyranno SA3 (TSA3) and Hi Nicalon S (HNS), as reinforcement for ceramic composites for nuclear applications requires the characterization of its structural stability and mechanical behavior under irradiation. Regarding the radiation stability, ion-amorphization kinetics of these fibers have been studied and compared to the model material, i.e. 6H-SiC single crystals, with no significant differences. For all samples, full amorphization threshold dose yields ∼0.4 dpa at room temperature and complete amorphization was not achieved for irradiation temperatures over 200 °C. Successively, ion-amorphized samples have been thermally annealed. It is reported that thermal annealing at high temperatures not only induces the recrystallization of the ion-amorphized samples but also causes unrecoverable mechanical failure, i.e. cracking and delamination. Cracking is reported to be a thermally driven phenomenon characterized by activation energy of 1.05 eV. Regarding the mechanical irradiation behavior, irradiation creep of TSA3 fibers has been investigated using a tensile device dedicated to *in situ* tests coupled to two different ion-irradiation lines. It is reported that ion-irradiation (12 MeV C^{4+} and 92 MeV Xe^{23+}) induces a time-dependent strain under loads where thermal creep is negligible. In addition, irradiation strain is reported to be higher at low irradiation temperatures due to a coupling between irradiation swelling and irradiation creep. At high temperatures, near 1000 °C, irradiation swelling is minimized hence allowing the characterization of the irradiation creep. Irradiation creep rate is characterized by a linear correlation between the ion flux and the strain rate and square root dependence with the applied load. Finally, it has been reported that the higher the electronic energy loss contribution to the stopping regime the higher the irradiation creep of the fiber.

Résumé

L'utilisation des fibres SiC de troisième génération, Tyranno SA3 (TSA3) et Hi Nicalon S (HNS), pour le renforcement de composites céramiques dédiées aux applications nucléaires impose létude de leur stabilité microstructurale et de leur comportement mécanique sous irradiation. En ce qui concerne la stabilité sous irradiation, la cinétique d'amorphisation des fibres a été étudiée et comparée à celle d'un matériau modèle, 6H-SiC monocristallin, sans que des différences significatives puissent être observées. La dose seuil d'amorphisation totale a été évaluée à ∼0,4 dpa à température ambiante. En outre, aucune amorphisation complète n'a pas être obtenue pour des températures d'irradiation supérieures à 200 °C. Les échantillons amorphes ont ensuite été recuits thermiquement ce qui a conduit, pour des températures élevées, à leur recristallisation mais également à une fissuration et une délamination de la zone irradiée. L'analyse de ces résultats a permis de conclure que ce processus d'endommagement était activé thermiquement avec une énergie d'activation de 1,05 eV. En ce qui concerne le comportement mécanique, le fluage d'irradiation des fibres TSA3 a été étudié en utilisant une machine de traction in situ implantée sur deux plateformes d'irradiation aux ions. On montre que sous irradiation (12 MeV C^{4+} et 92 MeV Xe^{23+}) ces fibres se déforment en fonction du temps avec des chargements thermique et mécanique o le fluage thermique est négligeable. De plus, cette déformation est plus élevée pour les faibles températures d'irradiation en raison d'un couplage entre le gonflement et le fluage d'irradiation. Pour des températures plus élevées voisines de 1000 °C, le gonflement devient négligeable ce qui permet l'étude spécifique du fluage d'irradiation dont la vitesse de déformation présente une dépendance linéaire au flux d'ions et en racine carrée avec la charge appliquée. Finalement, il a également été montré que le fluage d'irradiation croît lorsque la contribution du régime de ralentissement électronique augmente.